Imperial College London

Synthesis, Physicochemical Characterisation and Biological Evaluation of Polymer-Functionalised Gold Nanoparticles for Cancer Treatment

Marie Bachelet

Department of Chemical Engineering
Imperial College London
South Kensington Campus
London, SW7 2AZ
United Kingdom

THESIS SUBMITTED IN ACCORDANCE WITH THE REQUIREMENTS OF IMPERIAL COLLEGE LONDON FOR THE DEGREE OF DOCTOR OF PHILOSOPHY. *VIVA VOCE* EXAMINATION PASSED ON 28TH JUNE 2017.

Declaration of originality

This thesis is submitted for the degree of Doctor of Philosophy at Imperial College London. I can confirm the research presented within this thesis is the result of my own work. Any results obtained in collaboration are specifically indicated and acknowledged within the text. The research reported herein was carried out under the supervision of Dr Rongjun Chen between October 2013 and February 2017.

This thesis contains 121 figures, 18 tables, 14 schemes and 75143 words in length excluding the bibliography and appendices.

This thesis does not contain material that has been previously accepted for the award of any qualification at Imperial College London or any other educational institution. Sections of this work have been presented at:

- the Imperial College PhD symposium, department of Chemical engineering, London, UK (June 2016);
- the Materials Research Society Spring Meeting, Phoenix, U.S. (March 2016); the 4th Workshop on biomaterials and their interactions with biological and model membranes, Salou, Spain (October 2015);
- the "Fundamentals and Applications of Lipid Membrane Biophysics" workshop, East Horsley, UK (September 2015);
- the "Crossroads of Particle Science and Technology" joint conference of the 5th UK-China and 13th UK Particle Technology Forum, Leeds, UK (July 2015);
- the 4th Postgraduate Symposium on Nanotechnology, Birmingham, UK (December 2014);
- the Imperial College Summer Research Symposium, London, UK (July 2014) and the Chemical Engineering PhD symposium, Imperial College London, UK (July 2014).

Parts of this work have been or will be reported in the following publications:

M. Bachelet, R. Chen. Doxorubicin-loaded, endosomolytic polymer-functionalised gold nanoparticles for overcoming multidrug resistance through combined chemotherapy and phototherapy. *Manuscript in preparation.*

M. Bachelet, T. Ellis, B. Othman, D. Zhou, A. Porter, R. Chen, Hybrid biomimetic gold nanoparticles with pH-triggered cytoplasmic delivery enhancement. *Manuscript in preparation.*

M. Bachelet, R. Chen. Self-assembly of PEGylated gold nanoparticles with satellite structures as seeds. *Chemical Communications* **2016**, *52*, 9542-9545.

Bachelet, M. Design of pH-responsive gold nanoparticles in oncology. *Materials Science and Technology* **2016**, *32*, 794-804.

Marie Bachelet
April 2017

Published by:

Marie Bachelet
Department of Chemical Engineering
Imperial College London
South Kensington Campus London
SW7 2AZ United Kingdom

'The copyright of this thesis rests with the author and is made available under a Creative Commons Attribution Non-Commercial No Derivatives licence. Researchers are free to copy, distribute or transmit the thesis on the condition that they attribute it, that they do not use it for commercial purposes and that they do not alter, transform or build upon it. For any reuse or redistribution, researchers must make clear to others the licence terms of this work'

Copyright © 2017, Marie Bachelet

Acknowledgements

The PhD thesis is a long adventure of 4 years. Today, I feel glad to have met and been through the multiple demotivating obstacles along the way but this is not without a certain nostalgia that I reach the finish line. The list of people who helped me, pushed me, encourage me, or were simply present, is long and I hope not to forget too many of them.

First of all, I would like to thank my supervisor, Dr. Rongjun Chen. Thank you for the consideration, the encouragements, the trust, the corrections, the weekly meetings and the group lunches and dinners.

My sincere acknowledgements go to the department of Chemical Engineering for providing me a full PhD scholarship but also to the Trustees of the IC Trust and the Old Centralians' Trust for enabling me to attend the 2016 Materials Research Society Spring Meeting and Exhibit, in Phoenix, USA.

Many thanks to Patricia Carry (ICP, DLS, FTIR), Andrew Macey (undergraduate laboratory tutorials, ICP), Dr. Roberto Ibarra Hernandez (laser), Dr. Ana Luz Quiroga Campano (flow cytometry) from the department of Chemical Engineering, Dr. Edward Parsons (AFM) from the department of Chemistry. Steve Rothery and the FILM facility (confocal microscopy) from the department of Life Science, Dr. Mahmoud Ardakani, Dr. Ecaterina Ware and Catriona McGilvery (SEM, TEM, EDX), Dr. Claudio Ferraro (porosimetry), Tim Ellis (cell fixing), Dr. Basmah Othman (TEM of fixed cells), Kella Kapnisi (DMA) and Ignacio Villar Garcia (XPS) from the department of Materials for their help in my experiments.

Special thanks to all my colleagues: Dr. Siyuan Chen, Kira Watkins, Michal Kopytynski, Shiqi Wang, Liwei Wu and Isabel Neto for their advice but mostly for all the good memories we have together in the lab as well as outside. I am so thankful to have spent the last 4 years with such remarkable persons.

Thank you to all the undergraduates and Msc students that I had the opportunity to supervise in our lab: Zhenbo Gao, Kingson Opasina, Bukki Adedapo, Yifan Zhan and to all

the students who supported me in the undergraduate teaching lab and in the Chemistry tutorials. It has been an impressive learning curve for me. I have even surprised myself to be able to teach Organic Chemistry (or at least the students make me believe it!). I am also very grateful to Yubai Zhang who worked with me on the hydrogel project and provided me some of her hydrogel samples.

Je souhaite remercier toute ma famille, ma maman, mon petit frère, Guy, mon grand-père et ma grand-mère qui ont toujours été très fiers bien que je n'aie jamais réussi à leur expliquer clairement ce que je faisais. Merci de croire en moi.

Now comes the time when I need to tell about the friends that I have met at Imperial. We have lived so many memorable moments that I would not exchange for anything. We have shared celebrations but also many frustrations, since yes, the PhD was part of our lives. The PhD life has been an amazing experience thanks to you and it will be hard leaving this place because of you. In no particular order: thank you Claudia Menichini, Diego Alonso Martinez, Franky Esteban Bedoya, Mark Allenby, Lisa Kleiminger, Manuela Nania, Nick Farandos, Saulius Lukauskas, Marine Michel, Selene Pirola, Assen Batcharov, Ajay Gupta, Akaki Jamburidze, James Freeman, Christiana Udoh, Paul Sapin, Oyeniyi Oyewunmi, Christoph Kirmse, Aly Taleb, Naima Ali, Axel Huerre, Diego Baresch, Vincent Poulichet, Angelo Pommella, Marc Tinguely, Marco de Corato, Niccolo Lebrun, my Imperial friends. Finally, thanks to the young consultants from TYC: Ascanio Digiacomo, Pahini Pandya, Andrew Leung, Esin Gurpinar, Frederike Jaeger, Luis Santos, Justin Tan, Alastair Gregory, Minh Ngoc Pham and Eliana Grant.

Thank you to all my friends outside Imperial. I wish to apologise for all the get-togethers I have missed. Thank you for still being there. See you very soon.

Last but not least, I wish to express my deepest gratitude to my life companion, Claudio Ferraro. Sharing my successes and failures has not been the easiest challenge but you have always managed to cheer me up and that is thanks to you that I made it. Gracias para seguir tomándome el pelo. Grazie a te.

To my grandmother

"The wise man, however, will avoid partial views of things. He will not, with the miser, look to gold and silver as the only blessings of life; nor will he, with the cynic, snarl at mankind for preferring them to copper and iron. He will contemplate society as the proper state of man, and its artificial but necessary institutions and principles will appear to him the correct and advantageous result of natural causes. That which is convenient is that which is useful, and that which is useful is that which is valuable. It is in the relative position of things one to the other that they are to be considered and estimated; and whilst a man makes use of them no otherwise than wisely to supply his wants and virtuous pleasures, the avaricious trader has no reason to call him a fool of nature, nor the moral philosopher to name him the victim of society."

— Michael Faraday

From 13th Lecture in 1818, Bence Jones, The Life and Letters of Faraday (1870), Vol. 1, 255.

Abstract

Most of the chemotherapeutics employed today are facing important limitations, including the inability to provide targeted therapy and intracellular drug degradation within the lysosomal compartments. These explain why the average survival rate, throughout all cancer types, is still as low as 50%. The aim of the present thesis is to develop multifunctional AuNPs for intracellular delivery.

PEGylated AuNPs were prepared via grafting poly(ethylene glycol) onto the AuNP surface. The influence of the PEG chain length and grafting densities on the colloidal stability, the grafted polymer conformation, the stealth character and the interparticle interactions have been extensively investigated. Longer chain lengths favoured the stability of the colloids in aqueous solution and the preparation of long-range and ordered assemblies via "flexible" interparticle interactions whereas shorter chain lengths led to denser layers and "hard-to-contact" spheres.

Highly stable biocompatible pH-responsive AuNPs were obtained through the grafting with the anionic poly(L-lysine isophthalamide) (PLP) conjugated with L-phenylalanine at 75 mol% (PP75). The polymer pH dependent coil-to-globule conformational change was retained between pH 5-6, tuned to the endosomal pH. The AuNPs@PP75 nanohybrids demonstrated a quick and highly reversible agglomeration-deagglomeration cycle.

Doxorubicin was loaded at 0.6 wt% onto the nanohybrids without compromising the overall stability in biological media and was effectively delivered into drug-resistant human uterus sarcoma cell line. The synergistic effect of the chemotherapy with photothermal treatment increased the killing efficiency by 6 folds compared to the conventional free drug.

The nanohybrids were finally entrapped into pH-responsive PLP hydrogels. The composite hydrogels retained a high pH-responsive swelling behaviour and demonstrated improved mechanical properties compared to the bare hydrogel. Controlled drug release ability and biocompatibility confirmed their suitability as potential cancer therapeutics via oral administration.

Table of contents

Declaration of originality 3

Acknowledgements 5

Abstract 11

Table of contents 13

List of Figures 19

List of Schemes 33

List of Tables 35

Nomenclature and abbreviations 37

Chapter 1 Introduction 43

1.1 AuNPs: definition, properties and scope of applications 44

1.1.1 Nanotechnology and nanoparticles 44

1.1.2 Introduction to AuNPs and past applications 45

1.1.3 Common synthesis methods 47

1.1.4 Properties and current applications 51

1.2 AuNPs in oncology 55

1.2.1 Current challenges in cancer therapy 55

1.2.2 AuNPs as a drug delivery carrier 56

1.2.3 Phototherapy 58

1.2.4 Imaging, sensing and diagnostics 59

1.2.5 Advantages and drawbacks of AuNPs compared to other nanoparticles 68

1.3 Design of AuNPs as cancer therapeutics 69

1.3.1 Common surface modification strategies 69
1.3.2 Colloidal stability and PEGylation 70
1.3.3 Therapeutics: drug loading, drug release and phototherapy 72
1.3.4 Targeting 73
1.3.5 Nanoparticles hydrogel composites 74
1.4 Polymeric hybrid AuNPs for intracellular delivery 76
1.4.1 Challenges for the drug delivery using nanoparticles 76
1.4.2 Enhancement of intracellular delivery 79
1.4.3 PP75 83
1.4.4 AuNPs for cytosolic delivery 85
1.5 Aims of the investigation 87
1.6 Research gaps, novelties and impacts of the investigation 89
1.7 Thesis outline 93
Chapter 2 Materials and Methods 95
2.1 Materials 96
2.2 Synthesis 97
2.2.1 Synthesis of AuNPs 97
2.2.2 Synthesis of AuNPs@PEG 97
2.2.3 Synthesis of PLP 98
2.2.4 Synthesis of PP75 99
2.2.5 Functionalisation of PP75 with cysteamine 100
2.2.6 Synthesis of AuNPs@PP75 101
2.2.7 Synthesis of AuNPs@DOX@PP75 101
2.2.8 Synthesis of PLP hydrogel and AuNPs@PP75/PLP hydrogel 101
2.3 Methods for the physico-chemical characterisation 102

2.3.1 UV-vis spectrophotometric measurement 102

2.3.2 Fluorescence measurement 109

2.3.3 Dynamic Light Scattering (DLS) and zeta potential measurement 110

2.3.4 Transmission Electron Microscopy (TEM) and Energy Dispersive X-ray Spectrometry (EDX) 112

2.3.5 Nuclear Magnetic Resonance (NMR) 113

2.3.6 Porosimetry via the Archimede method 114

2.3.7 Scanning Electron Microscopy (SEM) imaging 114

2.3.8 Atomic Force Microscopy (AFM) measurement 115

2.3.9 Determination of the gold amount in hydrogels via Inductively Coupled Plasma-Optical Emission Spectroscopy (ICP-OES) 116

2.3.10 X-ray photoelectron spectroscopy (XPS) measurement 116

2.3.11 Compression test using Dynamic Mechanical Analysis (DMA) 117

2.3.12 Swelling studies 119

2.4 Methods for the biological evaluation 119

2.4.1 Cells culture 119

2.4.2 Cytotoxicity measurement via alamarBlue assay 120

2.4.3 Cellular uptake quantification via inductively coupled plasma optical emission spectrometry (ICP-OES) and flow cytometry 121

2.4.4 TEM observation of intracellular localisation 123

2.4.5 Confocal laser scanning microscopy (CLSM) imaging 123

2.4.6 Phototherapy 125

Chapter 3 PEGylation of AuNPs: stability and assembly 127

3.1 Introduction 128

3.2 Results and discussion 130

3.2.1 AuNP characterisation 130

3.2.2 AuNPs@PEG synthesis and characterisation 136

3.2.3 Influence of the PEG concentration on the colloidal stability in different media 138

3.2.4 Grafting density 145

3.2.5 Polymer conformation 148

3.2.6 Serum protein adsorption 153

3.2.7 Cell viability assay 156

3.2.8 Assembly 157

3.3 Chapter summary 168

Chapter 4 pH-responsive nanohybrids 169

4.1 Introduction 170

4.2 Results and Discussion 172

4.2.1 Physico-chemical characterisation of AuNPs@PP75 172

4.2.2 pH-response 179

4.2.3 Reversibility of the pH response 188

4.2.4 Membrane interaction 192

4.2.5 In-vitro biological evaluation 195

4.3 Chapter summary 205

Chapter 5 Chemo- and phototherapy 207

5.1 Introduction 208

5.2 Results and discussion 209

5.2.1 Synthesis strategies 209

5.2.2 Drug loading optimisation 212

5.2.3 Grafting with PP75 215

5.2.4 Physico-chemical characterisation 221

5.2.5 Biological evaluation of the multimodal therapy 223

5.3 Chapter summary 233

Chapter 6 AuNPs loaded hydrogels 235

6.1 Introduction 236

6.2 Results and discussion 238

6.2.1 Optimisation of the synthesis of hybrid hydrogels 238

6.2.2 Characterisation of the hybrid hydrogels 242

6.2.3 pH-responsiveness 246

6.2.4 Cell viability 252

6.2.5 Potential of hybrid hydrogels in therapy 253

6.3 Chapter summary 256

Chapter 7 257

7.1 Conclusions 258

7.1.1 PEGylated AuNPs 258

7.1.2 Properties and therapeutic potential of AuNPs@PP75 259

7.1.3 Hybrid hydrogels 260

7.2 Future work 261

7.2.1 Dual functionalisation with PP75 and PEG 261

7.2.2 Multivalent theranostic platform 262

7.2.3 AuNPs loaded hydrogels for intracellular delivery 263

Bibliography 265

Appendix A 289

Appendix B 295

Appendix C 299

Appendix D **303**

Appendix E Copyright permissions **309**

List of Figures

Figure 1-1 Examples of NPs used for cancer treatment and diagnosis. a) polymeric nanoparticles, b) liposomes, c) QDs, which usually possess a CdSe core, d) AuNPs, e) zeolite L, f) magnetic NPs, traditionally iron oxide, g) dendrimers, h) nanotubes, i) upconverting nanophosphors. 46

Figure 1-2 The lycurgus cup, Roman glass vessel covered with scenes representing the death of King Lycurgus. The glass is dichroic: it turns from green (A) to ruby (B) when light shines through the glass due to the presence of colloidal gold (40ppm) and silver (300ppm) contributing to light scattering phenomena. (C) Top view. (D) Zoomed in image of the cup illuminated from the inside. Reprinted from the British museum website, copyright The Trustees of the British Museum, with permission from the British museum. 46

Figure 1-3 Schematic drawing representing the Turkevich method. 48

Figure 1-4 Brust-Schiffrin synthesis of thiolated AuNPs followed by the ligand exchange reaction. 49

Figure 1-5 Scanning electron microscope and transmission electron microscope micrographs of gold nanostructures of various shapes and sizes. 50

Figure 1-6 Schematic representation of the SPR effect. 52

Figure 1-7 (A) TEM micrographs of Au nanoparticles with various mean diameters 53

Figure 1-8 Main areas of applications of AuNPs in oncology. 56

Figure 1-9 Schematic illustration of drug delivery via 'active' and 'passive' targeting, solid and dotted line respectively. 57

Figure 1-10 Schematic describing the principle of photothermal light to heat conversion by plasmonic nanostructures. 59

Figure 1-11 (A) Contrast enhancement of OCT images of an in vivo tumour model. 3D volumes (4mm× 2mm) of spectral contrast signal in blood vessels of tumour (circled by dashed white line) and adjacent healthy tissue before and 0, 16, and 24h after injection. (B) (a)–(c) Combined ultrasound and photoacoustic images, and (d)–(f) photoacoustic-

based thermal images. The arrow represents the direction of CW laser irradiation (808 nm, 1 W). (C) Schematic illustration of SERS-based cell imaging for the rapid detection and quantification of growth factor receptors on breast cancer cell membranes. 60

Figure 1-12 The principle of AGR2 detection based on hybridisation chain reaction amplification. 61

Figure 1-13 Schematic representation of synthesis of DOX@Gold NMs and their potential theranostic application. 62

Figure 1-14 Viability data (derived from MTT assay) collected from recent literature on HeLa cells incubated with AuNPs of different sizes and at different concentrations. AuNPs are differently functionalised. Each line refers to a specific reference which can be retrieved from the original paper. 63

Figure 1-15 Nanoparticle size (a), shape (b) and surface charge (c) dictate biodistribution among the different organs including the lungs, liver, spleen and kidneys. 64

Figure 1-16 Schematic illustration of established nanotherapeutic platforms. 65

Figure 1-17 Total number of publications (Web of Science®) (A) and clinical trials (clinicaltrials.gov) during the last 10 years (B) 66

Figure 1-18 Multifunctional nature of AuNPs. 69

Figure 1-19 Representation of how PEGylation avoids clearance of NPs by the RES. 71

Figure 1-20 Schematic illustration for the enhanced cellular uptake of AuNPs by anti-EGFR antibody and glutathione-mediated intracellular release of AuNP-2 carriers. 74

Figure 1-21 Different forms of hydrogel nanocomposites: bulk nanocomposites, particle nanocomposites, and core-shell nanocomposites 75

Figure 1-22 Framework of sequential biological barriers to nanoparticle drug delivery. 76

Figure 1-23 Schematic of endocytosis and exocytosis patterns of nanoparticles. Nanoparticles the cell via four types of pathway: clathrin/caveolar-mediated endocytosis, phagocytosis, macropinocytosis, and pinocytosis. Nanoparticles exit the cell via three types of pathway: lysosome secretion, vesicle-related secretion, and non-vesicle-related

secretion. Reproduced from Oh and Park[157], copyright 2014, with permission from Oh and Park.....77

Figure 1-24 (A) Schematic of the lipid bilayer. (B) Internalisation process of PEGylated NPs. Snapshots of PEGylated NPs used in the dissipative particle dynamics (DPD) simulations with two grafting densities: 0.2 and 1.6 chains nm^{-2}. The diameter of the NP core is about 8 nm.....78

Figure 1-25 (A) Mechanisms of MDR towards cancer chemotherapeutic drugs. B. Proposed drug efflux mechanism for ABC transporters. Substrate and ATP bind to ATP transporters. After ATP hydrolysis, the substrate is effluxed out of the cell. Phosphate group is released and the substrate is then excreted to extracellular matrix.....79

Figure 1-26 Mechanism of endosomal escape of nanocarrier.....80

Figure 1-27 pH-dependent ionisation of polyelectrolytes.....81

Figure 1-28 (A) Synthesis of PLP. (B) Synthesis of PLP derivatives (PP series). (C) Description of PP75.....84

Figure 1-29 (A) Schematic illustration of the monolayer protected AuNPs used as transfection vectors. (B) Schematic description of DNA nanomachine.....86

Figure 3-1 Citrate coated AuNPs characterisation. (A) UV-vis scan. (B) Physico-chemical characteristics obtained via UV-spectroscopy and DLS. (C) TEM image of citrate coated AuNPs (scale bar 50nm). (D) Size distribution obtained via ImageJ (inset ImageJ mask image of (C) used for the determination of the average size. 131

Figure 3-2 (A) Reproducibility: mean values for physicochemical properties of the citrate coated AuNPs from 27 independent batches. (B) Effect of time on the optical properties. Values are given as mean ± standard deviation of triplicate measurements. 133

Figure 3-3 Effect of the centrifugation parameters on the absorbance. (A) $A/A_{ref\ (520nm)}$ corresponding to the ratio between the absorbance post and pre-centrifugation at 520 nm. (B) Protocols for the centrifugation parameters optimisation. 134

Figure 3-4 (A) Effect of different folds of dilution in H_2O and MES buffer (50 mM, pH5.5) on the absorbance. (B) Picture of the AuNPs solution after dilution in H_2O and MES buffer. 135

Figure 3-5 Effect of the PEGylation on the dispersion via TEM. (A) TEM images of AuNPs at low magnification (scale bar 100 nm) and (B) high magnification (scale bar 50 nm). (C) TEM image of AuNPs@PEG0.8k at low magnification (scale bar 100 nm) and (D) high magnification (scale bar 50 nm). (E) DLS results (values are given as mean ± standard deviation of triplicate measurements). (F) Particle size distribution (PSD) obtained with ImageJ for AuNPs@PEG0.8k. Mask image as inset..... 137

Figure 3-6. Time-dependent colloidal stability of the PEGylated AuNPs at different concentrations of PEG with the three chain lengths Mw 0.8k (first row); 2k (second row) and 6k (third row), redispersed in H_2O (first column) and MES buffer (50 mM, pH5.5) (second column). A_t/A_{t0} corresponds to the ratio between the A_{SPR} at time t and the A_{SPR} at time t_0. Note: the SPR wavelength was fixed for each concentration of PEG. The legend gives the quantity of PEG added expressed as nmol mL^{-1} AuNPs..... 139

Figure 3-7 Determination of the minimum amount of PEG required for stabilisation of 10 nM AuNPs in 50mM MES buffer pH 5.5 via UV-vis. 141

Figure 3-8 (A) Picture of AuNPs@PEG0.8k from 0 to 10 nmol mL^{-1} AuNPs after redispersion in H_2O. (B) Hydrodynamic diameters and (C) zeta potential values with increasing PEG concentration for AuNPs@PEG0.8k measured via DLS..... 142

Figure 3-9 Grafting density of the PEGylated AuNPs calculated with the Ellman assay. 145

Figure 3-10 Relative absorbance (ratio of the SPR absorbance 6h after, A_{6h}, and before redispersion, A_{t0}) of the AuNPs and the PEGylated AuNPs in different media: H_2O (pH∼6); Buffer 1 (50 mM PBS at pH 7.4, 0.15 M NaCl) and Buffer 2 (50 mM MES buffer at pH 5.5, 0.15 M NaCl)..... 147

Figure 3-11 TEM images showing the polymer layer of the AuNPs@PEG0.8k (A-B) and AuNPs@PEG6k (C-D), scale bar 10 nm for A-C and 5 nm for D. 149

Figure 3-12 Adsorption of BSA protein on the citrate-coated and PEGylated AuNPs: AuNPs@PEG0.8k (15 nmol mL^{-1} AuNPs), AuNPs@PEG2k (10 nmol mL^{-1} AuNPs) and AuNPs@PEG6k (7 nmol mL^{-1} AuNPs). A_t/A_{t0} ratio measured after redispersion (A) in 10 mM PBS pH7.4 (0.15 M NaCl) over time, (B) in PBS with 5 mg mL^{-1} BSA and (C) A_t/A_{t0} ratio 6 h after redispersion in PBS, PBS + BSA (0.1 mg mL^{-1}, 0.5 mg mL^{-1} and 5mg mL^{-1}). Error bars represent the standard deviations of triplicate measurements. 154

Figure 3-13 Concentration-dependent relative viabilities of HeLa cells treated with A. AuNPs@PEG2k for 24 h as determined by alamarBlue assay. Error bars represent standard deviations of five replicates. 156

Figure 3-14 TEM images of zoomed in individual satellites structures (A-C) (scale bar: 20 nm) and assembled satellites structures (D-F) scale bar (100 nm) for AuNPs@PEG0.8k (first row), AuNPs@PEG2k (second row) and AuNPs@PEG6k (third row). 157

Figure 3-15 TEM images of self-assembled PEGylated AuNPs. (A, D) AuNPs@PEG0.8k, (B, E) AuNPs@PEG2k and (C-F) AuNPs@PEG6k. First row: scale bar 200 nm, second row: scale bar 100 nm. 158

Figure 3-16 Particle size analysis of the satellite structures in the AuNPs@PEG (0.8k first column, 2k second column, 6k third column). ImageJ mask (A-C) and obtained PSD (D-F). G. Table giving the percentage of the number of NPs present in all the satellite structures relative to the total number of NPs present in the self-assembly. 159

Figure 3-17 TEM images of (A) AuNPs@PEG2k under defocused conditions (scale bar 50 nm) and (B) representative satellite structure in the AuNPs@PEG2k assembly under defocused conditions (scale bar 20 nm). 162

Figure 3-18 Multilayer assemblies. (A) AuNPs@PEG6k at low magnification (scale bar 200 nm). (B) AuNPs@PEG2k high magnification (scale bar 50 nm). (C) Apparent chain-like structures in AuNPs@PEG6k (scale bar 50nm). (D) A Moiré pattern in AuNPs@PEG2k (scale bar 20 nm). Figures (C) and (D) are adapted from Bachelet and Chen[232], copyright 2016, with permission from The Royal Society of Chemistry. 164

Figure 3-19 TEM images of AUNPs@PEG6k with S/L ratio (small size to large size) of (A) 50/50 and (B) 90/10. Scale bar 100 nm. 166

Figure 4-1 FTIR spectra of PP75 conjugated with 5 mol% cysteamine: SH-PP75 (5%) and SH-PP75 conjugated with AuNPs: AuNPs@PP75. 173

Figure 4-2 Physico chemical characterisation of AuNPs@PP75. (A) UV scans of AuNPs and AuNPs@PP75. (B) TEM image of AuNPs@PP75 (scale bar 100 nm). 174

Figure 4-3 Influence of the polymer concentration on the colloidal stability in 100 mM PBS (0.15 M NaCl) pH7.4 measured via UV-vis spectrophotometry one day after redispersion. (A) UV scan of AuNPs@PP75 between 0 and 100 ug PP75 per mL AuNPs,

(B) Absorbance at the SPR and (C) wavelength at the SPR with increasing PP75 concentration..... 175

Figure 4-4 Influence of the polymer concentration on the hydrodynamic size (A) and the zeta potential (B) in 100mM PB pH7.4 measured via DLS. 176

Figure 4-5 Influence of the media on the colloidal stability measured via UV spectrophotometry. UV-scans of AuNPs@PP75(30), AuNPs@PP75(100) and AuNPs@PEG2k redispersed (A) in 100mM PBS pH7.4 (0.15M NaCl) buffer and (B) in DMEM media containing 10% w/w FBS. (C) Absorbance and (D) wavelength values at the SPR for in H_2O, 100mM PB buffer pH7.4, 100mM PBS pH7.4 (0.15M NaCl) buffer and DMEM media containing 10% w/w FBS for AuNPs@PP75(30); AuNPs@PP75(100); AuNPs@PEG2k..... 177

Figure 4-6 Influence of the media on the hydrodynamic diameter. D_H in H_2O, 100mM PB buffer pH7.4, 100mM PBS pH7.4 (0.15M NaCl) buffer and DMEM media containing 10% w/w FBS for AuNPs@PP75(30); AuNPs@PP75(100) and AuNPs@PEG2k..... 178

Figure 4-7 pH-response of ~10 nM AuNPs@PP75 redispersed in ultra-pure water adjusted at pH7.4 with 0.1 M NaOH and titrated with μL of 0.1 M HCl: (A) UV-vis spectra, (B) absorbance at the SPR and (C) SPR wavelengths with pH. 180

Figure 4-8 pH-response via titration of AuNPs@PP75(30) redispersed in 100 mM PB buffer pH 7.4 and titrated with μL of 0.1 M HCl: (A) UV-vis spectra, (B) absorbance at the SPR and (C) SPR wavelengths with pH. 181

Figure 4-9 pH for transition determined via absorbance measurements. AuNPs@PP75(30) are redispersed in buffers: 100 mM PB buffers from pH 7.4 to 6 and 100 mM citrate buffers from pH 5.5 to 3. (A) UV spectra, (B) absorbance at the SPR and (C) Wavelength at the SPR measured 24 h after redispersion. 182

Figure 4-10 Transmittance of PP75 solution at 1 mg mL^{-1} at λ=480 nm measured via (A) titration after redispersion in ultra-pure water using 0.1 M HCl, (B) redispersion in buffers for 3 h: 100 mM PB buffers from pH 7.4 to 6 and 100 mM citrate buffers from pH 5.5 to 3. 183

Figure 4-11 pH-dependent change of (A) the mean hydrodynamic diameter and (B) the zeta potential of the AuNPs@PP75 measured one day after redispersion in buffers: 100 mM PB buffers from pH 7.4 to 6 and 100 mM citrate buffers from pH 5.5 to 3. 183

Figure 4-12 TEM images of AUNPs@PP75 redispersed in 100mM PB buffer pH 7.4 (A-B) and 100 mM citrate buffer pH 4.0 (C-D). Scale bar 100 nm (A, C) and 20 nm (B, D)..... 184

Figure 4-13 Colloidal stability over time in different media. AuNPs, AuNPs@PLP and AuNPs@PP75 redispersed (A) in H_2O, in 50 mM MES buffer (0.15 M NaCl) (B) pH 7.4, (C) pH 6.5, (D) pH 5.5..... 185

Figure 4-14 Reversible change of (A) the SPR absorbance, (B) the SPR wavelength, (C) the hydrodynamic size and (D) the zeta potential of the AuNPs@PP75(30) solution with pH cycling between low pH (pH~3.0) and high pH (H~pH7.4). 188

Figure 4-15 Influence of the polymer concentration (expressed as μg PP75 added per mL of ~10 nM AuNPs) on the reversibility of the pH response. (A) Absorbance values at the SPR and (B) wavelength values at the SPR for AuNPs@PP75 with the PP75 concentration ranging from 0 to 40 μg per mL AuNPs redispersed in 100 mM PB pH 7.4 (H); then the pH was adjusted to pH~3-4 with 0.1 M HCl (L); and adjusted to pH~7 with 0.1 M NaOH (H). pH (H~pH7.4)..... 190

Figure 4-16 Relative haemolysis of sheep RBCs by 30ug mL^{-1} PP75 and AuNPs@PP75 at pH 6.5 incubated at 37°C for 1h. Error bars represent standard deviations of triplicate measurements. pH (H~pH7.4). 193

Figure 4-17 Evaluation of the pH-dependent membrane activity with calcein loaded liposomes as a model. (A) Fluorescence levels obtained after incubation for 90 min at 37°C of liposomes (Lip), AuNPs; AuNPs and liposomes (AuNPs+Lip), liposomes with PP75 at 15 μg mL^{-1}(P(15)+Lip), with PP75 at 100 μg mL^{-1} (P(100)+Lip) and with PP75 at 1000 μg mL^{-1} (P(1000)+Lip) at pH 7.4. (B) Calcein release profiles of liposomes only and liposomes incubated with PP75 in buffers from pH 4.5 to 7.4. (C-E) Calcein release profiles of liposomes only and liposomes incubated with AuNPs@PP75 obtained on different days. pH7.4)..... 194

Figure 4-18 Concentration-dependent relative viabilities of HeLa cells treated with (A) AuNPs@PP75(30) and (B) citrate-coated AuNPs for 2 h, 24h and 48h as determined by alamarBlue assay. 196

Figure 4-19 (A) Concentration dependant uptake of AuNPs@PP75 with HeLa cells after 24 h of treatment measured via ICP-OES and FACS. (B) Percentage of viable, mid-apoptotic and necrotic cells after 24 h of treatment with AuNPs@PP75 measured via flow cytometry. 198

Figure 4-20 TEM images of HeLa cells treated with 3 nM AuNPs (A-B) and 10 nM AuNPs@PP75(30) (C-D) for 24 h (scale bar 200 nm, acceleration voltage 120 kV). 199

Figure 4-21 Confocal microscopy images of HeLa cells untreated, treated with 3 nM AuNPs and 10 nM AuNPs@PP75. Nuclei and lysosomes were stained with Hoechst and LysoTracker Red respectively. Images were acquired with a Zeiss LSM-510 inverted confocal unit (x63 magnification) after 24 h of uptake and fixing (scale bar: 20 μm)... 201

Figure 4-22 Confocal microscopy images of HeLa cells treated with 10 nM AuNPs@PP75. (A) Colocalisation of AuNPs fluorescence and bright field for Hela cells after 24h uptake. Colocalisation of AuNPs@PP75 with lysotracker at (B) 2h and (C) 24h. Nuclei and lysosomes were stained with Hoechst and LysoTracker Red respectively. Images were acquired with a Zeiss LSM-510 inverted confocal unit (x63 magnification) after 2 h (B) and 24 h (A, C) of uptake and fixing (scale bar: 5 μm). 202

Figure 4-23 Confocal microscopy images of HeLa cells treated with 2.0 mg mL^{-1} calcein only, both 2.0 mg mL^{-1} calcein and 10 nM AuNPs, both 2.0 mg mL^{-1} calcein and 10 nM AuNPs@PEG2k and both 2.0 mg mL^{-1} calcein and 10 nM AuNPs@PP75. Images were acquired with a Zeiss LSM-510 inverted confocal unit (x40 magnification) after 24 h of uptake and 6h of further incubation. Scale bar: 20 μm. 204

Figure 5-1 Optimisation of DOX loading. (A) UV-vis scans of AuNPs@DOX at increasing DOX/AuNP loading ratios (expressed in wt%). (B) SPR absorbance and (C) SPR wavelength at increasing DOX/AuNP ratios. 213

Figure 5-2 Characterisation of the loading efficiency of AuNPs@DOX at increasing DOX/AuNP loading ratios. (A) Fluorescence measurement (475nm/580-640 Exc/Em) of as synthesised AuNPs@DOX. (B) Fluorescence of the supernatants after centrifugation. (C) Drug loading (circles) and loading efficiency (squares) with the DOX/AuNPs loading ratio. 214

Figure 5-3 Optimisation of AuNPs@DOX@PP75 prepared with initial drug loading of 1.3 wt%. (A) UV-vis scans of AuNPs@DOX at increasing PP75/AuNP ratios. (B) SPR absorbance and (C) SPR wavelengths at increasing PP75/AuNP ratios. 217

Figure 5-4 Characterisation of the loading efficiency of AuNPs@DOX@PP75 at increasing PP75@AuNP ratios with an initial DOX/AuNPs loading of 1.3 wt%. (A) Fluorescence measurement (475nm/580-640 Exc/Em) of as synthesised AuNPs@DOX@PP75. (B) Fluorescence of the supernatants after centrifugation. (C) Drug loading (circles) and loading efficiency (squares) with the PP75/AuNPs loading ratio. 218

Figure 5-5 UV-vis spectra of AuNPs@DOX after one centrifugation (red long-dashed line); AuNPs@DOX@PP75 after two centrifugations (grey short-dashed line) and AuNPs@DOX@PP75 after one centrifugation (orange solid line). 220

Figure 5-6 UV-vis spectra of AuNPs@DOX@PP75 solutions redispersed in H_2O (blue solid line), 100mM PB pH 7.4 (orange long-dashed line); 100mM PBS (0.15 M NaCl) at pH 7.4 (red dotted line) and 100 mM PBS (0.50 M NaCl) at pH 7.4 (grey dotted-dashed-line). 221

Figure 5-7 TEM images of AuNPs@DOX and AuNPs@DOX@PP75. (A) AuNPs@DOX at low magnification (scale bar 200 nm). (B) AuNPs@DOX@PP75 at low magnification (scale bar 200 nm). (C) AuNPs@DOX at high magnification (scale bar 20 nm). (D) AuNPs@DOX@PP75 at high magnification (scale bar 20 nm). (E) Zoomed in image of AuNPs@DOX@PP75 (scale bar 5 nm). 223

Figure 5-8 Concentration-dependent relative viabilities of MES-SA cells treated with (A) AuNPs@PP75 and (B) AuNPs@DOX@PP75 for 2 h (open bars) and 24 h (close bars) as determined by alarmarBlue assay. 224

Figure 5-9 Concentration-dependent relative viabilities of MES-SA-Dx5 cells treated with (A) AuNPs@PP75 and (B) AuNPs@DOX@PP75 for 2h (open bars) and 24h (close bars) as determined by alarmarBlue assay. 224

Figure 5-10 Optimisation of the laser power. (A) HeLa cell solution temperature monitoring with time. (B) Influence of the laser power on the viability of HeLa cells irradiated for 120 s as determined by alamarBlue assay. (C) Temperature monitoring of AuNPs@DOX@PP75 in DMEM medium under irradiation at 2.3 W cm^{-2}. (D) Temperature

monitoring of cells only and cells incubated with AuNPs@DOX@PP75 at 10 nM for 24 h and then washed before irradiation at 2.6 W cm^{-2}. 225

Figure 5-11 Concentration-dependent relative viabilities of MES-SA cells irradiated at 2.6W cm^{-2} for 120 s. The cells were treated with laser only (green striped bars); free DOX (red bars); free DOX and laser (red stripped bars); AuNPs@DOX@PP75 (blue bars); AuNPs@DOX@PP75 and laser (blue striped bars) as determined by alamarBlue assay. 227

Figure 5-12 Confocal microscopy images of MES-SA cells treated with free DOX (1 μg mL^{-1}), AuNPs@DOX@PP75 (1 μg mL^{-1} DOX equivalent) for 24 h and irradiated (+) or not (-) for 120s at 2.6W cm^{-2}. Images were acquired with a Zeiss LSM-510 inverted confocal unit (x40 magnification). Scale bar: 10 μm. 228

Figure 5-13 Concentration-dependent relative viabilities of MES-SA/Dx5 cells irradiated at 2.6W cm^{-2} for 120 s. The cells were treated with laser only (green striped bars); free DOX (red bars); free DOX and laser (red striped bars); AuNPs@DOX@PP75 (blue bars); AuNPs@DOX@PP75 and laser (blue striped bars) as determined by alamarBlue assay. 229

Figure 5-14 Confocal microscopy images of MES-SA/Dx5 cells treated with free DOX (10 μg mL^{-1}), AuNPs@DOX@PP75 (10 μg mL^{-1} DOX equivalent) for 24 h and irradiated (+) or not (-) for 120s at 2.6W cm^{-2}. Images were acquired with a Zeiss LSM-510 inverted confocal unit (x40 magnification). Scale bar: 10 μm. 232

Figure 6-1 PLP hydrogels loaded with AuNPs@PLP, AuNPs@PP75 and AuNPs@PEG2k at 0.24 wt% respectively (from left to right). Hybrid hydrogel samples (A) after overnight synthesis, (B) drying on filter paper, and (C) after purification in H_2O after 5 days. 238

Figure 6-2 Choice of the loading ratio AuNPs/PLP. (A) Samples drying on the filter paper. (B) Purification process in H_2O after 1 day and (C) after 5 days. From left to right on all pictures: PLP hydrogels unloaded; loaded with AuNPs@PLP at 0.03 wt%, AuNPs@PP75 at 0.03 wt% and 0.08 wt%; AuNPs@PLP at 0.08 wt%. 240

Figure 6-3 SEM images of the hybrid hydrogels. (A) Side view of pore channels (scale bar 200 μm). (B) Front view of pores channels (scale bar 100 μm) and (C) zoom image of the pores (scale bar 20 μm). 242

Figure 6-4 (A) XPS spectra of the PLP hydrogel and the AuNPs@PP75/hydrogel. (B) Determination of the crosslinking ratio via XPS data. (C) Au4f, (D) S2p, (E) O1s, (F) N1s and (G) C1s spectra of the AuNPs@PP75/hydrogel..... 243

Figure 6-5 (A) EDX spectrum and (B) related TEM image of AuNPs@PP75/hydrogel (scale bar 200 nm)..... 244

Figure 6-6 Concentrations of Au in AuNPs@PP75/hydrogels obtained via ICP (A) for different AuNPs/PLP ratios (solid content fixed at 5.9 wt%) and (B) for different solid contents (AuNPs/PLP ratio fixed at 0.12 wt%). Before ICP measurements hydrogels have been immersed in H_2O, PB buffer at pH 7.4 and citrate buffer at pH 3.0. 246

Figure 6-7 Compression profiles (stress vs. deformation factor) for hydrogels previously immersed in 0.1M PB buffer at pH 7.4 and citrate buffer at pH 3.0 of (A) PLP hydrogel and (B) AuNPs@PP75/hydrogel Gel 1 (0.16 wt% - 5.9 wt%) obtained via DMA. 247

Figure 6-8 Comparison of the tensile storage modulus E' obtained via DMA at pH 7.4 and pH 3.0 for the PLP hydrogel and AuNPs@PP75/hydrogel Gel 1 (0.16 wt% - 5.9 wt%). 248

Figure 6-9 SEM images of Gel 6 (A, B) and Gel 3 (C, D) at pH 3.0 (A, C) and pH 7.4 (B, D) (scale bar 20 um). 250

Figure 6-10 TEM images of hydrogels at different AuNPs/PLP ratios and solid contents after stabilisation in buffer at pH 7.4. (A) PLP hydrogel, (B) Gel 6 (0.24 wt% - 5.9 wt%), (C) Gel 3 (0.12 wt% - 7.7 wt%) and (D) Gel 11 (0.24 wt% - 7.7 wt%). Scale bar 20 µm. 251

Figure 6-11 Concentration dependant cytotoxicity of Gel 1 (0.16 wt% - 5.9 wt%) evaluated via alamarBlue assay after 24 h (grey bars) and 72 h of treatment (striped bars) of HeLa cells. 252

Figure 6-12 (A) Drug release profiles at pH 7.4 and pH 3.0 obtained for Gel 3 (0.12 wt%-7.7 wt%). (B) Drug released after 24 h and 48 h of Gel 1 (0.16 wt% - 5.9 wt%), Gel 2 (0.12 wt% - 5.9 wt%) and Gel 3 (0.12 wt% - 7.7 wt%). (C) pH dependence and reversibility of the swelling ratios..... 254

Figure A-1 (A) A_{SPR}/A_{450} vs. ln (d) using the fit parameters from the experimental results reported by Haiss et al.[42]. (B) ln(Ɛ) vs ln(d) obtained from the fit to the theoretical

extinction efficiencies for AuNPs in the size range 2 to 100 nm reported by Haiss et al.[42]. (C) Table giving the fit values for the slope and intercept of Figures A and B. 289

Figure A-2 FTIR spectra for AuNPs@PEG0.8k. 289

Figure A-3 A_{SPR} of PEGylated AuNPs redispersed in H_2O versus quantity of PEG added. 290

Figure A-4 Calibration curves for the Ellman assay obtained via UV-vis. B. Calibration characteristics. 290

Figure A-5 ImageJ mask images (A, C, E) and related PSD (B, D, F) of the TEM images of PEGylated AuNPs. Reproduced from Bachelet and Chen[232], copyright 2016, from The Royal Society of Chemistry. 293

Figure A-6 Individual satellites structures for (A) AuNPs@PEG0.8k, (B) AuNPs@PEG2k and (C) AuNPs@PEG6k. Reproduced from Bachelet and Chen[232], copyright 2016, from The Royal Society of Chemistry. 293

Figure A-7 Images of the self-assembled AuNPs@PEG6k. (A) SEM image on silicon wafer (scale bar 500 nm). (B) SEM image on TEM grid (scale bar 200 nm) with zoomed satellite structure as inset (scale bar 20 nm). (C) AFM image under tapping mode with zoomed assembly as inset on mica sheet (scale bar 500 nm). (D) SEM image of large scale assembly (scale bar 500 nm). (E) Short-scale assembly (scale bar 100 nm). 294

Figure B-1 ^{1}H-NMR spectra of PP75 in d^6-DMSO at 400 MHz. 295

Figure B-2 ^{1}H-NMR spectra of PP75 (top) and SH-PP75(5%) (bottom) in d^6-DMSO at 400 MHz. 296

Figure B-3 FTIR spectra of PP75 polymer and PP75 conjugated with 5 mol% cysteamine: SH-PP75 (5%) 297

Figure B-4 Influence of the polymer concentration on the hydrodynamic size in H_2O measured via DLS. Error bars represent standard deviations of three samples with six runs each. 298

Figure B-5 (A) Calibration curve of RBCs haemoglobin. (B) Calibration linear fit parameters. 298

Figure C-1 (A) Calibration of DOX via fluorescence. (B) Calibration linear fit parameters. 301

Figure C-2 FTIR spectra of DOX and AuNPs@DOX@PP75. 301

Figure C-3 Set up for laser-therapy. (A) Laser power, (B) laser head, (C) fibre, (D) collimator. 302

Figure C-4 (A) Calibration of the laser power density vs. current based on the specifications sheet provided and the power measured with the laser power meter. (B) Calibration linear fit parameters. 302

Figure D-1 EDX spectra of AuNPs. The hydrogels samples were provided by Yubai Zhang. 303

Figure D-2 EDX spectra of AuNPs@PP75. The hydrogels samples were provided by Yubai Zhang. 303

Figure D-3 TEM images of PLP hydrogel at A. pH 3.0 and B. pH 7.4. Scale bar 20 μm. .. 304

Figure D-4 TEM images of gel 5 at pH 7.4. Scale bar 100 μm. 305

Figure D-5 Concentration dependant cytotoxicity of Gel 2 evaluated via alamarBlue assay for 24h treatment (grey bars) and 72h treatment (striped bars) of HeLa cells. Error bars represent the deviation between 10 replicates. 305

Figure D-6 Concentration dependant cytotoxicity of Gel 3 evaluated via alamarBlue assay for 24h treatment (grey bars) and 72h treatment (striped bars) of HeLa cells. Error bars represent the deviation between 10 replicates. 306

Figure D-7 Curve of the fluorescein via absorbance and relative linear fit data. 306

Figure D-8 Drug release profiles at pH 7.4 and pH 3.0 obtained for AuNPs@PP75/hydrogels (A) Gel 1 and (B) Gel 2 307

List of Schemes

Scheme 2-1 PLP synthesis. 98

Scheme 2-2 DCC/DMAP coupling. 99

Scheme 2-3 PP75 synthesis 100

Scheme 2-4 PLP hydrogel synthesis via EDC/NHS coupling 102

Scheme 3-1 Model of the thiol-PEG modification process of AuNPs. 144

Scheme 3-2 Schematic of the polymer layer conformations on a nanoparticle surface (A) in a mushroom regime and (B) in a brush regime. 150

Scheme 3-3 Schematic illustrating the influence of PEG density (Mw 5,000) on serum protein adsorption to gold nanoparticles and their subsequent uptake by macrophages. Reprinted from Walkey et al.[205], copyright 2011, with permission from the American Chemical Society 156

Scheme 3-4 Droplet-evaporation-induced formation of ordered Au nanorod superstructures. 165

Scheme 3-5 Schematic of the suggested self-assembly mechanism during the slow evaporation process on a carbon-coated grid, first row: side view, second row: top view of the carbon grid. Adapted from Bachelet and Chen[232], copyright 2016, with permission from The Royal Society. 166

Scheme 4-1 Schematic of (A) the coupling reaction between PP75 and cysteamine and (B) the functionalisation of the gold nanoparticles with SH-PP75. 172

Scheme 4-2 Schematic representation of pH-responsive stability of the AuNPs functionalised by the anionic amphiphilic polymers PP75 and PLP 187

Scheme 4-3 Schematic representation of the mechanism of the pH-triggered reversible agglomeration-deagglomeration process 189

Scheme 5-1 (A) Preparation of AuNPs@DOX@PP75. (B) Principle of the dual therapy. 211

Scheme 6-1 Optimised synthesis process of the AuNPs loaded hydrogel. 241

List of Tables

Table 1-1 Inorganic nanoparticles in clinical trials. 67

Table 1-2 Summary of the thesis' research gaps, aims and novelties 92

Table 3-1 Polymer layer characteristics of the PEGylated AuNPs. 151

Table 3-2 Theoretical and experimental chains lengths 153

Table 3-3 Typical independent satellite structures in AuNPs@PEG0.8k, AuNPs@PEG2k and AuNPs@PEG6k and their characteristics via TEM image analysis. 160

Table 3-4 Theoretical and experimental chains lengths 163

Table 5-1 Initial loading concentrations of DOX. 212

Table 5-2 Initial loading concentrations of PP75. 216

Table 5-3 Drug loading and loading efficiencies for an initial loading ratio of DOX/AuNPs=0.9 wt% 219

Table 5-4 Hydrodynamic sizes and zeta potential values obtained via light scattering measurements. 222

Table 5-5 Evaluation of the synergistic effect of the dual therapy for MES-SA/DX5 cells. 230

Table 6-1 Calculated densities and porosities of the hydrogel via the Archimede's method. 239

Table 6-2 Description of the hydrogels in solid content and AuNPs/PLP ratio. 245

Table 6-3 Weight incorporations and loading efficiencies. 253

Table A-1 Results of grafting density for AuNPs@PEG0.8k obtained via the Ellman's assay. 291

Table A-2 Results of grafting density for AuNPs@PEG2k obtained via the Ellman's assay. 291

Table A-3 Results of grafting density for AuNPs@PEG6k obtained via the Ellman's assay. 292

Table D-1 AuNPs loaded hydrogels formulae. 303

Nomenclature and abbreviations

Nomenclature

Symbol	Definition	Units
ε	Molar Extinction Coefficient	$M^{-1}\ cm^{-1}$
λ	Wavelength	nm
σ	Grafting Density	Chain per nm^2
ξ	Zeta potential	mV
A	Absorbance	A.U.
c	Concentration of AuNPs	nM
CV	Coefficient of Variation	%
d	Diameter Size	nm
D_H	Hydrodynamic Diameter	nm
E'	Tensile Storage Modulus	Pa
E''	Tensile Loss Modulus	Pa
FP	Foot Print	nm^2 per chain
G'	Shear Storage Modulus	Pa
G''	Shear Loss Modulus	Pa
IC_{50}	Half Maximal Inhibitory Concentration	nM
M	Molar Concentration	Mole per litre
Mw	Molecular Weight	$g\ mol^{-1}$
PDI	Polydispersity Index	NA
RCF	Relative Centrifugal Force	g
R_F	Flory Radius	nm

Abbreviations

A

ABC	ATP-binding cassette
AFM	Atomic Force Microscopy
AgNPs	Silver Nanoparticles
ATP	Adenosine Triphosphate
AuNPs	Gold Nanoparticles
AuNRs	Gold Nanorods

B

BSA	Bovine Serum Albumin

C

CLSM	Confocal Laser Scanning Microscopy
CPP	Cell Penetrating Peptides
CTAB	Cetyl Trimethylammonium Bromide

D

DCC	N,N'-dicyclohexylcarbodiimide
DLS	Dynamic Light Scattering
DMA	Dynamic Mechanical Analysis
DMAP	4-Dimethylaminopyridine
DMEM	Dulbecco's Modified Eagle Medium

DMF	N,N-Dimethylformamide
DMSO	Dimethyl Sulfoxide
DNA	Deoxyribonucleic Acid
DOX	Doxorubicin
D-PBS	Dulbecco's Phosphate Buffered Saline
DTNB	5,5'-dithiobis-(2-nitrobenzoic acid)

E

EDL	Electric Double Layer
EDX	Energy Dispersive X-ray Spectrometry
EPR	Enhanced Permeability and Retention

F

FACS	Fluorescence-Activated Cell Sorting
FBS	Fetal Bovine Serum
FCS	Fetal Calf Serum
FDA	Food and Drug Administration
FRET	Fluorescence resonance energy transfer
FTIR	Fourier-Transformed Infra-Red

G

GI	Gastro-intestinal
GSH	Glutathione

H

HeLa	Human cervical cancer cell line (Henrietta Lacks)

I

ICP-OES	Inductively Coupled Plasma Optical
IONPs	Iron Oxide Nanoparticles

L

LSPR	Localised Surface Plasmon Resonance

M

MDR	Multi Drug Resistance
MES	2-ethanesulfonic acid (buffer)
MES-SA	Drug-sensitive human sarcoma cell line
MES-SA/Dx5	Drug-resistant human sarcoma cell line
MVB	Multivesicular Body
MPS	Mononuclear Phagocyte System

N

NIR	Near Infra-Red
nm	Nanometer
nM	Nanomoles per Litre
NM	Nanomicelle

NMR	Nuclear Magnetic Resonance
NPs	Nanoparticles

O

OCT	Optical Coherence Tomography

P

PAI	Photoacoustic Imaging
PB	Phosphate Buffered
PBS	Phosphate Bufferes Saline
PDT	Photodynamic Therapy
PEG	Polyethylene Glycol
PEGylation	Functionalisation with PEG
PEI	Poly(ethylenimine)
PET	Positron Emission Tomography
P-gp	P-glycoprotein
PLL	Poly(L-lysine)
PLP	Poly(L-lysine) isophthalamide
PNIPAM	Poly(N-isopropylacrylamide)
PP75	Poly(L-lysine) isophthalamide conjugated
PSD	Particle Size Distribution
PTT	Photothermal Therapy

Q

QDs	Quantum Dots

R

RBCs	Red Blood Cells
RES	Reticuloendothelial System

S

SEM	Scanning Electron Microscopy
SERS	Surface Enhanced Raman Scattering
SPR	Surface Plasmon Resonance

T

TEM	Transmission Electron Microscopy
TGA	Thermogravimetric Analysis
TNF	Tumour Necrosis Factor

Chapter 1 Introduction

This chapter introduces the main challenges in the field of cancer therapy with special attention given to intracellular delivery. The properties, historical developments, current status and applications of gold nanoparticles (AuNPs) as therapeutics are then described. This first chapter provides some design criteria for the successful application of AuNPs as a therapeutic carrier. It also emphasises the advantages of using amphiphilic anionic polymers as carrier vectors for cytoplasmic delivery and highlights the potential interests of the polymeric AuNPs nanohybrids presented in this research work with regards to the alternative solutions that has been reported in the literature.

1.1 AuNPs: definition, properties and scope of applications

1.1.1 Nanotechnology and nanoparticles

Nanotechnology is the engineering of systems at the molecular or atomic scale. These systems usually exhibit sizes of less than 100 nm. Richard Feynman was one of the first physicists to mention the possibilities of a nano-world in the 1950's and since then nanotechnology has spread and conquered almost all the industries in our society: electronics, construction, cosmetics, agriculture, medicine, clothing and defence to name a few.[1,2]

The attractiveness of nanomaterials is explained by the uncommon properties, (e.g. mechanical, electrical, magnetic and optical) they develop at the nanoscale. At the nanoscale, electromagnetic forces are dominant and gravitational forces are negligible. Considerably smaller than bulk solids but still larger than individual atoms or molecules, nanomaterials properties do not obey to the classical physics either to the absolute quantum mechanical laws but lie in between.[2] Furthermore, the ratio of surface to core atoms is much higher than at the macroscale. Consequently, a slight change in diameter has important impact on the properties.

For instance, optical properties of gold nanoparticles are considerably different than bulk gold since gold colloids solutions appear red whereas bulk gold is yellow due to the electron confinement influence on the absorption properties. Second, the melting point for gold nanoparticles is considerably lower than for bulk gold (e.g. 300-400°C vs. 1064°C) due to surface melting.[3] Third, bulk gold is inert however AuNPs are efficient catalysts in mild conditions. [4-6]

Their remarkable properties have been applied to many applications in today's world and new opportunities are still appearing. The most common examples of nanomaterials applications exploit their (i) high surface to volume ratio in particular for catalytic purposes; (ii) narrow size distribution which provide them uniform properties; (iii) ability to assemble into organised structures via molecular bonding for high performance films for instance. Customers of the cosmetic industry are familiar with nanoparticles

(NPs) such as liposomes, spherical vesicles made of one or several phospholipid layers, being included in their cream formulation as delivery carriers of active ingredients.[2] Titanium oxide (TiO_2) and zinc oxide (ZnO_2) NPs are often incorporated in sun creams for their enhanced absorption of UVA-B but also for their interesting reflection and scattering properties compared to the microscale since they offer transparency to the final formulation.[7] Silver nanoparticles (AgNPs) are currently used in water treatment systems, wounds dressings, medical devices and textiles for their antimicrobial activity.[8-10]

AuNPs have been incorporated into the ink for ink-jet printing of electro-conductive patterns for integrated circuits thanks to their low melting point compared to bulk gold.[11] AuNPs have also been successfully employed as a catalyst in many organic reactions such as the oxidation of carbon monoxide below 0°, the most common industrial uses being the synthesis of vinyl acetate monomers by BP chemicals, a key material for preparation of paintings, coatings and textiles, and the production of gas masks.[4-6]

These are only few applications amongst many. The nanotechnology market is evaluated at $39 billion today across all industries and is expected to reach $90 billion in the next five years according to a report published by bcc research*.

1.1.2 Introduction to AuNPs and past applications

Solid nanomaterials can be classified into three categories (i) zero dimensional (e.g. nanoparticles); (ii) one dimensional (e.g. nanowires); and (iii) two dimensional (e.g. thin films) materials. NPs constitute a diverse family which includes semi-conductors NPs (e.g. quantum dots (QDs)); metallic NPs (e.g. gold, silver); magnetic NPs (e.g. iron); polymeric NPs.[12] Polymeric nanoparticles, liposomes and metallic NPs have gained popularity for medical applications (Figure 1-1). The present review will focus especially on AuNPs.

* McWilliams, A. 2016, The Maturing Nanotechnology Market: Products and Applications [Online]. Bcc Research. Available at: http://www.bccresearch.com/market-research/nanotechnology/nanotechnology-market-products-applications-report-nan031g.html [Accessed: 23rd December 2016].

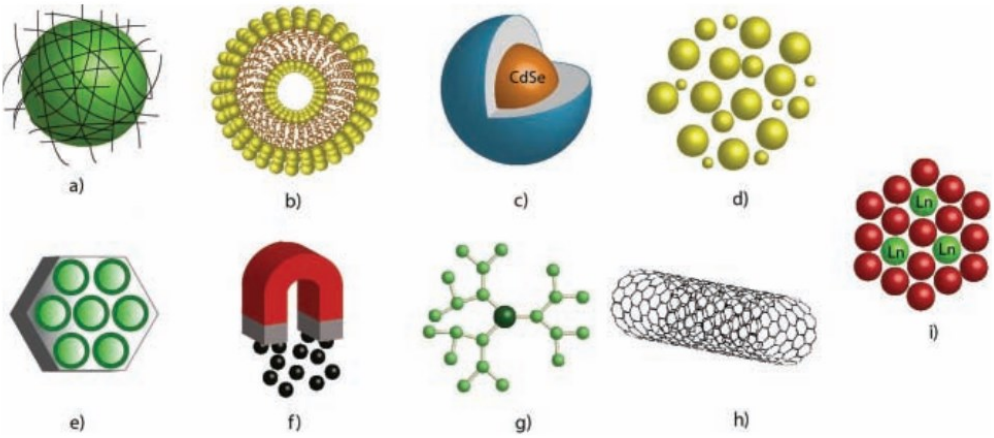


Figure 1-1 Examples of NPs used for cancer treatment and diagnosis. a) polymeric nanoparticles, b) liposomes, c) QDs, which usually possess a CdSe core, d) AuNPs, e) zeolite L, f) magnetic NPs, traditionally iron oxide, g) dendrimers, h) nanotubes, i) upconverting nanophosphors. Reprinted from Barreto *et al.*[13], copyright 2011, with permission from WILEY-VCH Verlag GmbH & Co. KGaA, Weinheim.

AuNPs sizes usually vary between 1 and 100 nm and their colloidal solution is red-purple in colour. Gold colloids have been known for several centuries since the Romans were using them for colouring purposes in ceramics with the most illustrious example being the Lycurgus Cup (Figure 1-2) produced in the 5th-4th BC that can be admired at the British Museum, London. They have also been greatly used during the Middle Age in stained glasses to give the ruby colour thanks to the agglomeration with tin dioxide.[3]



Figure 1-2 The lycurgus cup, Roman glass vessel covered with scenes representing the death of King Lycurgus. The glass is dichroic: it turns from green (A) to ruby (B) when light shines through the glass due to the presence of colloidal gold (40ppm) and silver (300ppm) contributing to light scattering phenomena. (C) Top view. (D) Zoomed in image of the cup illuminated from the inside. Reprinted from the British museum website, copyright The Trustees of the British Museum, with permission from the British museum.

Furthermore, gold has been used as a therapeutic agent long before its colloid nature was discovered since the first known use of gold in Medicine appeared in China around 2500

BC. Later, in the Middle age, it was not rare to receive prescriptions of gold salts for conditions such as dysentery, epilepsy or even for the diagnosis of syphilis, whereas today oral preparations are advised for the treatment rheumatoid arthritis. [3,14,15]

1.1.3 Common synthesis methods

The growing interest that AuNPs have gained in the last decades is also explained by their ease of synthesis and the ability to prepare particles with a high control on the size distribution. Synthesis methods are classified into top-down and bottom-up approaches, while the first one usually employs physical methods such as electron-beam lithographic method,[16] radiolysis,[17] sonochemistry,[18] ultra-violet radiation[19] or laser ablation,[20] the second one generally concerns chemical methods.[3,15]

Chemicals methods mostly rely on two mechanisms: (i) the reduction of the gold salt into gold metal and (ii) the stabilisation, via electrostatic or steric interactions, of the resulted particles. The most common reducing agents are borohydrides, citric acids, hydroxylamines and polyols while thiolates, citrates, oxygen/phosphorus/nitrogen based ligands, polymer chains and surfactants are commonly used to prevent aggregation of the newly synthesised particles. [21] Faraday was the first to attribute the red colour of the AuNPs solution to their colloidal nature in 1857 after preparing a suspension via the reduction of tetrachloroaurate solution by phosphorus in carbon disulfide in a biphasic system.[3] Nevertheless, the reference work for the AuNPs synthesis is still today the synthesis reported by Turkevich in 1951 under the name “sodium citrate sols”. [22] Upon addition of citrate in a boiling solution of $HAuCl_4$, the citrate is oxidised in acetone dicarboxylic acid, which will stabilise the overall system, and the auric salt is reduced in aurous salt and Au^0 and last, the Au^0 atoms form the AuNPs (Figure 1-3). The nucleation, or formation of particles in a single-phase system, and the growth, deposition of additional material on the nuclei, occur simultaneously during the synthesis. In this method, the citrate is used as both reducing and stabilising agent. [22] More recently, J. Polte *et al.*[23] reported a four-step mechanism according to in situ small-angle X-ray scattering (SAXS) and X-ray absorption near edge spectroscopy (XANES) including: a fast nucleation followed by the coalescence of the nuclei, then two steps of growth, one slow and one fast.

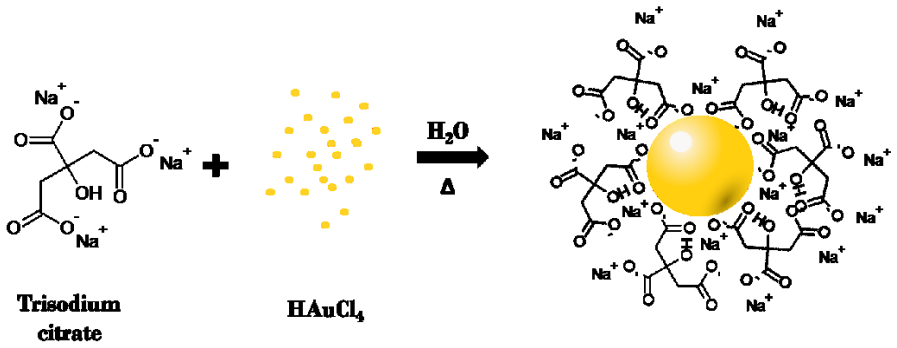


Figure 1-3 Schematic drawing representing the Turkevich method.

The particles size, distribution and shape can be tuned with a change of the experimental conditions such as the reducing agent concentration[24], temperature[25] or pH.[26,27] Turkevich obtained particles sizes between 145 and 200 nm varying the concentration of salts with an approximate deviation of 9-12%. [22] The Turkevich method was improved in 1973 by Frens with a more accurate control of the particle size from 15 to 150 nm with changes in the gold to citrate ratio.[28]

However, the reducing strength of citrate is limited and, even after optimisation of all the parameters, sizes of the synthesised AuNPs are generally over 10 nm in aqueous media.[29] Nevertheless, in 2011, Sivaraman *et al.*[30] succeeded in preparing particles in the range 5-10 nm with the Turkevich-Frens method by reversing the order of addition. He suggested that the rate-limiting step was the oxidation of citrate which depended on the concentration of active chloroauric acid and reaction mixture pH.

Unfortunately, the citrate coated nanoparticles can undergo irreversible aggregation during synthesis and strategies may be required to prevent this, such as the use of a surfactant or thioctic acid as an intermediate in a two-step synthesis. The second drawback is the need for high dilution making the large scale production challenging.[31]

Over the years, the Turkevich-Frens method has been improved and a library of reducing and stabilising species has been investigated. In 1994, Brust and Schiffrin presented the preparation of alkanethiol-stabilised AuNPs in a two-phase system with tetraoctylammonium bromide (TOAB) and sodium borohydride ($NaBH_4$) as the phase transfer reagent and reducing agent respectively (Figure 1-4).[32] The thiol stabilisation is,

by far, the most common and robust stabilisation discovered until now. The strong Au-S bond (47 kcal mol^{-1}), the interligand Van der Waals attractions and the inhibition of the growth process by the sulphur help to produce particles from 1.5 to 5 nm with a low dispersity and a greatly limited aggregation.[31] Besides, the thiols enable an easy subsequent functionalisation via the substitution of the thiolate ligand or ligand exchange.[29] Thanks to the place ligand exchange reaction, mixed monolayer protected AuNPs can be prepared. In this reaction, thiolate ligands displace the original capping ligands (e.g. citrates, thiols) in an equilibrium reaction whose rate is dominated by the ligand concentration, size and chain length.[33,34]

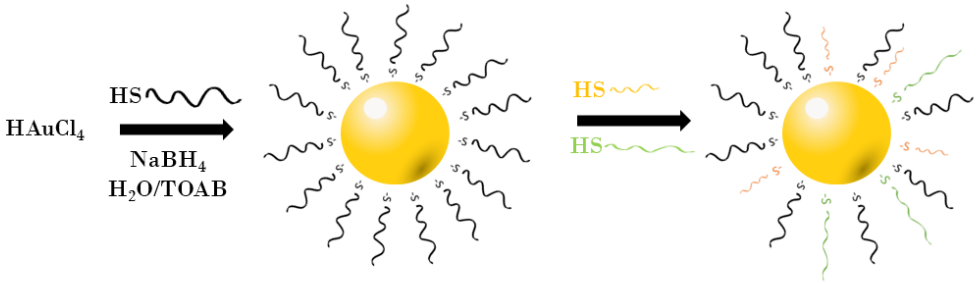


Figure 1-4 Brust-Schiffrin synthesis of thiolated AuNPs followed by the ligand exchange reaction.

This synthesis has been improved in 1995 in a single-phase system with methanol as a solvent to avoid the use of TOAB, and with p-mercaptoethanol as thiolated ligand. Particles of 5 nm average diameter were obtained.[35] Other types of thiols, disulfides or thioacetates have also been used in the Brust reaction. Further examples of ligands include phosphinines, amino, carboxyl or phenol groups. [29]

Then, the seed growth method is an efficient method to control the size and shape of the nanoparticles by progressively enlarging their diameter in a two-step synthesis: preparation of the AuNP seeds and growth via a solution containing $HAuCl_4$, stabilising and reducing agents. Due to the mild nature of the reducing agents used, citrate, ascorbic acid or hydroxylamine amines are common examples, no seed formation occurs during the growth step and the particle size and size distribution can be finely tuned by one or successive growth steps. This method is particularly useful for the preparation of non-

spherical nanoparticles such as gold nanorods (AuNRs) as it generates higher yields and a better controlled dispersion than the electrochemical or photochemical reduction methods also employed for AuNRs preparation. Besides, by variation of the reducing agent or salts concentration, changes in the temperature, pH, Au precursors/surfactants ratio used in the growth solution, other shapes can be designed via the seed growth method such as Au nanocubes, Au hollow nanocages and Au nanopolyhedra (Figure 1-5).[29]

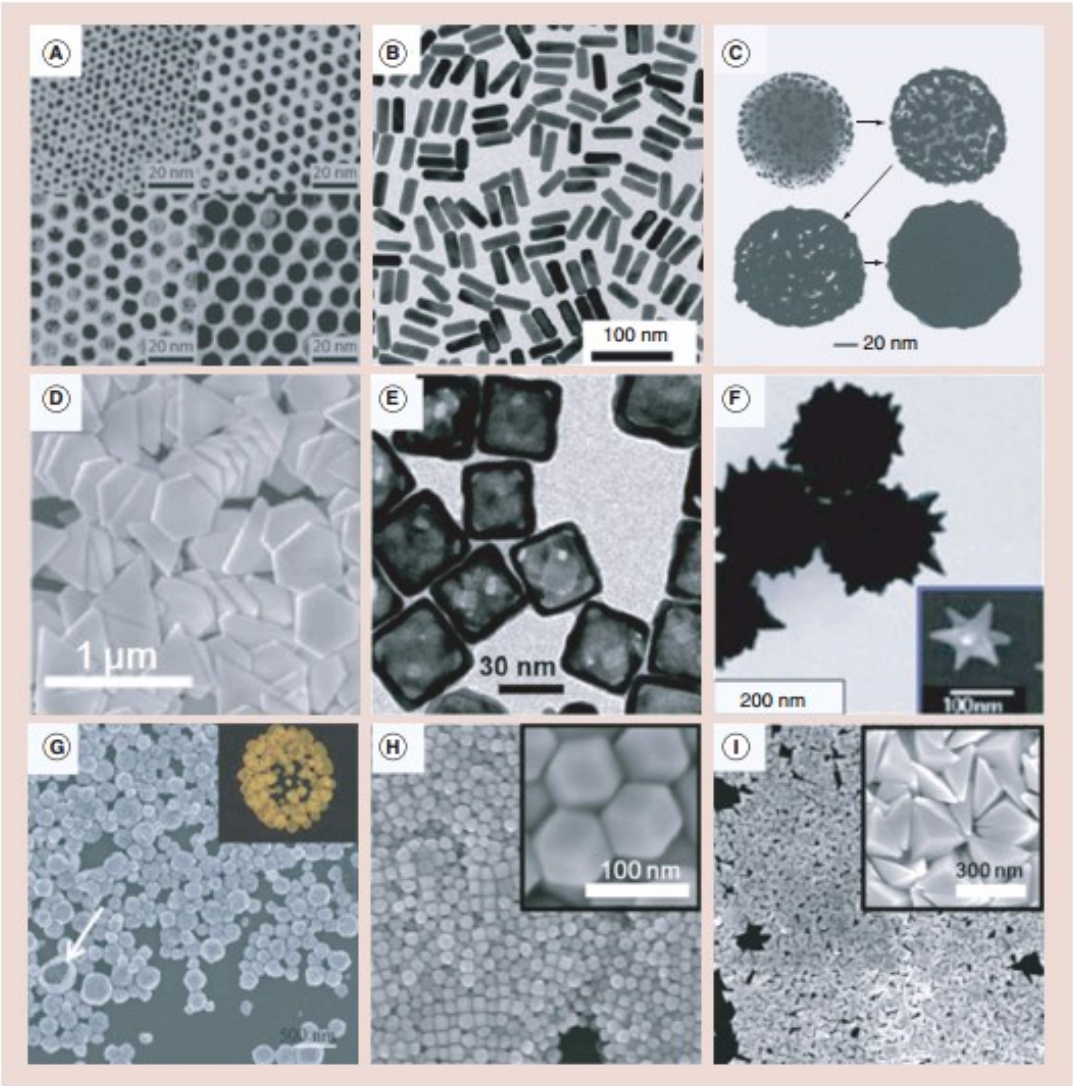


Figure 1-5 Scanning electron microscope and transmission electron microscope micrographs of gold nanostructures of various shapes and sizes. (A) Nanospheres, (B) nanorods, (C) nanoshells, (D) nanoprismss, (E) nanocages, (F) nanostars, (G) nanovesicles, (H) rhombic dodecahedras, and (I) bipyramids. Reprinted from Li and Chen[36], copyright 2015, with permission from future Medicine Ltd.

There are also other less traditional AuNPs synthesis routes. First, thanks to natural compounds such as chitosan, plant extracts (e.g. arabic gum, hibiscus, aloe vera, lemon), or even microbes (e.g. yeast), acting as reducing agent and stabiliser, particles can be prepared via "green" or environmental-friendly processes. Using naturally occurring products is of interest for applications in nanomedicine since it can reduce the risk of adverse effects.[21,29] Second, in the electrochemical method, the gold salts in solution originating from a gold plate, the anode, are converted into AuNPs at the cathode, a silver or platinum plate, benefiting from surfactant stabilisation. The main advantages of this method are: ambient temperature conditions, controlled yields, and low costs.[21,24,37] Last, AuNPs have been prepared using ionic liquids as solvent, reducing and stabilising agent, but also with pulse-radiolysis, where gold salts are reduced under gamma-ray irradiation via radicals formation or via the immobilisation on supports such as oxides solids, carbons (e.g. carbon nanotubes), or mesoporous materials (e.g. MOFs) for applications in catalysis.[29]

A wide range of sizes and shapes can be obtained by varying the experimental conditions as already mentioned. Some more complex structures such as nanoshells, where a dielectric core is covered by a thin layer of gold, or alloy nanoparticles have been synthesised.[38]

1.1.4 Properties and current applications

1.1.4.1 Optoelectronic properties

The first and high interesting feature of the AuNPs are their unique size- and shape-related optical properties. Unlike bulk gold, AuNPs present an energy gap between the valence band and the conduction band due to quantum size effect observed when the de Broglie wavelength of the valence electrons is of the same order as the particle size.[39] When small metal particles are irradiated with a light whose wavelength is superior to their size, the electrons at the surface from the conduction band are oscillating in resonance with the incident electromagnetic radiation thus enhancing the electromagnetic field at the surface; this phenomenon is known as "surface plasmon resonance" (SPR) effect (Figure 1-6). For gold, the resonance frequency lies in the visible

region of the electromagnetic spectrum and explain the red colour of a 20 nm gold colloids suspension as reported by Mie in 1908.[40] Solving the Maxwell's equations for an electromagnetic light wave interacting with small spheres he was able to demonstrate the correlation between the size of the nanoparticles and their SPR properties. [41]

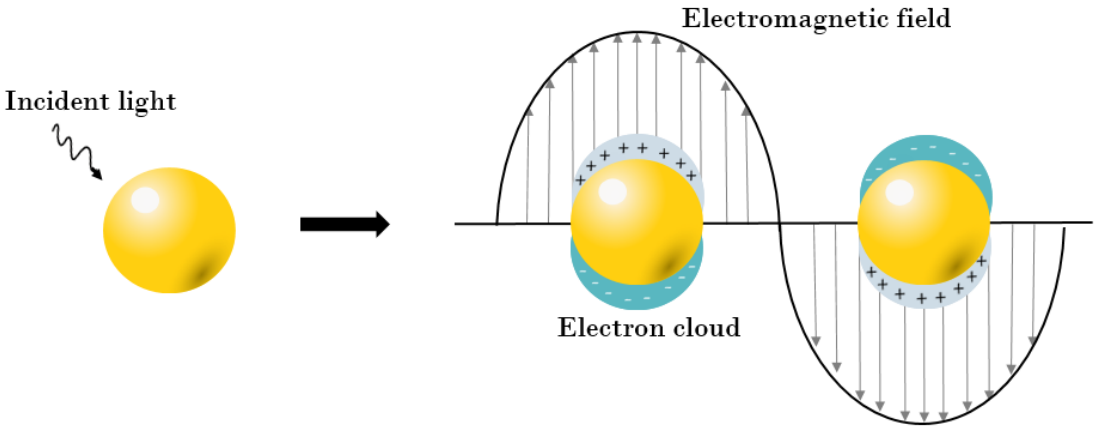


Figure 1-6 Schematic representation of the SPR effect.

Since the surface area to volume ratio of the nanoparticles is very high, the plasmon frequency and intensity are highly sensitive to small changes in the environment (e.g. refractive index, surface modification, aggregation state, shape, size, temperature…) and colorimetric variations can be detected (Figure 1-7). For instance, the colour of a solution of AuNPs will change from purple to red, orange and finally brown if their diameter increases from 2 to 100 nm, it is thus possible to determine the size of the AuNPs from their absorbance spectra (see 2.3.1.3).[42]

Besides showing a difference in diameter size, the colour can also indicate a change of the agglomeration state, solutions of AuNPs (10-20nm) will turn from orange-red to blue with agglomeration due to surface plasmons coupling, the spectra will be red-shifted and the surface plasmon band broaden. The surface plasmon band is a characteristic specific to nanoparticles since it is absent for bulk materials and nanoparticles smaller than 2 nm.

The changes of colour with changes of the environment (e.g. ligand substitution or hydrogen bonding followed by aggregation) has been exploited for colorimetric

sensing.[43,44] Kim *et al.*[45] detected mercury in aqueous media with a detection limit as low as 100 nM.

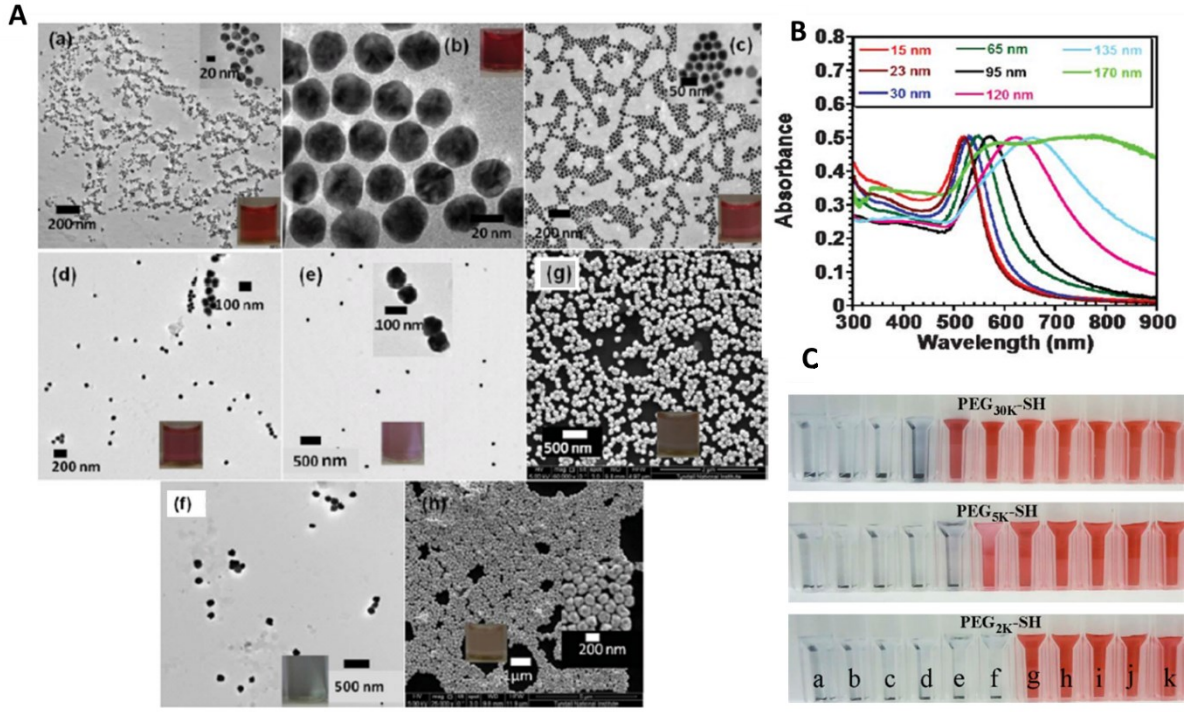


Figure 1-7 (A) TEM micrographs of Au nanoparticles with various mean diameters ~15 nm, (b) ~23 nm, (c) ~30 nm, (d) ~63 nm, (e) ~93 nm and (f) ~135 nm. SEM images of Au nanoparticles with mean diameters of (g) ~115 nm and (h) ~170 nm. The insets show higher magnification electron micrographs, and optical photographs of the corresponding colloidal solutions. (B) UV-visible spectra of Au NPs with different mean diameters (absorbance adjusted to the same value). Reprinted from Rahme *et al.*[46], copyright 2013, with permission from The Royal Society of Chemistry. C. Photograph of (AuNP/PEG-SH) overnight/adenine. The PEG-SH concentrations in vials a to k are 0, 0.0003, 0.003, 0.03, 0.17, 0.3, 0.7,1.3, 2, 2.7, and 3.3 μM, respectively. Adapted with permission from Siriwardana *et al.*[47], copyright 2014, with permission from American Chemical Society.

Besides the SPR, the optoelectronic properties of the AuNPs also include the surface enhanced Raman scattering (SERS) ability. When an incident photon is absorbed by a material, three case scenarios can occur: (i) the energy of the photon corresponds to the resonance energy of the molecule, the photon is absorbed, the molecule switches to an excited state and after a certain time the molecule regains the ground energy state reemitting a photon of lower energy (due to loss of energy via vibrational relaxation generally caused by collisions with solvent molecules), this is called fluorescence; (ii) at any energy level, a photon is absorbed and reemitted at the same energy level this is called Rayleigh scattering or elastic scattering; (iii) the emitted photon has a different

energy level than the absorbed photon, this is called Raman scattering or inelastic scattering. AuNPs can enhance the Raman scattering signal intensities of a molecule adsorbed on its surface by several orders of magnitudes via two mechanisms: electromagnetic and chemical. Electromagnetic enhancement originates from the amplification of the electromagnetic field at the surface of the metal NPs when the plasmons get excited by light irradiation (the enhancement is in the order of 10^6 to 10^7). Chemical enhancement is explained by the change of polarizability observed for the adsorbed molecule (the enhancement is in the order of 10^6 to 10^7). [15,41,48] This phenomenon is of great interest for applications in detection. Herrera *et al.*[20] have prepared TNT SERS sensors with AuNPs deposited on an aluminium sheet and reached a detection level of 7.8 ag ($7.8\ 10^{-18}$ g). Recently, a particular interest has arisen for the preparation of self-assembled AuNPs structure since it has been observed that the SERS signal can be considerably enhanced in the gap regions between assembled particles compared to single nanoparticles.[49,50]

Last, AuNPs have the strong ability to quench the fluorescence of dye molecules at short distances due to the overlap of the molecule's emission wavelengths with the nanoparticle's surface plasmon band. The transfer of energy between the dye and the AuNP is called fluorescence resonance energy transfer (FRET). The quenching is induced by the transfer of electrons from the dye molecule to the gold core, this phenomenon, called photoinduced electron transfer (PET), have been applied to sensing applications.[31]

1.1.4.2 Surface reactivity

The surface of the AuNPs is highly reactive especially with thiol adsorption. Furthermore, based on the ligand exchange reaction (see 1.1.3) other thiolate ligands can be substituted on the nanoparticles surface with a rate dependent on the thiolate species chain length, steric bulk, and the AuNPs charge. Multifunctional AuNPs can be easily obtained by this technique since a large range of molecules can be introduced on the AuNPs surface (e.g. alkenes, sulfonates, nitriles, electroactive and photoactive groups).[3]

In the above section, the physico-chemical properties of the AuNPs have been cited and some of their related applications, the next section will detail the advantages of these

properties for biotechnological applications, in particular for cancer therapy, imaging and diagnostics.

1.2 AuNPs in oncology

This section demonstrates how the AuNPs can respond to the current challenges in oncological treatments based on their intrinsic properties and their capabilities.

1.2.1 Current challenges in cancer therapy

Cancer is the name given to a series of conditions where a mutated cell starts to divide at a much higher rate than normal cells until forming a tumour or mass of abnormal cells that are highly vascularised. The growth of the tumour leads to the displacement and death of healthy cells. According to the Macmillan Cancer Support report from 2015, 2.5 million people are living with cancer in the UK and this number is expected to increase since it is expected than one in two people will get cancer by 2020. Even though people live ten times longer with cancer than 40 years ago, the mean survival rate for 10 years does not exceed 50%, the most lethal cancers being breasts, prostate, colorectal and lung cancers. †

Undeniably cancer therapy is a colossal challenge. The actual treatments involve surgeries followed by periods of chemotherapy and radiotherapy. They are responsible for dramatic adverse effects (e.g. osteoporosis, infertility, gastrointestinal lesions…)[51] due to the elevated drug doses or the invasiveness of the treatment and often fail in preventing recurrence of the cancer.[52]

The main reason limiting the effectiveness of the actual chemotherapeutics is their large volume distribution resulting from their targeting inability. The transportation and distribution of the drugs depend mainly on their physico-chemical characteristics and the tumour tissue's (e.g. size, charge, hydrophobicity) and if they do not correspond to each other's the drugs will accumulate in healthy tissues.[52] Besides, the chemotherapeutic

† Macmillan Cancer Support fact sheet, updated January 2015, retrieved from http://www.macmillan.org.uk/documents/aboutus/research/keystats/statisticsfactsheet.pdf (December 2016)

needs to fulfil a series of requirements on top of its sole therapeutic efficiency: high level of stability in biological media to enable long circulation time, reproducible and optimised release kinetics for the specific condition and biocompatibility. Last, most of the chemotherapeutics exhibit low levels of solubility in aqueous media so that solvents with toxic side effects may be employed for their preparation. [52]

There is a current need for novel therapeutic systems able to protect, transport and deliver the drugs in a targeted manner thus achieving high efficiency and low side effects. The use of nanocarriers, and especially metallic nanoparticles, encapsulating chemotherapeutics has appeared as a solution and investigations in the last decades have shown promising results compared to conventional therapies. Thanks to their highly tuneable nature various strategies have been designed to overcome the biological limitations. AuNPs have attracted interests as drug delivery carriers but also as imaging, sensing, diagnostics and theranostic platform (Figure 1-8).

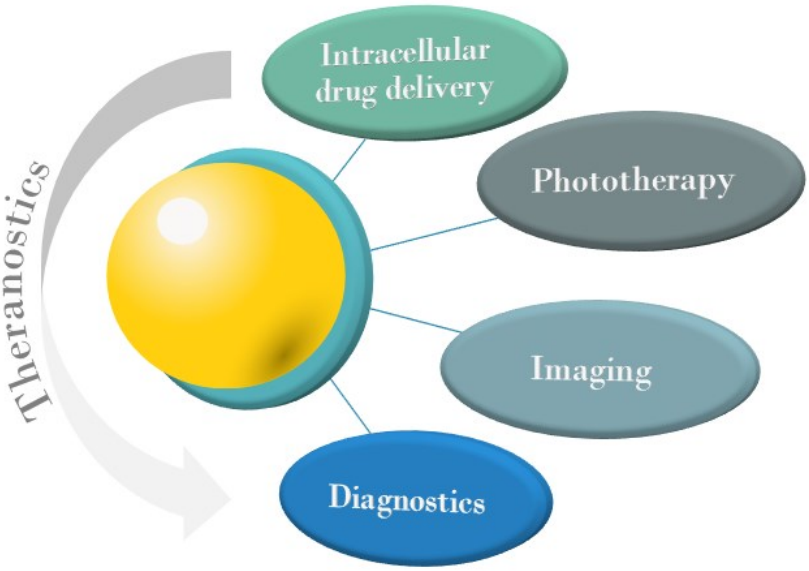


Figure 1-8 Main areas of applications of AuNPs in oncology.

1.2.2 AuNPs as a drug delivery carrier

The nanometric size of AuNPs enables their easy intravenous injection and circulation in the body via the blood stream and with an optimised design they can escape the immune

system and demonstrate the improved circulation time compared to the chemotherapeutic alone. Their high surface to volume ratio and surface functionality allows the loading and stabilisation of large amounts of drug, hydrophilic and hydrophobic, depending on the loading strategy without resorting to pharmaceutical solvents and improving the overall therapeutic half-life.[52]

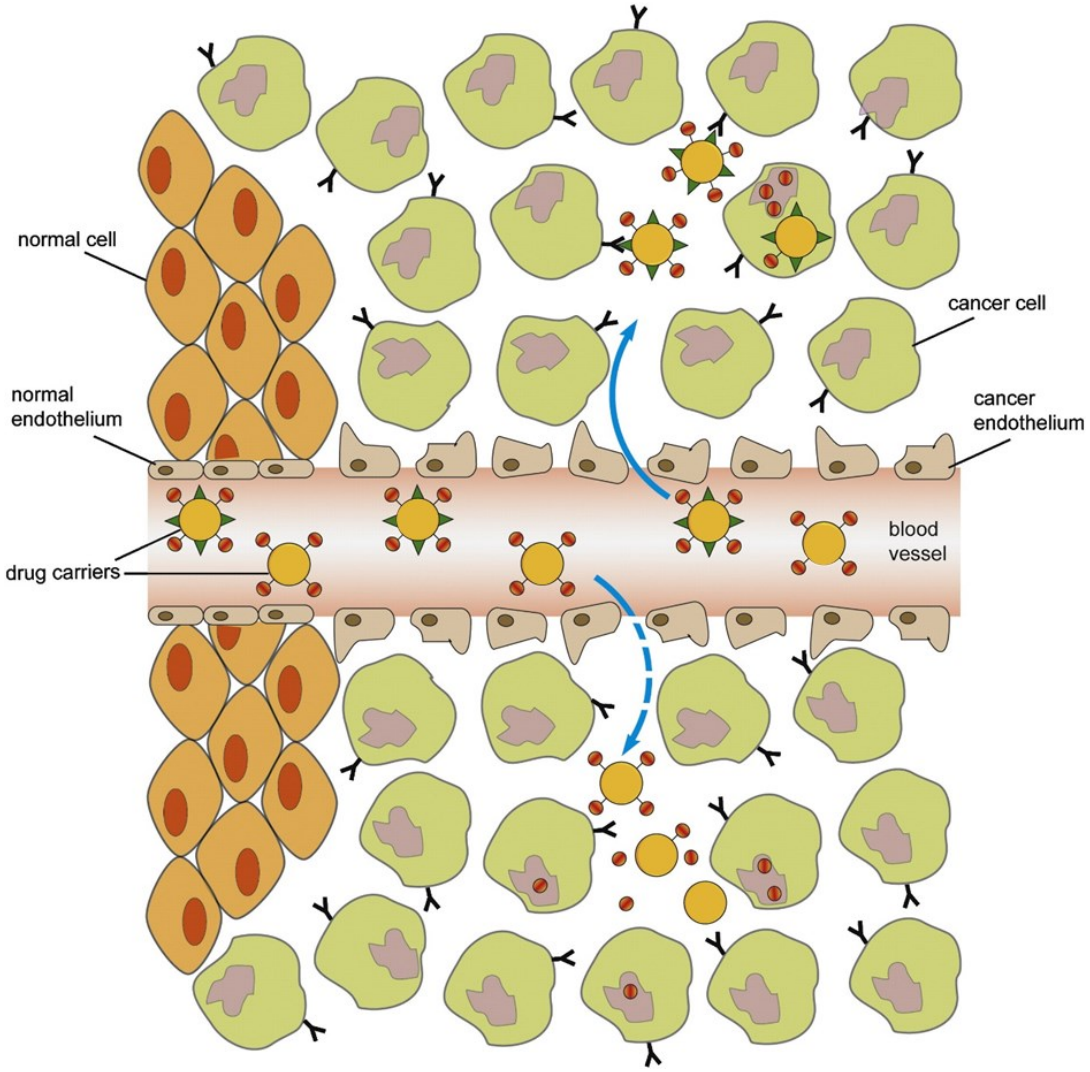


Figure 1-9 Schematic illustration of drug delivery via 'active' and 'passive' targeting, solid and dotted line respectively. Adapted from Barreto *et al.*[13], copyright 2011, with permission from WILEY-VCH Verlag GmbH & Co. KGaA, Weinheim.

AuNPs have also demonstrated targeting abilities following two distinct mechanisms: passive and active targeting (Figure 1-9). The passive targeting is a direct consequence of the Enhanced Permeability and Retention (EPR) effect. Tumorous tissues present a

leaky vasculature with hyper-permeability and large interstitial spaces allowing the AuNPs to enter the tumour. Besides the lack of efficient lymphatic drainage contribute to the retention of the AuNPs within the tumour. The EPR effect contributes to the action of macromolecular anticancer drugs and has been exploited for the delivery of nanocarriers.[53] A major drawback of the EPR effect is the discontinuous blood flow that can lead to the accumulation of nanovectors away from the tumour site especially since the biodistribution of nanoparticles can be strongly affected by interparticle interactions, contacts with plasma proteins or retention in extracellular matrices for instance.[52] To take advantage of the EPR effect particles must be in the size range 10 to 100 nm since smaller particles will face renal clearance and larger particles will be eliminated by the Mononuclear Phagocyte System (MPS).[54]

The active targeting involves the functionalisation of AuNPs with ligand specific to receptors present on the tumour cell surface. The ligand-receptor interaction enhances the internalisation of the nanoparticles via a process called receptor-mediated endocytosis. This strategy offers a more efficient targeting than the passive targeting since targeting ligands (e.g. antibodies, saccharides, hormones) can be designed to specifically corresponds to receptors expressed on certain tumour cells but minimally expressed on normal cells.[52]

1.2.3 Phototherapy

AuNPs have also proved to be efficient in converting the energy from a laser into heat. Under laser irradiation, the electron gas is excited and rapidly cools down via thermal relaxation exchanging its energy with phonons in the nanoparticles lattices. The whole process occurs on a timescale of hundreds of picoseconds and contributes to raise the temperature of the surrounding medium.[41] Even with low laser powers (as low as 100nJ) a temperature increase of several tens of degrees can be obtained (Figure 1-10).[55]

This property is particularly interesting for the application in hyperthermia or photothermal therapy (PTT) where cell damage (e.g. protein denaturation; mechanical stress) caused by a slight increase of the environment temperature (estimated at a distance in the order of tens of nm around the single NP)[56] can lead to cell death.

Consequently, the use of AuNPs in laser therapy offers not only efficiency due to the strong absorption cross section and the lack of photobleaching but also specificity and low toxicity since the laser power needed will not cause damage to healthy cells where AuNPs are not present. Many research groups have exploited the photothermal properties of AuNPs for cancer treatment, also in addition to chemotherapy, and the results hold great promises for the future of cancer therapy.[57-61] PTT will be discussed further in Chapter 5.

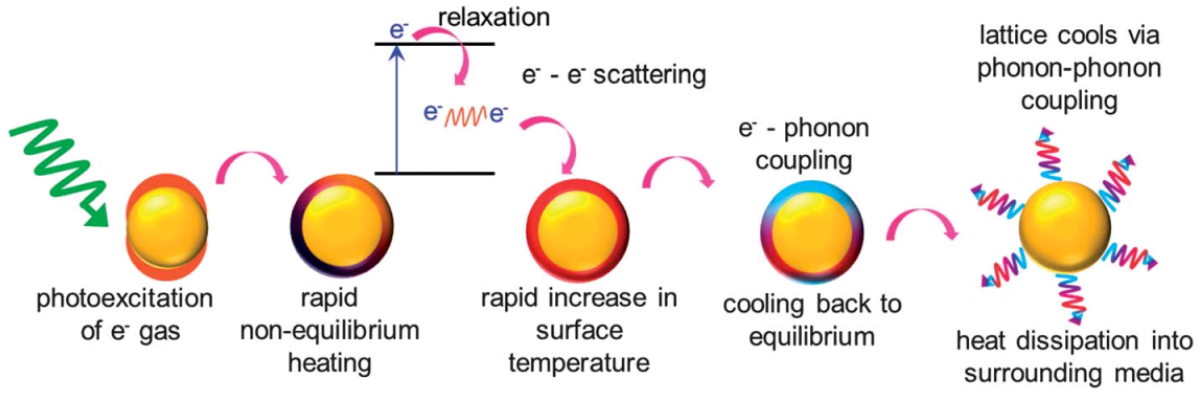


Figure 1-10 Schematic describing the principle of photothermal light to heat conversion by plasmonic nanostructures. Reprinted from Webb and Bardhan[62], copyright 2014, with permission from The Royal Society of Chemistry.

Photodynamic therapy (PDT) or photochemotherapy involves the light irradiation of photosensitisers and the subsequent generation of reactive oxygen species responsible for cells apoptosis or necrosis.[55] The major limitation of photosensitisers is their hydrophobicity, required to get through the lipophilic membrane, and this leads to their lack of solubility in biological media and significant time for accumulation and post-treatment elimination at the target site responsible for systemic toxicity and side effects. PEGylated AuNPs have demonstrated to significantly reduce the transport time of photosensitisers providing an hydrophilic carrier with targeting abilities to the hydrophobic payload.[63]

1.2.4 Imaging, sensing and diagnostics

One of the most important advantages of AuNPs is their optical properties as described in 1.1.4.1. Furthermore, their biocompatibility, ease of synthesis and modification; but

also their lack of photobleaching unlike common fluorophores and their high electron density encouraged their applications in imaging techniques, in particular photoacoustic imaging (PAI),[36,64], X-ray imaging,[65,66] optical imaging (e.g. optical coherence tomography (OCT) (Figure 1-11);[67,68] dark field light scattering; fluorescence microscopy[69]), magnetic resonance imaging (MRI)[70] and SERS[71]. AuNPs have demonstrated 4-5 orders of magnitude higher absorption than rhodamine-6 G, one of the strongest conventional dye used in fluorescence spectroscopy and the light scattering intensity 5 orders of magnitude higher than fluorescein, a common fluorophore.[72]

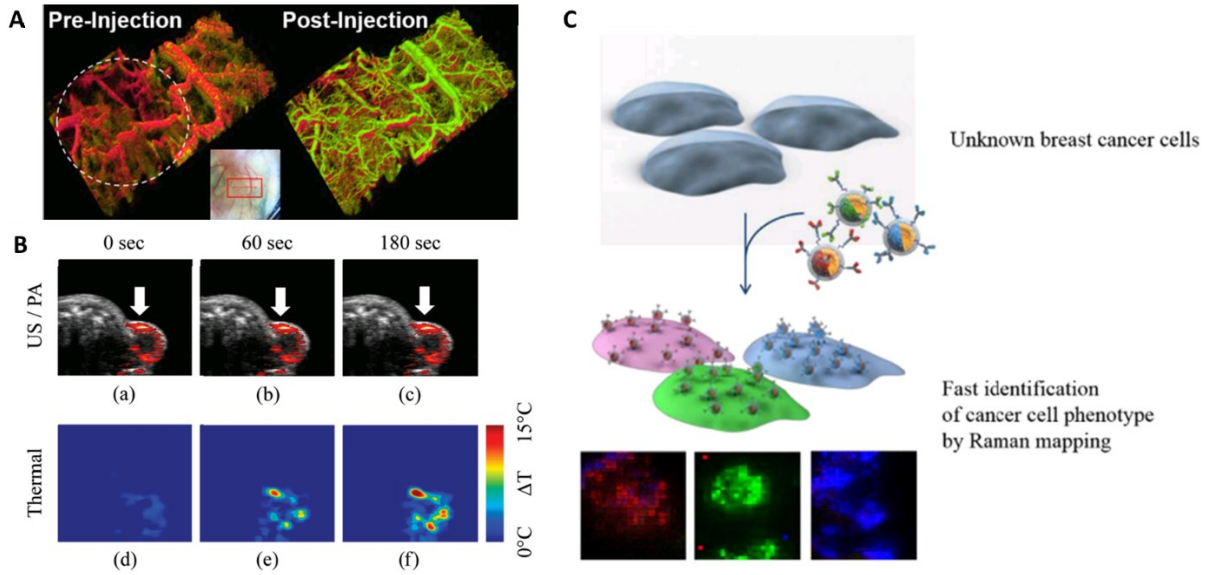


Figure 1-11 (A) Contrast enhancement of OCT images of an in vivo tumour model. 3D volumes (4mm× 2mm) of spectral contrast signal in blood vessels of tumour (circled by dashed white line) and adjacent healthy tissue before and 0, 16, and 24h after injection. (B) (a)–(c) Combined ultrasound and photoacoustic images, and (d)–(f) photoacoustic-based thermal images. The arrow represents the direction of CW laser irradiation (808 nm, 1 W). (C) Schematic illustration of SERS-based cell imaging for the rapid detection and quantification of growth factor receptors on breast cancer cell membranes. (A) is reprinted from Liba *et al.*[68], copyright 2016, with permission from Nature Publishing Group. (B) is reprinted from Kim *et al.*[73], copyright 2014, with permission from IEEE. (C) is reprinted from Lee *et al.*[74], copyright 2013, with permission from Elsevier BV.

AuNPs employed in imaging have multiple purposes: (i) contrast enhancement;[59, 64] (ii) diagnostic imaging via passive or active targeting[74,75] and (iii) therapy and surgery guidance [36,76]. AuNRs and gold nanoshells (AuNSs) are the most popular shapes for imaging purposes since their absorbance is tuned to correspond to the near infra-red (NIR) region (700-900 nm), also called the "biological window" where the tissues and the blood are less absorbing than at the visible wavelengths and thus a higher contrast can be obtained for deep objects.[36,72]

AuNPs have been widely investigated for *in-vitro* clinical diagnostic of conditions such as Alzheimer, hepatitis B, HIV, diabetes but also cancers including leukaemia, breast, oral, cervical and prostate[77]. The AuNPs based sensing relies on three different strategies: [78] (i) colorimetric;[79] (ii) fluorescence[80,81] and (iii) electrochemical.[82] For instance, Li *et al.*[80] designed a sensitive and specific diagnostic tool based on the fluorescence quenching ability of AuNPs to measure levels of anterior gradient homolog 2 (AGR2), protein commonly found in various cancers (Figure 1-12).

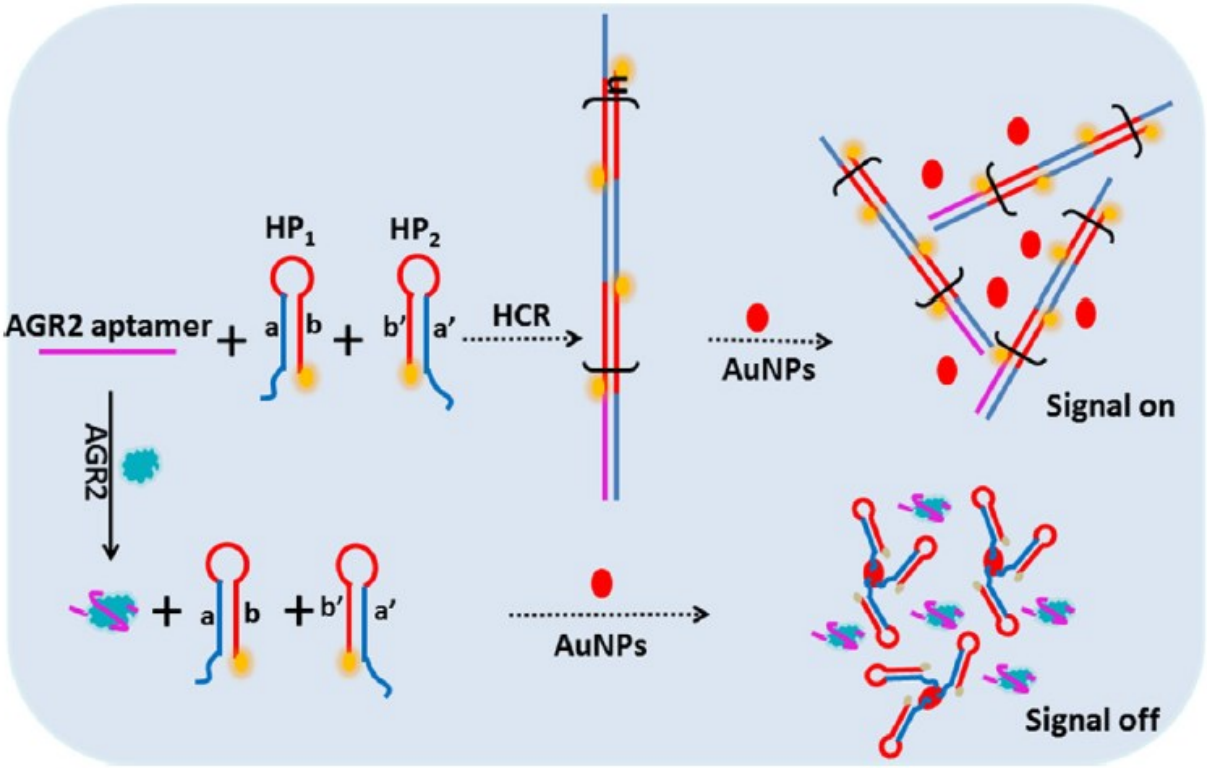


Figure 1-12 The principle of AGR2 detection based on hybridisation chain reaction amplification. Reprinted from Li *et al.*[80], copyright 2016, with permission from Elsevier B.V.

1.2.4.1 Theranostics

Sections 1.2.2 to 1.2.4 have demonstrated the use of AuNPs in oncology as nanoscale drug delivery vectors or photothermal agents for therapy and as contrast agents or signal enhancers for imaging and diagnostics. The need for more targeted and personalised therapies has triggered the development of theranostic platforms, combining diagnostic and therapeutic modalities. Their undeniable advantage is the real-time guiding or monitoring of the therapy provided by the simultaneous imaging (Figure 1-13).

Theranostic nanoparticles are still in their early-stage of development but there have been an increasing attention to this area in the last decades.[51,83-85] The combination of phototherapy with imaging ability, in particular CT, PA or SERS-based imaging, is amongst the most popular approaches. [85]

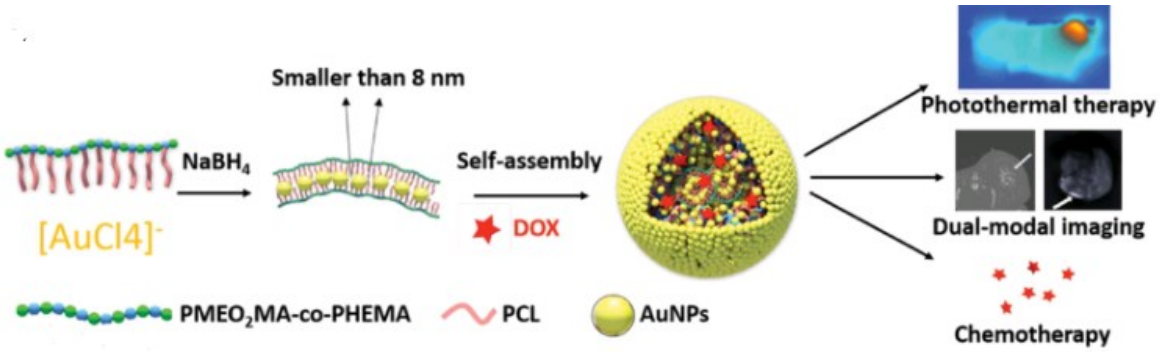


Figure 1-13 Schematic representation of synthesis of DOX@Gold NMs and their potential theranostic application. Reprinted from Deng *et al.*[86], copyright 2015, with permission from WILEY-VCH.

1.2.4.2 Toxicity and limitations

However, despite their numerous applications in cancer therapy, AuNPs are still not available commercially as drug delivery vectors due mainly to the concerns about the potential toxicity of nanomaterials. Gold is known to be an inert and highly biocompatible material which explains why it has been widely used in medicine for centuries. Nevertheless, many materials, especially those at the nanometric scale, can prove to be toxic at a sufficiently high concentration, so the real question is whether AuNPs can be used at the required level for its purpose, therapeutic as well as imaging, estimated at 1-100 AuNPs per cell,[78] without noticeable cytotoxicity.[87] Many studies have confirmed the very low cytotoxicity of AuNPs,[88-90] however, some other researches have demonstrated toxicity of AuNPs *in vitro*[91] and *in-vivo*.[92] Evaluating the toxicity of AuNPs systems is of paramount importance to evaluate their potential as nanotherapeutics however it is also a real challenge.

First, the nanoparticles characteristics such as size (Figure 1-14),[93] surface charge,[94] ligand types,[94,95] shape[96] and concentration, but also the cells types[97] and the interactions with biological media (serum proteins) have a strong impact on their cell uptake[98] and tissue accumulation thus most probably have one on their toxicity. Besides, when

evaluating the toxicity of AuNPs it is important, but not always simple, to differentiate the toxicity of the AuNPs core and the toxicity of the ligands.[99]

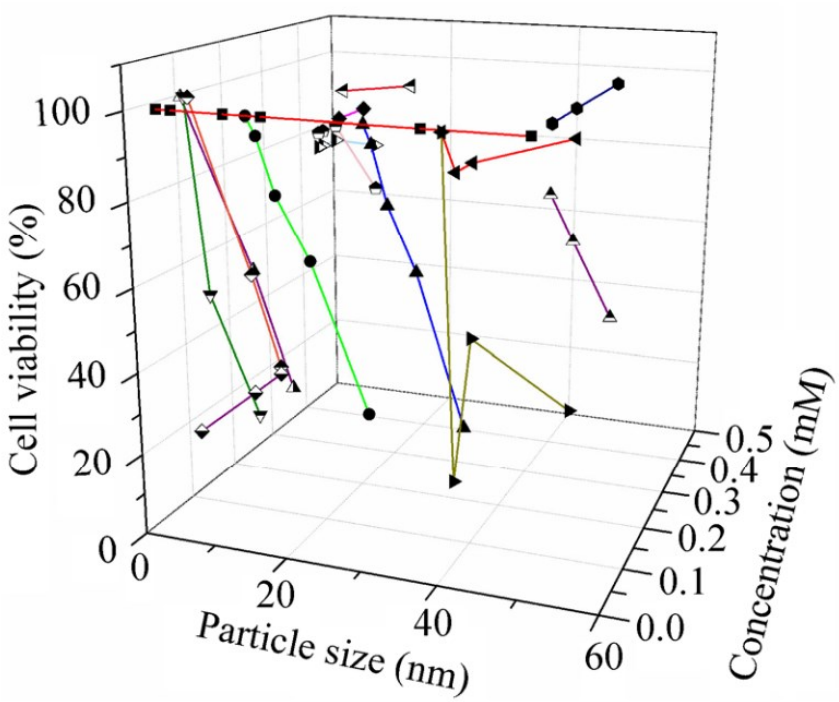


Figure 1-14 Viability data (derived from MTT assay) collected from recent literature on HeLa cells incubated with AuNPs of different sizes and at different concentrations. AuNPs are differently functionalised. Each line refers to a specific reference which can be retrieved from the original paper. Reprinted from Fratoddi *et al.*[100], copyright 2014, with permission from Nature America, Inc

Second, foreign materials can induce toxicity in different manners and a series of parameters might be tested to fully understand their biological risks. Morphological changes can be directly visualised under microscopy, disruption of the cell membranes, and metabolic activity are usually assessed using colorimetric methods. Less common tests include the evaluation of the oxidative stress, the inflammation levels or the DNA damage.[101] Furthermore it is important to consider both cytotoxicity and cellular damage as some particles can proved to be non-cytotoxic with standards assays but can still lead to the formation of abnormal actin filaments, for instance, responsible for a decrease in cell proliferation, adhesion and mobility.[91]

Third, *in-vivo* studies are crucial to obtain pharmacokinetics profiles, *in-vivo* distribution (e.g. spleen, liver, lung, etc…) and to evaluate further the cytotoxicity of the platform

according to the organ-specific toxicity, the metabolic response and the administration route (Figure 1-15).[92]

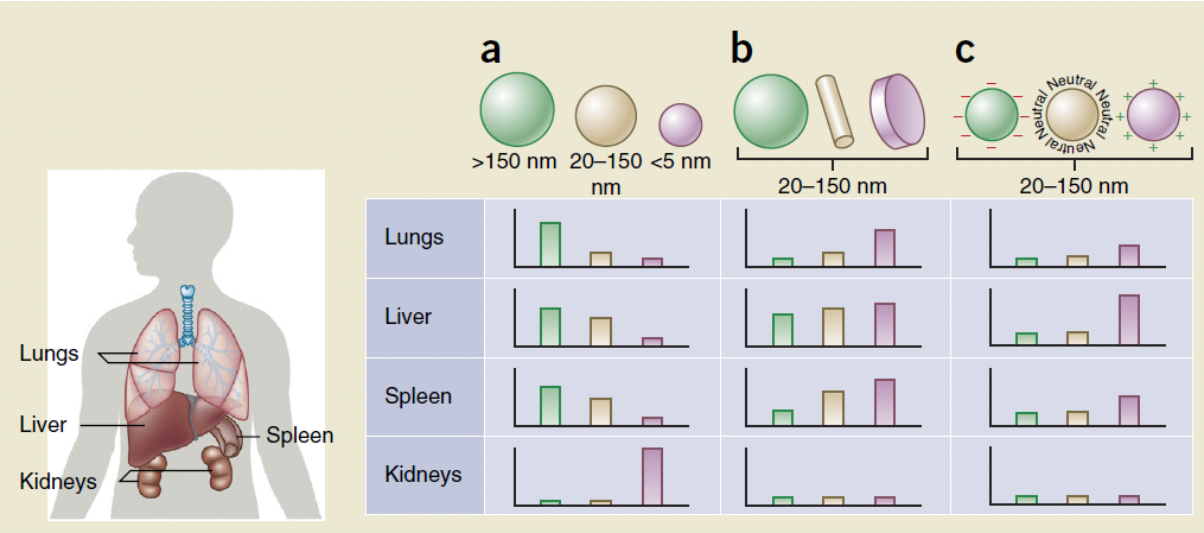


Figure 1-15 Nanoparticle size (a), shape (b) and surface charge (c) dictate biodistribution among the different organs including the lungs, liver, spleen and kidneys. Reprinted from Blanco *et al.*[102], copyright 2015, with permission from Nature America, Inc

In summary, despite numerous investigations on the toxicological profile of AuNPs, no clear correlation has been drawn between their toxicity and their characteristics mostly due to the variability in the physicochemical properties of the AuNPs and the experimental conditions used for the assays. Systematic *in-vitro* and *in-vivo* studies need to be achieved before any therapeutic application can be intended in humans. Nevertheless, the high tunability of the surface with biocompatible molecules and the possibility to use green synthesis methods support their promising potential in nano-oncology.[103]

1.2.4.3 Clinical use of nanoparticles for cancer therapy

The nanomaterials that receive the most attention as cancer therapeutics are: viral nanoparticles, lipid based carriers (e.g. liposomes, solid lipid nanoparticles), polymer based nanocarriers (e.g. polymeric nanoparticles), drug conjugates (e.g. polymer-drug, protein-drug) and inorganic nanoparticles (e.g. metal nanoparticles, silica nanoparticles, carbon nanotubes, quantum dots, magnetic nanoparticles)[13,104] (Figure 1-16).

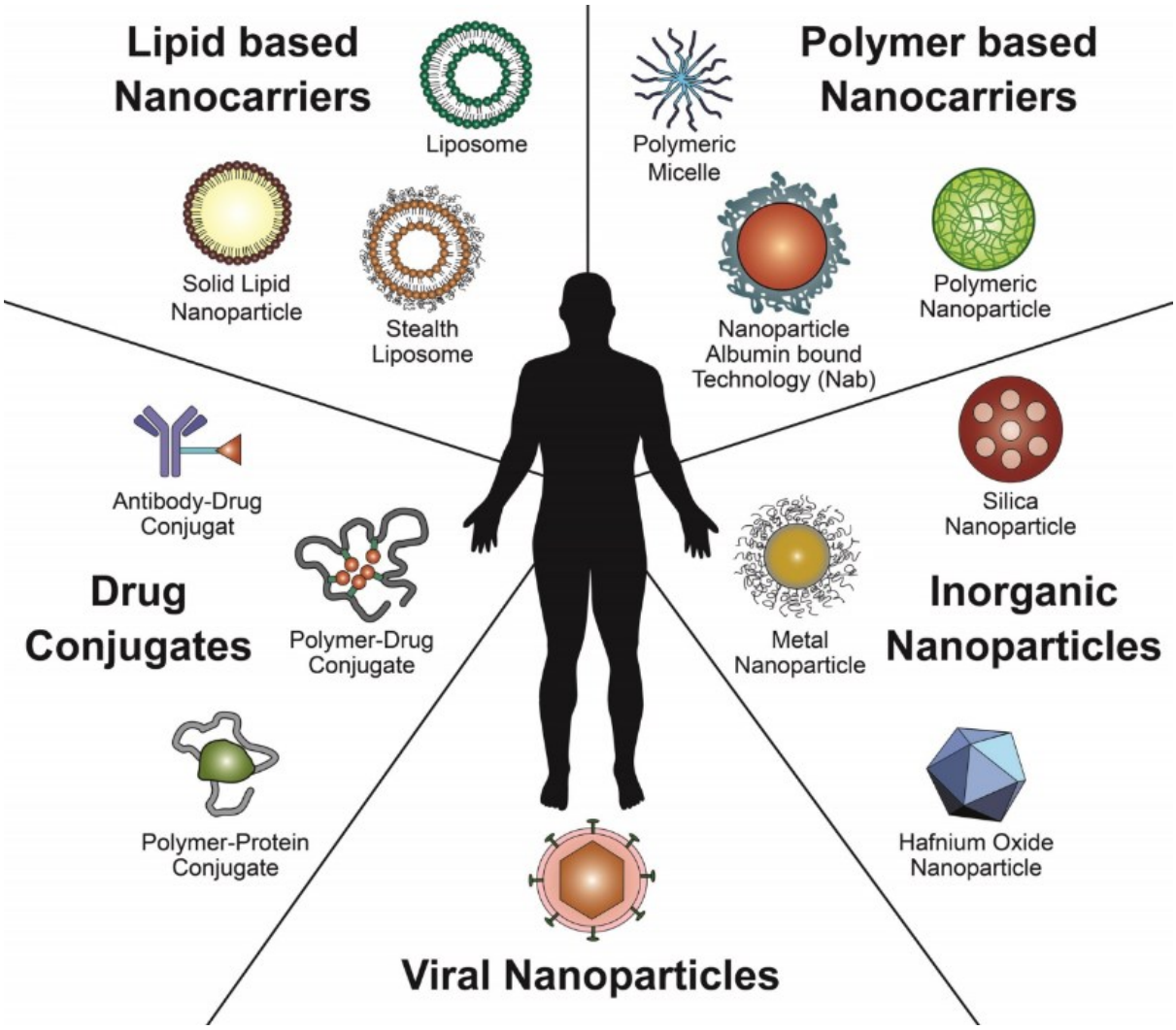


Figure 1-16 Schematic illustration of established nanotherapeutic platforms. Reprinted from Blanco *et al.*[102], copyright 2015, with permission from Nature America, Inc

However, very few intravenous systems of these nanoparticles for cancer therapy have been approved and commercialised, amongst which polymer-protein conjugates, albumin bound nanoparticles and liposomes are the most represented.[54,104,105] The first nanoparticle therapeutic was approved by the Food and Drug Administration (FDA) in 1983, it is a micelle-based system composed of cyclosporine drug and chremophore surfactant (Sandimmune®, Novartis).[54] Few years later, Doxil, PEG functionalised liposomes encapsulating doxorubicin, was the first liposomal based system to be approved (FDA 1995, EMA 1996) for commercial use to treat ovarian cancer. Since then

other liposomal and lipid-based systems have reached the market (e.g. Marqibo for leukemia (2012, Spectrum) and Onivyde for pancreatic cancer (2015, Merrimack) for instance.[106] Protein based nanoparticles (Abraxane, Celgene 2005) and polymer-drug conjugates (e.g. Oncospar, Enzon, 2014) also entered the short list of approved nanomaterials.[54] Iron oxides nanoparticles are the only inorganic nanoparticles that are currently approved for human use. NanoTherm® (Magforce Nanotechnologies) has reached the market in 2010 in a few European countries and is used for magnetic thermal ablation.[104]

1.2.4.4 Clinical use of AuNPs for cancer therapy

Despite the great promises that AuNPs hold for the future in oncology especially as imaging and therapeutic agent, no AuNPs based system is clinically available. Besides, a significant discrepancy exists between the number of publications on nanoparticles-based therapeutics and the number of actual clinical trials (Figure 1-17).

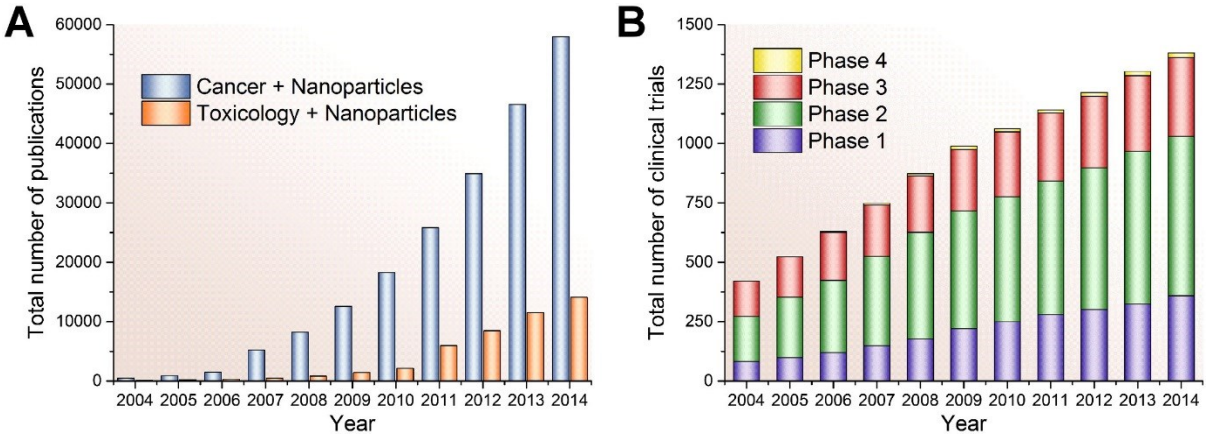


Figure 1-17 Total number of publications (Web of Science®) (A) and clinical trials (clinicaltrials.gov) during the last 10 years (B). Reprinted from Wicki *et al.*[104], copyright 2014, with permission from Elsevier B.V.

A total of six inorganic nanoparticles systems are currently under clinical trial (Table 1-1) one for drug delivery; three for imaging; one for PTT and the last one for radiotherapy. Two of them concerns AuNPs based therapeutics. The first one, AuroLase®, developed by Nanospectra Biosciences, Inc., concerns gold coated silica nanoparticles functionalised with polyethylene glycol (PEG) with a size of 150 nm aimed at photothermal ablation via laser-therapy. The clinical trials focused on refractory and/or recurrent head, lung and

neck cancers. The second one involves 27 nm PEGylated AuNPs coated for the delivery of Tumour Necrosis Factor alpha (TNF-α), AurImune™ CYT-6091, CytImmune Sciences, Inc, aimed at disrupting the tumour blood vessels to increase the efficiency of the chemotherapy. It is designed for patients who are not responding to conventional treatments. The results of the phase I clinical trial are very promising and show an effective and specific delivery of the drug into target cells with low toxicity for healthy cells at a dose three times higher than the previous tolerated dose. The Phase II clinical trial is expected to start shortly.

Table 1-1 Inorganic nanoparticles in clinical trials. Adapted from Wicki *et al.*[104], copyright 2014, with permission from Elsevier B.V.

Product [company]	Platform	Application	Indication	Status
Aurimune (CYT-6091) CytImmune Sciences]	Colloidal gold	Tumor necrosis factor delivery	Solid tumours	Phase 1/2
AuroLase [Nanospectra]	Gold-coated silica nanoparticle	Photothermal ablation	Head and neck cancer	Phase 1
Ferumoxtran-10 (Sinerem/Combidex) [Guerbet/AMAG]	Iron oxide nanoparticle	Magnetic resonance imaging	Prostate cancer	Phase 3
Ferumoxytol (Feraheme) [MD Anderson/AMAG]	Iron oxide nanoparticle	Magnetic resonance imaging	Head and neck cancer, lymph node cancer	Phase 1
NanoXray (NBTXR3) [Nanobiotix]	Hafnium oxide nanoparticle	Radiotherapy	Solid tumours	Phase 1/2
Targeted SNP [Memorial Sloan Kettering Cancer Center]	Silica nanoparticle	Lymph node imaging	Head and neck melanoma	Phase 0

1.2.4.5 Challenges for nanomaterials translation to clinic

The main challenges that nanomaterials are facing for their clinical translations are the lack of standardised physico-chemical characterisation techniques; unsuited *in-vitro* and

in-vivo assessments that have been developed for micro-sized formulations; the absence of specific guidelines for regulatory approval and large-scale production; and the high cost of manufacturing since they are usually more expensive to produce than their free drugs counterparts due to multi-steps processes and high costs of the raw materials. Besides, toxicity concerns have been raised not only for human but also for the environments. These factors explain why most of the clinical trials involve already commercialised systems based on FDA approved drugs, polymers or liposomes for alternative applications since regulatory institutions and manufacturers prefer to minimise the risks.[104]

1.2.5 Advantages and drawbacks of AuNPs compared to other nanoparticles

Provided by their metallic nature AuNPs have a unique advantage compared to the other organic nanoparticles to serve as a multimodal platform combining imaging, sensing and therapeutic abilities simultaneously. Besides they can be synthesised with a wide range of sizes (from 2 to 200nm) and shapes (e.g. spheres, rods, prisms, stars, hollow, cages, core-shell) with great reproducibility and narrow size distribution which enable them to be designed for specific purposes.[107] For instance, the aspect ratio of AuNRs and the shell thickness of the core-shell systems can be controlled to adjust the maximum absorption at the wavelength of common lasers for phototherapeutic purposes.

Due to their lipid structure, liposomes are considered safer than metallic nanoparticles and are amongst the most popular FDA-approved nanomaterials however their drawbacks include: shorter circulation time[104] and drug leakage.[108] Polymer-drug conjugates also belong to the FDA-approved nanodrugs however their drug loading capacity is limited and may greatly influence the polymer properties.[104] Lastly, amongst inorganic nanoparticles, carbon nanotubes (CNT) have attracted great attention in therapy however their insolubility in aqueous solvents, large size distribution and their toxicity are major concerns.[109]

The main drawbacks of AuNPs as delivery systems concern their fragile colloidal stability and their limited biodegradability. The surface modification with stabilising agents is compulsory to provide the system with long-term circulation ability, however some

stabilising agents such as PEG are also responsible for lower cellular uptake due to steric hindrance and charge neutralisation.[110] In order to be eliminated by the kidney AuNPs sizes should not exceed 5.5 nm, however to achieve some applications such as phototherapy or imaging the size required is much larger than 5.5 nm which leads to the long-term accumulation of the nanoparticles in the system with potential side effects for the patient.[111]

1.3 Design of AuNPs as cancer therapeutics

This section highlights the parameters to be taken into consideration when designing a platform for cancer therapy and gives details of synthesis methods from recent investigations.

1.3.1 Common surface modification strategies

As already mentioned in 1.1.4.2, the AuNP surface is highly reactive and the large area to volume ratio of nanometric sized materials enable the loading of a large quantity of molecules. The AuNP surface has been functionalised for various purposes, mostly for providing colloidal stability, targeting, sensing and drug loading functions (Figure 1-18). Each strategy will be reviewed in the following sections.

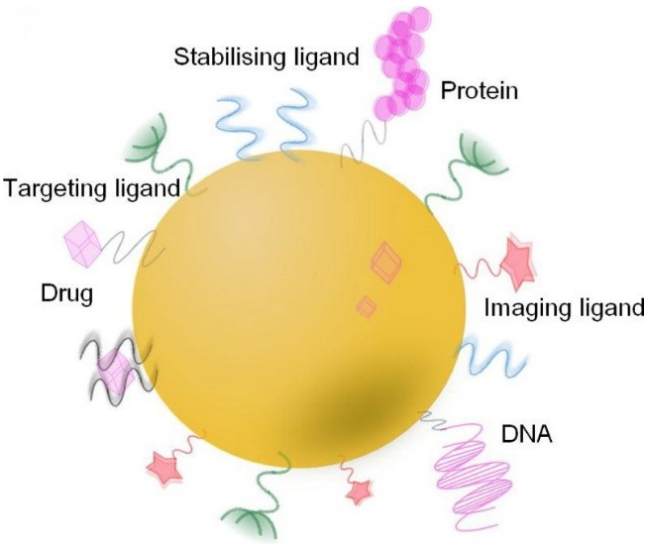


Figure 1-18 Multifunctional nature of AuNPs. Reprinted from Bachelet[112], copyright 2016, with permission from the Institute of Materials, Minerals and Mining

Two main strategies are used for surface loading: (i) physical entrapment (e.g. via electrostatic and hydrophobic interactions) or (ii) covalent bonding of a thiolated molecule of interest (strong Au-S adsorption) which can be further modified (e.g. place exchange reaction; polymerisation).[113]

The first strategy is usually simpler and adapted to molecules that may lose their function upon conjugation (e.g. proteins, drugs) but it usually leads to loosely bound molecules that are easily detached from the surface during the purification process for instance and exhibits lower loading levels than the second strategy. This strategy is generally used for drug delivery or sensing purposes. For example drug molecules can be entrapped within a polymeric shell via hydrophobic or electrostatic interactions.[31]

The second strategy leads to stronger and more stable bonds and is usually employed for imaging, targeting and stability purposes. While AuNPs can be stabilised by various molecules (e.g. polymers, surfactants, biomolecules) thiolated ligands are by far the most employed for the strong stabilisation they provide to the colloidal system.[78] They can be grafted to the AuNP surface once AuNPs are formed or during their synthesis via the Brust-Schiffrin reaction mentioned earlier. A wide range of ligand-stabilised AuNPs can be obtained using this reaction and molecules containing sulfurs: alkanethiol; thiolated PEG; mercaptophenol; glutathione are a few examples.[34]

Following the functionalisation of ligands on the AuNP surface, further reactions can be applied to create additional covalent bonds between the grafted ligands and free molecules to prepare multifunctional AuNPs. The two mains strategies are the formation of amide bonds between carboxy groups and amines using carbodiimides and the click reaction which links an alkyne and an azide.[78] Other methods include amides and ester couplings, nucleopholic substitutions with alkylamines and polymerisations reactions.[34]

1.3.2 Colloidal stability and PEGylation

Several types of ligands can be used to stabilise AuNPs such as the phosphor, oxygen or nitrogen based ligands and particularly those composed of amine groups. AuNPs can also be prepared with polymers or dendrimers as stabilisers. The polymers have many

advantages as they increase the long term stability and solubility of the AuNPs but also their amphiphilicity and compatibility.[114] Polymer-stabilised AuNPs can be obtained through three main routes: "grafting to", "grafting from" and "one-pot". The "grafting to" strategy is the simple grafting of a polymer chain usually via Au-S bonding. The "grafting from" strategy involves the polymerisation of a short pre-grafted ligand with the aid of an initiator. In the "one-pot" strategy the polymerisation occurs during the ANPs formation.[114] The main polymeric ligands include thiolate end-capped polystyrene (PS), thiolate PEG, thiolate poly(N-isopropylacrylamide) (PNIPAM) and thiolatepoly(vinyl pyridine) (PVP).

PEG is the most common polymer used in drug delivery systems since it is biocompatible, FDA-approved and it provides AuNPs with long term stability in both aqueous and organic solvents but also in biological fluids. First, PEG is able to shield the AuNP surface charge, increasing their hydrophilicity and decreasing their toxicity. The second important effect of PEGylation is the ability to repel opsonins and to hinder phagocytosis providing the longer circulation time (Figure 1-19).[13]

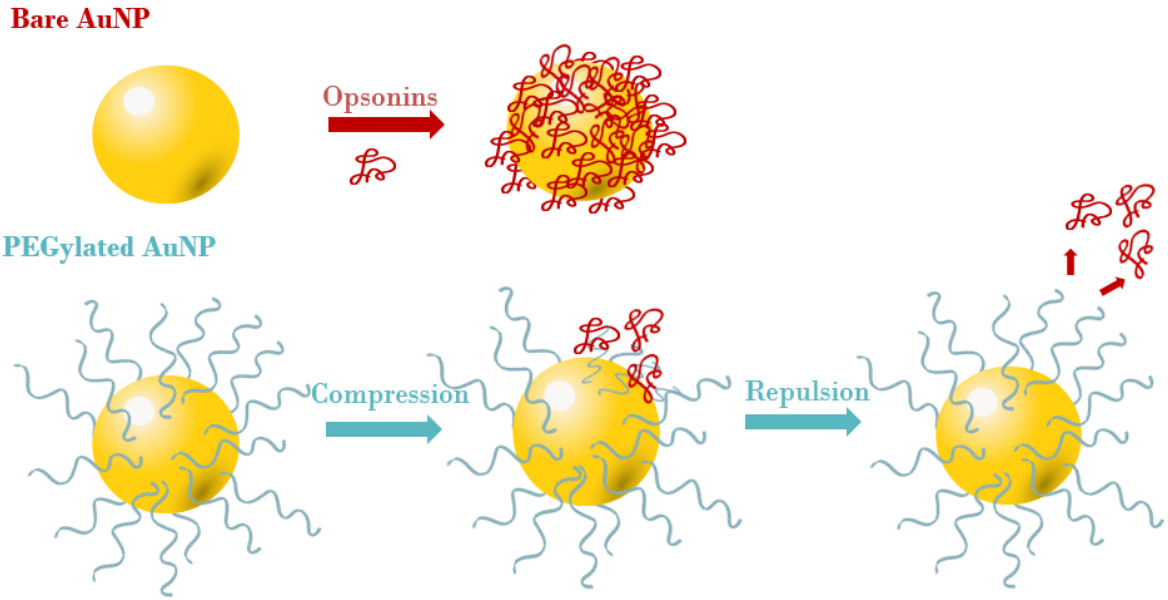


Figure 1-19 Representation of how PEGylation avoids clearance of NPs by the RES. Adapted from Barreto *et al.*[13] copyright 2011, with permission from Wiley.

1.3.3 Therapeutics: drug loading, drug release and phototherapy

As already mentioned, molecules can be loaded to AuNPs via non-covalent and covalent bindings and both strategies have been employed for drug loading.

Non-covalent loading into the AuNP monolayer is generally based on electrostatic interactions between charged molecules and the AuNPs surface[115,116] or performed for hydrophobic drugs that can be entrapped into an inner hydrophobic layer. [117] C.K. Kim *et al.*[117] designed AuNPs with a hydrophobic alkanethiol interior and a hydrophilic shell of tetra(ethylene glycol) (TEG) terminated with a zwitterionic group to increase the stability. They demonstrated that the two hydrophobic drugs tamixofen (TMF) and ß-lapachone (LAP) and the dye Bodipy could be efficiently entrapped in the hydrophobic pocket and suggested that the *in vitro r*elease into MCF-7 cells was successful via a membrane-mediated diffusion mechanism with low toxicity where the drug diffused from the hydrophobic interior of the NP coating to the cytoplasm of the cell directly without NP uptake. When the drug loading is performed via electrostatic interactions the drug release can be achieved via pH trigger.[118]

Covalent bindings are stronger than non-covalent ones but while burst release are observed for non-covalent bindings, the efficiency of the release of covalently loaded drugs is at stake. After conjugation via Au-S bonding, the release can be performed via ligand exchange by intracellular thiols. Glutathione is the most abundant thiol in the cytoplasm and its intracellular concentration (1-10 mM) is much higher than its extracellular concentration (2 μM in the plasma)[119] which is an interesting feature for stimuli triggered release via ligand exchange[119-123] or reduction of disulfide linkage[124]. Additionally, the release of the drug from AuNPs can be triggered via external stimuli. One of the most common external stimuli used for intracellular drug release is the pH. When a molecule is internalised through receptor-mediated endocytosis, it is entrapped in endosomes where the pH gradually decreases. The endosomes have a cell sorting function and the acidification enables the dissociation of the ligands from their receptors so that the receptors can be recycled back to the cell surface. The acidity is maintained by ATP-dependent proton pumps.[125] The acidity of the endosomal compartment has been exploited to trigger the release of drugs conjugated via acid-cleavable bonds with

hydrazine bonds being the most popular.[126-131] Other strategies for pH triggered release involve the dissolution of a pH degradable layer where the drug is encapsulated[132] and the pH-dependant conformational switch of DNA strands with entrapped drugs.[133]

Another external stimulus of interest is the light that can be generated with a laser. Various research groups have employed photocleavable bonds[134-136], temperature-induced release[61] and the shrinking of thermoresponsive hydrogel-AuNPs composites to trigger drug release with the use of light.[137-139]

The design of phototherapeutic AuNPs does not require a high level of functionalisation since the metallic core properties are primarily exploited.[57,60] The most common approaches include the use of stabilised AuNPs (e.g. PEG[140]; glucose[141]) combined with the use of a laser (NIR[61,140], visible[142], X-ray[141]) whose wavelength depends on the size and the geometry of the particles. Indeed, hollow nanospheres and nanoshells with a silica core and a gold layer are the most common[143].

1.3.4 Targeting

The targeting ability of the AuNPs, or the capacity to selectively target tumour cells and not healthy cells, is crucial for an optimised drug delivery via the specific uptake of the tumour cells. It is known that targeted nanoparticles usually deliver more payload into specific cancer cells than their untargeted counterparts.[144] An ideal nanocarrier combines passive targeting via the Enhanced Permeability and Retention (EPR) effect and active targeting via the use of targeting ligands, antibodies, aptamers or small molecules (e.g. vitamins) at the surface of the nanoparticle[144,145]

Folate receptors are overexpressed on the surface on numerous tumour cells (e.g. brain, kidney, breast, lung)[146]. Folic acid (FA)[147] and methotrexate (MTX)[123] have been conjugated to AuNPs for the specific targeting of these receptors. Furthermore, MTX has the advantage to also act as an anticancer drug[89,123]. As well as MTX, TNF is a targeting moiety and an anticancer drug which have been frequently combined with AuNPs. The other common targeting ligands are the anti-epidermal growth factor (anti-EFGR)[122] (Figure 1-20), the transferrin (Tf)[144] and the tamixofen (TMX).[148] Conjugation of targeting

ligands to AuNPs are usually carried out via chemical modification of the ligand followed by grafting[147], through the use of a PEG spacer[148], or less frequently via the direct conjugation on the AuNPs surface[123].

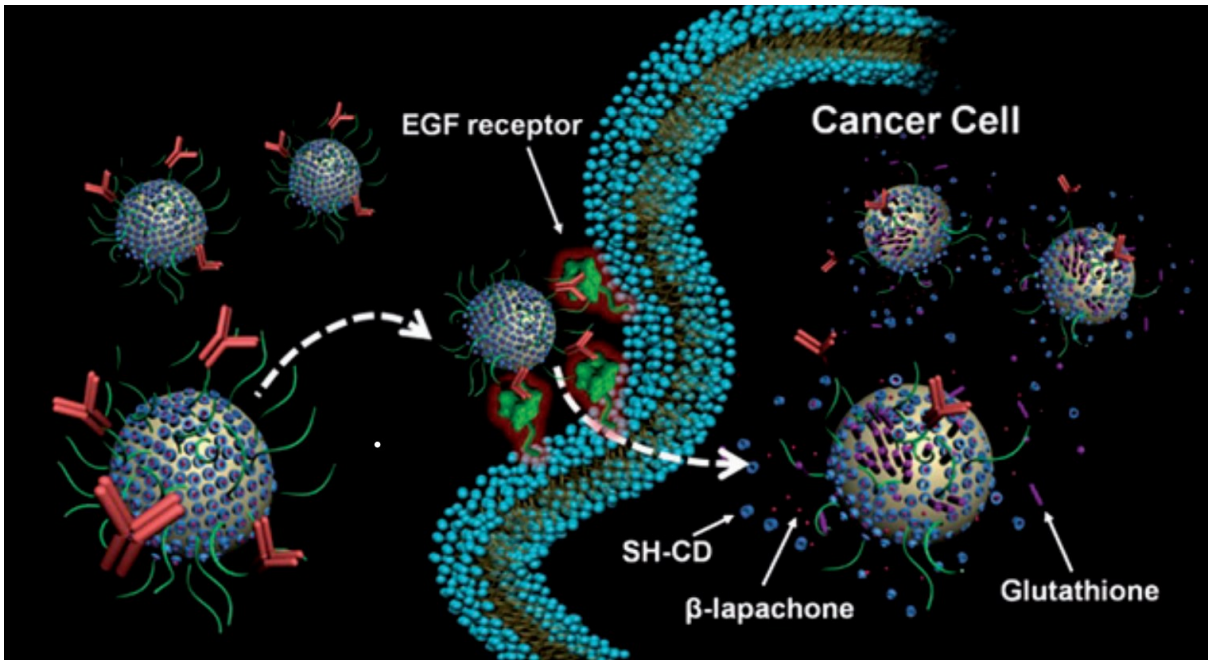


Figure 1-20 Schematic illustration for the enhanced cellular uptake of AuNPs by anti-EGFR antibody and glutathione-mediated intracellular release of AuNP-2 carriers. Reproduced from Park *et al.*[122], copyright 2009, with permission from the Royal Society of Chemistry.

Important factors to be considered when designing a ligand-based targeting nanotherapeutic are: specificity of binding, stimulation process of the receptor-mediated endocytosis, biocompatibility, easy synthesis and modification and impact on the drug release kinetics.[149]

1.3.5 Nanoparticles hydrogel composites

Hydrogels are 3D networks of hydrophilic polymers crosslinked via physical or chemical interactions. They have attracted great interests in the biomedical field for their remarkable biocompatibility due to their high-water content and their capacity to load a wide range of molecules thanks to their porous structure, without impairing their biological functions, and to deliver them in a sustained manner (e.g. diffusion, swelling, environmental trigger).[150]

Recently, research groups have started to draw their interests on the development of NP-hydrogel composites.[151] The incorporation of NPs within a polymer network can bring numerous synergistic advantages: higher mechanical strength to the overall gel, and better stability of the NPs hence a diminished risk of agglomeration. For application in bioengineering, the hydrogel is useful to prevent the direct contact between the NPs and the cells for instance.[152] The vast majority of the applications in oncology involves temperature responsive hydrogels for phototherapy and/or controlled drug release.[137,139]

Three main types of NPs hydrogel composites can be found in the literature (i) bulk nanocomposites,[137,153] (ii) particles nanocomposites[139] and (iii) core-shell nanocomposites (Figure 1-21).[154] [155] The particles and core-shell nanocomposites are usually intended for intravenous applications or passive tumour targeting and generally imply faster swelling response.[152]

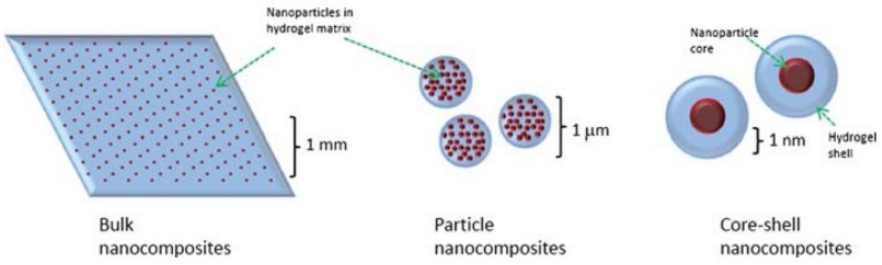


Figure 1-21 Different forms of hydrogel nanocomposites: bulk nanocomposites, particle nanocomposites, and core-shell nanocomposites. Reproduced from Satarkar *et al.*[152], copyright 2010, with permission from the Royal Society of Chemistry.

The synthesis of the hydrogel can be performed simultaneously with the NPs synthesis (i.e. one pot synthesis),[156] before (i.e. NPs loading or reduction within the hydrogel network),[153] or after (i.e. post-polymerisation).[137]

1.4 Polymeric hybrid AuNPs for intracellular delivery

1.4.1 Challenges for the drug delivery using nanoparticles

Even though nanoparticles-based drug delivery carriers have been designed to safely transport free drugs to the target site they still have to face a series of barriers before delivering their payload (Figure 1-22). First, in the blood stream opsonins proteins cover any foreign element and allow its recognition by the macrophages, from the MPS, that will transport it to the liver and spleen for its elimination resulting in non-specific distribution.[157] The second major extracellular obstacle faced by injected molecules or particles is the blood vessel wall and successful crossing depends on the molecules characteristics (geometry, size) but also on the blood flow dynamics.[102] Additionally, once they reach the extracellular membranes several challenges still need to be overcome before they can efficiently delivery their payload to the site of interest, cytoplasm or nucleus. The three major intracellular challenges discussed below are: (1) cellular uptake; (2) lysosome degradation and secretion and (3) multidrug resistance.

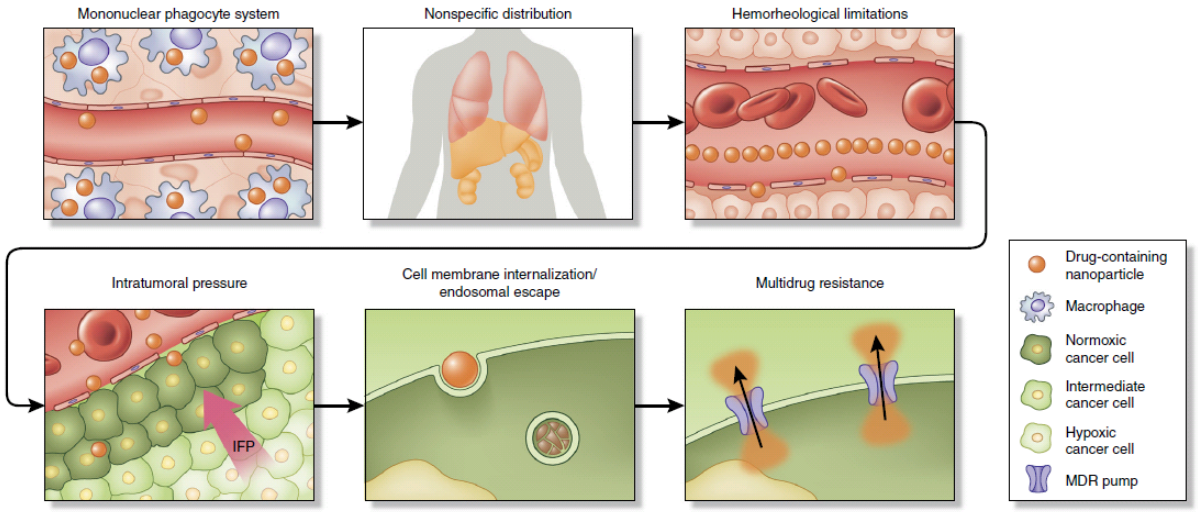


Figure 1-22 Framework of sequential biological barriers to nanoparticle drug delivery. Reprinted from Blanco *et al.*[102] copyright 2015, with permission from Nature America, Inc.

Ions and biomolecules enter cells via an energy-dependent process called endocytosis used by all the cells in the body. They are four main routes for endocytosis: (i) clathrin or caveolin mediated; (ii) phagocytosis; (iii) micropinocytosis and (iv) pinocytosis (Figure

1-23). The first two mechanisms are receptor-mediated and are the main pathways for the internalisation of nanoparticles larger than 10 nm however, phagocytosis is reserved for phagocytic cells internalising usually particles larger than 500 nm.

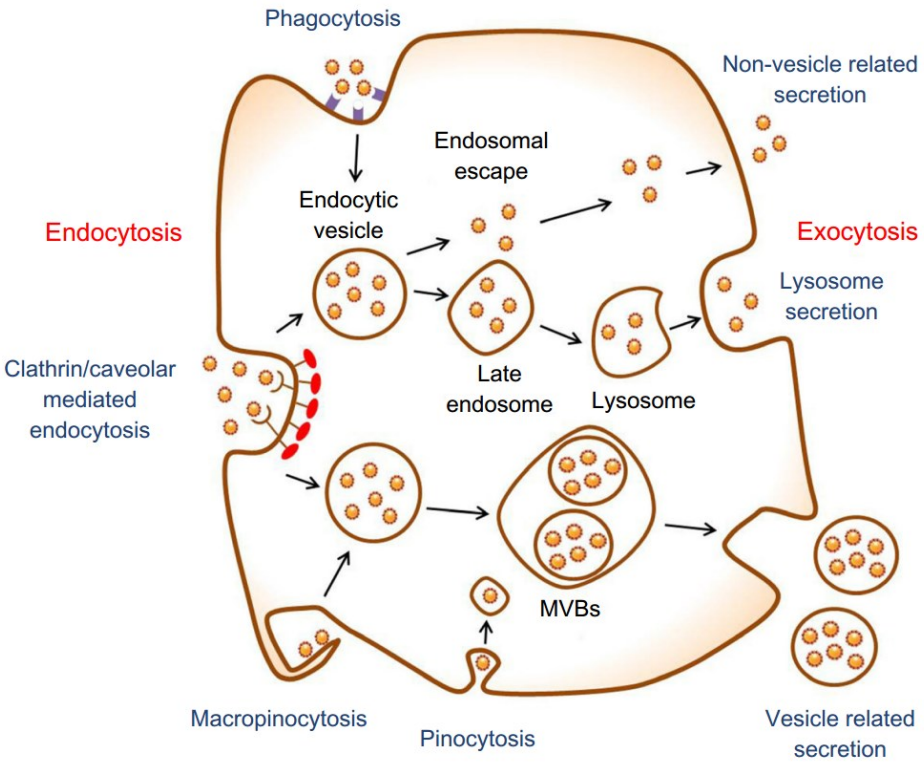


Figure 1-23 Schematic of endocytosis and exocytosis patterns of nanoparticles. Nanoparticles the cell via four types of pathway: clathrin/caveolar-mediated endocytosis, phagocytosis, macropinocytosis, and pinocytosis. Nanoparticles exit the cell via three types of pathway: lysosome secretion, vesicle-related secretion, and non-vesicle-related secretion. Reproduced from Oh and Park[157], copyright 2014, with permission from Oh and Park.

Internalisation is dependent on numerous factors such as size, surface charge and shape of the nanoparticles but also on the specific interaction between the nanoparticles and the membrane. The cellular membrane is made of a lipid bilayer and thus the successful internalisation of a molecule relies on the transduction through the hydrophobic (tail) and hydrophilic (head) compounds (Figure 1-24).

The second important intracellular barrier is the endocytic pathway. Once a molecule has successfully entered the cell via the receptor-mediated endocytosis pathway, it is entrapped into a cellular compartment named endosome which will mature following a multi-step process into a lysosome where the molecule will be cleaved and degraded, and

then recycled back to the cytoplasm or to the extracellular medium (exocytosis). The process of maturation comprises an acidification of the vesicle from pH~7.2 to pH~5 from the early endosome to the lysosome.[158] Each compartment has its own optimal pH, critical for their activity of sorting, which includes the cleavage between ligands and receptors. The acidity is maintained thanks to an adenosine triphosphate (ATP) proton pump.[125]

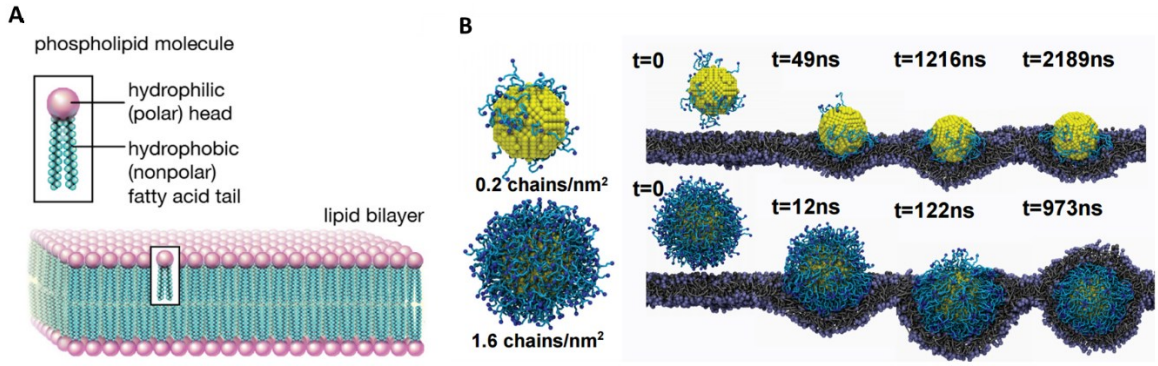


Figure 1-24 (A) Schematic of the lipid bilayer. (B) Internalisation process of PEGylated NPs. Snapshots of PEGylated NPs used in the dissipative particle dynamics (DPD) simulations with two grafting densities: 0.2 and 1.6 chains nm^{-2}. The diameter of the NP core is about 8 nm. (A) is an illustration retrieved from Encyclopedia Britannica Online, accessed February 2017, copyright 2009, Encyclopedia Britannica Inc. (B) is reproduced from Shen *et al.*[159] open access.

The third major limitation to the efficiency of the chemotherapeutic delivery is the drug resistance and in particular the multidrug resistance (MDR) which is a capacity of tumour cells, when exposed to one specific class of chemotherapeutics, to develop cross-resistance to previously unexposed or structurally unrelated classes (Figure 1-25). The resistance mechanisms include a decrease in the drug uptake and an increase of the efflux (efflux pumps), alteration of the drug targets and metabolism of the drug.[160] ATP-binding cassette (ABC) transporters are membrane proteins that use the energy of ATP hydrolysis to pump out toxins and drugs to the extracellular medium. P-glycoprotein (P-gp) is one of the most recognised transporters. It is overexpressed in the plasma membrane of MDR cells.[161]

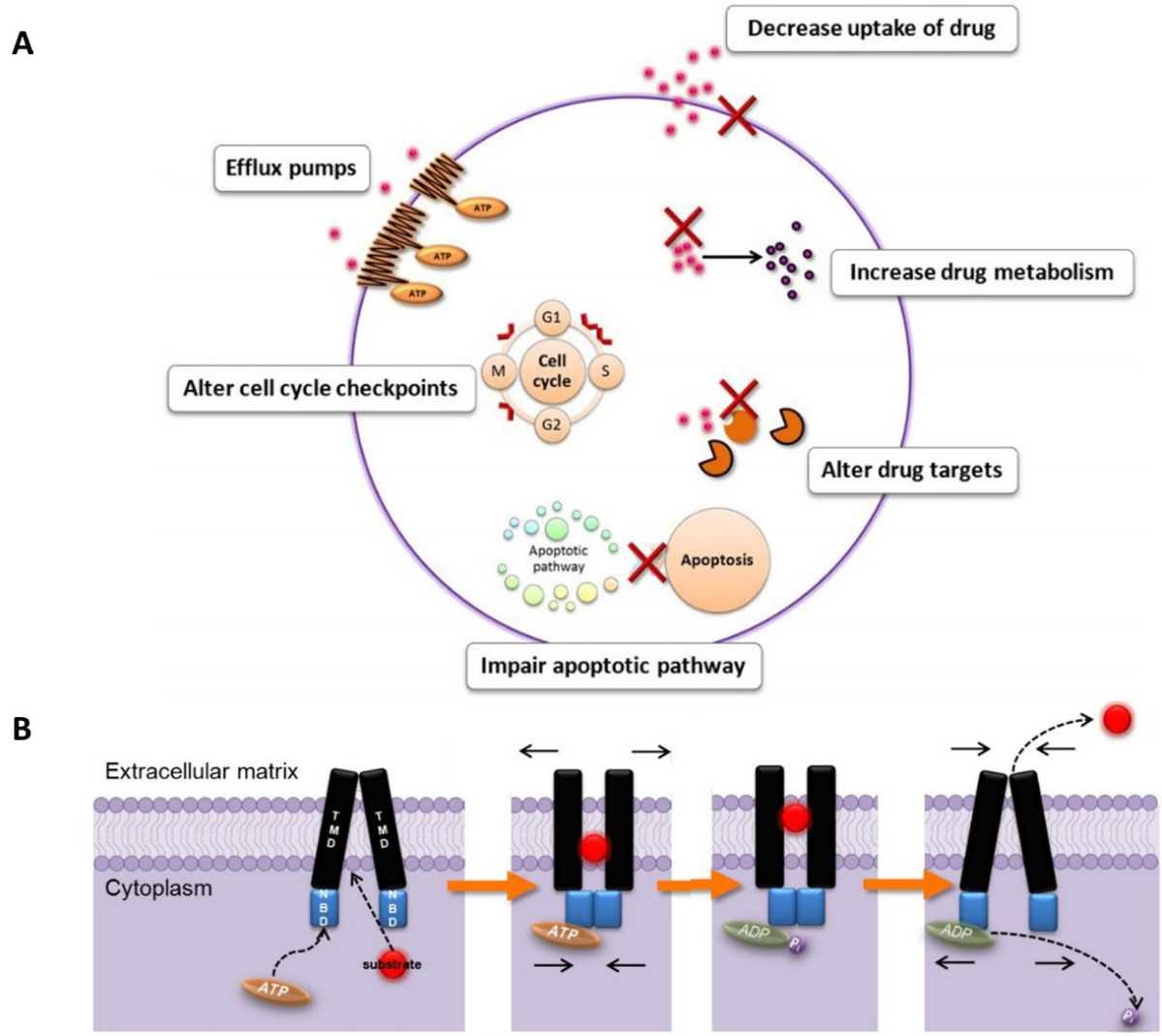


Figure 1-25 (A) Mechanisms of MDR towards cancer chemotherapeutic drugs. B. Proposed drug efflux mechanism for ABC transporters. Substrate and ATP bind to ATP transporters. After ATP hydrolysis, the substrate is effluxed out of the cell. Phosphate group is released and the substrate is then excreted to extracellular matrix. Adapted from S. Chai *et al.*[160], copyright 2010, open access.

1.4.2 Enhancement of intracellular delivery

To solve the challenges cited in 1.4.1 (i.e. limited cellular uptake; lysosome degradation and secretion and multidrug resistance) two major strategies have encountered great success: the use of membrane active compounds and nano-carriers. In order to overcome the degradation of the drug by the lysosome some scientists have investigated the development of carriers that were able to escape the endosomes by interacting with the endosomal membrane relying on the acidification mechanism during the endosomal maturation. Four different interactions have been mainly reported: (i) the pore

formation; (ii) the fusion with the endosomal membrane (e.g. HA-2 subunit); (iii) the photochemical disruption (e.g. dendrimer with phthalocyanine) and (iv) the proton sponge or pH-buffering effect (e.g. tertiary amines compounds) although some endosomal escape agents present mechanisms which are still not elucidated (Figure 1-26).[162]

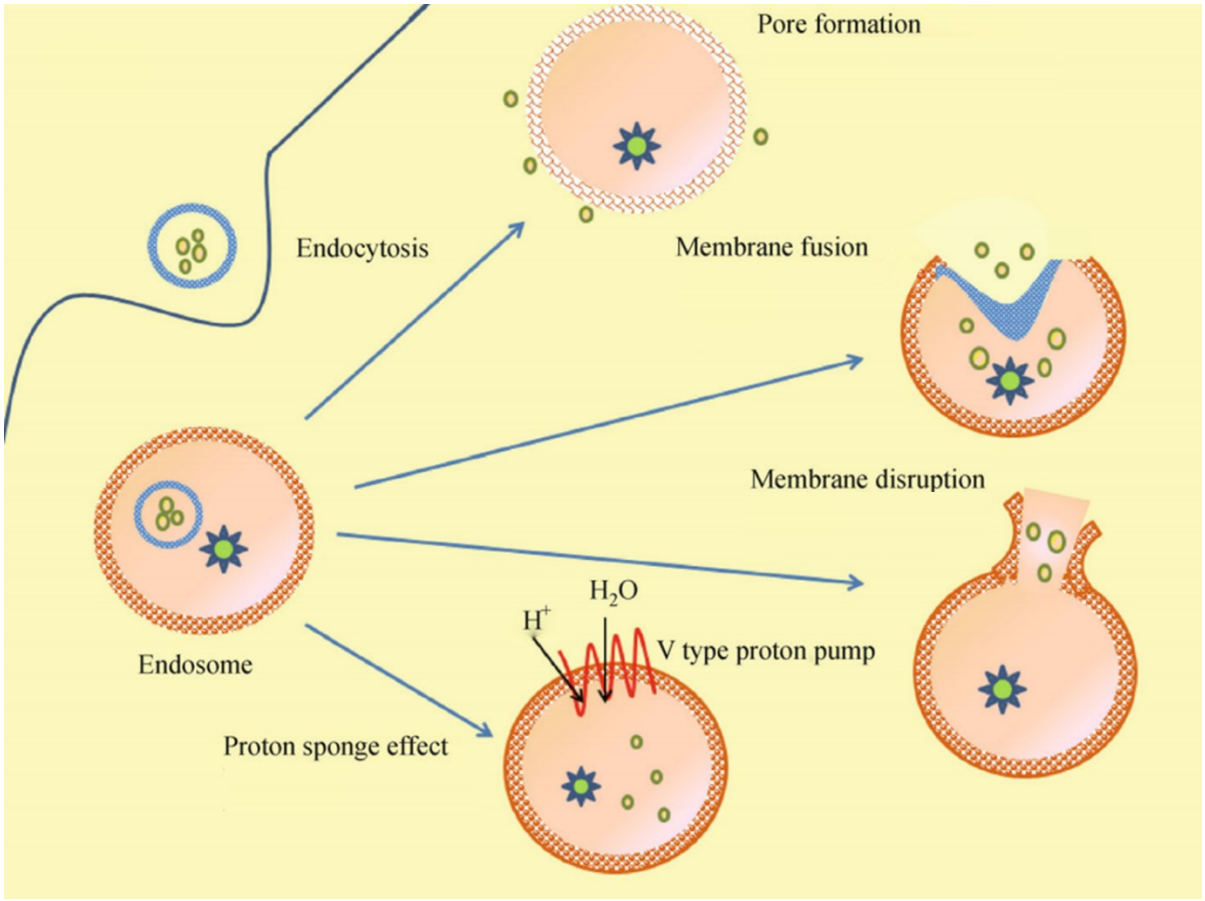


Figure 1-26 Mechanism of endosomal escape of nanocarrier. Uptake of nanocarriers by endocytosis leads to entrapment of drugs and nucleic acid drugs within the endosomes and is not available for pharmacological action. Acidification of endosomes by V type proton pump is utilised as stimuli by nanocarriers and virus for formation of pores across the membrane, for fusion of endosomal membrane and carrier, for disruption of membrane and for osmolysis of endosomes by proton sponge effect. Adapted from Mundra and Mahato[163], copyright 2014, with permission from Higher Education Press and Springer-Verlag Berlin Heidelberg.

Viruses possess a high transfection efficiency. When close to the cellular membrane some viruses can bind to receptors on the cell surface and induce their fusion with the membrane or their direct penetration. The influenza virus enters the cell via receptor-mediated endocytosis. The acidification in the endosome triggers the conformation change of the fusion peptide, hemagglutinin subunit HA-2 located at the N-terminus of

the protein, which is sent around 10 nm away from the viral surface in order to interact with the cell membrane. Following the insertion of the fusion peptide, the cellular membrane is destabilised which enables the payload to be released in the cytosol.[164] Based on this strategy employed by nature, endosomolytic, cell penetrating peptides (CPP) have been designed, biomimicking the endosomal escape mechanism of the viral peptides but with lower toxicity. Differences of pH in the endosomal pathway but also in-between extracellular pHs for healthy and tumour cells, or the so-called Warburg effect,[165] have been seen as a potential tool for intracellular delivery enhancement and pH-sensitive polymers have received much attention. The two main classes of endosomolytic polyelectrolytes are: (i) cationic aminated polymers and (ii) anionic carboxylated polymers (Figure 1-27).

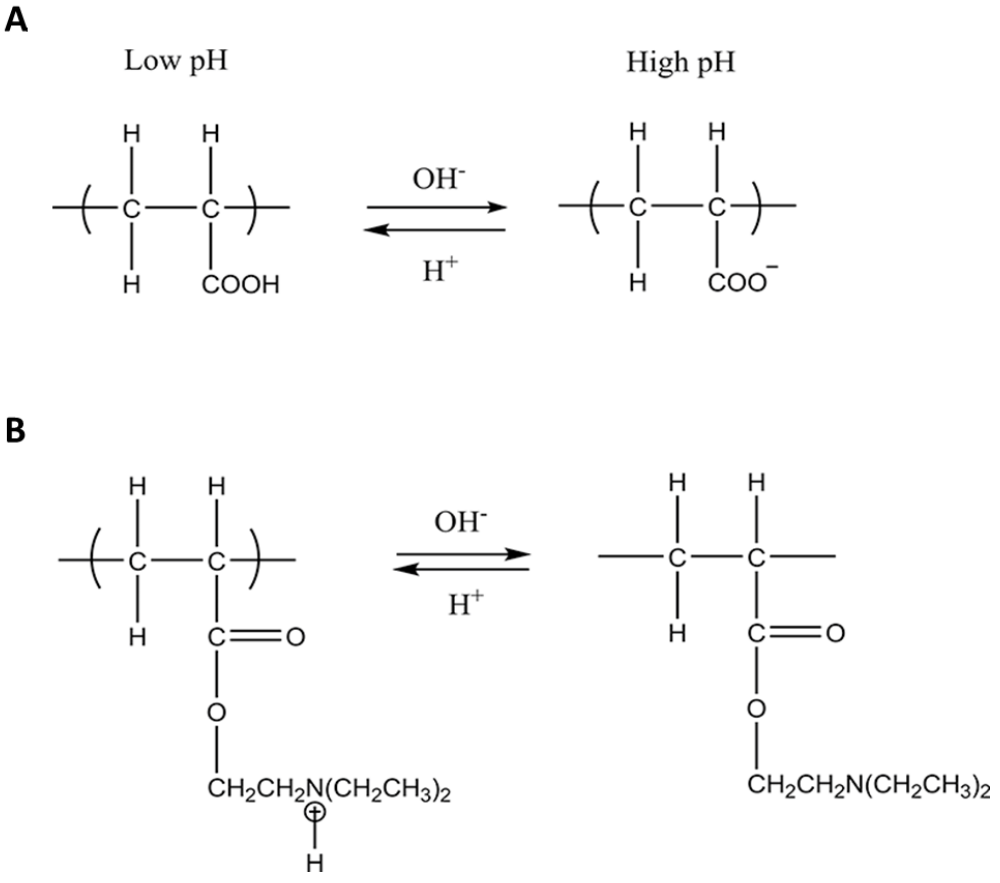


Figure 1-27 pH-dependent ionisation of polyelectrolytes. (a) Poly(acrylic acid) and (b) poly(N,N'-diethylaminoethyl methacrylate). Reproduced from Bahram *et al.*[166] copyright 2016, open access

Poly(L-lysine) (PLL), poly(ethylenimine) (PEI) and poly(amidoamine) (PAA) belong to the first class. Upon acidification, the protonated amines interact via electrostatic interactions with the negatively charged membrane and promote the internalisation. Furthermore, these polymers present a high buffering capacity which neutralises the acidification of the endosome, thus leading to an increased influx of ions and the disruption of the endosomal membrane via "pH-buffering effect" or "proton sponge effect".[167] However, cationic polymers usually suffer from high toxicity[168] and low transfection efficiencies.[169] Furthermore, their positive charges, which enable them to interact with negatively charged membranes have the major drawback to promote the binding with serum proteins and their elimination by the MPS.[102]

The second class involves polymers with pendant carboxylic groups. At neutral pH, they present an overall negative charge which limit the binding with serum proteins. Upon acidification, the protonation of the carboxylic groups triggers a conformational change of the polymer, from an extended chain to a collapsed structure, also called the coil-to-globule transition, due to the formation of hydrophobic domains. Poly(ethylacrylic acid) is the most represented of this category. Several endosomolytic mechanisms (e.g. membrane permeabilisation or membrane solubilisation) can be involved depending on the polymer structure and concentration.[167] Yet, vinyl-based polymers are not ideal for medical applications since they are not biodegradable and the molecular weight is greatly limited to avoid bioaccumulation. Thus, attention for non-cytotoxic and biodegradable pseudo-peptides based on naturally occurring amino acids such as L-lysine have grown.[170]

On the other hand nanoparticles, lipid-based NPs, polymer-drug conjugated and inorganic NPs, have proved to efficiently overcome the P-gp mediated MDR according to several mechanisms in particular via downregulation of the P-gp expression, enhancement of the endocytic uptake and early endosomal escape.[161] Interestingly, it has been reported that gold nanoparticles can help to overcome MDR via the delivery of P-gp inhibitors, cell entry with endocytosis, targeted delivery and PTT.[171]

F. Wang *et al.*[128] demonstrated significant growth inhibition in MDR cells with PEGylated AuNPs@DOX thanks to the combination of high internalisation and pH-triggered drug release at early endosomal pH. The $IC_{50,}$ half maximal inhibitory concentration was fivefold lower for AuNPs@DOX than for free drug after 72h treatment of MDR cells (1.82 ± 1.68 μg mL^{-1} vs. 10.12 ± 1.07 μg mL^{-1}).

In summary, the use of amphiphilic endosomolytic pseudo-peptides seems to be a smart strategy to enhance the cellular uptake and to promote the endosomal escape via active interactions with the membrane, and the use of AuNPs has proven to be efficient to overcome multi-drug resistance. Thus, the aim of the research project presented here is to investigate whether the combination of both strategies is able to substantially increase the intracellular delivery of payloads to cancer cells. Below are described in more details the polymer used in this research project, poly(L-lysine isophthalamide conjugated with L-phenylalanine at 75 mol%, PP75, and few examples from the literature of hybrid AuNPs designed for intracellular delivery via endosomolytic enhancement.

1.4.3 PP75

PP75 is a pseudo-peptide based on L-lysine derived from the poly(L-lysine isophthalamide) (PLP) family. M.E. Eccleston *et al.*[170] have prepared PLP via condensation of the amine groups of L-lysine with isophthaloyl chloride (Figure 1-28). Even though PLP lacks of hydrophobic side chains present in fusogenic peptides, it demonstrated pH responsive conformational change and membrane activity.[170]

However, its membrane activity is relatively weak and starts from pH 4.6 and below corresponding to the pH at which hydrophobic domains are forming, $pH_{h,}$ and can associate with the membrane.[172-174] The permeabilisation mechanism of the polymer is mainly due to the hydrophobic associations overcoming the electrostatic repulsions below pH_h.[170] The pH_h of PLP is below the characteristic pH of lysosome (~ pH 5.5) which greatly limits the application of PLP as endosomolytic agent.

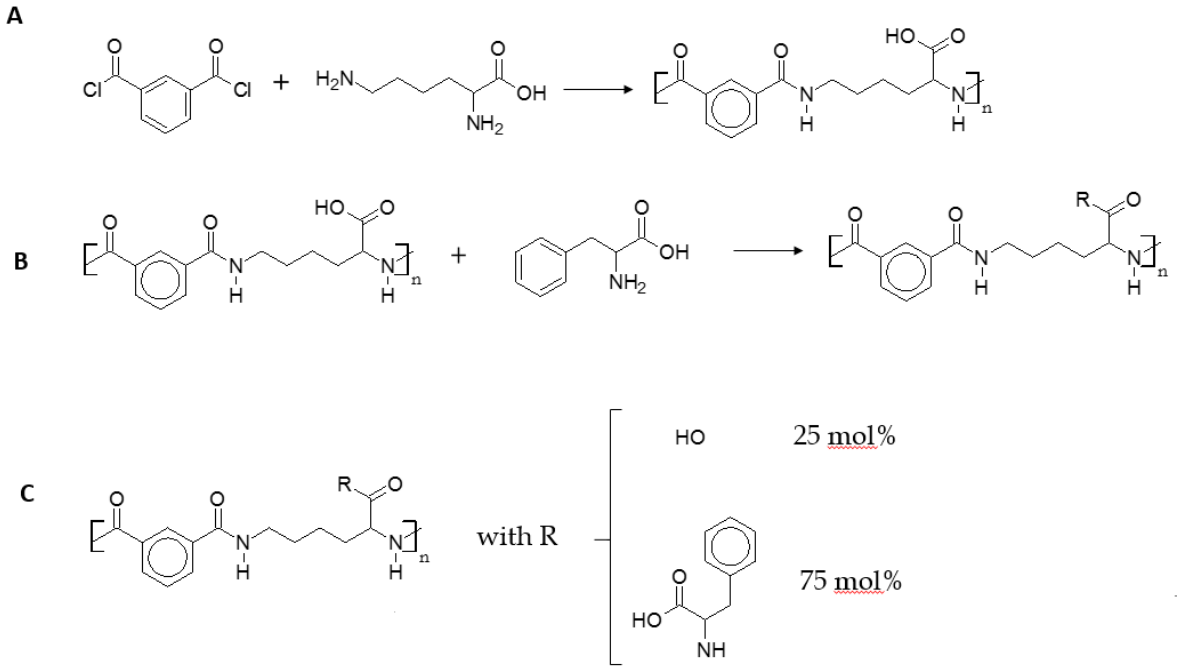


Figure 1-28 (A) Synthesis of PLP. (B) Synthesis of PLP derivatives (PP series). (C) Description of PP75

The conformational change characteristics of PLP mainly depend on the balance between hydrophobicity and hydrophilicity and the degree of ionisation, hence the pH of transition have been successfully increased by decreasing the density of carboxylic acid on the backbone via esterification or by copolymerisation with a hydrophobic polymer. One of the most efficient modification had been presented by [175]. Grafting with L-phenylalanine on the pendant carboxylic acid moiety of PLP at 75 %mol (PP75) rised the pH at the onset of hydrophobic association to 7.2. PP75 exhibited a 90% haemolysis of sheep red blood cells at pH 6.5 after 60 min incubation at 0,025 mg mL^{-1} with low toxicity towards mammalian cells.[176]

Khormaee *et al.*[177] highlighted that the membrane interaction ability of PP75 was not only based on its hydrophobicity but was also due to the presence of aromatic rings. Zhang *et al.*[174] demonstrated a significant interaction of PP75 with the phospholipid monolayer used in a biomembrane model. Furthermore, the interaction was found to be highly pH-dependant and reversible.

The mechanism for endosomal escape is still unclear since different hypotheses have been formulated: membrane disruption[176]; membrane penetration[178] and pore formation.[179] Further studies focused on the ability of PP75 to deliver model drugs[180] and proteins[181] in vitro and in particular in 3D tumour model[180] but also in vivo with the efficient delivery of siRNA.[179]

Overall, the pseudo peptide PP75 can offer many advantages as a drug delivery vector thanks to its properties: negative charge (limits aggregation *in-vivo* usually caused by binding with serum proteins), pH-responsiveness within the pH range typical of endosomes and especially early endosomes, efficient cell membrane destabilisation, transport and effective release of model drugs, biodegradability (made from naturally existing amino acids), biocompatibility (no haemolysis at physiological pH), controllable cell entry pathway and low cytotoxicity.

1.4.4 AuNPs for cytosolic delivery

Numerous research groups have considered the potential advantages of combining AuNPs and agents to promote the delivery to the cytoplasm. The most common approaches involve cationic AuNPs prepared by combination with cationic peptides (e.g. PEI[182,183]), aminoacids (e.g. lysine[184]) or lipids[185]. The polymer chain is either conjugated on the AuNPs surface via thiol chemistry[182,184], or is used as a reducing agent for AuNPs formation[183,186,187]. These platforms were, in particular, investigated for the loading, transport and efficient transfection of plasmid DNA[184,187] or siRNA.[186] Anionic by nature, plasmids can easily bind to the positively-charged cationic nanoparticles (e.g. ammonium groups) via ion-pairing and form stable complexes.

Some promising results show that the nanohybrid is more efficient to transfect cells than the cationic agent alone.[184,187,188] P.S. Ghosh *et al.*[184] reported that AuNPs-lysine DNA complexes were 28 times more efficient for *in vitro* transfection than poly-L-lysine alone. Joydeep *et al.*[187] successfully delivered plasmid DNA to human mesenchymal stem cells, considered one of the most difficult cell lines to transfect, with an improved gene transfection efficiency compared to the commercially available transfection agents lipofectamine 2000 and unmodified PEI (Figure 1-29).

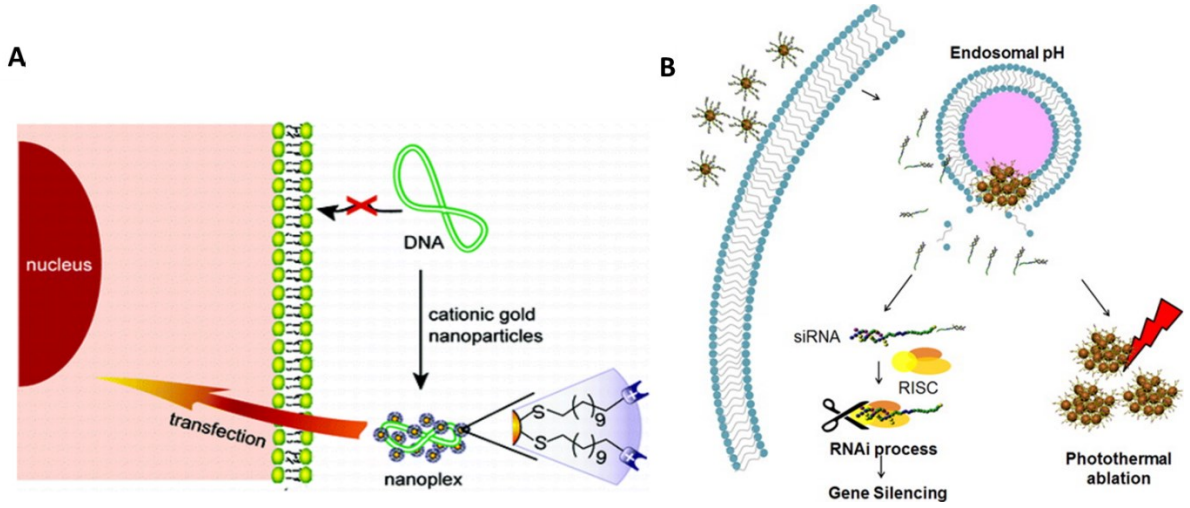


Figure 1-29 (A) Schematic illustration of the monolayer protected AuNPs used as transfection vectors. (B) Schematic description of DNA nanomachine. The i-motif DNA is covalently conjugated to AuNP, and siRNA was linked to AuNP via hybridisation of i-motif DNA with linker DNA. pH-responsive aggregation of siRNA-i-motif-AuNP for endosomal escape, siRNA release, and photothermal ablation. (A) is reproduced from P.S. Ghosh *et al.*[184], copyright 2008, with permission from the American Chemical Society. (B) is reproduced from S. Son *et al.*[189], copyright 2014, with permission from the American Chemical Society.

As already mentioned cationic polymers present several drawbacks and lately some research groups have developed alternative strategies to overcome the lysosome degradation. One of the most drastic radical solutions has been suggested by Rotello and co-workers.[190] They developed nanoparticles stabilised nanocapsules with an oil core that can circumvent the endocytosis pathway and enter via membrane fusion between the oil core and the cell membrane leading to the direct entry in the cytoplasm.

Another strategy for endosomal escape without cationic compounds has been developed by S. Son *et al.*[189]. si-RNA was loaded onto AuNPs via hybridisation with an i-motif and a linker. The i-motif shows a pH responsive conformational change at endosomal pH for simultaneous payload release and AuNPs aggregation. They observed the successful endosomal escape of the "DNA nanomachine" and attributed it to the pH responsive cluster formation. Furthermore, they use the aggregation of the nanohybrids to elicit photothermal ablation for synergistic gene and PTT.

1.5 Aims of the investigation

The present project aims at designing AuNPs able to transport, protect and deliver drugs to the cytoplasm of tumorous cells.

AuNPs appear to be as one of the most promising nanocarrier in cancer therapy thanks to their ease of synthesis, tunability, biocompatibility, interesting cellular imaging modalities and photothermal properties. They are able to overcome most of the extracellular barriers thanks to their low size and added properties adduced by further modification with stabilising ligands. However, their transfection efficiency depends on a high number of inter-dependent parameters (e.g. size, charge, shape, surface ligands) that have a dramatic influence on the internalisation and intracellular fate.

In the last decades, vectors have been developed as transfection agents and endosomal escape promoter via pore formation, proton-sponge effect, fusion or photochemical disruption using virus-derived or synthetic peptides. The two main classes of endosomolytic agents are cationic and anionic chains. Cationic chains have the ability to load negatively charged payloads and to interact actively with cells membrane via electrostatic interactions. However, they present severe drawbacks such as non-specific binging with serum proteins and degrees of toxicity. In order to avoid the use of cationic compounds, anionic cell penetrating peptides have been considered. Amphiphilic polymers bearing pendant carboxylic groups have been designed to mimic the viral transfection via pH-responsive conformational change. In particular, PP75 have proved to efficiently cross the cellular membrane of different cells lines, including *in-vitro* tumour models, and to deliver payloads such as apoptin and siRNA to the cytoplasm via endosomal escape.

Although numerous research groups have exploited the combination of cationic ligands and AuNPs for enhanced transfection and plasmid delivery via ion pairing and showed higher transfection efficiency than for the vectors alone, to my knowledge, no anionic pH-responsive nanohybrid has been reported with AuNPs for enhanced endosomal escape. The aims and novelty of this research project lies in the design and characterisation of a

novel hybrid system based on AuNPs and PP75 polymer and the following key objectives has been investigated accordingly.

1. Synthesis of the nanohybrids
    a. Synthesis and characterisation of citrate-coated AuNPs
    b. Synthesis and characterisation of PP75 polymers
    c. Synthesis of polymer-functionalised AuNPs using SH-PEG as a model
    d. Synthesis of thiolated PP75 using cysteine and covalent grafting with cysteamine for the preparation of PP75 hybrid AuNPs
    e. Preparation of payload loaded AuNPs for delivery
    f. Preparation of AuNPs loaded hydrogels

2. Physico-chemical characterisation of the nanohybrids
    a. Evaluation of the successful functionalisation of PEG, PP75 and derived polymers to the AuNPs surface
    b. Evaluation and comparison of the physico-chemical properties (size, concentration, zeta potential) of the nanohybrids
    c. Investigation and optimisation of the colloidal stability of the nanohybrids in biological buffers
    d. Investigation and optimisation of the pH-responsive properties of the nanohybrids in particular the pH-responsive agglomeration state and reversibility
    e. Quantification and optimisation of the loading efficiency of payloads
    f. Optimisation of the laser settings for efficient photothermal therapy
    g. Optimisation, evaluation of the pH-responsive and mechanical properties

3. Biological evaluation of the nanohybrids
    a. Quantification of the cellular uptake as a function of the surface ligands type, concentration and treatment time
    b. Investigation of the endosomal escape efficiency as a function of the nanohybrids concentration and treatment time

c. Visualisation of the intracellular AuNPs localisation as a function of surface ligand type and treatment time
d. Investigation of the intracellular delivery of free and loaded payloads
e. Evaluation of the cytotoxicity as a function of concentration and time
f. Quantitative *in-vitro* assessment of the phototherapeutic action

1.6 Research gaps, novelties and impacts of the investigation

The research gaps, novelties and impacts of the investigation of the present thesis are summarised below (Table 1-2):

- AuNPs colloidal stability is extremely sensitive to changes of the environment (e.g. pH, ionic strength). The most common approach to provide stabilisation to the AuNPs is via the grafting of hydrophilic agents. However, in addition to the stabilisation, the grafting is responsible for dramatic changes in the AuNPs properties. Many articles have been published reporting several aspects of the physico-chemical properties (e.g. grafting density; hydrodynamic size; stability in buffer). In the present research, the main objective was to achieve a full characterisation of the influence of the grafting, and in particular the ligand chain length, on the physico-chemical properties of the AuNPs. Polyethylene glycol has been used as a model since it is still the most popular stabilising agents amongst FDA approved polymers. This investigation can bring valuable information for the optimisation of the design of polymer-grafted AuNPs.

- Nanocrystal superlattices have attracted a growing interest in the last decades for their exceptional properties derived from their nanostructure. AuNPs based assemblies have also been widely prepared for application in catalysis, photovoltaics and sensing, however current preparation methods are either complex or costly and the mechanism of assembly is unknown or not properly defined. In this thesis is reported a simple preparation method based on the evaporation of the colloidal solution of PEGylated AuNPs on a flat substrate. The

mechanism of assembly has been investigated and, for the time according to my knowledge, the influence of the polymer corona has been discussed in detail.

- Multi responsive platforms have recently become popular to enable a targeted and controlled drug delivery. However, many responsive systems rely on external stimuli, such as temperature, which cannot prevent the unfortunate systemic release of the drug and the subsequent side effects. Intracellular stimuli, such as the pH enable safer intracellular drug delivery. Membrane-active pH-responsive pseudo-peptides have emerged as efficient agents for the enhancement of the endosomal escape which most nanoparticulate systems lack of. Current endosomolytic agents present toxicity concerns and anionic amphiphilic pseudo-peptides have been designed as a safer alternative. The present work reports the successful preparation and characterisation of the properties of the pH-responsive nanohybrids designed for enhancement of the intracellular delivery. To my knowledge, no analogous study with AuNPs and anionic amphiphilic pseudo-peptides for intracellular delivery have been reported yet.

- Doxorubicin is one of the most used chemotherapeutic drug however it suffers, as his chemotherapeutic drugs counterparts, from low biodistribution and high systemic toxicity, furthermore cells have developed MDR mechanisms which dramatically decreased its efficiency. AuNPs have proven to improve the therapeutic index thanks to long term stability in the circulation and targeting ability. Additionally, they have demonstrated to counteract the MDR mechanism. This thesis reports the preparation of an effective intracellular drug delivery carrier based on AuNPs using DOX as a model drug and anionic amphiphilic pseudo-peptides. The successful *in-vitro* delivery paves the way for a safer alternative to cationic and viral endosomolytic agents.

- AuNPs-based photothermal therapy has attracted a growing interest for its pinpointed action. Nevertheless, photothermal therapy used alone cannot eradicate the tumour. The present work investigates the synergistic action of the

laser therapy combined with the chemotherapy from the DOX nanocarrier. The efficiency of the synergistic therapy provides further evidence to the important potential of the developed nanohybrids.

- Both AuNPs and hydrogels have a long track record of applications in therapy for their respective advantages. Recently, attention has risen for the development of AuNPs hybrids hydrogels for catalysis applications mainly. In medicine, the incorporation of AuNPs into temperature-responsive hydrogels is leading to the development of hydrogels for chemo-photothermal cancer therapy. Few pH-responsive hybrids hydrogels have been reported and they usually concern micro- or nanogels designed for intracellular delivery. To my knowledge the work presented in this thesis is the first one on the preparation of hybrid pH-responsive hydrogels for oral delivery. These hydrogels exhibit an exciting potential for the combination of oral and intracellular delivery.

Table 1-2 Summary of the thesis' research gaps, aims and novelties

	Research gaps	Aims	Novelties and impacts
Chapter 3 PEGylation: stability and assembly	▪ No complete study on the impact of the chain length on the physico-chemical properties of AuNPs ▪ Current methods for the preparation of AuNPs based superlattices are complex/costly and/or the mechanism is not well understood/defined	▪ To rigorously investigate the influence of the chain length on the physico-chemical properties ▪ To characterise the assemblies formed and investigate the mechanism	▪ Systematic study on the influence of the polymer corona on the AuNPs properties ▪ Simple preparation of self-assemblies of PEGylated AuNPs
Chapter 4 pH-responsive nanohybrids	▪ Few triggered intracellularly responsive systems ▪ Low cytoplasmic delivery for NPs based therapy ▪ Toxicity of the current endosomolytic agents	▪ To characterise the physico-chemical and biological properties of AuNPs@PP75 ▪ To assess the intracellular delivery potential	▪ First report on the characterisation and *in-vitro* application of anionic AuNPs for cytoplasmic delivery ▪ Safer alternative than cationic polymers and viral vectors
Chapter 5 Chemo- and phototherapy	▪ DOX causes serious side effects as a free drug and many cells have developed MDR ▪ Phototherapy used alone is not efficient to destroy completely the tumour	▪ To prepare stable and efficient intracellular carrier for drug delivery ▪ To investigate the efficiency of AuNPs to counter MDR to DOX ▪ To test the synergistic effect of the dual therapy	▪ First combination of anionic amphiphilic pseudo-peptides, AuNPs, drug and laser therapy for enhanced cytoplasmic delivery ▪ Further evidence to the potential of AuNPs@PP75
Chapter 6 AuNPs loaded hydrogels	▪ Few reports on the incorporation of AuNPs into pH-responsive hydrogels for therapy ▪ Limited knowledge on the influence of the AuNPs loading on the hydrogel properties	▪ To investigate the impact of the incorporation of AuNPs ▪ To evaluate the potential therapeutic application	▪ First report on pH responsive AuNPs-loaded hydrogels for oral drug delivery ▪ Future potential use as oral-intracellular therapy

1.7 Thesis outline

The thesis comprises seven chapters outlined as follows.

Chapter 1 introduces the main challenges in the field of cancer therapy with special attention given to intracellular delivery and describes the properties, history, current investigations and applications of AuNPs as therapeutics. This first chapter provides some element of design for the successful application of AuNPs as a therapeutic carrier. It also emphasises the advantages of using amphiphilic anionic polymers as carrier vectors for cytoplasmic delivery and highlights the potential interests of the polymeric AuNPs nanohybrids presented in this research work with regards to the alternative solutions that has been reported in the literature.

Chapter 2 details the materials and the methodologies used in the present research work to obtain the results presented in the following chapters.

Chapter 3 provides a summary of the results obtained for the synthesis and physico-chemical characterisation of AuNPs functionalised with PEGs of three different chain lengths. It covers in particular the optimisation and quantification of the surface coverage for enhanced colloidal stability. The last section concerns the investigation of the mechanism involved in the self-assembly of the hybrids under evaporation.

Chapter 4 describes the synthesis, physico-chemical characterisation and biological evaluation of the AuNPs-PP75 conjugates (AuNPs@PP75). The optimisation of the surface coverage for colloidal stability and pH responsiveness, the pH-reversibility, the mechanism involved in the pH-responsive conformational change, and the *in-vitro* evaluation of the internalisation, endosomal escape and cytotoxicity in human cervical cancer cells, HeLa cells, have been investigated.

Chapter 5 describes the synthesis of doxorubicin (DOX) loaded AuNPs for chemo-photothermal therapy, in particular the optimisation and characterisation of the synthesis, the quantification of the loading efficiency, the optimisation of the laser

settings and the *in-vitro* biological evaluation of the intracellular delivery and cytotoxicity in human uterine sarcoma cells, MES-SA and their DOX resistant analogue MESSA-Dx5.

Chapter 6 describes the preparation, optimisation and investigation of the physico-chemical and mechanical properties of the pH-responsive hydrogels loaded with different hybrid nanosystems in particular the changes in swelling, rheology, appearance with pH, the drug loading and release properties and the *in-vitro* toxicity evaluation.

Chapter 7 highlights the key points of the research work presented in Chapters 3 to 6 and outlines the implications of the findings in the context of the state-of-the-art in the field of nanomaterials for drug delivery. The second part of the chapter introduces recommendations for future work on the basis of the achieved results but also additional investigations carried out within the PhD project but not reported in the thesis.

Chapter 2 Materials and Methods

This chapter details the materials and the methodologies used in the present research work to obtain the results presented in the following chapters.

2.1 Materials

Trisodium citrate dihydrate, paraffin oil, potassium chloride (KCl), D-glucose anyhrous, dimethylsulfoxide (DMSO), dimethylformamide (DMF), 4-and dimethylaminopyridine (DMAP), nitric acid (HNO_3), sodium chloride (NaCl), sodium phosphate dibasic ($Na_2HPO_4 \bullet 7H_2O$) and monobasic (NaH_2PO_4), potassium dihydrogen orthophosphate (KH_2PO_4), triethylamine, LysoTracker Green DND26, LysoTracker Red DND-99, Hoechst 33342, were obtained from Fisher Scientific (Loughborough, UK).

Ethylenediaminetetraacetic acid (EDTA), anhydrous ethanol, acetone, potassium carbonate (K_2CO_3), hydrochloric acid (HCl) 37% and sodium hydroxide (NaOH) were acquired from VWR (Lutterworth, UK).

alamarBlue reagent was purchased from Bio-Rad Laboratories (Hemel Hempstead, UK).

Hydrogen tetrachloroaurate (III) hydrate ($HAuCl_4$), cysteamine, poly(ethylene glycol) methyl ether thiol M_n 800 g mol^{-1} (PEG0.8k), M_n 2000 g mol^{-1} (PEG2k) and M_n 6000 g mol^{-1} (PEG6k), 2-(N-morpholino), ethanesulfonic acid (MES) monohydrate and 5,5'-dithiobis-(2-nitrobenzoic acid) (DTNB), calcein, penicillin, doxorubicin (DOX), anhydrous iso-phthaloyl chloride, L-cystine dimethyl ester dihydrochloride (CDE), *N*-hydroxysuccinimide (NHS), *N*-(3-dimethylaminopropyl)-*N'*-ethyl carbodiimide hydrochloride (EDC), 1,4-dithiothreitol (DTT), bovine serum albumin (BSA); sodium fluorescein, Dulbecco's modified eagle medium (DMEM), McCoy's 5A modified medium, fetal bovine serum (FBS), trypsin-EDTA, Dulbecco's phosphate buffer saline (D-PBS) were obtained from Sigma-Aldrich (Dorset, UK).

Triton® X-100, L-lysine methyl ester dihydrochloride, L-phenylalanine methyl ester hydrochloride were purchased from Alfa Aesar (Heysham, UK).

Guava ViaCount Reagent was purchased from Merck Millipore (Nottingham, UK).

Glycerol Based Antifade Reagents with PBS was purchased from Citifluor (London, UK).

Defibrinated sheep red blood cells (RBCs) were obtained from TCS Biosciences Ltd (Buckingham, UK).

Glutaraldehyde, piperazine-N,N′-bis (PIPES), osmium tetroxide, acetonitrile were purchased from Sigma-Aldrich (Dorset, UK). Quetol, nonenyl succinic anhydride (NSA), methyl nadic anhydride (MNA), benzyl dimethylamine (BDMA) obtained from Agar scientific (Stansted, UK).

2.2 Synthesis

2.2.1 Synthesis of AuNPs

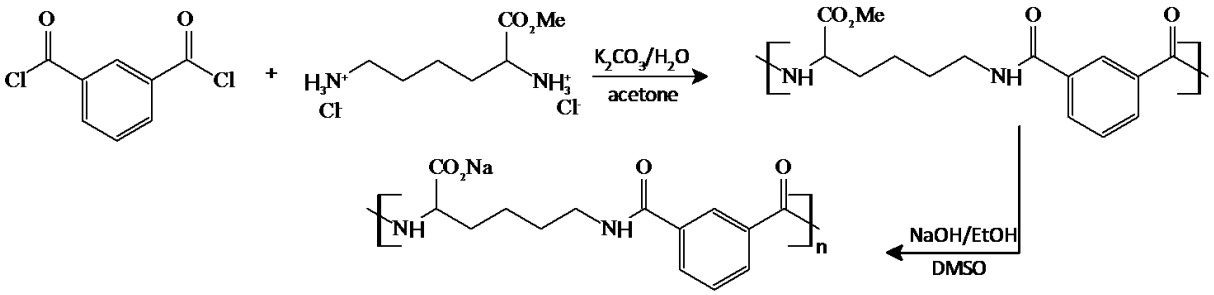
Prior to the synthesis, the glassware and the utensils were soaked in aqua regia and rinsed with MilliQ water. $HAuCl_4$ (200 mL, 1 mM) was heated under reflux while stirring, followed by addition of trisodium citrate (20 mL, 39 mM). After 15 s the colour of the solution changed from yellow to deep red and the solution was stirred for a further 50 min. The solution was then allowed to cool under stirring and the final AuNPs were stored at 4˚C until further use. The particle size and concentration, 14.1 nm and 10.0 nM respectively, were calculated via UV-vis spectroscopy using the Haiss method. In order to obtain larger size AuNPs the concentration of the citrate solution was decreased.

2.2.2 Synthesis of AuNPs@PEG

Aqueous PEG-SH solution (60 μL) at various concentrations was added to the as-synthesised AuNPs (1.2 mL) and stirred for 2 h. The final mixture was then centrifuged at 15,000 g or 10,000g or 30 to 60 min depending on the volume of the solution, and after removal of the supernatant and 5 min sonication, the particles were redispersed in the required media (H_2O or buffers) and sonicated for a further 15 min. A second washing step via centrifugation was usually performed for redispersion in biological media for which the purity of the colloidal solution was the most critical.

2.2.3 Synthesis of PLP

PLP (M_n = 17.9 kDa, polydispersity = 1.99) was synthesised as previously reported by M.E. Eccleston *et al.*[170] (Scheme 2-1).



Scheme 2-1 PLP synthesis.

2.2.3.1 Polycondensation

Within an ice bath L-lysine methyl ester dihydrochloride (0.15 mol, 35 g) and potassium carbonate (0.6 mol, 83 g), were dissolved in 750 ml H2O and constantly stirred. 750 ml pre-cooled anhydrous isophthaloyl chloride in dried acetone (0.2 M, 30.5g) were rapidly poured. The reaction was left to proceed for 30 min stirring at full speed, allowing precipitation of poly(L-lysine methyl ester *iso*-phthalamide). The polymer was then removed and washed with H_2O to remove excess solvent, and left to oven-dry at 55˚C for two days. The stiff polymer was then blended.

2.2.3.2 Ester hydrolysis

Sodium hydroxide (1.25 M) solution in anhydrous ethanol (2.5 molar equivalents to poly (PLP) was added in several portions to the PLP dissolved in dry DMSO at the same volume (0.5 M). Hydrolysed products precipitated in 2-3 min and were collected by vacuum filtration. Dry poly(L-lysine *iso*-phthalamide) (PLP) was the re-dissolved in H_2O using droplets addition of 0.1M NaOH. Once the PLP was completely dissolved, droplets of 0.1M HCl were added until complete precipitation of the PLP (around pH 3). PLP was then collected by vacuum filtration and redissolved in H_2O. Three acidification/neutralisation cycles were carried out.

2.2.3.3 Purification

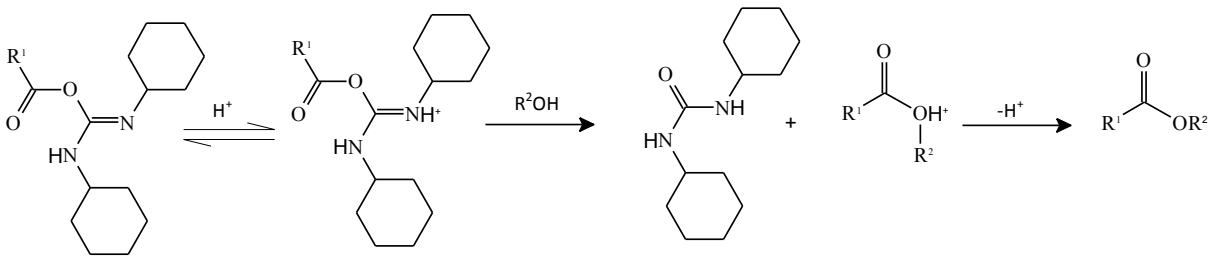
1 week Dialysis of the PLP solution against H_2O was carried out in Visking membrane tubing (Medicell, molecular weight cut-off 12-14 kDa) to remove any inorganic salts, residual solvent and low molecular weight oligomers. The salt form was obtained after the dialysis solution pH was adjusted to pH 7.4 and lyophilised. The acidic form was obtained after precipitation at pH 3.0, collection and lyophilisation.

2.2.4 Synthesis of PP75

PP75 was synthesised as previously reported (M_n = 24.9 kDa, polydispersity = 1.99)[175].

2.2.4.1 DCC mediated coupling with phenylalanine

At room temperature 3 g PLP of acidic form (10.87 mmol [COOH][191]) was dissolved in 60 ml (1:3 v/v) anhydrous DMSO: DMF. To this was added 0.6 g DMAP (20 wt% of PLP), 1.76 g (8.15 mmol [NH_2]) L-phenylalanine methyl ester hydrochloride and triethylamine (2.4 molar equivalents of L-phenylalanine methyl ester hydrochloride. 5.05 g DCC (3 molar equivalents to L-phenylalanine methyl ester hydrochloride) in 20 ml anhydrous DMF were added dropwise. The reaction was allowed to proceed for 60 h at room temperature (Scheme 2-2 and Scheme 2-3).

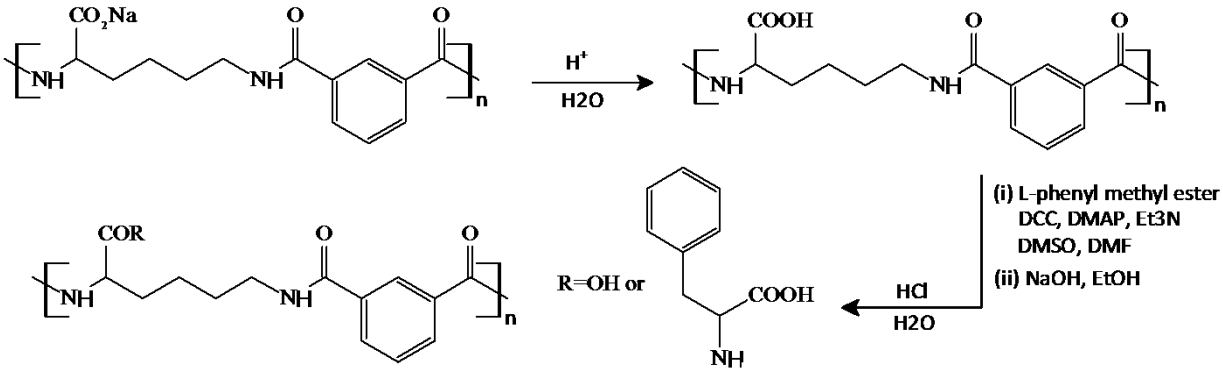


Scheme 2-2 DCC/DMAP coupling.

2.2.4.2 Ester hydrolysis and purification

Solid impurities and the dicyclohexylurea side product were removed by vacuum filtration. NaOH (5 wt%) in anhydrous EtOH (2.5 molar equivalents to PLP) was added to the polymer for ester hydrolysis (about 1.1 g NaOH/28mL Et OH). After 3 h the solution was rapidly poured into five volumes of diethyl ether to precipitate the PP75.

Precipitates were collected and re-dissolved in H_2O. Three acidification/neutralisation cycles and 1-week Dialysis of the PP75 solution against H_2O were carried out in Visking membrane tubing (Medicell, molecular weight cut-off 12-14 kDa) to remove any inorganic salts, residual solvent and low molecular weight oligomers. The salt form was obtained after the dialysis solution pH was adjusted to pH 7.4 and lyophilised. The acidic form was obtained after precipitation at pH3.0, collection and lyophilisation.



Scheme 2-3 PP75 synthesis.

2.2.5 Functionalisation of PP75 with cysteamine

PP75 was further conjugated with 5 mol% cysteamine via a standard DCC/DMAP coupling in a binary solvent mixture of DMSO and DMF at room temperature. Typically, 4.07 mmol PP75 was dissolved in 30 mL of DMSO:DMF (1:3 v/v). To this was added DMAP (20 wt%) and 0.20 mmol cysteamine. 0.82 mmol DCC was dissolved in 10 mL of anhydrous DMF and then added dropwise to the previous mixture over 30 min under magnetic stirring. The reaction was allowed to proceed for 60 h. The impurities were removed via filtration and the product was purified via three acidification/neutralisation cycles and dialysis against deionised water in a Visking tubing membrane (Medicell, molecular weight cut-off 12-14 kDa) to remove any inorganic salts, residual solvents and low molecular weight oligomers. The pH was adjusted to 7.4 and the SH-PP75 obtained was lyophilised and stored for further use.

2.2.6 Synthesis of AuNPs@PP75

To prepare the PP75-functionalised AuNPs, 50 µL of SH-PP75 solution at the desired concentration was added to 1 mL of the as-synthesised, citrate-stabilised AuNPs solution. The mixture was left under stirring at room temperature for 48 h. The resultant functionalised AuNPs were separated by centrifugation at 10,000 rpm for 40 min, sonicated for 5 min, re-dispersed in deionised water or buffer, and then further sonicated for 15 min. This procedure was repeated twice to remove any unbound polymers.

2.2.7 Synthesis of AuNPs@DOX@PP75

150 µL of DOX solution at the desired concentration was added to 1 mL of the as-synthesised, citrate-stabilised AuNPs solution. The mixture was left under stirring at room temperature for 2 h. Then 50 µL of SH-PP75 solution at the desired concentration was added. The resultant functionalised AuNPs were separated by centrifugation at 10,000 rpm for 40 min, sonicated for 5 min, re-dispersed in deionised water or buffer, and then further sonicated for 15 min.

2.2.8 Synthesis of PLP hydrogel and AuNPs@PP75/PLP hydrogel

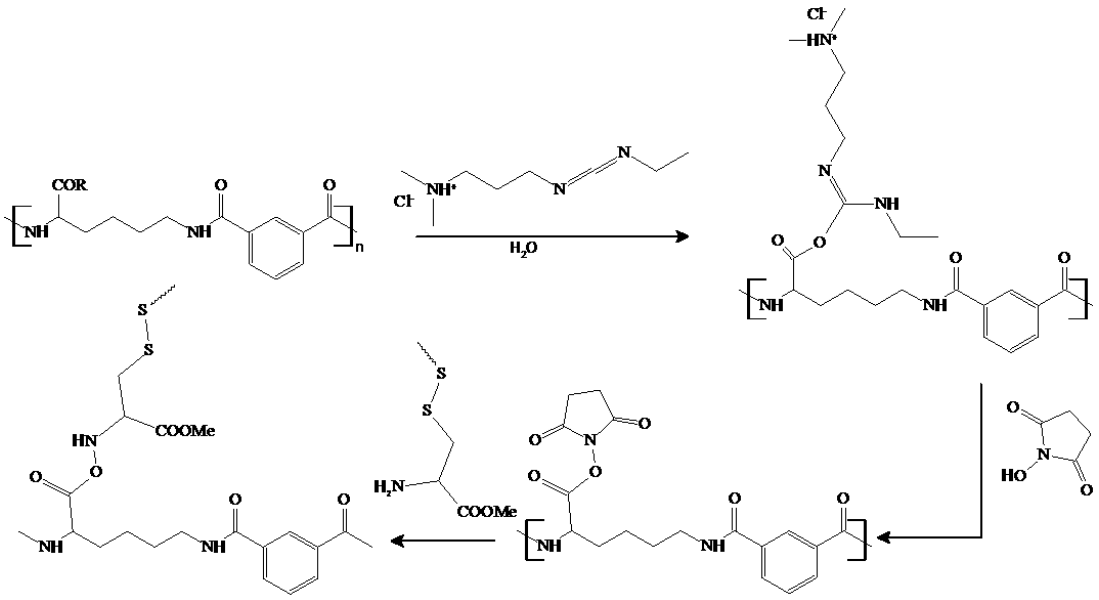
75 mg of PLP was dissolved with 600 µL of AuNPs@PP75 at 10 nM. CDE (0.2 molar equivalents of PLP residual) was dissolved in 200 µL H_2O and added to the mixture. EDC (2 molar equivalents of PLP residual) and NHS (0.5 molar equivalents of PLP residual) were dissolved in 400 µL and added to the PLP-AuNPs mixture under stirring at 200rpm. After 15 min, when the solution became foggy, the stirrer was removed and the mixture was left at room temperature overnight to form hydrogels. The hydrogels were then transferred to a tube with deionised water for a week and the water was changed once per day to remove impurities. Prepared hydrogels were stored in deionised water before use or were frozen and lyophilised if necessary (Scheme 2-4).

The initial AuNPs/PLP loading ratio and the solid content were defined as:

$$AuNPs/PLP\ loading\ ratio\ (wt\%) = \frac{m_{AuNPs}}{m_{PLP}}.100 \qquad (2\text{-}1)$$

$$Solid\ content\ (wt\%) = \frac{m_{solid}}{m_{tot}} \cong \frac{m_{PLP+CDE}}{m_{PLP+CDE}+m_{H_2O}} . 100 \qquad (2\text{-}2)$$

Where m_{AuNPs} is the mass of AuNPs considering a concentration of 0.2 g L^{-1}; m_{PLP} is the initial mass of PLP. m_{solid} is the initial mass of solid materials (PLP, CDE and AuNPs) which is approximately equal to the mass of PLP and CDE only since the mass of AuNPs is relatively low; m_{tot} is the total initial mass including the mass of solid materials and the weight of H_2O (m_{H2O}).



Scheme 2-4 PLP hydrogel synthesis via EDC/NHS coupling.

2.3 Methods for the physico-chemical characterisation

2.3.1 UV-vis spectrophotometric measurement

2.3.1.1 Spectrophotometry

In spectrophotometric measurements, a light beam is sent through a sample and the intensity of the light (number of photons) absorbed or transmitted is recorded. The absorbance of a sample is dependent of its constituent and more particularly on the interaction of the photons with the electrons of the material. Each material will then exhibit specific absorbance characteristics. Furthermore, the intensity of the transmitted

or absorbed light is relative to the concentration of the material and this technique is widely employed for quantitative analysis using the Beer-Lambert law:

$$A = \varepsilon . l . c \tag{2-3}$$

Where A is the absorbance of the sample; ε the molar extinction coefficient; l the path length; and c the concentration of the absorbing specie.

The equipment consists of a light source, a monochromator (prism), a wavelength selector (slit) and a detector (photometer). UV-visible spectrophotometer usually uses light from 200 to 800 nm.

2.3.1.2 Method

UV-vis spectrophotometry spectra were recorded on a Genesys 10S UV-Vis spectrophotometer (Thermo Scientific, UK) between 400 and 800 nm with 0.5 nm increments.

2.3.1.3 Determination of the size and concentration of AuNPs via the Haiss method

The diameter d, and concentration c, of the AuNPs in solution have been calculated based on the absorbance spectra by the Haiss method as follows: [42]

$$d\ (nm) = \exp\left(B_1 \frac{A_{SPR}}{A_{450}} - B_2\right) \tag{2-4}$$

Where A_{SPR} is the absorbance of the surface plasma resonance peak; A_{450} is the absorbance at 450 nm (450 nm is the default reference value which gave the best correlation between A/A_{ref} and d according to Haiss); B_1 and B_2 are obtained from the linear experimental fit of A_{SPR}/A_{450} vs. ln (d) for d ranging from 3 to 75 nm: B_1 is the inverse of the slope m (B1=1/m), $B_2=B_0/m$ with B_0 the intercept where m=0.33, B_0=0.73, B_1=3.03 and B_2=2.21 (Appendix A Figure A-1).

$$\text{c (M)} = \frac{A_{450}}{\varepsilon_{450}} \tag{2-5}$$

Where ε_{450} is the extinction coefficient at λ=450 nm derived from the linear fit of $\ln(\varepsilon_{450})$ vs. ln(d) using theoretical extinction efficiencies for AuNPs in water with diameter d ranging from 2 to 100 nm for a path length of 1 cm assuming absorption is the only interaction between the light and the sample (no reflection, scattering nor fluorescence phenomena) and a monochromatic radiation.

The above method can be applied for the calculation of sizes and concentrations of gold colloids assuming monodisperse, perfectly spherical, uncoated AuNPs in the size range 10-35 nm redispersed in water.

2.3.1.4 Study of the colloidal stability

In order to study the colloidal stability of the AuNPs solutions at different pHs and ionic strengths, the concentrated solutions obtained after centrifugation at 10,000 g or 15,000 g for 30-60 min and removal of the supernatant were sonicated for 5 min, then redispersed in various media, *e.g.* deionised water (H_2O, pH∼6), PBS buffer (50 mM, 0.15 M NaCl, pH 7.4) and MES buffer (50 mM, 0.15 M NaCl, pH 5.5), and sonicated for 15 min before being left under stirring at room temperature for several hours or overnight. The absorbance was recorded over time. Each sample was prepared in triplicate.

2.3.1.5 Determination of the minimum amount for colloidal stability

AuNPs@PEG and AuNPs@PP75 were prepared with 50 µL at different concentrations of polymer solution added to 1 mL AuNPs solution. At the end of the functionalisation the solutions were centrifuged and redispersed in H_2O or buffer and the absorbance was recorded after at least 4 h stabilisation.

2.3.1.6 Determination of the PEG grafting density via the Ellman's assay

A calibration curve was prepared with PEG-SH solutions at different concentrations (500 µL) mixed with PB buffer (190 µL of 0.1 M PB buffer at pH 8.0 with 1 M EDTA) and DTNB (Ellman's reagent, 10 µL, 3 mM). In presence of a thiol group the DTNB reagent reacts and forms TNB^{2-} which can be further quantified via absorbance. The solutions were mixed and incubated for 15 min and the absorbance was then read at 412 nm. The same

procedure was applied to the supernatants of the PEGylated AuNPs after being centrifuged at 15,000g or 1 h to separate residual AuNPs. Each sample was prepared in triplicate.

The detail of the calculations of the grafting density is presented below:

$$c_{sup}(\mathrm{M}) = \frac{A_{sup} - b}{a \times 10^3} \tag{2-6}$$

$$n_{g1}(\mathrm{mol}) = n_i - c_{sup}.V_{sup} \tag{2-7}$$

$$n_{g2}\left(\frac{\mathrm{chain}}{\mathrm{NP}}\right) = \frac{n_{g1}}{c_{AuNPs} \times V_{AuNPs}} \tag{2-8}$$

$$\sigma_{Ellman}\left(\frac{\mathrm{chain}}{\mathrm{nm^2}}\right) = \frac{n_{g2}}{4\pi\left(\frac{d}{2}\right)^2} \tag{2-9}$$

$$FP\ (nm^{-2}) = \frac{1}{\sigma_{Ellman}} \tag{2-10}$$

Where c_{sup} is the molar concentration of -SH groups in the supernatant, equal to the molar concentration of PEG chains since one thiol is grafted per PEG chain; A_{sup} is the absorbance of the supernatant at 412 nm; *a* and *b* are the slope and intercept of the linear fit of absorbance at 412 nm vs. PEG concentration (Appendix A Figure A-4); n_{g1} is the number of PEG chains grafted; n_i is the initial amount of PEG chains added in the solution which is equal to the molar amount of PEG added, V_{sup} is the volume of the supernatant, n_{g2} is the number of chains grafted per AuNPs,; c_{AuNPs} is the molar concentration of the AuNPs solution; V_{AuNPs} is the volume of AuNPs solution; σ_{Ellman} is the grafting density expressed as number of chains grafted per nm^2; d is the diameter obtained from the Haiss method; FP is the footprint of the PEG chain defined as the inverse of the grafting density. The results are presented in Appendix A (Table A-1, Table A-2 and Table A-3).

2.3.1.7 Serum protein adsorption

Citrate coated and PEGylated AuNPs were centrifuged and redispersed in 10 mM PBS buffer (pH7.4, 0.15M NaCl) containing 0, 0.1, 0.5 and 5 mg mL^{-1} BSA. The solutions were left under gentle stirring and their absorbance of the solution was recorded over time.

2.3.1.8 Determination of the pH of phase transition via titration

For the determination of the pH of phase transition, the functionalised AuNPs were re-dispersed in H_2O and the pH was adjusted to pH 7.4 with 0.1 M NaOH. Then,10-20 µL of 0.1 M HCl were added, the pH and the absorbance spectra were recorded after each addition.

2.3.1.9 Determination of the pH of phase transition via redispersion in different buffers

For the determination of the pH of phase transition, the functionalised AuNPs were re-dispersed in a 100 mM citrate buffer in the pH range of 3.0-5.0 or a 100 mM phosphate buffer in the pH range of 5.5-7.4. After 24 h, the absorbance spectra were recorded.

2.3.1.10 pH responsive phase transition of the polymer determined via titration

1 mg mL^{-1} PP75 was prepared in H_2O and the pH was adjusted to 7.4. Then, 10-20 µL of 0.1 M HCl were added, the pH and the transmittance were recorded at λ=480 nm after each addition.

2.3.1.11 pH responsive phase transition of the polymer determined via redispersion in different buffers

1 mg mL^{-1} PP75 was prepared in the buffers at different pHs and the transmittance was recorded at λ=480 nm after 3 h.

2.3.1.12 Reversibility study

For the reversibility study, the functionalised AuNPs were first re-dispersed in 100 mM PB buffer at pH 7.4 and left under stirring for stabilisation for 24 h. The AuNPs@PP75 solution was then titrated under vigorous stirring to pH 3.0 using 6 M HCl and back to pH

7.4 using 6 M NaOH, and then repeated for several cycles. The absorbance profile was recorded within minutes of pH titration.

2.3.1.13 Haemolysis assay

The haemolysis assay was used in order to investigate the lytic activity of the PP75 and the AuNPs@PP75. Stock solutions of PP75 and AuNPs@PP75 were prepared in 100 mM PB buffer and then were diluted into buffers from pH 4.5 to 7.4 in triplicates (equivalent final concentrations of PP75). Sheep RBCs were washed in 150 mM NaCl and the number of cells was determined with a haemocytometer. Then 10-15 µL of RBCs solution were added to the samples within the range 1-2 x 10^8 RBCs mL^{-1} to ensure the final haemoglobin concentration would stay in the linear range for the absorbance measurement (Appendix B Figure B-5). Negative controls (RBCs in buffer only, without the presence of polymer) and positive controls (RBCs lysed with deionised water) were prepared with the same cell density. For the AuNPs@PP75 the negative and positive controls contained AuNPs at the same concentration of the samples. After incubation for one hour at 37°C in a shaking water bath (120 rpm), the samples were centrifuged at 4,000 rpm for 4 min (12,000 rpm for 12 min for AuNPs containing samples) and the absorbance of the supernatants was measured at 541 nm corresponding to the wavelength of maximal absorbance for the haemoglobin.

The relative haemolysis was calculated as follow:

$$Relative\ haemolysis\ (\%) = \frac{A_{sample} - A_{negative}}{A_{positive} - A_{negative}} . 100 \qquad (2\text{-}11)$$

Where A_{sample} is the absorbance of the supernatant of the sample at a specific pH at 541 nm; $A_{positive}$ is the absorbance of the positive control, RBCs in deionised water, at 541 nm; and $A_{negative}$ is the absorbance of the negative control, RBCs in buffer at the same pH, at 541 nm.

2.3.1.14 Fluorescein loading and release from hydrogel samples

Note: The loading and release studies were performed by Yubai Zhang and are presented in the thesis to complete the results and discussion on the potential applications of the hybrid hydrogels for therapeutic purposes.

Hydrogel disks (12mm x 15 mm) were immersed in a 5 mM citrate buffer at pH 3.0 for 48 h at room temperature before drug loading. Then the hydrogel disks were transferred to 5 mL loading solution (5 mg mL^{-1} fluorescein sodium in 20 mM phosphate buffer at pH 7.4) and immersed for another 48 h with protection from light. Then 25 µL 14% HCl (v/v) was added, followed by further incubation for 24 h. After rinsing with H_2O, hydrogel disks were immersed in 20 mL buffers (20 mM citrate buffer at pH 3.0 and 20 mM phosphate buffer at pH 7.4, respectively) for the release study. The samples were incubated in a shaking water bath (Grant LSB Aqua Pro) at 37 °C at 120 rpm. At specific time points, 100 µL samples were removed from each tube and then diluted (dilution fold ~6 at pH 3.0 and ~360 at pH 7.4) before measurement of the absorbance at 488 nm.

The loading efficiency and weight incorporations were calculated as below:

$$loading\ efficiency\ (\%) = \frac{m_l}{m_t}.100 \tag{2-12}$$

$$weight\ incorporation\ (\%) = \frac{m_l}{m_d}.100 \tag{2-13}$$

Where m_l is the amount of drugs loaded into the hydrogels determined from the calibration curve (Appendix D Figure D-7) and m_t is the total amount of drugs present in the loading solution (25 mg), m_d is the dry weight of hydrogel.

The percentage of released drugs was calculated as follows:

$$\%\ cumulative\ release = \frac{m_r}{m_l}.100 \tag{2-14}$$

where m_r is the cumulative amount of released drugs and m_l is the amount of drug loaded into the hydrogels.

2.3.2 Fluorescence measurement

2.3.2.1 Fluorescence spectrometry

Fluorescence spectrometry is similar to absorbance spectrometry, however fluorescent compounds emit light at a different wavelength that the wavelength of the irradiated light. When a fluorescent specie absorbs a photon, it passes from a ground state to an excited state, after 1-10 nanoseconds, the fluorophore returns to the ground state emitting a photon. Due to energy dissipation in the excited state, the energy of the emitted photon is lower than the excitation photon. The process is cyclical (in the absence of photobleaching) which means the fluorophore can be excited repeatedly. Like UV-vis spectrophotometry, the concentration of the analyte is proportional with the intensity of the emission and can be calculated. A relative low number of compounds exhibit fluorescence and non-fluorescent molecules can fluoresce when labelled with a fluorophore.

2.3.2.2 Method

The fluorescence of samples was measured by GloMax®-Multi Detection System (Promega, U.S.) or FluoroMax (HORIBA, Japan) in black, flat-bottom, 96-well plates.

2.3.2.3 Evaluation of the membrane activity using calcein-loaded liposomes as a model

Stock solutions of calcein loaded liposomes (provided by Dr. Siyuan Chen), PP75 and AuNPs@PP75 were prepared. For each sample, 100 µL of liposome solution and 100 µL of polymer or AuNPs solution were added to 500 µL buffer between pH 4.5 and 7.4. Before the incubation, aliquots of 50 µL were removed from each sample, added to 150 µL PB buffer at pH 7.4 and the fluorescence, $F_{initial}$, was read (Exc/Em 490/510-570). The samples were incubated for 90 minutes in a shaking water bath at 120 rpm, 37°C during which the samples were regularly reversed by hand to help the mixing. Another aliquot of 50 µL was then taken and diluted with PB pH 7.4 before fluorescence measurement

(F_{sample}). Then 10 µL Triton solution at 10% (w/v) was added to each well. The plate was stirred for 1 min and the fluorescence was read again (F_{final}).

The calcein release was determined as follows:

$$Calcein\ release\ (\%) = \frac{F_{sample} - F_{initial}}{F_{final} - F_{initial}} . 100 \quad (2\text{-}15)$$

Where F_{sample} is the fluorescence of the sample after 90 minutes incubation at 37°C in buffer; $F_{initial}$ is the fluorescene of the sample before incubation and F_{final} is the fluorescence of the sample after the addition of triton, a highly lytic substance that can lyse completely the liposomal membrane.

2.3.2.4 Determination of DOX loading efficiencies of AuNPs

AuNPs@DOX and AuNPs@DOX@PP75 samples were centrifuged and the fluorescence of the supernatant was read (Exc/Em 490/510-570 nm). The concentration of DOX was deduced from the calibration curve (Appendix C Figure C-1).

2.3.3 Dynamic Light Scattering (DLS) and zeta potential measurement

2.3.3.1 DLS

In DLS a sample containing particles is illuminated by a laser beam and the emitted light is recorded at a specific angle. Small particles in suspension are oscillating randomly (Brownian motion) and consequently the light scattering fluctuates over time.

The intensity fluctuation is represented by an intensity correlation function which enables the determination of the diffusion coefficient D. The radius of the particles R is then determined using the Stokes Einstein equation:

$$D = \frac{k_B T}{6\pi\eta R} \quad (2\text{-}16)$$

Where k_B is the Boltzmann-constant, T the temperature and η the viscosity.

The technique is usually employed to determine the size of micrometric to nanometric particles. It is important to note that the size obtained corresponds to the size of the sphere that diffuses the same way as the particle measured. The calculated size is thus an hydrodynamic diameter which for AuNPs corresponds to the size of the core plus the size of the corona.

2.3.3.2 Zeta potential

The zeta potential is the electrical potential difference between the medium and the stationary layer of fluid attached to a particle (at the slipping plane). The determination of the surface charge of a colloidal solution is a key parameter to define its stability. The zeta potential can be measured with electrophoretic light scattering (ELS). When an electrical field is applied with two electrodes immersed in a dispersion, the charged particles migrate to the electrode of opposite charge at a certain velocity or electrophoretic mobility relative to their zeta potential.

2.3.3.3 Method

Hydrodynamic size (DH) and zeta potential (ξ) measurements with dynamic light scattering (DLS) were carried out on a Brookhaven instrument with ZetaPALS software (Holtsville, USA) at 20 ˚C with an angle of 90˚ and a wavelength of 659 nm for a density of 0.2 mg mL^{-1}. The samples were prepared in triplicate. For the hydrodynamic diameter, approximately 5-10 runs of 20 cycles each were measured for each sample. Measurements were reported as volume average diameters. For the zeta potential, at least 5 runs were recorded per sample.

The DLS methods used for the determination of the minimum amount of polymer for AuNP stabilisation, the time-dependent stability study, the determination of the pH of phase transition and the reversibility study were the same with the ones used via absorbance measurements. Please refer to 2.3.1 for more details.

2.3.4 Transmission Electron Microscopy (TEM) and Energy Dispersive X-ray Spectrometry (EDX)

2.3.4.1 TEM and EDX

In TEM a high energy beam of electrons is accelerated and focused on a thin section (typically less than 100 nm) of sample, the electrons interact with the atoms of the specimen and the transmitted beam of scattered electrons is then focused and detected by fluorescence on a phosphor screen or visualised with a camera. In bright field mode, the areas of high electron density will appear dark and the areas of low electron density bright. Thanks to the low size of the electrons the resolution obtained enable the visualisation of single atoms (if the density is high enough).

In EDX the X-ray (electromagnetic radiation with wavelengths around 0.01-10 nm) spectrum emitted by a sample irradiated by of beam of electrons enables the chemical analysis since each element has their own X-ray characteristics. It is then possible to obtain the map of chemical elements in a sample.

2.3.4.2 Method

Transmission Electron Microscopy (TEM) at 200 kV was performed on a JEOL FX2000 and JEOLFX2100 (Tokyo, Japan) after deposition of a droplet of AuNPs solution on a 300-mesh, carbon-coated copper grid. After 5 min the excess of solution was absorbed with filter paper and the grid was left to dry at room temperature overnight. The EDX was conducted on the Oxford Instruments INCA EDS 80 mm X-Max detector system.

2.3.4.3 Visualisation of the self-assemblies

After deposition of a droplet on the carbon-coated grid, the grid was left at room temperature overnight before being imaged. The particle sizes and distributions were analysed with ImageJ software.

2.3.4.4 Fourier-Transform Infra-Red Spectroscopy (FTIR)

The FTIR relies on the use of IR light (from 4000 to 40 cm^{-1}). Each chemical bond exhibits a natural vibration frequency when absorbing light and thus shows a characteristic peak on

the absorbance spectrum. A Michelson interferometer creates interferences by dividing the IR signal into two optical paths and reuniting them. In that way it is possible to shine the sample with a broad range of IR frequencies simultaneously, thus significantly reducing the analysis time. A Fourier transformation is then performed on the interferogram to obtain the spectrum of the IR source and to represent the transmittance vs. frequency graph. This technique is useful for the identification of compounds or specific chemical groups.

FT-IR spectra (500-4000 cm^{-1}) were recorded on a Spectrum 100 FT-IR Spectrometer (Perkin Elmer, USA) on a pellet-like dry sample of polymers or functionalised AuNPs after freeze drying.

2.3.5 Nuclear Magnetic Resonance (NMR)

Atomic nuclei are electrically charged. When subjected to an external magnetic field they are excited to a higher energy level and they emit energy at a frequency specific of the energy gap of the atom and its environment when they return to the ground state. In NMR, electromagnetic radiation with a specific frequency is applied to a sample immersed in an external magnetic field and the absorption signal of the nuclei is recorded. The frequency is converted into chemical shift and a proton reference frequency is used as a shift of 0 since the resonant frequencies depends on the magnetic field (tetramethylsilane (TMS) is usually employed as reference. The position of the shift gives information of the electronegativity of the atom, the intensity on the quantity and the number of peaks (or splits) on the environment. If an atom is chemically bonded with another atom, there will be coupling and the peak will split in two. The final spectrum enables the determination of the chemical structure and purity of a sample. NMR of the proton is the most current but C-NMR is also employed.

Acidic form polymer powders were dissolved in d^6-DMSO and ^{1}H-NMR spectra were obtained using a 400 MHz NMR spectrometer (Bruker, Germany) at room temperature.

2.3.6 Porosimetry via the Archimede method

The measure of the porosimetry via the Archimede's method relies on the Archimede's principle which states that the force exerted on a body immersed in a fluid is equal to the weight of the fluid displaced by the body.

The weight of the hydrogel was measured (after purification in H_2O), m_w, when fully immersed in water, m_{H2O} and after lyophilisation, m_d. The porosity could be calculated as follows:

$$Density\ (w/w) = \frac{m_d}{m_w - m_{H_2O}} \quad (2\text{-}17)$$

$$Relative\ density\ = \frac{Density}{Real\ density} \quad (2\text{-}18)$$

$$Open\ porrosity\ (\%) = \frac{m_w - m_d}{m_w - m_{H_2O}} \quad (2\text{-}19)$$

$$Total\ porosity\ (\%) = (1 - Relative\ density)\ \bullet\ 100 \quad (2\text{-}20)$$

$$Closed\ porosity\ (\%) = Total\ porosity - Open\ porosity \quad (2\text{-}21)$$

Where real density corresponds to the density of the materials used for the hydrogel (PLP).

2.3.7 Scanning Electron Microscopy (SEM) imaging

2.3.7.1 SEM

SEM involves the use of an electron beam under vacuum moving over the surface of a sample. Electromagnetic lenses are used like for TEM but unlike TEM, the image is obtained from the electrons emitted from the sample and not transmitted. The resolution of modern SEM is about 2 nm. Some SEM have two detectors for secondary electrons

2.3.7.2 Method

SEM was performed on a LEO Gemini 1525 FEGSEM (Zeiss, Germany) at 5 kV and on a JSM 6010 LA (JEOL, Japan) at 20 kV. Lyophilised samples were deposited on a double-sided tape and sputtered with gold or chromium before imaging. Images acquired on the LEO used the InLens secondary electrons detector. This detector is located in the electron column and, thanks to a magnetic field, electrons can be collected efficiently which provide an enhanced contrast at low voltage.

2.3.7.3 Visualisation of the assemblies of AuNPs@PEG

For the visualisation of the assemblies, a droplet of AuNPs@PEG solution was deposited on silicon wafer or a TEM grid attached to the double-sided tape and left to dry overnight at room temperature.

2.3.8 Atomic Force Microscopy (AFM) measurement

2.3.8.1 AFM

Note: The AFM images were acquired by Dr. Edward Parsons.

AFM is a type of scanning force microscopy using a piezolelectric element, a cantilever tip, to scan over a sample. When the tip gets close to the surface it gets attracted until a certain distance and then repulsive forces deflects it from the surface. Shining the cantilever with a laser beam enable the recording of the tip movement by detecting the changes in the reflected beam with a position-sensitive photo diode. Thanks to a feedback loop the height of the cantilever is adjusted to keep the laser at a constant position. AFM can produce topographic maps with resolution of fraction of nanometers. It can also be used for force measurements and manipulation (e.g. local stimulation…).

2.3.8.2 Method

The samples were prepared by depositing a droplet of AuNPs@PEG solution on a mica sheet and drying via spin-coating (2,000 rpm for 2 min). Samples were loaded into a Veeco Multimode IV AFM, and images were acquired in tapping mode in the air (scan rate

1 Hz, 512 samples/line) using gold-coated tips cantilevers. The images were analysed using Nanoscope software.

2.3.9 Determination of the gold amount in hydrogels via Inductively Coupled Plasma-Optical Emission Spectroscopy (ICP-OES)

2.3.9.1 ICP-OES

In ICP the sample is sprayed into a plasma generated via the ionisation of argon gas using a high frequency electric current. The atoms of the sample got excited and return to a lower energy levels by releasing a photon whose wavelength is characteristic of the atom. The photons are then collected by a lens or a mirror and the optical signal is converted into an electric signal which is analysed by a computer. The intensity of the signal being relative to the amount of each element ICP enables their quantification. The samples usually need to be digested for effective elemental analysis.

2.3.9.2 Method

20 mg of dry hydrogel was digested with 2 mL HNO_3 for 3 h at 60 °C. After complete digestion, the solution was topped up with ultra-pure water to 5 mL and filter sterilised with 0.22 µm filter before being measured via ICP-OES using a PE Optima 2000 DV ICP-OES (PerkinElmer, Wokingham, UK). One blank with PLP hydrogel and three calibration samples, prepared using blank hydrogel mixed with known amounts of gold nanoparticles (0.2, 0.5 and 10 ppm), were prepared following the same procedure.

2.3.10 X-ray photoelectron spectroscopy (XPS) measurement

2.3.10.1 XPS

XPS enables the elemental characterisation of the surface of a sample up to a depth of 5 nm. In XPS, the sample surface is exposed to X-rays (electromagnetic radiations with wavelengths ranging from 0.01 to 10 nm) leading to the ejections of some electrons from their atomic orbital. The electrons are then collected and an analyser measures their kinetic energy and a graph intensity vs. binding energy is produced. The energy peaks are then related to specific elements and their intensity can be used for quantitative analysis. The binding levels can help identifying the type of bonds (single or double bonds for

instance). The analysis is performed in ultra-high vacuum to slow down the degradation of the sample under X-ray, to limit the surface contamination and to enhance the quality of the analysis avoiding the interference that could originate from the gas phase collisions with the emitted electrons.

2.3.10.2 Method

Note: The XPS spectra were provided by Dr. Ignacio Villar Garcia.

XPS data was obtained for lyophilised hydrogels samples from a K-alpha$^+$ XPS spectrometer equipped with an MXR3 Al Kα monochromated X-ray source (hν = 1486.6 eV). X-ray gun power was set to 72 W (6 mA and 12 kV). All high-resolution spectra (S2p, C1s, O1s and Au4f) were acquired using 20 eV pass energy, 0.1 eV step size and 1 second (50 ms x 20 scans = 1000 ms) dwell times. Thermo Avantage software was used for data interpretation. According to the atomic composition of the PLP backbone and the crosslinkers, each crosslinker bears 2 sulfurs and 2 nitrogens per molecule and each PLP unit has 2 nitrogens. The crosslinking ratio could be deduced from the percentage of sulfur and nitrogen:

$$\%Crosslinking\ ratio = \frac{\%\ Crossliner}{\%PLP\ residual} = \frac{\%S}{\%N - \%S} \times 100 \qquad (2\text{-}22)$$

Where $\%S$ refers to the atomic percentage of sulfur and $\%N$ refers to the atomic percentage of nitrogen.

2.3.11 Compression test using Dynamic Mechanical Analysis (DMA)

2.3.11.1 DMA

In DMA, a material is characterised by his mechanical response to a minor, usually sinusoidal, force. The analysis can also be done under controlled stress mode, relative to the force or load applied to the sample or controlled strain mode, relative to the deformation or displacement of the sample. The DMA measures the stiffness and damping of the material reported as in-phase (storage) and out-of-phase (loss) tensile modulus, E' and E'', and tan δ the ratio of E'' to E' with δ the phase angle.

2.3.11.2 Method

A compression test was performed using a DMA apparatus in controlled force mode. The tests were performed on 8 mm by 5 mm wet hydrogel using an ElectroForce 3200 (Bose, U.S.) and a load of 22 N. Hydrogels were soaked in PB buffer at pH 7.4 or citrate buffer at pH 3.0 48 h before the measurement. The hydrogels were then clamped between parallel plates. Using the controlled stress mode, compression tests were performed from 0.02 to 1 N at a rate of 0.02 N s^{-1}. The force and displacement were collected with Win Test 7 software. The stress and the deformation factor λ, ratio of the deformed to the undeformed height of the sample, were calculated according to the following equations:

$$Stress\ (Pa) = \frac{Load_{ti+1} - load_{ti}}{\pi\left(\frac{d}{2}\right)^2} \quad (2\text{-}23)$$

$$\lambda\ (mm/mm) = \frac{h - (disp_{ti+1} - dis_{ti})}{h} \quad (2\text{-}24)$$

Where $load_t$ is the load at time t; d is the diameter of the hydrogel (8 mm); $disp_t$ is the displacement at time t and h is the height of the hydrogel (5 mm).

The tensile storage modulus, E', was calculated as the slope of the linear region of the stress vs. λ curve.

The tensile storage modulus E' could be converted into shear storage modulus G' to allow comparison with the oscillatory shear rheology results via the following formula:

$$G'(Pa) = \frac{E\prime}{2\ (1+\nu)} \quad (2\text{-}25)$$

Where ν is the Poisson ratio. The Poisson ratio corresponds to the ratio of transverse contraction strain to longitudinal extension strain. For swollen hydrogel, the Poisson ratio is usually considered similar to the one measured for rubber ($\nu = 0.5$). [192]

2.3.12 Swelling studies

Note: The swelling studies were performed by Yubai Zhang and are presented in the thesis to complete the results and discussion on the potential applications of the hybrid hydrogels for therapeutic purposes.

Before swelling study, as synthesised hydrogel disks were transferred from H_2O to 100 mM PB buffer at pH 7.4 for 48 h, to ensure all samples were at the same pH at the initial point. These samples were then placed into 100 mM citrate buffer at pH 3.0 at room temperature. The wet weight of each sample was measured after 48 h. The process was repeated in buffer at pH 7.4 and pH 3.0. These samples were then soaked in H_2O for 48 h, followed by lyophilisation to obtain the dry weight of hydrogel disks. The swelling ratio q was defined as follows:

$$q = \frac{m_w}{m_d} \tag{2-26}$$

Where m_w is the wet weight of hydrogel disk after 48 h of incubation in buffer and m_d is the dry weight after lyophilisation.

2.4 Methods for the biological evaluation

2.4.1 Cells culture

HeLa adherent epithelial cells (human cervical cancer cells) were grown in DMEM medium supplemented with 10% (v/v) FBS and 100 U mL^{-1} penicillin. The HeLa cells were trypsinised using trypsin–EDTA and maintained in a humidified incubator with 5% CO_2 at 37°C.

MES-SA adherent epithelial cells (human uterus cancer cells) and the multi-drug resistant cells MES-SA/DX5 were cultured in McCoy's 5a medium containing 10% (v/v) FBS and

100 U mL^{-1} penicillin. The MES-SA and MES-SA/DX5 cells were subcultured with EDTA solution (0.8 mM disodium EDTA, 68.5 mM NaCl, 6.7 mM sodium bicarbonate, 5.6 mM glucose and 5.4 mM KCl) and maintained in a humidified incubator with 5% CO2 at 37°C.

2.4.2 Cytotoxicity measurement via alamarBlue assay

2.4.2.1 alamarBlue

Reazurin, the alamarBlue® reagent, is a permeable compound that is converted within living cells into resofurin, a highly fluorescent compound. The concentration of resofurin can be measured via fluorescence and is directly correlated to the number of healthy living cells since damaged and non-viable cells will generate a lower signal due to their limited reducing capacity.

2.4.2.2 Method

Cells were plated in 96 well-plates (Corning, US) at a density of $1x10^4$ cells per well. After 24 h of incubation, cells were treated with the samples at different concentrations for the desired period of time. Medium only and cells with medium in the absence of treatment were prepared as negative and positive control respectively. The cells were then washed three times with D-PBS and treated with complete medium (DMEM or McCoy) containing 10% (v/v) alamarBlue for 4 h. The fluorescence was then recorded with a GloMax-Multi Detection System microplate reader (Promega, Madison, U.S.) at the excitation and emission wavelengths of 525 and 580-640 nm respectively. The relative cell viability was calculated as follows:

$$Relative\ cell\ viability\ (\%) = \frac{F - F^-}{F^+ - F^-}.100 \qquad (2-27)$$

Where F is the fluorescence of the sample; F^+ and F^- the fluorescence of the positive and negative controls respectively.

2.4.2.3 Cytotoxicity of polymers and functionalised AuNPs

HeLa cells (1 x 10^4 cells per well) were seeded in a 96-well plate. After 24 h the spent medium was removed and replaced with 100 µL of 0.22 µm filter-sterilised complete

DMEM medium containing polymers or functionalised AuNPs at specific concentrations. After incubation for a period ranging from 2 to 48 h, the cells were washed three times with D-PBS and further incubated in the complete DMEM containing 10% (v/v) alamarBlue before fluorescence measurement.

Note: McCoy media was used instead of DMEM when the alamarBlue assay was performed with MES-SA and MES-SA/Dx5 cells.

2.4.2.4 Cytotoxicity of hydrogels

Hydrogels were frozen, lyophilised and then crushed in a fine powder. The powder was sterilised under UV irradiation for 1 h and then redispersed in DMEM media at different concentrations. HeLa cells (1 x 10^4 cells per well) were seeded in a 96-well plate. After 24 h the spent medium was removed and replaced with 100 µL complete DMEM medium containing hydrogel. After incubation for 24 or 72h, the cells were washed three times with D-PBS and further incubated in the complete DMEM containing 10% (v/v) alamarBlue for 4 h before fluorescence measurement.

2.4.3 Cellular uptake quantification via inductively coupled plasma optical emission spectrometry (ICP-OES) and flow cytometry

2.4.3.1 Flow cytometry‡

A flow cytometer enables the quantification of fluorescently labelled cell components with a laser technology. The laser illuminates a flow of cells in single file and the fluorescence emitted from the cell component and the forward and side scattered light of the laser are collected. When a fluorescent cell passes through the laser a photon is emitted and the optical signal is converted into an electrical signal. The fluorescence response gives indication of the number of positively stained elements and the scattered light intensity indicates the concentration of cells and the size of different populations if present (e.g. viable cells, debris…).

‡ ICP-OES principle is explained in 2.3.9.1

2.4.3.2 Method

HeLa cells ($3x10^5$ cells per well) were cultured for 24 h in 6 well-plates (Corning, USA). The spent medium was removed and replaced with 2 mL of 0.22 μm filter-sterilised complete DMEM medium containing AuNPs@PP75 at specific concentrations. Blank and calibration samples were prepared with DMEM and cells only. After 24 h of incubation, the cells were washed three times with D-PBS. The cells were then trypsinised with trypsin-EDTA and rinsed with DMEM. For the cell counting an aliquot was mixed with Guava count reagent and cells were counted by flow cytometry (Guava® easyCyte 8HT benchtop flow cytometer, Merck Millipore, UK).

The cell suspension was then centrifuged at 10,000 rpm for 5 min, the supernatant was removed and 1 mL ultra-pure water and 3 mL HNO_3 were added to each tube. After complete digestion, the solution was topped up to 5 mL with ultra-pure water and filter sterilised with a 0.22 μm filter before being measured via ICP-OES (PE Optima 2000 DV ICP-OES, PerkinElmer, Wokingham, UK). One blank with cells only and three calibration samples, containing cells and known amounts of gold nanoparticles (0.2, 0.5 and 10 ppm), were prepared following the same procedure.

Calculation of the number of AuNPs per cells determined via FACS and ICP:

$$m_{Au}(g) = \frac{c_{Au}.V_{sol}}{10^3} \quad (2\text{-}28)$$

$$V_{AuNPs}(m^3) = \frac{4}{3}\pi\left(\frac{d}{2}\right)^3 \quad (2\text{-}29)$$

$$m_{AuNP}(g\ per\ AuNP) = \rho_{Au}.V_{AuNPs} \quad (2\text{-}30)$$

$$N_{AuNPs}(\text{number}) = \frac{m_{Au}}{m_{AuNP}} \quad (2\text{-}31)$$

$$N_{AuNPspercell}(number\ per\ cell) = \frac{N_{AuNPs}}{N_{cells}} \quad (2\text{-}32)$$

Where c_{Au} is the concentration of gold ions obtained via ICP measurements; V_{sol} is the volume of the solution for ICP; m_{Au} is the mass of gold ions; d is the average diameter of

the AuNPs determined via the Haiss method; V_{AuNPs} is the average volume of the AuNPs assuming perfectly spherical spheres and homogeneous solutions; ρ_{Au} is the density of gold and is equal to 19300 kg m^{-3}; m_{AuNP} is the mass of one AuNP; N_{AuNPs} is the number of AuNPs; N_{cells} is the number of total cells measured via FACS and $N_{AuNPspercell}$ is the number AuNPs per cell.

2.4.4 TEM observation of intracellular localisation

Note: Tom Ellis (PhD student) provided some help for the cell fixing and staining protocol and Dr. Basmah Othman helped me with the ultramicrotomy and the visualisation of the fixed cells sections under TEM.

HeLa cells ($3x10^5$ cells per well) were cultured for 24 h in 6 well-plates (Corning, USA). The spent medium was removed and replaced with 2 mL of 0.22 μm filter-sterilised complete DMEM medium containing AuNPs and AuNPs@PP75 at 10 nM. After 24 h of incubation the cells were rinsed with normal saline (0.9% w/v NaCl), fixed with 2.5% v/v glutaraldehyde in 0.1 M PIPES overnight at 4 °C. Cells were rinsed with 0.1 M PIPES and were scraped down, collected and centrifuged at 13,000 rpm for 10 min. Cells were stained with 1% w/v osmium tetroxide in 0.1 M PIPES for one hour and then washed with deionised H_2O. Cells were then dehydrated in a grade series of ethanol (50%, 70%, 95%, 100%) with 3 successive baths of 3 min each and submerged in acetonirile. Finally, the cells were infiltrated with a quetol based resin combining 8.75 g quetol, 13.75 g NSA, 2.5 g MNA and 0.62 g BDMA mixed with acetonitrile and then with pure resin. The samples were then polymerised at 60°C for two days and thin sections of 80 nm were cut with an ultramicrotome before being imaged under TEM.

2.4.5 Confocal laser scanning microscopy (CLSM) imaging

2.4.5.1 CLSM

Unlike optical microscopes CLSM does not use light but a laser beam to image a sample. Pinholes apertures are used after the laser beam to focus the light on a small part of the sample and at the focal plane of the objective lens to only detect the focused light. As the laser beam travels in a straight line the contrast is improved and the scattered light

reduced. The emitted light passes through a series of mirrors and is amplified before being converted in an electrical signal to obtain a final image. The confocal microscope can image bright field images and fluorescent images thanks to a dichroic mirror and a series of filters and fluorescent lamps. The laser scans the surface of the samples to reconstruct a 2D image. Successive sections of a sample can also be imaged by changing the height of the objective lens to produce a 3D projection which allows the precise spatial detection of fluorescent molecules. All the images in the present thesis were acquired with an CLSM-510 inverted confocal microscope (Zeiss, Germany)

2.4.5.2 Release of endocytosed calcein from intracellular vesicles

HeLa cells (2 x 10^5 cells per well) were cultured for 24 h in a 35-mm glass-bottom dish (MatTek, USA). The spent medium was removed and replaced with 2 mL of 0.22 μm filter-sterilised complete DMEM medium containing 10 nM AuNPs with or without PP75 functionalisation and 2.0 mg mL^{-1} calcein. In the control sample, HeLa cells were treated with 1 mL of DMEM containing 0.22 μm filter-sterilised 2.0 mg mL^{-1} calcein only. After 24 h incubation, the cells were washed three times with D-PBS and further incubated in DMEM for 6 h. The distribution of calcein within the cells was examined with a 40x objective at the excitation and emission wavelengths of 488 and 505-550 nm respectively.

2.4.5.3 Visualisation of intracellular trafficking of AuNPs via colocalisation

HeLa cells (3 x 10^5 cells per well) were cultured for 24 h on coverslips at the bottom of 6-well plates (Corning, USA). The spent medium was removed and replaced with 2 mL of 0.22 μm filter-sterilised complete DMEM medium containing 10 nM AuNPs with or without PP75 functionalisation and 2.0 mg mL^{-1} calcein. In the control sample, HeLa cells were treated with 1 mL of DMEM containing 2.0 mg mL^{-1} calcein only. After 24 h incubation, the cells were washed three times with D-PBS, stained with 2 μM Hoechst 33342 for 30 min and 500 nM Lysotracker red DND 99 for 20 min, for nucleus and lysosomes/endosomes staining respectively, and then fixed with ice cold methanol at -20°C for 5 min. The cells were then rinsed with D-PBS and H_2O and the coverslip was mounted on a microscope slide with glycerol based antifade reagent and sealed with nail

varnish. The samples were imaged with a 63x oil objective at the excitation and emission wavelengths of 405/420-480nm and 543/615nm for the imaging of Hoechst and lysotracker respectively. On a separate track light scattering from gold nanoparticles excited with a laser at 514 nm was recorded within the spectral band 505-550 nm.

2.4.5.4 Intracellular localisation of DOX

MES-SA and MES-SA/Dx5 cells (2 x 10^5 cells per well) were cultured for 24 h in a 35mm glass-bottom dish (MatTek, USA). The spent medium was removed and replaced with 2 mL of 0.22 μm filter-sterilised complete DMEM medium containing free DOX and AuNPs@DOX@PP75 at an equivalent DOX concentration of 1 μg mL^{-1}. After 24 h incubation, the cells were washed three times with D-PBS and stained with 2 μM Hoechst 33342 for 30 min and 500 nM Lysotracker red DND 99 for 20 min. The samples were imaged with a 40x oil objective at the excitation and emission wavelengths of 405/420-480nm, 488/560 and 543/615 for the imaging of Hoechst, DOX and lysotracker respectively.

2.4.6 Phototherapy

2.4.6.1 Laser specifications

The laser used was a LD pumped all-solid state green laser at 532 nm (MGL-FN-532, CNI laser, China) operating on a continuous wave mode for power between 1.8 and 3.4 W cm^{-2}. The laser was equipped with a fiber and a collimator (PAF-SMA-5-A, Thorlabs, U.S.)

2.4.6.2 Temperature monitoring

96 well-plates with medium, cells and/or AuNPs solution were irradiated with laser and the temperature was recorded using a hand-held thermometer (TC Direct, UK) with a thermocouple immersed in the solution.

2.4.6.3 Cytotoxicity after irradiation

After the treatment with AuNPs, the cells in 96 well plates were washed three times with D-PBS and were irradiated at the desired laser power and time. The cells were then incubated for a further 24 h before the alamarBlue assay was performed.

2.4.6.4 Intracellular localisation after irradiation

After the treatment with AuNPs, the cells in 35 mm dishes were washed three times with D-PBS and were irradiated at the desired laser power and time. 6 different locations were irradiated per dish to make sure to cover the whole surface. The cells were then incubated for a further 24 h before being imaged. The samples were imaged with a 40x oil objective at the excitation and emission wavelengths of 405/420-480nm, 488/560 and 543/615 for the imaging of Hoechst, DOX and lysotracker respectively. Images were acquired with an CLSM-510 inverted confocal microscope (Zeiss, Germany)

Chapter 3 PEGylation of AuNPs: stability and assembly

Chapter 3 provides a summary of the results obtained for the synthesis and physico-chemical characterisation of AuNPs functionalised with PEGs of three different chain lengths. It covers in particular the optimisation and quantification of the surface coverage for enhanced colloidal stability. The last section concerns the investigation of the mechanism involved in the self-assembly of the hybrids under evaporation.

This chapter is partially based on the following publication:

M. Bachelet; R. Chen. Self-assembly of PEGylated gold nanoparticles with satellite structures as seeds. *Chemical Communications* **2016**, *52*, 9542-9545.

Figures and texts were reproduced and adapted with permission of The Royal Society of Chemistry, copyright 2016.

3.1 Introduction

Citrate coated AuNPs are amongst the most commonly synthesised AuNPs due to their ease of synthesis in a one-pot method where citrate is used as reducing and stabilising agent simultaneously.[22,23,25,27,29,30] Their stability is only provided by weak electrostatic repulsions between the negatively charged citrates on the AuNPs surface. They suffer from a poor stability in solution and rapidly agglomerate in buffers. However, a high colloidal stability is crucial to ensure a controlled and safe delivery within the body.

PEG is probably the most employed polymer in medicine. Simple structure, controllable chain length and water solubility are amongst the interesting properties that make PEG a polymer of choice for numerous applications in the industry.[193,194] Thanks to its biocompatibility and biodegradability PEG has attracted a considerable interest in therapeutics and is one of the few polymers approved by the FDA for human use.[195,196] Its neutral charge has been extensively exploited to shield drug delivery systems and to protect them from serum proteins binding and agglomeration thus providing long-term circulation in the biological fluids.[195-198] As a promising cancer nanotherapeutic, gold nanoparticles have also been covered with PEG to bring serum stability.[127,140,199] Thanks to the high flexibility of the PEG backbone, molecules can be conjugated to the end of a PEG chain that is grafted on the AuNPs surface, and still be able to interact efficiently with the surrounding environment. This feature is of particular interest for the functionalisation of drugs[128], imaging agents[126,200] and targeting ligands.[126,201] Surprisingly, the use of PEGylated nanoparticle as drug nanocarriers is still limited to research laboratories and the majority of approved nanoparticulate systems does not hold PEG possibly because of the negative impact of the PEGylation on the tumour penetration.[195]

Numerous PEGylated AuNPs have been reported in the literature and the influence of the PEGylation, in particular the influence of the concentration,[202,203] the chain length,[47] the charge,[47,204] and the AuNPs size[205] on the stability,[206-208] the proteins binding,[47,205] the cellular internalisation[204,209] and clearance[210] have been investigated. However, only the effect of one or two factors on one parameter such as the effect of the grafting density on

the colloidal stability or the effect of the chain length on the polymer conformation are usually reported. The aim of this research project was to draw a complete and comprehensive study including the rigorous investigation of the influence of the chain length and the polymer concentrations on the colloidal stability in various buffers, but also on the physico-chemical characteristics including the hydrodynamic sizes and the zeta potential, the serum protein adsorption, the polymer conformation and the interparticle interactions. To this end, three PEG chain lengths, Mw 800, 2000 and 6000 g mol^{-1}, namely PEG0.8k, PEG2k and PEG6k, respectively, were grafted on the surface of AuNPs.

In the first part of this chapter, the physico-chemical properties of the PEGylated nanoparticles have been studied and, in particular, the influence of the PEG chain length and the concentration of polymer on the colloidal stability in various media have been investigated. The grafting density and polymer conformation on the surface have been determined thanks to UV-vis spectrophotometry and DLS measurements. Interestingly, TEM images have highlighted a specific and reproducible assembly of the polymeric nanoparticles. The mechanism of assembly has been discussed in the second part of this chapter based on the findings of the first part.

Recently, nanocrystal superlattices or ordered three-dimensional arrays at the nanoscale have attracted a growing interest for electronic and sensing applications due to the exceptional properties provided by the collective interactions between subunits.[3,211-215] Various synthesis methods have been developed to create arrays of nanoparticles in 1D,[216] 2D,[217] or 3D,[218] in solution[219] or at an interface,[213] assisted via an electric[220] or magnetic field[221] and under light irradiation.[222] AuNPs assemblies have been investigated for applications in catalysis but also in medicine where the selective hybridisation of DNA strands have proved to be extremely useful to link neighbouring particles and form large-scale patterns.[223,224] However, DNA is still expensive and not widely accessible.

Herein, the assemblies are formed due to the evaporation process of the colloidal solution. Larson-Smith and Pozzo[225] employed long PEG chains (Mw 10,000) and short

alkane chains to create amphiphilic AuNPs and generate assemblies in solutions. In the present study, assemblies were observed with AuNPs functionalised with PEG only. The mechanism of the formation of the assemblies have been investigated. The polymeric corona was found to play a major role in this process directly influencing the final patterns. The solvent evaporation method has already been reported by several groups for the assembly of AuNPs,[218,219,226-230] however to my knowledge it is the first time that PEG alone is employed. Additionally, I am not aware of any analogous study investigating the effect of the chain length in the brush regime on the assemblies. The potential impact of this study for researchers working in the preparation of nanostructures assemblies is significant.

3.2 Results and discussion

3.2.1 AuNP characterisation

3.2.1.1 Concentration and size

AuNPs were prepared via citrate reduction of gold salts according to the Turkevich method.[22] Auric salts were boiled in water and reduced with citrates that stabilise the final nanoparticles by electrostatic repulsion. Figure 3-1 summarises the main physico-chemical characteristics of the as-synthesised citrate-coated AuNPs. Figure 3-1(A) shows the characteristic absorbance spectrum of a solution of AuNPs particles with an absorbance peak at 522 nm (A_{SPR}=3.133 nm). The diameter *d*, and concentration *c*, of the AuNPs in solution have been calculated based on the absorbance spectrum by the Haiss method (Chapter 2 Materials and Methods 2.3.1.3 and Appendix A Figure A-1) and the following results were obtained: d (nm)=13.9 and c(nM)=11.

These results, comparable to the literature for similar synthesis parameters, confirm the successful synthesis of citrate-coated AuNPs.[231] The diameter size obtained via the Haiss method lies between the hydrodynamic diameter (D_H) obtained via DLS (Figure 3-1(B)), 23.8 ±0.9 nm, and the size obtained via the TEM image analysis (Figure 3-1(D)), 11.4 ±2.8 nm (count for 138 particles). The reasons for these differences are threefold: (i) the hydrodynamic diameter was calculated from the relation between the light scattering

intensity and the diameter of the particles which is a sixth power relation and favours the larger size particles for the calculation of the mean diameter; (ii) the hydrodynamic diameter is an apparent diameter which includes the hydration layer (e.g. ligands, ions or molecules at the surface of the nanoparticles, here the citrates), and (iii) the TEM image analysis requires the use of an underestimated threshold between the background and the nanoparticles intensities to avoid the contact between neighbour particles that could be counted as single nanoparticles and thus the results reflect slightly lower diameter sizes than the reality.

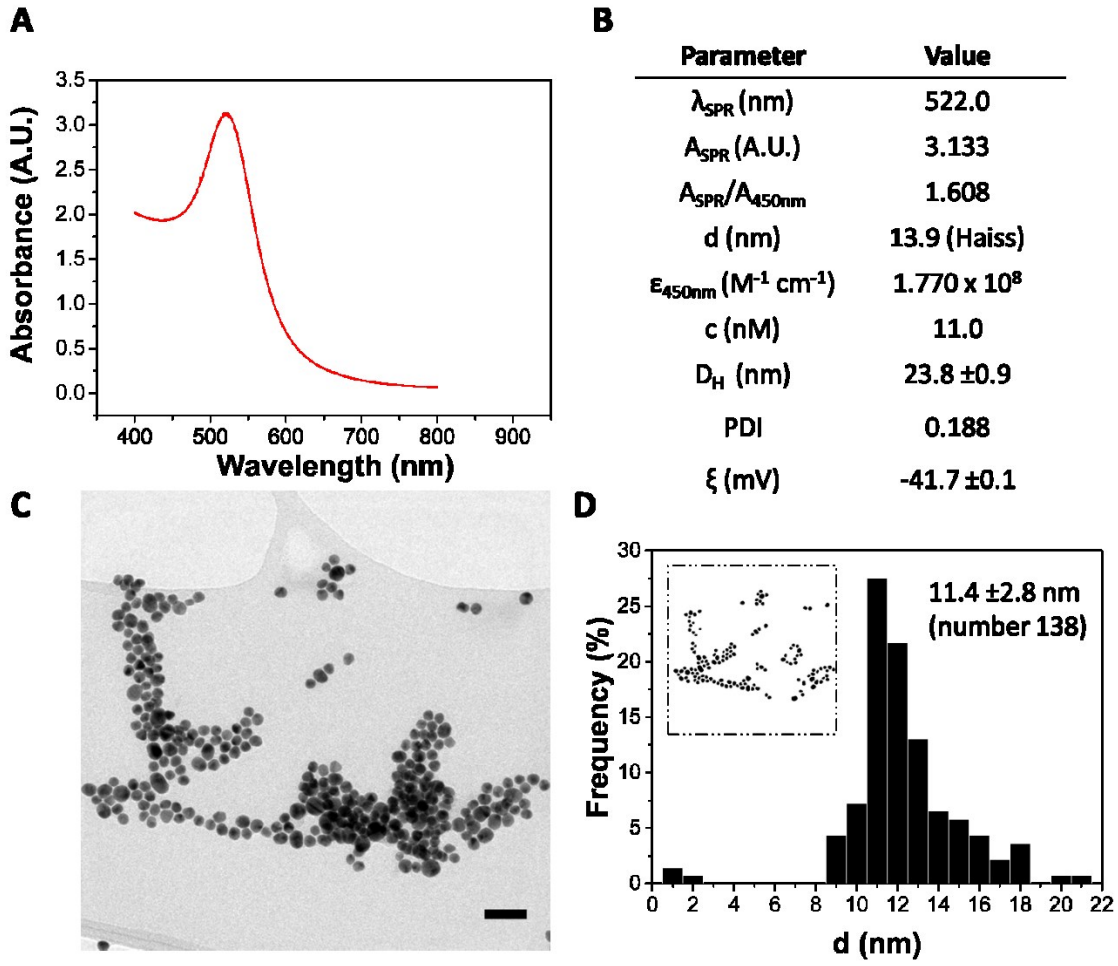


Figure 3-1 Citrate coated AuNPs characterisation. (A) UV-vis scan. (B) Physico-chemical characteristics obtained via UV-spectroscopy and DLS. (C) TEM image of citrate coated AuNPs (scale bar 50nm). (D) Size distribution obtained via ImageJ (inset ImageJ mask image of (C) used for the determination of the average size. Figures C and D are adapted from Bachelet and Chen[232] copyright 2016, with permission from The Royal Society of Chemistry

The TEM image (Figure 3-1(C)) shows particles that are not perfectly spherical but exhibit faceted structure, sign of their crystalline nature. A set of varied sizes and shapes with a high level of agglomeration can be observed. It is believed that the agglomeration mainly occurred during the evaporation of the water on the TEM substrate since the PDI in solution measured via DLS is very similar to the stabilised PEGylated AuNPs, ~0.20 (coefficient of variation, CV=44%), as presented below. It is also similar to the values reported in the literature for 17 nm citrate coated AuNPs.[207] The agglomeration is explained by the weak electrostatic repulsion between citrate layers on the surface of AuNPs. This hypothesis is confirmed by a relatively low absolute value of the zeta potential (ξ=-33.35 ±1.10 mV).

As described by Derjaguin, Landau, Verwey and Overbeek in the DLVO theory,[233] the total force between two particles from a colloidal solution, F_{tot}, can be expressed as the sum of the attractive (Van der Waals) and repulsive (electric double layer, EDL) forces, F_a and F_r respectively.

$$F_{tot}(D) = F_a(D) + F_r(D) \quad (3\text{-}1)$$

Where D is the distance between two particles surface.

The Van der Waals forces take into account the electromagnetic effect between electron clouds of two particles whereas the EDL forces are related to the electrostatic forces and the surface potential. Charged particles present two main layers of surface potential: a compact inner layer of counter ions (the Stern layer) and a larger diffuse outer layer. They both form the EDL and the thickness of the EDL corresponds to the Debye length. The total potential interaction energy vs. distance curve presents a maximum which corresponds to the aggregation barrier. If two particles come close enough to each other and the attractive forces are stronger than the repulsive forces then the particles will agglomerate.[233] The zeta potential is a measure of the electric potential at the slipping plane located at the boundary between the EDL and the medium. The absolute value of the zeta potential gives a good indication of the stability of the colloidal system and it is generally assumed that a good stability is provided by high values of zeta. However,

according to the DLVO theory, the Van der Waals forces have also to be taken into account and low Van der Waals forces may result in stability even at low absolute values of zeta potential.[234] The zeta potential values of citrate coated AuNPs of ~ 15-20 nm in size have been reported to be around ~ -40 mV. [207,235]

3.2.1.2 Reproducibility, long term stability, resistance to dilution and centrifugation

This section investigates critical properties of AuNPs for clinical translation: batch-to-batch variability, long-term stability in aqueous solutions, resistance to centrifugation, which is a common step for purification and impact of the dilution since most AuNPs-based therapeutics are designed for intravenous injections and need to face very large dilutions in the blood.

A

Parameter	Value
λ_{SPR} (nm)	521.2 ±2.3
A_{SPR} (A.U.)	2.994 ±0.309
d (nm)	14.5 ±2.0
c (nM)	10.2 ±3.4

B

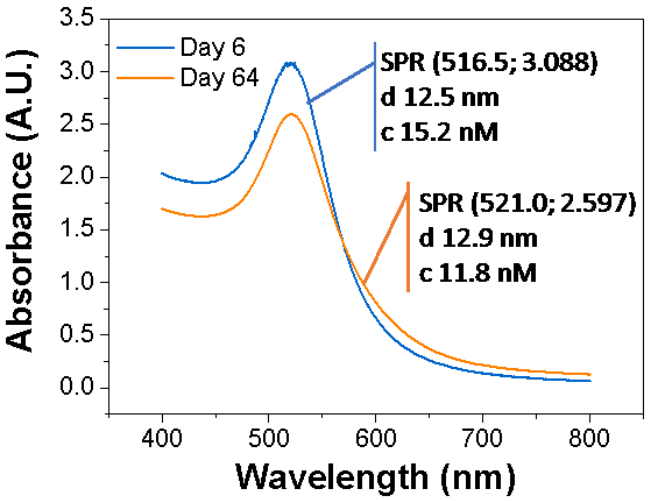


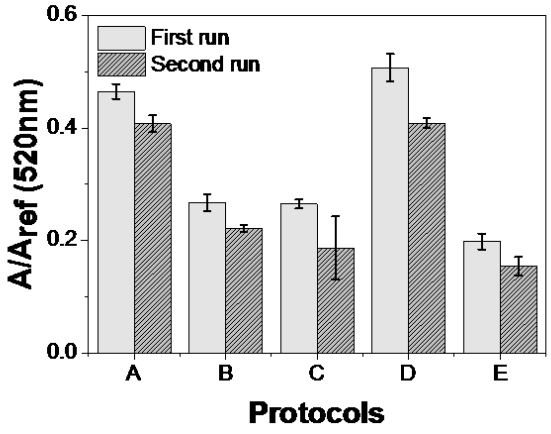
Figure 3-2 (A) Reproducibility: mean values for physicochemical properties of the citrate coated AuNPs from 27 independent batches. (B) Effect of time on the optical properties. Values are given as mean ± standard deviation of triplicate measurements.

First, the reproducibility of the AuNPs synthesis was investigated by comparing the physicochemical characteristics of 27 independent batches prepared from 2013 to 2017 and the results are presented in Figure 3-2. Overall, very low variation was observed in terms of the optical parameters and the mean values for the size and concentrations obtained were: d (nm)=14.5 ±2.0 and c (nM)=10.2 ±3.4, even though a slight increase of the size and a consequent decrease of the AuNPs concentration was observed over

batches with the aging of the gold salts. One of the possible cause is the increase of the moisture level for the reagent with storage time which leads to errors in the calculations of reagent quantity and thus of the gold to citrates ratio in direct correlation with the final size and concentrations of the AuNPs.

The long-term stability of AuNPs solutions kept at 4°C in the dark was also evaluated. Most of the batches did not show significant differences after a few months of storage, however some did. The agglomeration during storage could originated from defects in the capping layers of the AuNPs due to slight variations in the experimental synthesis (e.g. time, temperature) or the presence of contamination in the solution (e.g. glassware not clean, unfiltered water). Figure 3-2(B) shows an example of a poor colloidal stability, since the absorbance spectrum is red-shifted from 516 to 521 nm and the peak of absorbance decreases from 3.1 to 2.6 nm after only 2 months'storage. Even though the reproducibility between the as-synthesised AuNPs solutions is relatively decent, each AuNPs batch was specifically and regularly characterised via absorbance measurements and was disposed after a maximum of 2 months' storage or if the stability was considered too low.

A



B

Protocol	Speed [g]	Time [min]
A	15,000	30
B	20,000	30
C	20,000	15
D	15,000	60
E	20,000	60

Figure 3-3 Effect of the centrifugation parameters on the absorbance. (A) $A/A_{ref\ (520nm)}$ corresponding to the ratio between the absorbance post and pre-centrifugation at 520 nm. (B) Protocols for the centrifugation parameters optimisation. Error bars represent the standard deviations of triplicate measurements.

The influence of the centrifugation parameters on the colloidal stability was also investigated. The speeds and centrifuge times tested were 15,000 g and 20,000 g for 15 – 60 minutes, which are the durations commonly encountered in the literature for the purification of AuNPs solutions.[201,236,237] The absorbance peaks of the solutions were recorded before (A_{ref}) and after (A) each run of centrifugation and the ratio A/A_{ref} are presented in Figure 3-3(A).

All the ratios presented were below 0.5 which is a sign of a low redispersion capacity of the citrate coated AuNPs after centrifugation. Protocols A and D (15,000 g) show higher ratios than protocols B, C and E (20,000 g) and no significant difference was observed between 15 and 60 min centrifugation at a fixed centrifugation speed. These results clearly indicate that the speed of centrifugation is a critical factor and should be carefully chosen but also that the citrate molecules alone cannot provide a desirable resistance to centrifugation and redispersion.

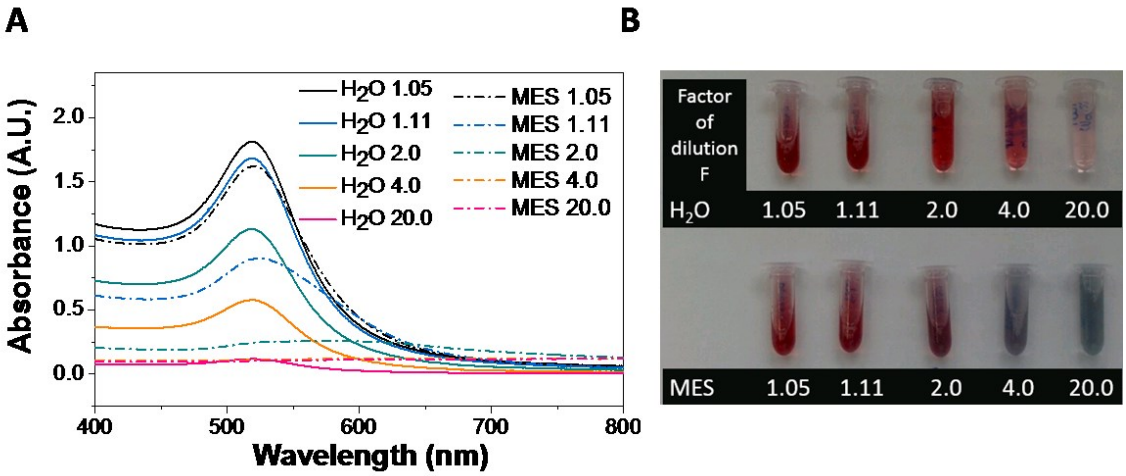


Figure 3-4 (A) Effect of different folds of dilution in H_2O and MES buffer (50 mM, pH5.5) on the absorbance. (B) Picture of the AuNPs solution after dilution in H_2O and MES buffer.

Last, the impact of the dilution on the stability was investigated. Figure 3-4 shows the absorbance spectra of AuNPs solution diluted at increasing dilution factors in H_2O and MES buffer (50 mM, 0.15 M NaCl, pH 5.5). With increasing the dilution factor in H_2O, the absorbance decreased as expected due to the decrease in AuNP concentration, but no significant shift was observed. As comparison, the dilution in MES buffer at pH 5.5 led to

a red-shift of the wavelength corresponding to the maximum absorbance, indicative of an increase in size of the colloidal solutions due to agglomeration.[46] The positively charged ions in the MES buffer, protons and sodium ions, would be responsible for neutralisation of the surface charge and the consequent annihilation of the electrostatic repulsion leading to the agglomeration. These changes were clearly visible to the naked eye and the picture of the corresponding AuNPs solutions is displayed in Figure 3-4(B). The colour of the AuNPs solutions diluted in H_2O became paler whereas the MES buffer dilution caused the solution colour to change from red to purple and then blue in agreement with the absorbance spectrum.

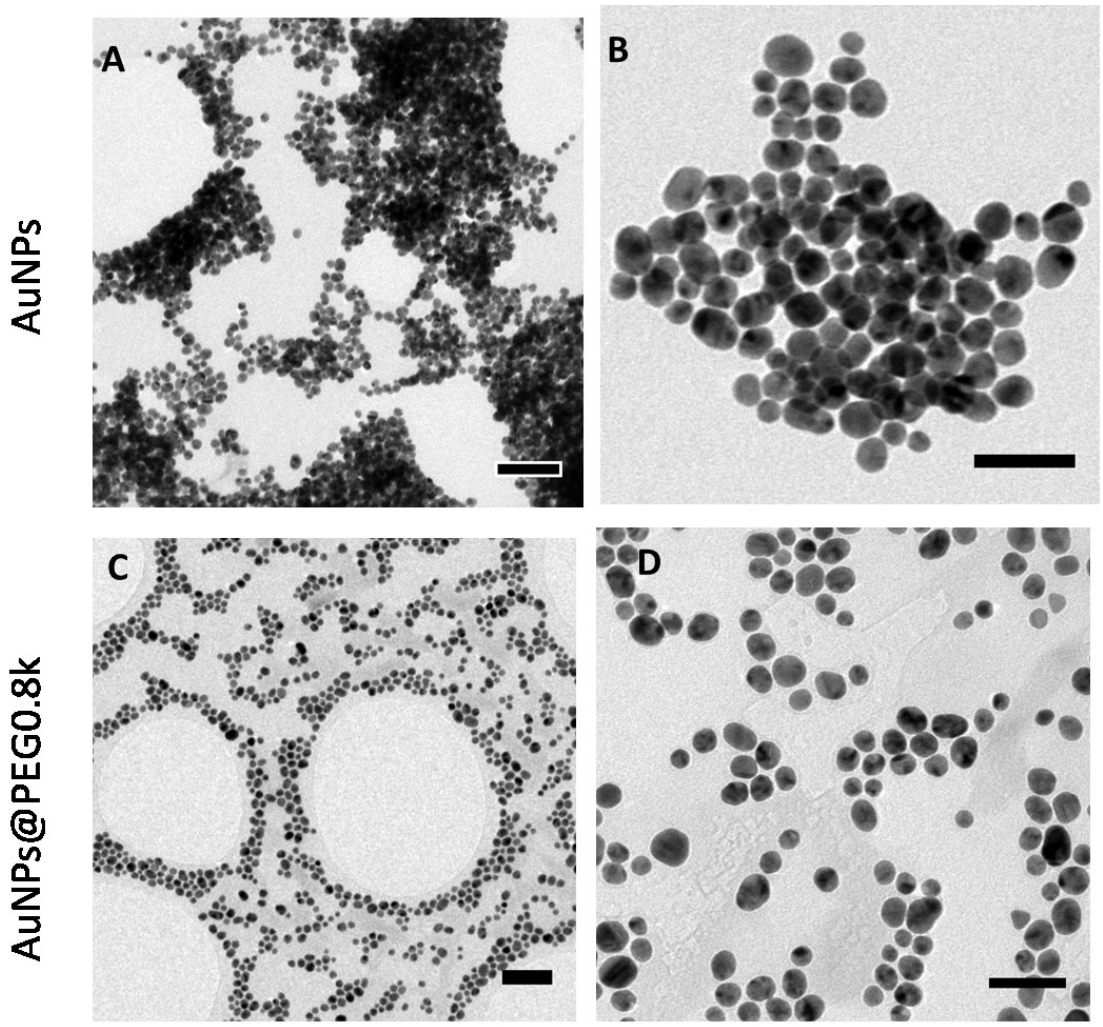
In summary, citrate is a very weak protective agent since the AuNPs easily agglomerate under different conditions so further stabilisation is required. The next sections investigate the impact of the PEGylation on the colloidal stability.

3.2.2 AuNPs@PEG synthesis and characterisation

AuNPs@PEG were obtained by surface functionalisation of the citrate coated AuNPs with thiolated PEG thanks to the attachment via the strong Au-S bond. The citrate coated AuNPs were simply mixed with the PEG solutions for 2 h and then further purified via two centrifugation steps at 15,000 g.

The impact of PEGylation was immediately visible after purification since the colour of the solution was not altered, indicating that the redispersion was successful. The successful PEGylation was confirmed via FTIR (Appendix A Figure A-2).

Figure 3-5(A-D) shows TEM images of the citrate coated AuNPs (A-B) and AuNPs@PEG0.8k (AuNPs functionalisation with PEG Mw 0.8k) (C-D). The PEGylation clearly enhanced the stability of the colloidal solution. The PEGylated AuNPs were more dispersed because the protective PEG layer prevented the AuNPs from entering into close contact and agglomerating.



E

Parameter	Value
D_H (nm)	38.3 ±0.8
PDI	0.284 ±0.008
ξ (mV)	-28.14 ±-0.98

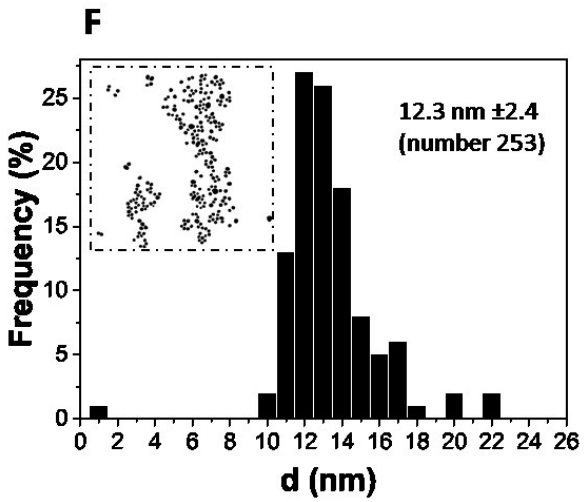


Figure 3-5 Effect of the PEGylation on the dispersion via TEM. (A) TEM images of AuNPs at low magnification (scale bar 100 nm) and (B) high magnification (scale bar 50 nm). (C) TEM image of AuNPs@PEG0.8k at low magnification (scale bar 100 nm) and (D) high magnification (scale bar 50 nm). (E) DLS results (values are given as mean ± standard deviation of triplicate measurements). (F) Particle size distribution (PSD) obtained with ImageJ for AuNPs@PEG0.8k. Mask image as inset.

As expected, the hydrodynamic diameter increased from 23.8 ± 0.9 nm to 38.3 ± 0.8 nm since the PEG layer (Mw 0.8k) was considerably thicker than the citrate layer (Mw 142 g mol^{-1}) (Figure 3-5(E)). But the mean diameter size obtained via TEM image analysis remained similar than citrate coated AuNPs (11.4 nm vs. 12.3 nm) since the polymer layer was hardly visible under electron microscopy due to its very low electronic density (Figure 3-5(F)). The PDI of AuNPs@PEG0.8k was slightly higher than that of the citrate coated AuNPs (0.3 vs. 0.2) and could be explained by an inhomogeneous coating resulting in some degree of agglomeration during centrifugation. The zeta potential also increased (-33.35 mV vs. -28.14 mV) confirming the successful displacement of the negatively charged citrate with the neutral polymer and the steric shielding provided by the PEG layer. Here, the increase of the zeta potential does not translate into less stabilised colloids since the steric forces, F_s, have to be integrated as a third component in the DLVO theory:

$$F_{tot}(D) = F_a(D) + F_r(D) + F_s(\mathrm{D}) \qquad (3\text{-}2)$$

When the distance between two sterically-stabilised particles decreases, the density of adsorbed chains increases thus the osmotic pressure increases which counteracts the agglomeration.[233] The steric forces include osmotic and elastic-steric interactions and are mainly governed by the polymer characteristics (e.g. molecular weight, grafting density, polymer solubility) rather than the diameter of the NP which, contrariwise, affects deeply the Van der Waals and EDL forces. [191]

3.2.3 Influence of the PEG concentration on the colloidal stability in different media

To optimise the polymer coating, the minimum amount of polymer required to resist the centrifugation and to provide a satisfactory level of colloidal stability in different environmental conditions has to be identified. First, the stability of the redispersions over time was investigated since the AuNPs solutions may need to circulate in the blood vessels for several hours or days before reaching the tumour. Systems that can be stabilised for this length of time without noticeable agglomeration are required. AuNPs were functionalised with various concentrations of PEG with three different chain lengths

and the absorbance was recorded over time during two days after redispersion in H_2O and MES buffer (50 mM, 0.15 M NaCl, pH 5.5). The results are presented in Figure 3-6.

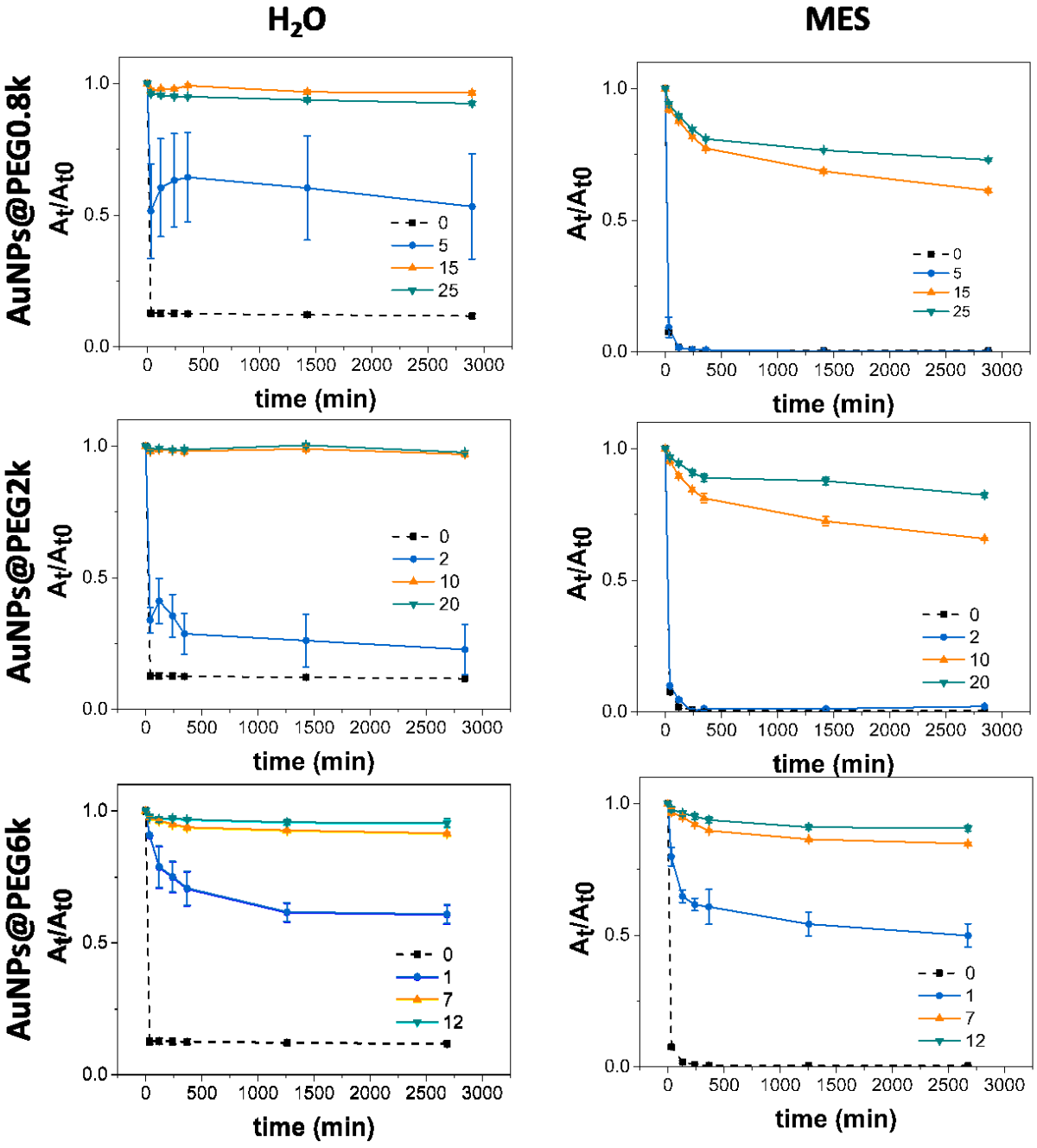


Figure 3-6. Time-dependent colloidal stability of the PEGylated AuNPs at different concentrations of PEG with the three chain lengths Mw 0.8k (first row); 2k (second row) and 6k (third row), redispersed in H_2O (first column) and MES buffer (50 mM, pH5.5) (second column). A_t/A_{t0} corresponds to the ratio between the A_{SPR} at time t and the A_{SPR} at time t_0. Note: the SPR wavelength was fixed for each concentration of PEG. The legend gives the quantity of PEG added expressed as nmol mL^{-1} AuNPs. Error bars represent the standard deviations of triplicate measurements.

It should be noted that out of the polymer concentrations tested, only three are represented corresponding to: (i) a concentration giving a medium-level stability for which the redispersion is not complete; (ii) a concentration above which the stability does not increase further and (iii) an excess concentration. All the graphs show that the citrate coated AuNPs (indicated with 0 nmol mL^{-1} AuNPs[§]) could not be redispersed in either of the media and rapidly agglomerated, since the ratio of absorbances A_t/A_{t0} was close to or equal to 0, whereas a small quantity of polymer as low as 1 nmol mL^{-1} AuNPs for PEG6k (Mw 6000 g mol^{-1}) considerably enhanced the redispersion. The AuNPs redispersed in MES media showed lower absorbance values for the same level of PEGylation due to the acidic and salt environment. It is known that both pH and ionic strength affect the stability of the colloidal system. The surface charge of the NPs is titrable by H^+ or OH^- and the increase in ionic concentration decreases the Debye length which translates into a lower stability for the NPs in solution.[191] At high ionic strengths the Van der Waals attractions dominate the electrostatic repulsions provided by the citrates or the steric shielding by PEG ligands, leading to AuNP agglomeration. [206] It is clear from Figure 3-6 that PEGylation enables the successful redispersion and long-term stability in both media provided that a minimum amount of polymer is employed as previously reported.[207]

To understand what is the minimum amount of PEG to be used for successful redispersion, AuNPs@PEG solutions prepared with increasing amount of PEG were redispersed in MES buffer pH 5.5 (50 mM, 0.15 M NaCl) and the absorbance was recorded after 6 h under stirring. 6 h was chosen as a suitable time length to reach equilibrium considering the results of the stability over time (Figure 3-6). Furthermore, 6 h is in the same order of magnitude of the typical circulation times of AuNPs@PEG in the blood vessels (the blood half-life has been reported to be 4 h for AuNPs@PEG2k and 29.7 h for AuNPs@PEG6k in mice[238]). MES buffer at pH 5.5 (50 mM, 0.15 M NaCl) was chosen as a buffer to test the stability of the AuNPs in environmental conditions they may face during their circulation. pH 5.5 corresponds to the potential lowest pH present on the journey to the tumour from the blood vessel to the intracellular medium.[158] By redispersing the

[§] 0 nmol mL^{-1} AuNPs refers to 0 nmol per mL of AuNPs solution

freshly synthesised PEGylated AuNPs in a buffer containing protons and ions it is possible to assess the requirements for the grafting degree in analogous environments via absorbance measurements. The results are presented in Figure 3-7

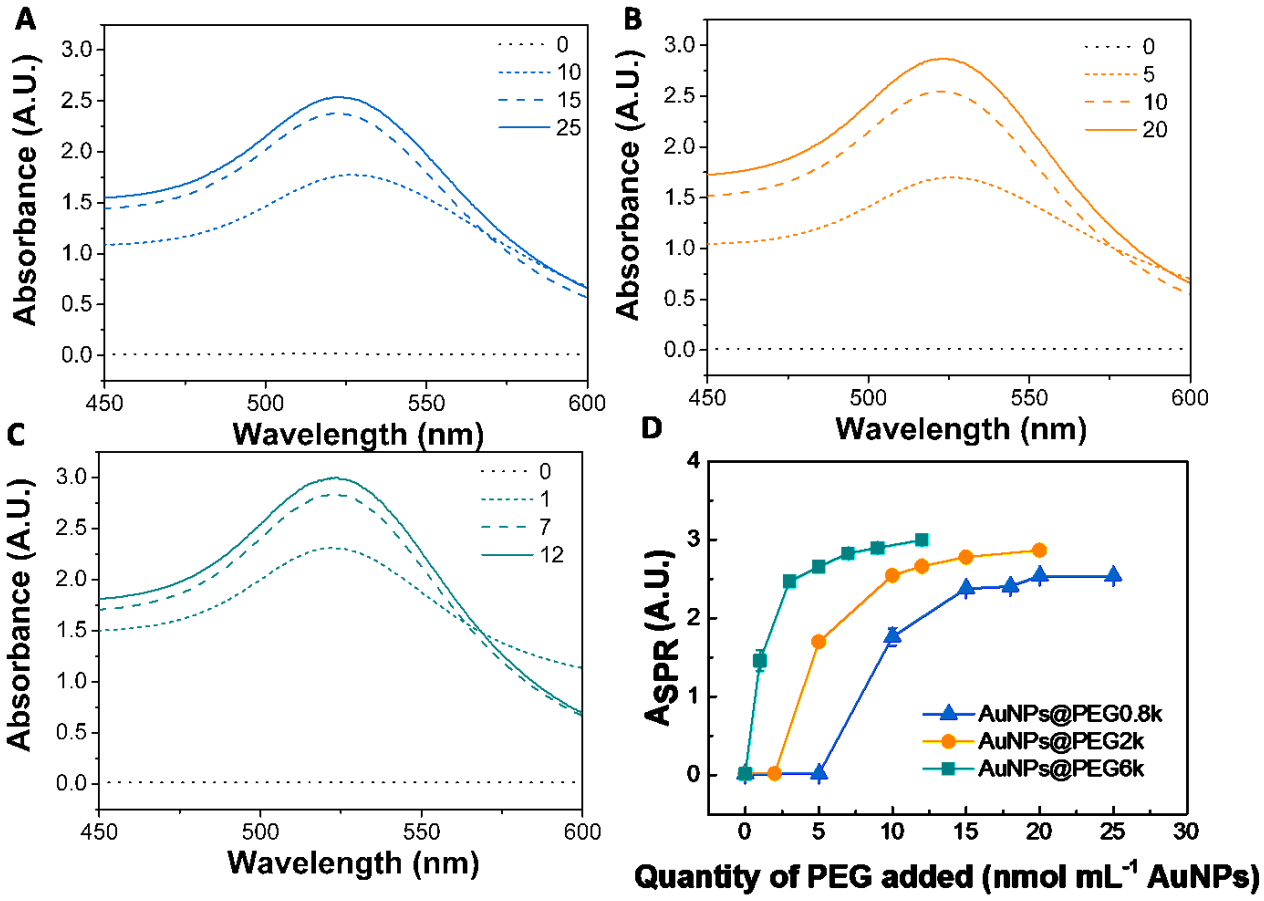


Figure 3-7 Determination of the minimum amount of PEG required for stabilisation of 10 nM AuNPs in 50mM MES buffer pH 5.5 via UV-vis. UV-vis scan of PEGylated AuNPs redispersed in MES buffer: (A) AuNPs@PEG0.8k, (B) AuNPs@PEG2k, (C) AuNPs@PEG6k. (D) A_{SPR} of PEGylated AuNPs redispersed in MES buffer versus quantity of PEG added. The legend gives the quantity of PEG added expressed as nmol mL^{-1} AuNPs. Error bars represent the standard deviations of triplicate measurements. Adapted from Bachelet and Chen[232], copyright 2016, with permission from The Royal Society of Chemistry .

AuNPs@PEG solutions displayed an absorption band around 522-524 nm. The slight red-shift compared to the citrate coated AuNPs (Figure 3-1) indicated a change in the dielectric environment of the AuNPs, thus validating the successful functionalisation that was observed via DLS and TEM (Figure 3-5).

With increasing the PEG concentration, the peak absorbance red-shifted until reaching a plateau, this phenomenon was observed for all the three chain lengths and the minimum amount for stabilisation was evaluated at ~15, ~10 and ~7 nmol mL^{-1} AuNPs for AuNPs@PEG0.8k, AuNPs@PEG2k and AuNPs@PEG6k, respectively. Interestingly, the number of chains needed for stabilisation decreased with the PEG chain length. The longer chain length has a higher conformational entropy and steric shielding ability and thus, the quantity needed for full coverage is lower.[46]. Furthermore, a longer chain also seems to lead to higher colloidal stability as evidenced by the higher absorbance values however changes in the environment for different chain length can also influence the level of absorbance and should be acknowledged. This experiment was also performed in H_2O instead of MES buffer and the minimum amount for stabilisation obtained in H_2O was expectedly found to be lower than in MES buffer since, in H_2O, the surface charges of the citrates are not neutralised and still enable relatively strong electrostatic repulsion forces. A lower steric shielding is then required (Appendix A Figure A-3).

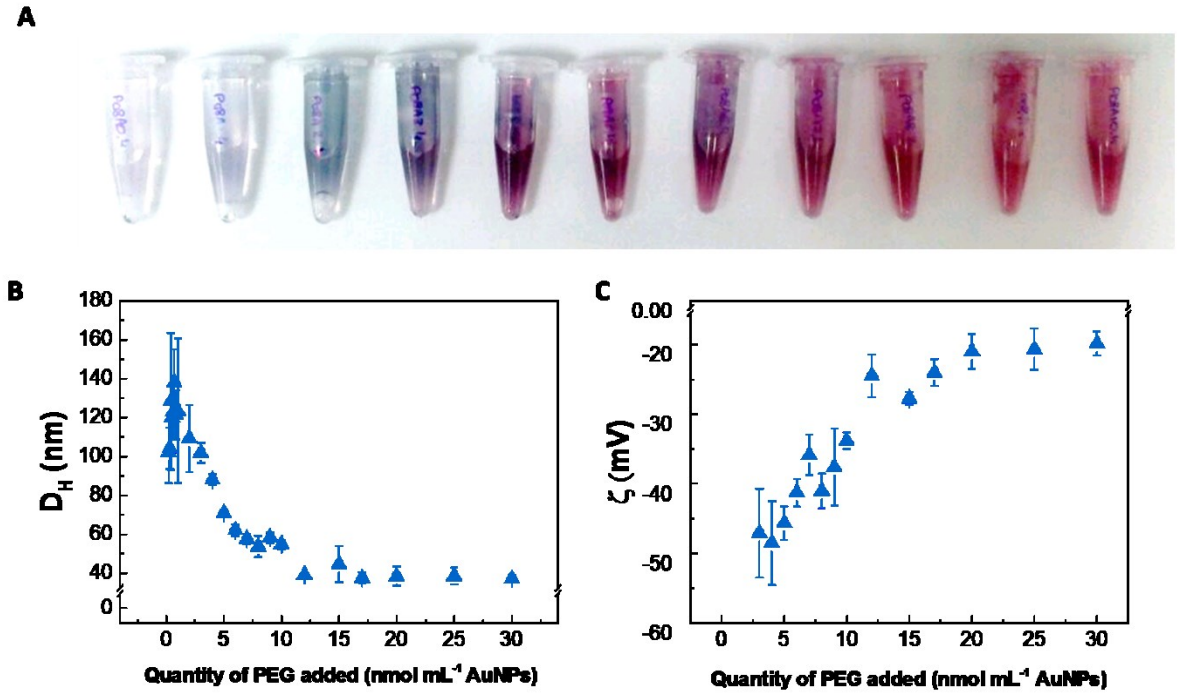
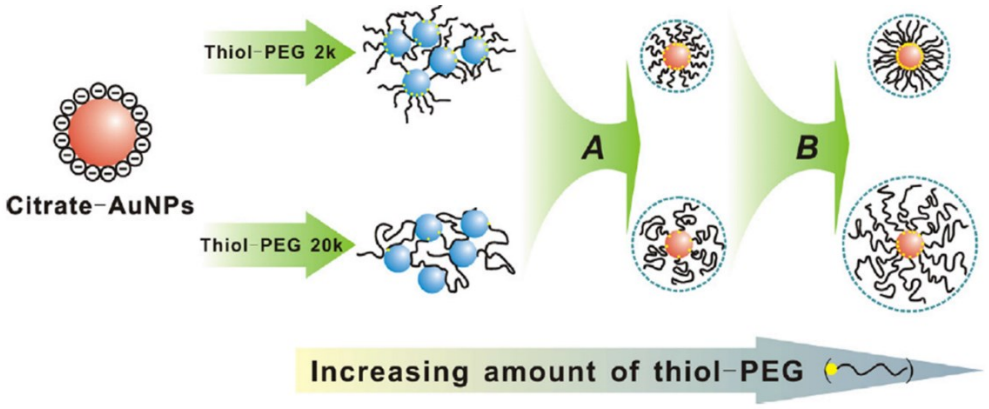


Figure 3-8 (A) Picture of AuNPs@PEG0.8k from 0 to 10 nmol mL^{-1} AuNPs after redispersion in H_2O. (B) Hydrodynamic diameters and (C) zeta potential values with increasing PEG concentration for AuNPs@PEG0.8k measured via DLS. Error bars represent the standard deviations of triplicate measurements.

Figure 3-8 shows the evolution of hydrodynamic sizes and zeta potentials at increasing PEG concentrations for AuNPs@PEG0.8k and the corresponding pictures of the AuNPs solutions. As expected the size of the AuNPs@PEG decreased from ~140 to ~40 nm with increasing the polymer concentration due to the enhanced steric stabilisation and the zeta potential value increased from ~-50 to ~-20 mV via charge screening while the colour of the colloidal solutions changed from transparent, when the AuNPs were completely agglomerated and settled by gravity at the bottom of the Eppendorf tube, to blue and red. Both D_H and ξ values reached a plateau from around 10 and 20 nmol PEG0.8k mL^{-1} AuNPs respectively. The stabilised D_H value was obtained at a PEG concentration close to the minimum amount of polymer for stabilisation determined via absorbance measurement in H_2O (Appendix A Figure A-3) whereas the zeta potential stabilisation was obtained for a higher value. It was concluded that the saturation of the surface via complete charge neutralisation was not necessary to reach the stabilisation via steric shielding since PEG interchain interactions favour an extended conformation hence provide a strong steric shielding. This hypothesis might explain why the AuNPs size did not increase further even though the grafting density increased. This hypothesis will be validated further below.

Interestingly, at very low levels of PEGylation (below 1 nmol mL^{-1} AuNPs), a peak of agglomeration could be observed with increasing D_H, from 102 nm at 0.2 nmol mL^{-1} AuNPs to 138 nm at 0.7 nmol mL^{-1} AuNPs, followed by a continuous decrease until stabilisation. This phenomenon was also observed by Wang *et al.*[208] who reported the existence of a maximum coagulation concentration (MCC) and a crucial stability concentration (CSC) (Scheme 3-1).



Scheme 3-1 Model of the thiol-PEG modification process of AuNPs. Reproduced Wang *et al.*[208], copyright 2013, with permission from Elsevier.

Below the MCC, the thiolated PEG were reported to enhance the agglomeration of the AuNPs, whereas after the MCC the dispersion of the AuNPs slowly increased with increasing PEG concentration until the CSC. Indeed, below 10 nmol PEG0.8k mL^{-1} AuNPs a slight agglomeration of particles was observed, with D_H ranging between 40 and 140 nm, however the zeta potential was inferior to -40 mV, so the agglomeration was unlikely to be caused by the charge shielding of the PEG. Wang *et al.*[208] suggested that at a low grafting density, the PEG chains could interact with neighbouring particles via weak adsorption between the C-O-C group and the AuNP surface, thus creating small agglomerates. When the grafting density of PEG increased, the weak interaction was then outweighed by the strong covalent bond between Au and S, thus the agglomerates disappeared to form individual nanoparticles. At the CSC, only well dispersed AuNPs@PEG were present and D_H was at its minimum value. Wang *et al.*[208] also noticed that the hydrodynamic diameter increased again above the CSC due to the polymer chain stretching at higher grafting densities, however this was not observed in Figure 3-8(B). This observation might be explained by the short chain length of the PEG (Mw 0.8k). Since shorter chain lengths have lower flexibility and shorter length variation ranges, the size increase might not be noticeable via DLS measurement. Indeed, the size increase was observed for PEG6k (data not shown).

3.2.4 Grafting density

To further confirm the hypothesis that a lower grafting density of PEG with a higher molecular weight is needed for stabilisation, the grafting density was calculated using the Ellman's assay. After functionalisation with increasing amounts of PEG, the supernatants of the AuNPs@PEG solutions were collected and mixed with DTNB (Ellman's Reagent) (5,5-dithio-bis-(2-nitrobenzoic acid) which reacts with the thiol group to form TNB^{2-}, a compound that strongly absorbs at 412 nm. The absorbance of the supernatants was then compared to a calibration curve (Appendix A Figure A-4) to quantify the quantity of PEG-SH adsorbed on the AuNP surface and then obtain the grafting density, σ_{Ellman}, in chain nm^{-2}. The details of the calculations are given in Chapter 2 Materials and Methods section 2.3.1.6 and the results are given in Figure 3-9 and Appendix A (Table A-1, Table A-2, Table A-3).

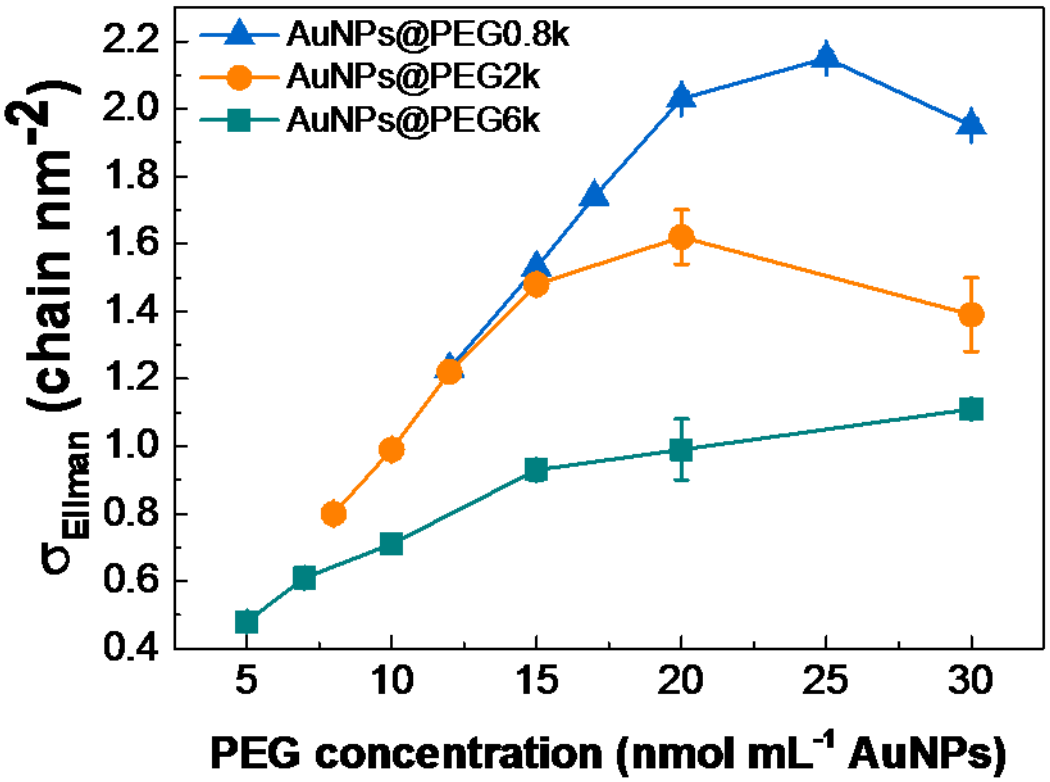


Figure 3-9 Grafting density of the PEGylated AuNPs calculated with the Ellman assay. Error bars represent the standard deviations of triplicate measurements. Adapted from Bachelet and Chen[232], copyright 2016, with permission from The Royal Society of Chemistry.

Between the three chain lengths the grafting density increased as follows: PEG6k < PEG2k < PEG0.8k with the maximum grafting density of 1.11 ± 0.03; 1.62 ± 0.08; 2.15 ± 0.02 chain nm^{-2} respectively.

It is well known that the grafting density is strongly dependent on the AuNP size,[205] shape,[202] ligand chain length,[46] initial ligand concentration,[204] initial capping molecule[202] and synthesis method[202] and can vary depending on the measurement method (e.g. TGA, fluorescence, absorbance, direct or indirect measurement), the equipment resolution and the calculation assumptions.[195] Consequently, it is complex, if not sometimes obsolete, to compare with data from the literature if the relevant parameters are not taken into account. The results for AuNPs@PEG2k, between 500-1000 chains per AuNPs, were in the same order with the data published by Rahme *et al.*[46] who reported 695 chains of PEG2.1k per 15 nm AuNPs and Wang *et al.*[208] who calculated a grafting density of 350 chains of PEG2k per 12 nm AuNPs. The results were obtained via TGA. Furthermore, Liu *et al.*[206] reported between 500 and 1000 chains of Mw 900 PEG were required per 10 nm and 20 nm AuNPs respectively to provide stabilisation in 1 M NaCl. However, Rahme *et al.*[46] reported exceptionally high grafting densities for PEG2.1k of 3.93 chains nm^{-2}, much higher than the range of grafting densities obtained herein (0.80-1.62 chain nm^{-2}). This difference might be explained by the differences in the experimental characterisation methods (TGA vs. Ellman's assay).

The grafting density for the three PEGs increased with increasing the PEG concentration until reaching saturation. This observation consolidates the results obtained with the study of the colloidal stability in MES buffer (Figure 3-7). Shorter chain lengths require a larger amount of polymer for stabilisation but present a higher grafting density thanks to the lower interchain steric hindrance.[46] This observation has to be taken into account when designing a therapeutic platform with ligands since high grafting densities may be desirable for high drug loadings but can impair the cellular uptake for instance.

A decrease in the grafting densities of AuNPs @PEG0.8k and AuNPs@PEG2k can be observed above 25 and 20 nmol PEG mL^{-1} AuNPs respectively. One possible explanation may be the discrepancies of the technique (e.g. absorbance errors, calibration fit). It is

unlikely that the decrease of grafting density with increasing polymer concentration originates from the detachment of grafted PEG chains but this hypothesis would need to be confirmed at higher PEG concentrations before reaching any conclusion. The selected minimum amount of PEG for stabilisation determined via absorbance measurement at pH 5.5 did not necessarily correspond to the amount to reach saturation since the charge shielding provided by the PEG chain was enough to provide a satisfactory level of stabilisation to the system (i.e. complete dispersion) even though some citrates were still present. 7, 10 and 15 nmol mL^{-1} AuNPs for PEG6k, PEG2k and PEG0.8k respectively were employed for all the further experiments presented below since it corresponds to the point where the loading efficiency is the maximum and thus the purification process can be facilitated by limiting the number of unbound chains.

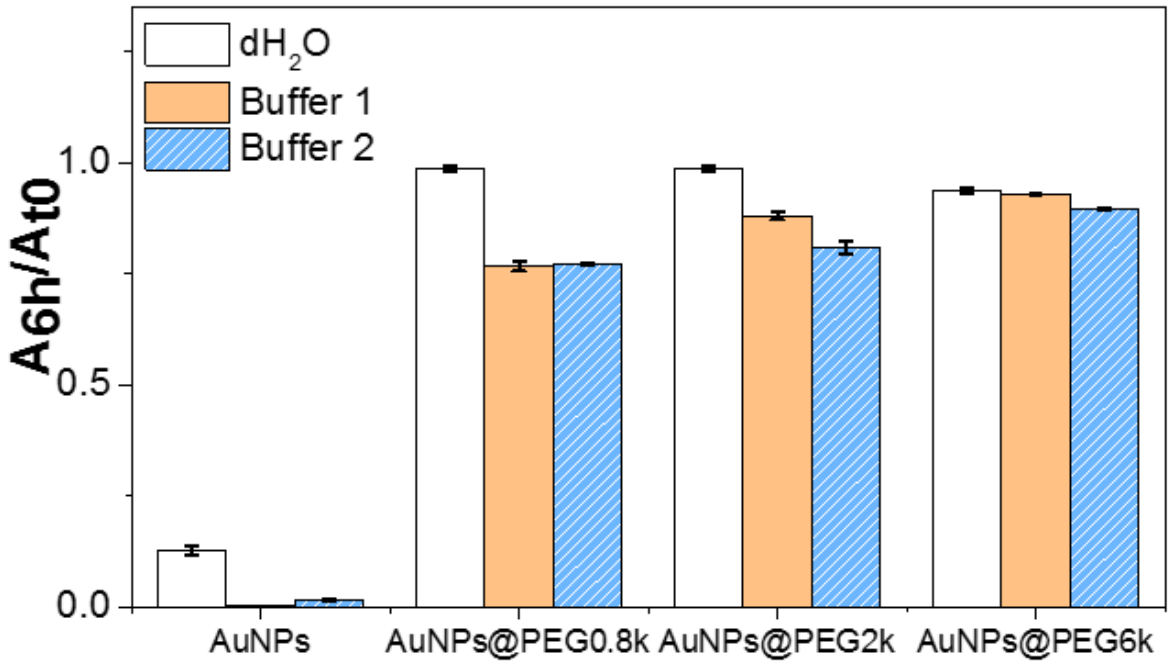


Figure 3-10 Relative absorbance (ratio of the SPR absorbance 6h after, A_{6h}, and before redispersion, A_{t0}) of the AuNPs and the PEGylated AuNPs in different media: H_2O (pH~6); Buffer 1 (50 mM PBS at pH 7.4, 0.15 M NaCl) and Buffer 2 (50 mM MES buffer at pH 5.5, 0.15 M NaCl). Errors bars represent the standard deviation of triplicate measurements. Adapted from Bachelet and Chen[232], copyright 2016, with permission from The Royal Society of Chemistry

Figure 3-10 summarises the results of colloidal stability at the minimum amount for stability for the three PEGylated AuNPs redispersed in H_2O, 50 mM PBS (0.15 M NaCl, pH 7.4) and 50 mM MES (0.15 M NaCl, pH 5.5) buffer. The PEGylation enhanced dramatically the colloidal stability of the AuNPs in the three media. Redispersion in buffers led to slightly lower redispersion efficiency due to the presence of ions and protons as mentioned earlier (section 3.2.3). However, the absorbance of the solutions after 6 h redispersion laid between 77-93% of the original absorbance before centrifugation whereas citrate-coated AuNPs solutions showed complete agglomeration. The longer the chain, the higher is the colloidal stability as previously reported (Figure 3-7). Interestingly the pH did not play an important role on the colloidal stability since the PEGylated AuNPs could be efficiently redispersed in both pH 7.4 and pH 5.5. It was concluded that the agglomeration observed in buffers was mainly due to the types of ions.

3.2.5 Polymer conformation

The sections 3.2.2 to 3.2.4 concerned the optimisation of the colloidal stability of the AuNPs via PEGylation. In this section, the confirmation of the polymer layer was further investigated. The TEM images in Figure 3-11 show the presence of a layer around the AuNPs that most likely corresponds to the PEG molecules. It is easy to understand from these images the role of barrier that plays the PEG layer in order to prevent the agglomeration observed with citrate-coated AuNPs (Figure 3-1(C) and Figure 3-5(A-B)). The observation of polymers under TEM is usually performed with staining agents such as osmium tetroxide or phosphotungstic acid that dope the polymer layer in electrons and make it more visible under the electron beam, however the contrast with the AuNPs is then decreased. With recent TEM microscopes, if the image is clean of artefact and aberrations, it is also possible to distinguish the polymer layer without using stains.

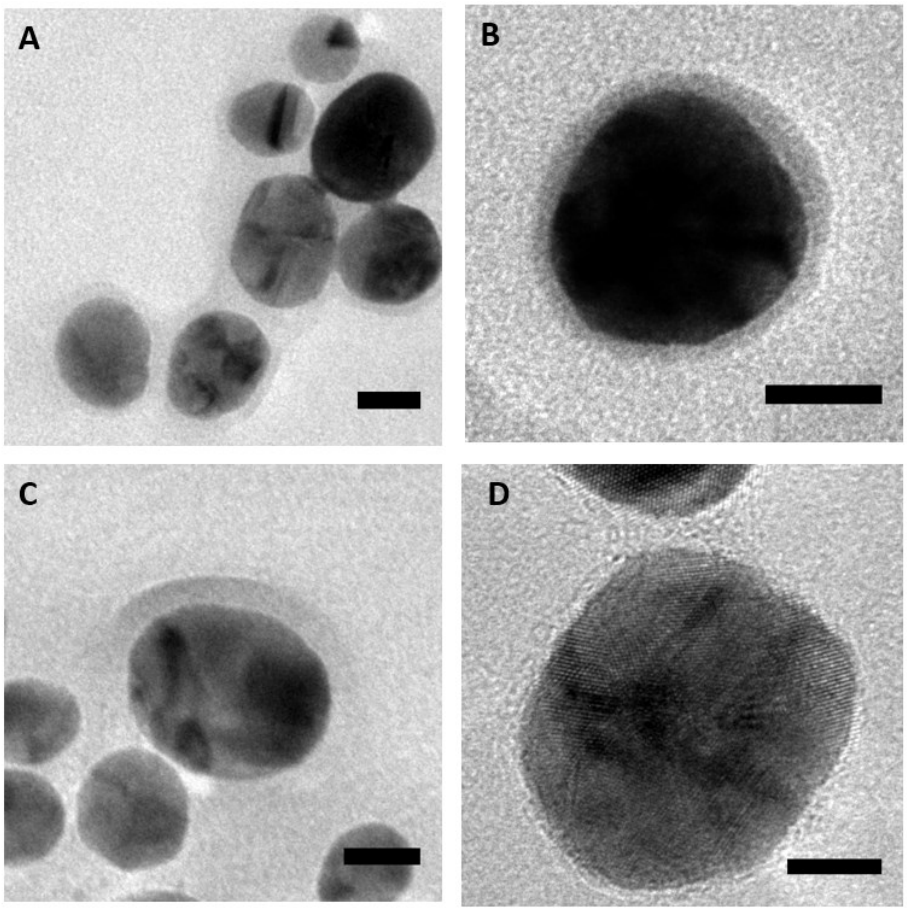
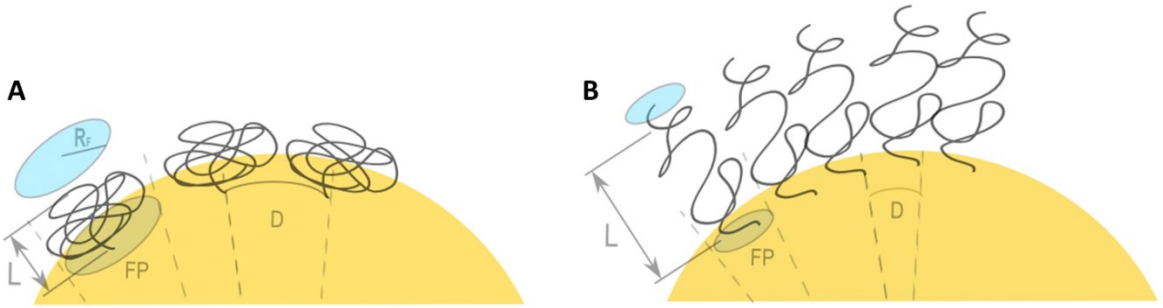


Figure 3-11 TEM images showing the polymer layer of the AuNPs@PEG0.8k (A-B) and AuNPs@PEG6k (C-D), scale bar 10 nm for A-C and 5 nm for D. Figure (A) and (B) are adapted from Bachelet and Chen[232], copyright 2016, with permission from The Royal Society of Chemistry

The layer is a few nm thick, nevertheless this measure does not represent the thickness of the polymer layer in aqueous systems which needs to be calculated via DLS measurements (equation (3-9) and Table 3-1). In solution, the polymer layer grafted on a surface can adopt two main conformations called brush or mushroom as represented in Scheme 3-2. The mushroom regime corresponds to a low level of grafting where each polymer chain is free to rotate without being disturbed by neighbouring chains (Scheme 3-2(A)). The free volume occupied by the polymer chain is characterised by his radius, Flory radius, R_F. In the brush regime, the density of grafting is higher and each chain has to adopt a stretched conformation, the footprint of the chain, *FP*, inverse of the grafting density, is then reduced (Scheme 3-2(B)).[195]



Scheme 3-2 Schematic of the polymer layer conformations on a nanoparticle surface (A) in a mushroom regime and (B) in a brush regime. *D* is the distance between PEG attachments, *L* is the height of the brush domain, R_F is the Flory radius and *FP* is the footprint of the polymer (nm² per chain). Adapted from Bachelet and Chen[232], copyright 2016, with permission from The Royal Society of Chemistry.

To determine whether the polymer chains were in mushroom or brush conformation, the distance *D* between PEG attachments was calculated and compared to the Flory radius. If *D* is superior to twice the Flory radius, the mushroom regime dominates whereas if it is inferior the polymer chains are in the brush regime.

D was calculated as follows assuming the footprint is a circular area in a close packed hexagonal arrangement: [239]

$$D(\mathrm{nm}) = 2\sqrt{\frac{1}{\pi.\sigma_{Ellman}}} \tag{3-3}$$

Where *A* is the monomer size (3.5 Å for PEG).

R_F was calculated as follows:

$$R_F = AN^{\frac{3}{5}} \tag{3-4}$$

Where *N* is the number of monomers in a PEG chain (18 for PEG0.8k, 44 for PEG2k and 133 for PEG6K).[195] The results are presented in Table 3-1.

Table 3-1 Polymer layer characteristics of the PEGylated AuNPs. Adapted from Bachelet and Chen[232], copyright 2016, with permission from The Royal Society of Chemistry.

PEG Mw	R_F	σ_{Ellman}	D	σ_{trans}	D_H
[g mol^{-1}]	[nm]	[chain nm^{-2}]	[nm]	[chain nm^{-2}]	[nm]
0.8k	2.0	1.53±0.00	0.31±0.43	0.079	38.3±0.8
2k	3.4	0.99±0.02	1.09±0.00	0.022	44.1±5.0
6k	6.6	0.61±0.01	1.52±0.01	0.0073	45.2±1.2

The distance between PEG attachments was overall much smaller than twice the Flory Radius for the three PEGs and since *D* was also smaller than the Flory Radius the polymer conformation could be qualified in "dense brush" regime.[195]

Another equivalent method was employed for the determination of the polymeric conformation on the surface. At the boundary between the mushroom and brush conformation the following equations are verified simultaneously:

$$FP = \pi . R_F^2 \quad (Mushroom) \tag{3-5}$$

$$FP = \frac{1}{\sigma} \ (Brush) \tag{3-6}$$

Which gives the following equation:

$$\sigma_{trans} \left(\frac{\text{chain}}{\text{nm}^2}\right) = \frac{1}{\pi . R_F^2} \tag{3-7}$$

Where σ_{trans} is the grafting density at the transition between the two conformations. In Table 3-1, the grafting densities obtained via the Ellman's assay, σ_{Ellman}, are much higher than the grafting densities at the transition between the two conformations, σ_{trans}. As a conclusion, the brush conformation is certainly adopted by the AuNPs@PEG for the three chain lengths.

At the minimum amount for stabilisation the brush regime was already reached. It is then unlikely that a mushroom conformation would be sufficient to bring stabilisation via

charge screening. The brush conformation was favoured by three factors: (i) the solvent, since water is a good solvent for PEG the polymer exhibits an extended conformation; (ii) the low amount of unbound PEG chains and (iii) the single attachment point, the strong Au-S bond.[239,240] It is important to note that the three PEGs have a relatively low Mw and it is possible that higher Mw chains in mushroom conformation would be sufficient for stabilisation.

Both brush and coil conformations have been found in the literature. Rahme *et al.*[46] obtained the brush conformation for thiolated PEG between 2100 and 51000 g mol^{-1} and AuNP diameter sizes between 15 and 170 nm. Chen *et al.*[204] also reported a stretched conformation for PEG5k grafted at 0.4 chain nm^{-2} on ~20 nm AuNPs however Manson *et al.*[207] claimed an extended random coil for ~18 nm AuNPs. Likewise, S. Takae *et al.*[203] reported a slightly stretched random coil conformation for the ~20 nm AuNPs and chains of PEG6k.

The height of the brush thickness in the brush regime can be obtained via:[195]

$$L = A\,N\left(\frac{A}{D}\right)^{\frac{2}{3}} \tag{3-8}$$

The polymer thickness was then deduced from the DLS measurements as follow:

$$L_{DLS} = \frac{D_H - d_{TEM}}{2} \tag{3-9}$$

Where d_{TEM} the diameter obtained from the TEM images analysis.

By comparison between the polymer layer measured via DLS and the theoretical chain length obtained for helical or zigzag conformations, the conformation of the PEG chains was suggested (Table 3-2).

Table 3-2 Theoretical and experimental chains lengths. Adapted from Bachelet and Chen[232], copyright 2016, with permission from The Royal Society of Chemistry.

PEG Mw [g mol^{-1}]	R_F [nm]	$L_{Helical}$[1] [nm]	L_{Zigzag}[2] [nm]	L [nm]	L_{DLS} [nm]
0.8k	2.0	5.0	6.4	3.32±0.00	13.5±2.8
2k	3.4	12.2	15.8	7.21±0.06	16.3±3.9
6k	6.6	37.0	47.6	17.51±0.10	16.9±1.8

[1]Considering 2.78 Å per unit[241]

[2]Considering 3.58 Å per unit[241]

PEG0.8k and PEG2k showed layer thicknesses more than four times the Flory radius thus a random coil conformation was not expected for any of these systems. Their layer thicknesses were also larger than the zigzag conformations thus the hypothesis of the dense brush regime could be confirmed. However, in the case of PEG6k the layer thickness was less than four times the Flory radius, it was suggested that the chains showed a conformation closer to a stretched random coil. Surprisingly, *L*, the thickness calculated from the grafting densities was very different from the chain length obtained via DLS for PEG0.8k and PEG2k. The inaccuracy of the DLS measurements for the lower chain lengths combined with the better stabilisation with longer chain lengths might explain this difference.

3.2.6 Serum protein adsorption

The protein binding was investigated using bovine serum albumin, BSA, as a model protein. AuNPs and AuNPs@PEG were redispersed in PBS containing BSA at different concentrations and the absorbance was recorded over time. Figure 3-12(A-B) shows the colloidal stability after redispersion over time in 50 mM PBS and 50 mM PBS containing a high level of proteins (5 mg mL^{-1} BSA). The presence of BSA quickly increased the absorbance ratio of all the AuNPs, in less than 30 min, however the effect was more intense for citrate coated AuNPs. The second important observation seen in Figure

3-12(C) is that there is no significant change in the ratio of absorbance after redispersion in media containing from 0.1 to 5 mg mL^{-1} BSA.

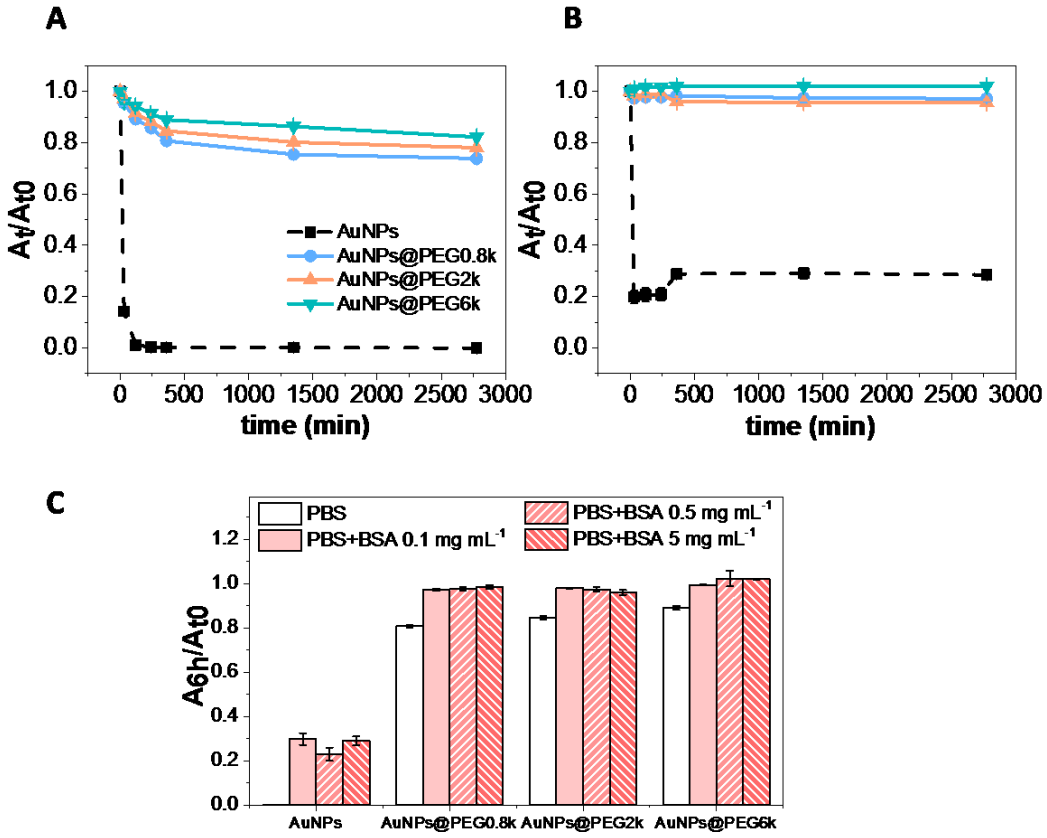


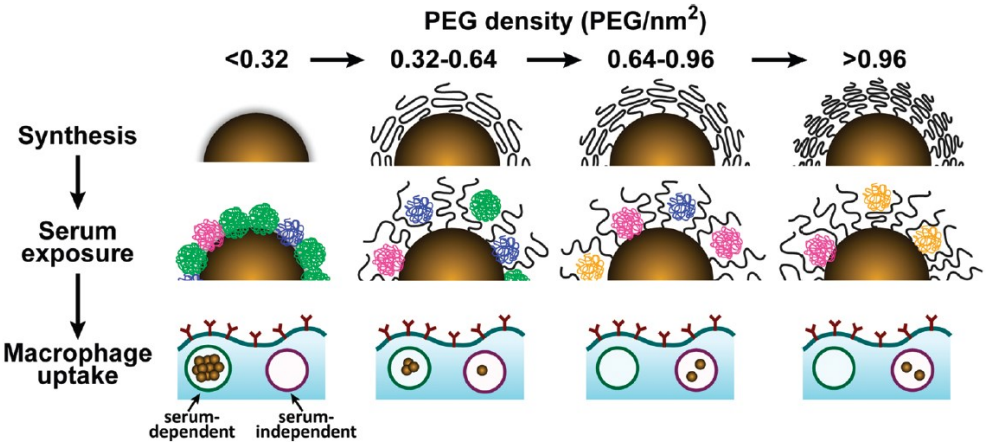
Figure 3-12 Adsorption of BSA protein on the citrate-coated and PEGylated AuNPs: AuNPs@PEG0.8k (15 nmol mL^{-1} AuNPs), AuNPs@PEG2k (10 nmol mL^{-1} AuNPs) and AuNPs@PEG6k (7 nmol mL^{-1} AuNPs). A_t/A_{t0} ratio measured after redispersion (A) in 10 mM PBS pH7.4 (0.15 M NaCl) over time, (B) in PBS with 5 mg mL^{-1} BSA and (C) A_t/A_{t0} ratio 6 h after redispersion in PBS, PBS + BSA (0.1 mg mL^{-1}, 0.5 mg mL^{-1} and 5mg mL^{-1}). Error bars represent the standard deviations of triplicate measurements.

Manson *et al.*[207] performed a similar experiment with 18 nm citrate coated AuNPs and AuNPs functionalised with Mw 5,000 PEG and noticed an increase of relative absorbance after purification, drying and redispersion in 10 mM PBS at pH 7.4 containing 0.05 wt% BSA (0.5 mg mL^{-1}) compared to PBS only. The higher increase was observed for the AuNPs grafted with the lower density of PEG (3.4 µg mL^{-1} corresponding to 0.68 nmol mL^{-1} AuNPs). Siriwardana *et al.*[47] reported a 6 nm red-shift wavelength for the SPR of AuNPs upon BSA binding and an increment of the SPR peak absorbance of 0.43. A net increase

of 0.7, 0.7-0.8, 0.5-0.6, and 0.3 A.U. for citrate, PEG0.8k, PEG2k and PEG6k coated AuNPs respectively for concentrations of BSA ranging from 0.1 to 5 mg mL^{-1} was also observed.

Likewise, the thiolated-PEG, BSA can bind specifically to the AuNPs surface through thiol-Au bonds, however due to the large quantity of thiols per BSA molecule (35), multivalent bonds are formed. It has been reported that BSA proteins exhibit more than 20 anchoring points that can attach to the AuNP surface. Additionally, BSA can bind non-specifically through electrostatic interactions.[47] This explains why, even at very low concentrations of 0.1 mg mL^{-1}, the BSA molecules can easily bind to the AuNPs surface and, by covering the surface charge, lead to the overall stabilisation and increase of absorbance of the colloidal solution. Sabuncu *et al.*[242] claimed that the adsorbed proteins acted like a "spring structure" preventing the contact between AuNPs via steric stabilisation.

The PEG chains grafted on the AuNP surface should act as a dynamic molecular cloud that repels the proteins. Furthermore, the brush conformation of the PEG chains, limiting the degree of gyration of the chains, should behave like a barrier to the protein diffusion so that a significant difference between bare and functionalised AuNPs would be expected in term of protein adsorption[199] (Scheme 3-3). Walkey *et al.*[205] reported that protein adsorption could not be completely eliminated even at a high PEG density, probably since it is difficult to achieve saturation on the AuNPs surface, and that smaller sized AuNPs (~15 nm) showed larger serum protein adsorption due to the high curvature of the surface enabling more free volume to the PEG chains and a weaker barrier to the protein diffusion. This explains why an increase of absorbance relative to the adsorption of proteins can be observed even with PEGylated AuNPs. One possible explanation concerning the similarity between the low and high levels of BSA would be that 0.1 mg mL^{-1} was already superior to the saturation density of the bare AuNPs and PEGylated AuNPs so no significant difference would be observed. To further investigate the ability of PEGylation to repel serum proteins, another series of experiments have been designed for the quantification of the bound proteins with increasing PEG chain length and concentration. Unfortunately, the results of these studies were not conclusive since no significant difference was observed between the PEGylated and the citrate AuNPs thus they will not be presented in the present thesis.



Scheme 3-3 Schematic illustrating the influence of PEG density (Mw 5,000) on serum protein adsorption to gold nanoparticles and their subsequent uptake by macrophages. Reprinted from Walkey *et al.*[205], copyright 2011, with permission from the American Chemical Society.

3.2.7 Cell viability assay

HeLa cells were incubated with AuNPs@PEG2k during 24 h and the cell viability was evaluated by the alamarBlue® assay. Reazurin, the alamarBlue® reagent, is converted within living cells into resofurin. The concentration of resofurin can be measured via fluorescence and is directly correlated to the number of living cells. As seen in Figure 3-13, AuNPs@PEG2k were well tolerated up to 200 nM after 24 h treatment. These results confirmed the very high biocompatibility of the AuNPs (cell viabilities reported in Chapter 4 Figure 4-18(B)) and the PEG polymer as previously reported in the literature.[46,140,200]

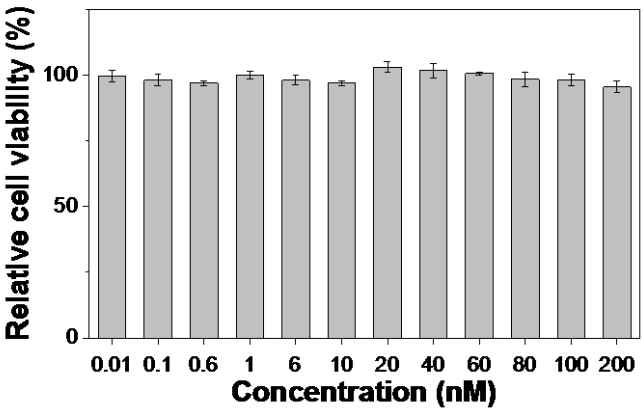


Figure 3-13 Concentration-dependent relative viabilities of HeLa cells treated with A. AuNPs@PEG2k for 24 h as determined by alamarBlue assay. Error bars represent standard deviations of five replicates.

3.2.8 Assembly

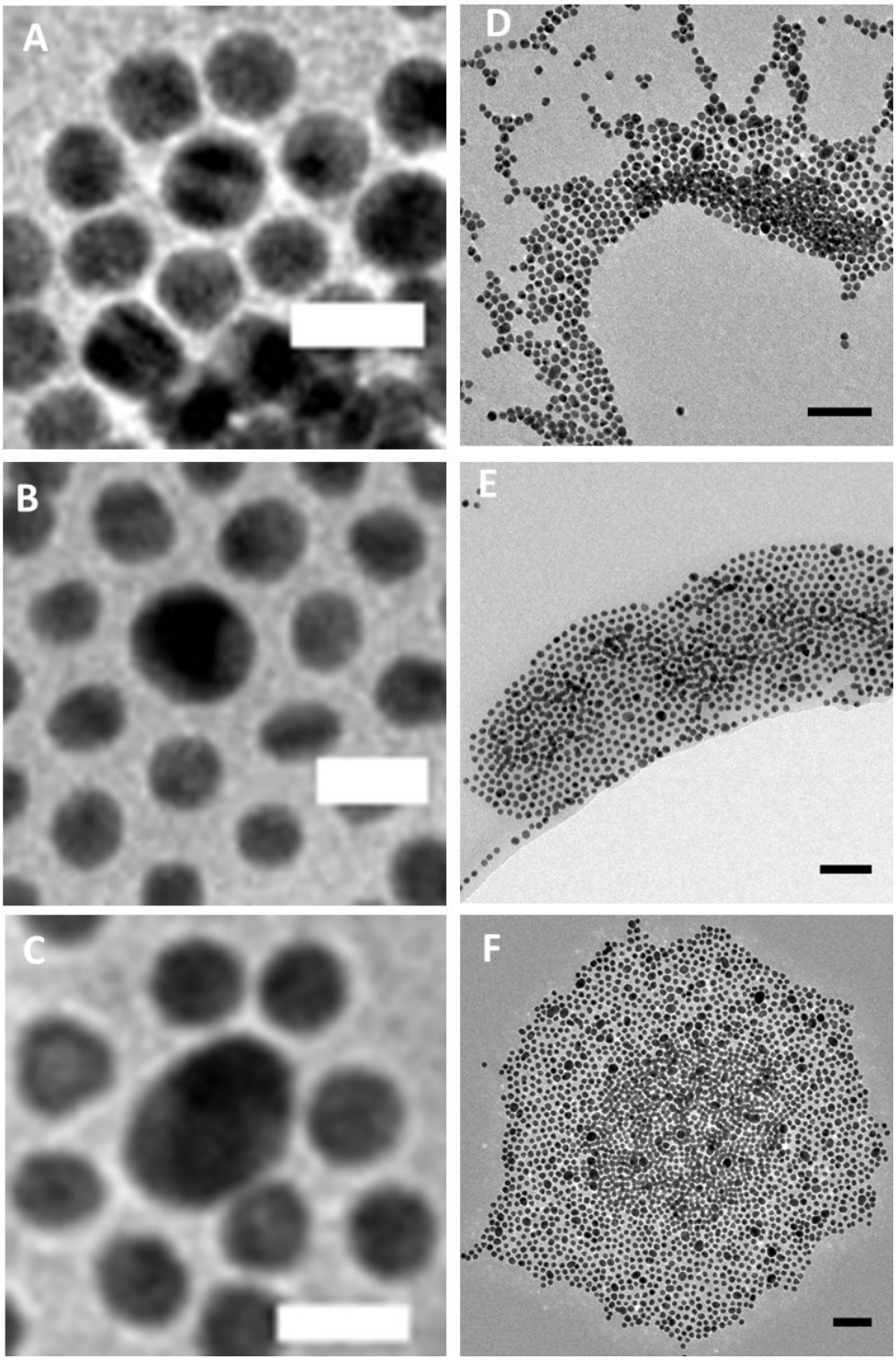


Figure 3-14 TEM images of zoomed in individual satellites structures (A-C) (scale bar: 20 nm) and assembled satellites structures (D-F) scale bar (100 nm) for AuNPs@PEG0.8k (first row), AuNPs@PEG2k (second row) and AuNPs@PEG6k (third row). Adapted from Bachelet and Chen[232], copyright 2016, with permission from The Royal Society of Chemistry.

In section 3.2.5 the polymer layer was characterised at the optimal concentration for colloidal stability. These PEGylated AuNPs were also studied under TEM and after evaporation, self-assembled structures of close packed AuNPs have been reproducibly observed with the three chain lengths (Figure 3-14).

These structures displayed a central AuNP or "core nanoparticle" surrounded by several "layer nanoparticles". They will be named as "satellites" structures from this point. The most commonly reported self-assemblies upon solvent evaporation in the literature concern chains, nanorings or hexagons.[230]

Figure 3-14 shows three examples of self-assemblies for the three chain lengths studied and a zoomed image of a satellite structure for each of them. Additional self-assemblies containing satellites structures at low and high magnification are also presented in Figure 3-15 to demonstrate the reproducibility of the assemblies.

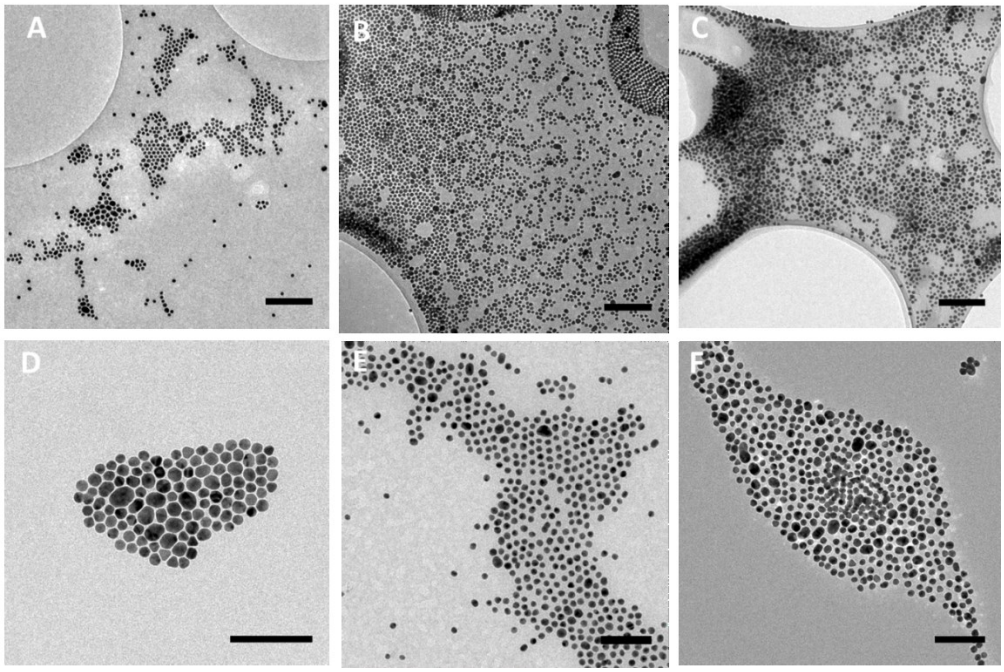
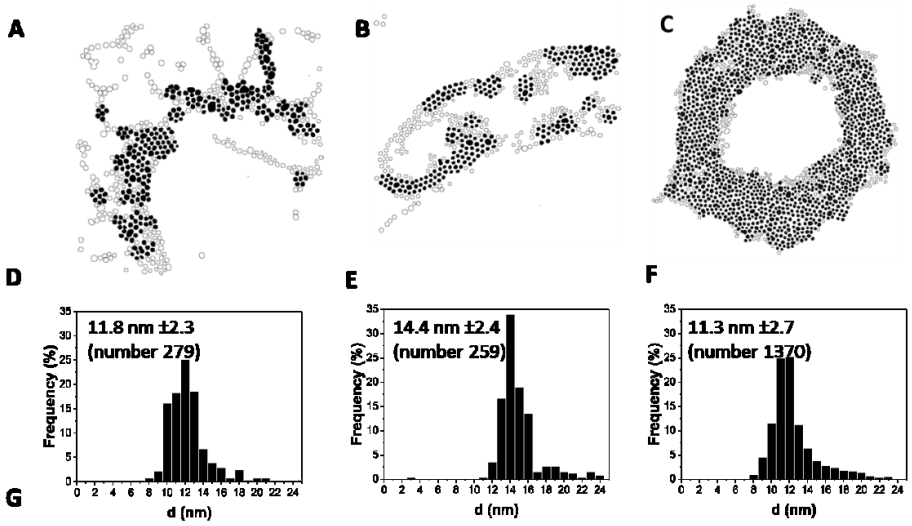


Figure 3-15 TEM images of self-assembled PEGylated AuNPs. (A, D) AuNPs@PEG0.8k, (B, E) AuNPs@PEG2k and (C-F) AuNPs@PEG6k. First row: scale bar 200 nm, second row: scale bar 100 nm.

The self-assemblies were characterised via analysis of the TEM images using ImageJ software. The images of Figure 3-14 were chosen as a representative model since they

contain a large number of particles (> 500) (Appendix A Figure A-5). The relative number of satellite structures and the respective size and number of core and layer nanoparticles were measured. The results are presented in Figure 3-16 and Table 3-3.



PEG Mw [g mol^{-1}]	0.8k	2k	6k
% Satellite Structures	51 (279/552)	54 (259/483)	85 (1370/1616)

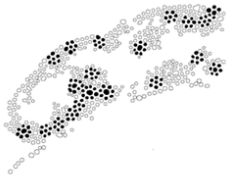
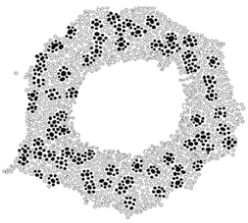
Figure 3-16 Particle size analysis of the satellite structures in the AuNPs@PEG (0.8k first column, 2k second column, 6k third column). ImageJ mask (A-C) and obtained PSD (D-F). G. Table giving the percentage of the number of NPs present in all the satellite structures relative to the total number of NPs present in the self-assembly. Adapted from Bachelet and Chen[232], copyright 2016, with permission from The Royal Society of Chemistry.

%Satellites structures represents the ratio between the number of AuNPs belonging to satellites structures and the total number of AuNPs.

More satellites structures were found for AuNPs@PEG6k (85%) than for the two other chain lengths (54% and 51% for AuNPs@PEG2k and AuNPs@PEG0.8k respectively). This observation was also true for other images from different samples. Nykypanchuk *et al.*[223] reported that DNA functionalised AuNPs would form high-ordered crystalline assemblies with flexible spacers whereas amorphous systems would be obtained with less flexible spacers. Consequently, it was suggested that the assembly was facilitated with longer chains due to their higher flexibility. This observation was in agreement with the discussion regarding the conformation of the PEG layer for PEG6k. Unlike PEG0.8k

and PEG2k, PEG6k did not exhibit a stretched conformation close to a helical or zigzag conformation but was closer to a random coil.

Table 3-3 Typical independent satellite structures in AuNPs@PEG0.8k, AuNPs@PEG2k and AuNPs@PEG6k and their characteristics via TEM image analysis. Adapted from Bachelet and Chen[232], copyright 2016, with permission from The Royal Society of Chemistry .

	PEG Mw [g mol^{-1}]	Core NP size [nm]	Layer NP size [nm]	N_{layer}/N_{core} [1]	d_{layer}/d_{core} [2]
	0.8k	14.9 ± 4.0 nm (N=18)	12.4±1.6nm (N=116)	6.4	0.8±0.4
	2k	15.5±4.2 nm (N=24)	14.9 ±1.9 nm (N=143)	6.0	1.0±0.4
	6k	16.7±2.9 nm (N=67)	9.6±2.1 nm (N=456)	6.8	0.6±0.2

[1]ratio of the number of layer AuNPs and the number of core NPs.
[2]ratio of the diameter of the layer AuNPs and the diameter of the core NPs.

The characteristics of the core and layer nanoparticles were determined for independent satellite structures only. Independent satellite structures do not share any AuNP with any other satellite structures (masks in Table 3-3 and Appendix A Figure A-6). Most core NPs showed larger and sometimes similar diameter than the layer NPs. Satellite structures usually comprise 6 to 8 layer NPs. This is not surprising since 6 is the theoretical highest number of spheres surrounding a sphere of the same diameter. A higher number of layer NPs is then expected when the core NP is larger. Mucic *et al.*[224] obtained satellite structures with a high number of layer NPs by functionalising AuNPs of two diameter sizes (8 nm and 31 nm) with complementary DNA strands. The small AuNPs preferably

assembled to large-sized AuNPs via hybridisation of the complementary strands. Herein, one AuNP size population with a single ligand type was used.

Since no change has been observed on the absorbance spectrum after PEGylation of the AuNPs it is likely that the assembly occurred essentially during the evaporation of water on the TEM grid as previously reported.[218,226,230] Interestingly, similar self-assemblies have been obtained using different substrates and imaging techniques: carbon coated copper grid, silicon wafer, mica sheet with TEM, SEM and AFM imaging techniques, on short and long-range scales (Appendix A Figure A-7).

The longer chain length favoured the self-assembly as previously mentioned. The density of ligands is a second critical factor. Indeed, a specific range of grafting density might be required to enable the formation of the self-assemblies. The PEGylated AuNPs used in this study have been functionalised with the lowest amount of polymer required for their stabilisation after redispersion in buffer containing salts at acidic pH (pH 5.5). As already discussed, using a lower amount of PEG would lead to the non-specific agglomeration of AuNPs and would then prevent the formation of ordered assemblies. Ming *et al.*[226] investigated the self-assembly of cetyltrimethylammonium bromide (CTAB)-coated gold nanorods (AuNRs), and reported the existence of a minimum amount of surfactant, corresponding to the amount needed to form a bilayer, in order to observe ordered assemblies. Below that concentration, the entropic depletion potential dominated the electrostatic repulsions and disordered assemblies were formed. On the other hand, an excess concentration of ligands may hinder the self-assembly. Qi and co-workers found that excess amount of CTAB tended to crystallise out of the colloidal solution under evaporation and restrained the self-assembly.[218] In summary, a specific range of ligand concentration must be ensured to equilibrate the attractive forces (e.g. Van der Waals, capillary forces) and the repulsive forces (e.g. steric hindrance and electrostatic repulsion) so that the self-assembly can occur.

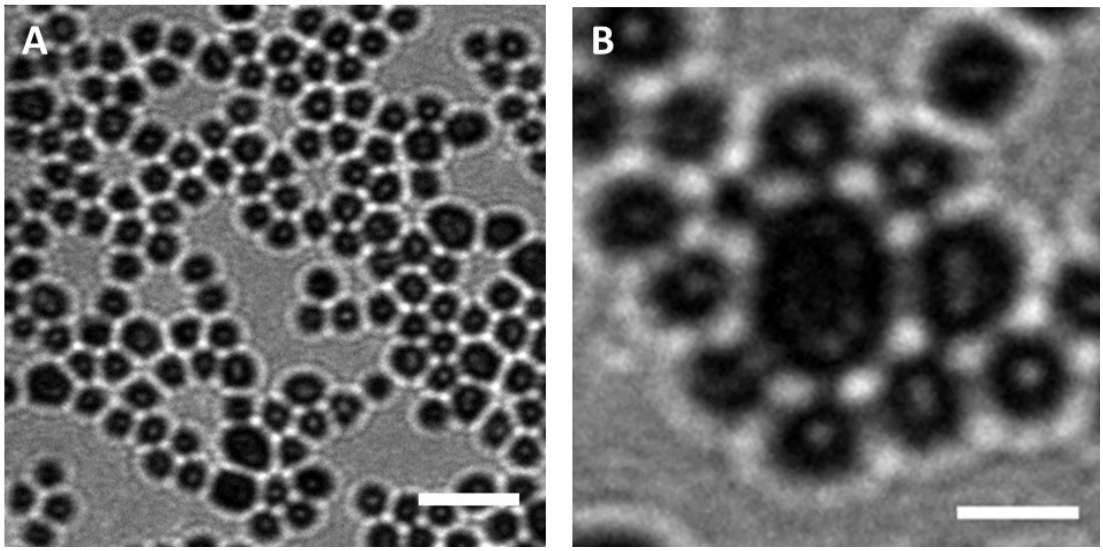


Figure 3-17 TEM images of (A) AuNPs@PEG2k under defocused conditions (scale bar 50 nm) and (B) representative satellite structure in the AuNPs@PEG2k assembly under defocused conditions (scale bar 20 nm). Adapted from Bachelet and Chen[232], copyright 2016, with permission from The Royal Society of Chemistry

The PEG chains can be visualised on the TEM images under defocus conditions (Figure 3-17).[211] The polymer chains were not homogeneously distributed on the AuNPs surface but rather protruded in specific directions to reach the neighbouring AuNPs. As molecular dynamic simulation predicted it, the ligands may associate into molecular bundles on the faces of the AuNPs.[243] This has also been reported by Wang[211] for the alkanethiol chains with truncated octahedral silver NPs and with non-perfectly spherical AuNPs by Stoeva *et al.*[243]

As mentioned in 3.2.5, at the grafting density used, the PEG chains adopted a brush conformation which implies that the driving force for grafting was superior to the lateral chain interactions.[244] However, under the evaporation of water, the polymer layer is likely to be faced with important forces that change its conformation. The interparticle distances within satellite structures were measured and once again compared to theoretical chain lengths for different conformations (Figure 3-4). Not surprisingly the interparticle distances were much smaller than the layer thicknesses measured via DLS but were also smaller than chains in helical conformations for the three PEGs. The distance was in the order of one to two Flory radii.

Table 3-4 Theoretical and experimental chains lengths.

PEG Mw [g mol^{-1}]	R_F [nm]	$L_{Helical}$[1] [nm]	L_{Zigzag}[2] [nm]	L [nm]	L_{TEM}[3] [nm]	L_{DLS} [nm]
0.8k	2.0	5.0	6.4	3.32±0.00	1-3	13.5±2.8
2k	3.4	12.2	15.8	7.21±0.06	6-8	16.3±3.9
6k	6.6	37.0	47.6	17.51±0.10	4-8	16.9±1.8

[1]Considering 2.78 Å per unit[241]

[2]Considering 3.58 Å per unit[241]

[3]Obtained on TEM image

According to Sau and Murphy[230], CTAB ligands grafted on neighbouring AuNPs will interact via counterion sharing when the distance between the central NP is equal to two chain lengths and, if the distance decreases, interdigitation of the chains will occur. Considering the interparticle distances herein, it is likely that the PEG chains will either interpenetrate and/or be forced to lie on the AuNPs surface.

The PEG conformation in water is dictated by the number of hydrogen bonds formed by the water molecules between oxyethylene units, also called "water bridges".[245] Under evaporation the concentration of AuNPs increases thus the interparticle distance decreases so the interchain interactions increases, furthermore the water bridges break leading to the change in the polymer conformation. This explain how the PEG chains play an active role in the assembly.

Some TEM images show 3D structures with the assembly of two superimposed layers (Figure 3-18) giving a misleading impression of agglomeration which is unlikely thanks to steric interactions. The formation of apparent chain like structures (Figure 3-18(C)) and Moiré patterns (Figure 3-18(D)) are also a sign of 3D assemblies. Moiré patterns are obtained when two repetitive patterns are overlapped with an imperfect alignment.

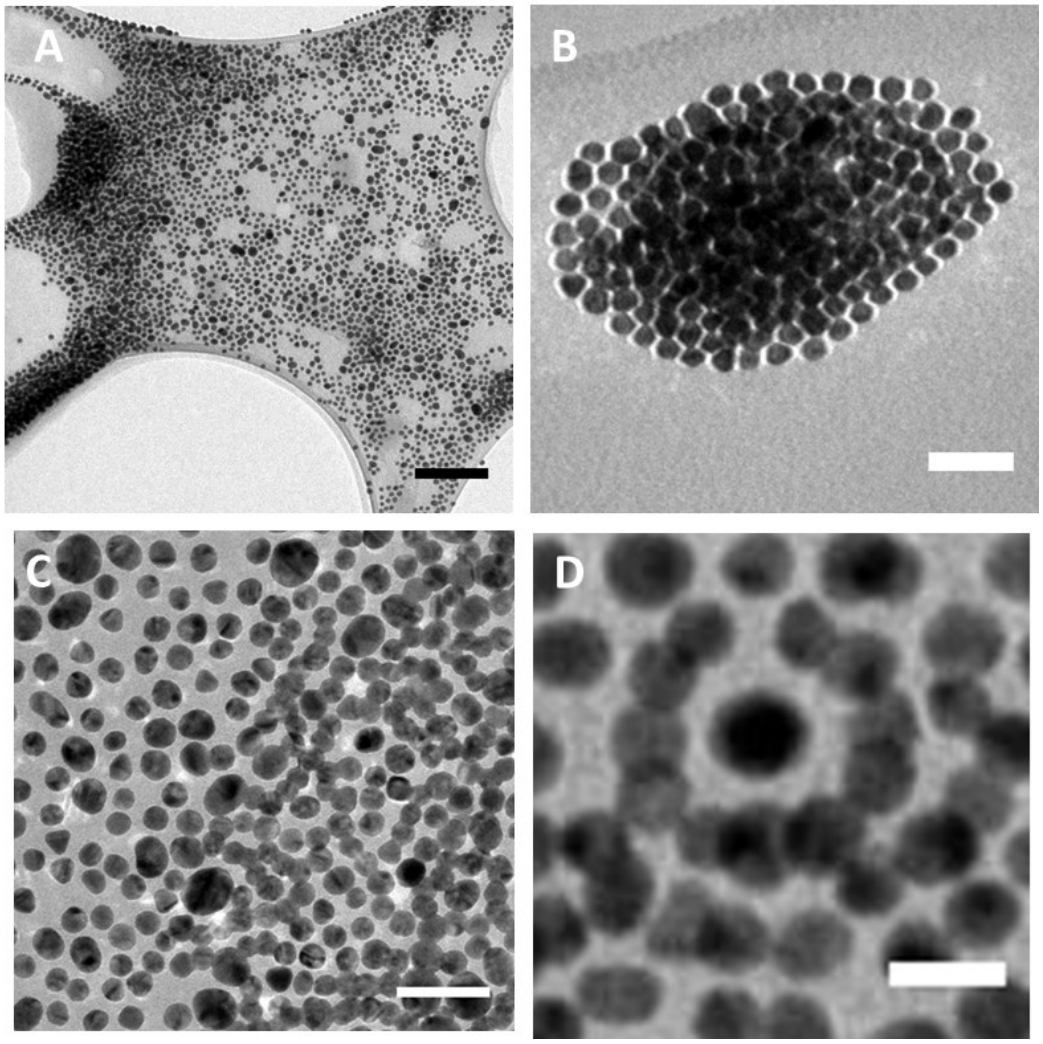
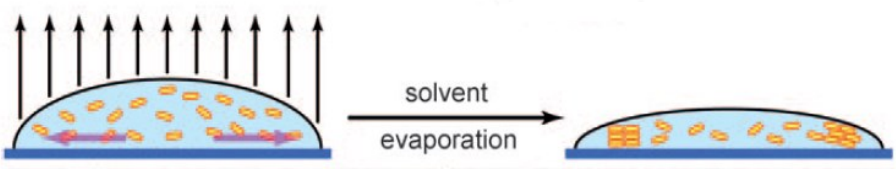


Figure 3-18 Multilayer assemblies. (A) AuNPs@PEG6k at low magnification (scale bar 200 nm). (B) AuNPs@PEG2k high magnification (scale bar 50 nm). (C) Apparent chain-like structures in AuNPs@PEG6k (scale bar 50nm). (D) A Moiré pattern in AuNPs@PEG2k (scale bar 20 nm). Figures (C) and (D) are adapted from Bachelet and Chen[232], copyright 2016, with permission from The Royal Society of Chemistry.

As reported in the literature,[246] when a droplet of colloidal solution is deposited on a flat surface, the evaporation causes the formation of ring patterns due to the pinning force bringing the nanoparticles to the substrate/liquid/air interface (Scheme 3-4). In the present study, the formation of 3D structures was generally observed in the centre of the assemblies and not at the outer edge so the mechanism of assembly might be different from the one causing the formation of coffee rings. The hydrophobicity of the substrate, the interparticle interactions and the inhomogeneity of the particle size may explain the distinctive assemblies reported herein. First, hydrophobic surfaces have been shown to create centred assemblies due to the modified contact angle.[247] Second, it has been

reported that strong interparticle forces could create assemblies far from the contact line. Third, the pinning forces can be counteracted by altering the surface tension. Yunker *et al.*[248] observed this phenomenon with ellipsoids added to a sphere suspension. Similarly, the AuNPs presented herein exhibited a non-spherical shape with a faceted grafting of ligands (Figure 3-17) that might alter the surface tension.



Scheme 3-4 Droplet-evaporation-induced formation of ordered Au nanorod superstructures. Reprinted from from Ming *et al.*[226], copyright 2008, with permission from Wiley-VCH Verlag GmbH & Co. KGaA, Weinheim.

After investigating the main interparticle forces that play a role in the assembly process it was important to understand how the process was initiated. Ohara *et al.*[249] studied the assembly of polydisperse AuNPs functionalised with alkylthiols and drew a parallel with a crystallisation process. They claimed that, even at very low concentration (2%) the larger size NPs were compulsory for the assembly process for which they played the role of seed. They suggested that the assembly was driven by size dependent Van der Waals forces since they obtained a clear size segregation in their TEM images: large size AuNPs were found in the centre of the assemblies. However, herein, large size AuNPs were mainly surrounded by small size AuNPs as previously discussed. To understand whether the assembly was driven by size dependent forces or not, AuNPs of two different sizes (small S ~15 nm and large L ~22 nm) were synthesised and mixed at two different ratio S/L (90/10 and 50/10). The TEM images are presented in Figure 3-19. Even at very high concentration of large size particles, size segregation was not significant. It was concluded that the ligand interactions were the main forces for the assembly process reported herein.

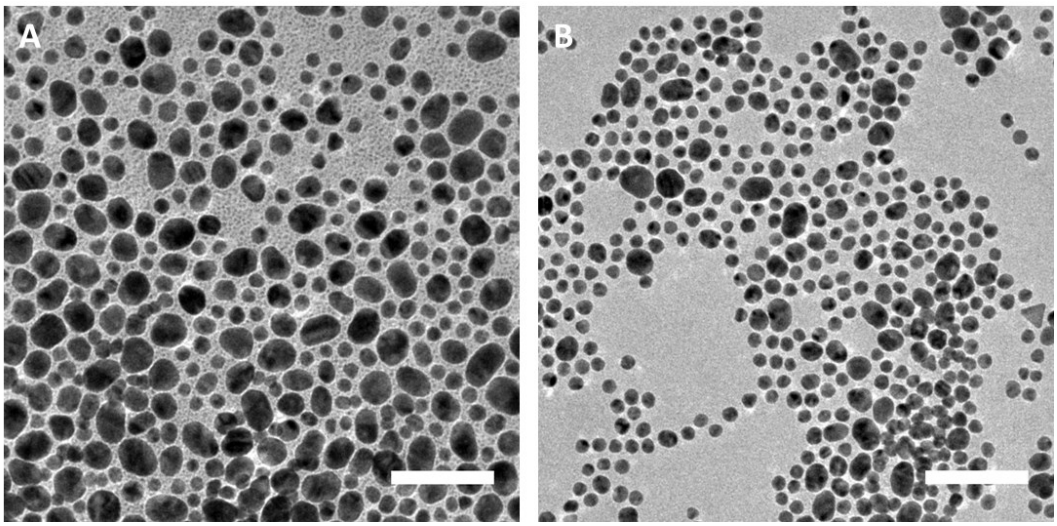
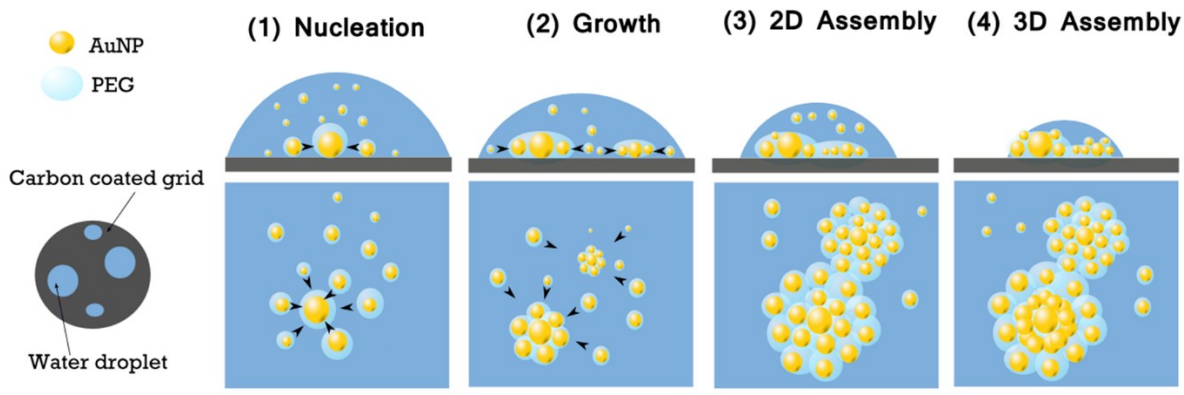


Figure 3-19 TEM images of AUNPs@PEG6k with S/L ratio (small size to large size) of (A) 50/50 and (B) 90/10. Scale bar 100 nm.

The main forces in the assembly process are: the hydrodynamic forces (the pinning force and the capillary forces when AuNPs protrude from the water) and the interparticle forces (electrostatic repulsion between citrate molecules, steric interaction and interdigitation between PEG chains, Van der Waals attraction). It is clear that in the case of the evaporation process of a colloidal solution, the DLVO theory reaches its limit since additional forces have to be taken into account. Furthermore, the heterogeneity of the system (e.g. shapes, size, interparticle interactions) conflict with some assumptions of the theory. [191]



Scheme 3-5 Schematic of the suggested self-assembly mechanism during the slow evaporation process on a carbon-coated grid, first row: side view, second row: top view of the carbon grid. Adapted from Bachelet and Chen[232], copyright 2016, with permission from The Royal Society.

The literature reports assemblies with much longer ranges than the assemblies presented here[212,226,228,250] nevertheless longer range of assembly might be obtained via optimisation of the process and the use of templates for instance.[218] Further work on the control of the 2D and 3D structures would need to be carried out for potential applications in sensing technologies whereas biological applications would require the process to be enabled in aqueous solution or to find a suitable solution to redisperse the assemblies in solution without damaging their structure.

3.3 Chapter summary

In summary, PEGylated AuNPs were successfully prepared with three different chain lengths. The impact of the chain length and concentration on the physico-chemical properties of the AuNPs, in particular the colloidal stability in different media and the hydrodynamic size and zeta potential were investigated. Unlike citrate-coated AuNPs, PEGylated AuNPs could be washed by centrifugation and redispersed in different solvents under mild or acidic conditions with a stability close or higher to the initial colloidal solution. However, a minimum amount of polymer was required for long-term redispersion with high stability. The grafting densities have been calculated via the Ellman's assay and it has been shown that longer chain lengths required lower grafting densities to bring colloidal stability due to a higher steric hindrance and flexibility of the chains. The grafting densities suggested that the three systems exhibited a dense brush conformation, nervertheless, PEG6k chains presented a slightly less stretched conformation than the PEG0.8k and the PEG2k. At the grafting density chosen, the adsorption of BSA proteins was still visible but seemed reduced compared to citrate-coated AuNPs. This was attributed to the unsaturated state of the AuNPs surface. HeLa cells well tolerated the PEGylated AuNPs with no sign of toxicity up to 200 nM.

Assemblies of AuNPs@PEG under solvent evaporation have been reproducibly observed and characterised. Satellites structures, formed by a central core NP surrounded by several layer NPs, have been mostly observed for AuNPs@PEG6k due to the higher flexibility of the chains. PEG polymer seemed to play an important role in the formation of the assemblies. During the evaporation process, PEG had an influence on the main driving forces of the assembly, in particular the balance between the attractive and the repulsive forces thus enabling the formation of ordered arrays. The influences of the chain length, the grafting density, the AuNP size heterogeneity, their faceted structure and the polymer conformation on the mechanism have been discussed. A mechanism similar to a crystallisation process, where the satellites would act as seeds, has been suggested. Further studies are required to provide longer-range assemblies for potential applications in electronics and sensing devices.

Chapter 4 pH-responsive nanohybrids

Chapter 4 describes the synthesis, physico-chemical characterisation and biological evaluation of the AuNPs-PP75 conjugates (AuNPs@PP75). The optimisation of the surface coverage for colloidal stability and pH responsiveness, the pH-reversibility, the mechanism involved in the pH-responsive conformational change, and the *in-vitro* evaluation of the internalisation, endosomal escape and cytotoxicity in human cervical cancer cells, HeLa cells, have been investigated.

Note: Dr. Siyuan Chen provided the calcein-loaded liposomes solution for Figure 4-17. Tom Ellis (PhD student) provided some help for the cell fixing and staining protocol and Dr. Basmah Othman helped me with the ultramicrotomy and the visualisation of the fixed cells sections under TEM for Figure 4-20. The contribution of collaborators is appropriately acknowledged in the captions of the relevant figures.

4.1 Introduction

Gold nanoparticles, as a wide range of nanomaterials, experience a cellular internalisation via endocytosis[157] and the following cytosol delivery of the payload is usually hindered by the lysosomal degradation.[158] Two main strategies have been developed to promote the cytoplasmic delivery: circumvention of the endocytic pathway and the endosomal escape. The first one is relatively recent and concerns the engineering of nanoparticles for direct translocation to the cytoplasm. Rotello and co-workers, as mentioned in Chapter 1 section 1.4.4, designed capsules consisting of an oil core and AuNPs at the surface. The co-delivery of the payload contained in the oil core and the siRNA, self-assembled with the AuNPs, was reported via direct entry thanks to the fusion between the oil core and the lipids of the cellular membrane.[190] While this method seems promising it is still at a very early stage. The successful cytoplasmic delivery has only been demonstrated via confocal images and further assessment of the overall stability is required. Additionally, the large size of the nanocapsules, around 150 nm, may prevent them to take advantage of the EPR effect[54] and the non-specific internalisation may lead to toxicity for healthy cells.

The second strategy for cytoplasm delivery of AuNPs involves the endosomal escape. It can be achieved via pH-responsive mechanisms exploiting the decrease of the endosomal pH including: clusters formation,[189] proton sponge effect,[183,186,187,251] ion pairing,[185] and membrane destabilisation.[184,252] The proton sponge effect, as introduced in Chapter 1 section 1.4.2, is mainly achieved using PEI or other types of cationic polymers. The main drawbacks of free cationic polymers are non-specific serum proteins bindings and toxicity. However, several groups have reported PEI-AuNPs conjugates exhibited good stability in serum-containing media and low toxicity since the free PEI are limited thanks to the purification of the nanoconjugates[182,188] although Lee *et al.*[186] still reported the further functionalisation with PEG to provide serum stability was necessary. Furthermore, an increased efficiency of the gene delivery was reported after grafting on AuNPs compared to free PEI.[187,188]

Cationic lipids can interact with the cellular membrane via ion pairing with the anionic lipids based on electrostatic interactions.[108] Kong *et al.*[185] designed polyelectrolytes from AuNP clusters protected by a lipid shell able to incorporate siRNA molecules. This complex demonstrated higher cellular internalisation than PEI-siRNA complex and this was attributed to the fusogenic lipid component facilitating the cell entry and subsequent endosomal escape. However, Guo *et al.*[251] claimed that the high binding affinity between DNA and PEI may limit the cargo release and thus require higher loading levels. His research group developed an alternative strategy based on charge reversal polymers, polymers able to switch charge depending on pH, deposited in a layer-by-layer fashion on the AuNP surface. Upon acidification, the outer PEI and a hydrolysable compound are released from the AuNPs to enable the gene delivery. The main disadvantage of this system is the non-reversibility which may cause uncontrolled drug release.

Finally, membrane destabilisation can be achieved via the use of relatively toxic but highly efficient viral peptides[252] or peptides and polymers mimicking the pH dependant conformational change exploited by viral vectors. GALA peptides[253] and the anionic poly(propylacrylic acid) (PPAA) are commonly employed to promote membrane destabilisation.[254] Hoffman and co-workers developed diblock polymers with dimethylaminoethyl methacrylate (DMAEMA), propylacrylic acid (PAA) and methacylate (BMA) with comb-like structures for enhanced membrane activity[254] and with cationic segments provided by DMAEMA for DNA complexation ability.[108,255] However, these polymers exhibit complex structures requiring multi-step synthesis.

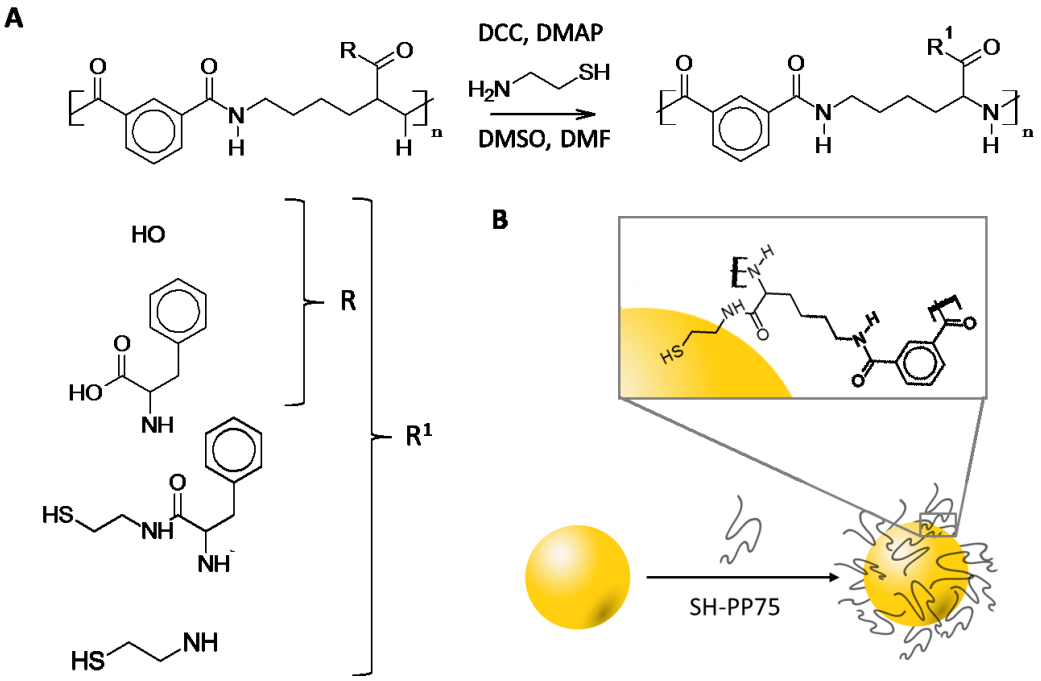
The aim of the study presented in this chapter is to prepare membrane active nanohybrids based on AuNPs via simple functionalisation with pH-responsive endosomolytic anionic PP75 polymer. pH responsive gold nanohybrids have previously been reported for pH-triggered drug delivery,[128,130,132,133,256] imaging,[49] sensing[50] and phototherapeutic[189] purposes mainly but the investigation of the combination of pH-responsiveness and endosomal escape applied in gold colloids is very limited and, to my knowledge, no anionic, membrane-destabilising AuNPs have been reported yet. The nanohybrids were optimised for colloidal stability and the influences of pH on the physicochemical properties and the reversibility of the pH response were investigated

via DLS, spectroscopy and TEM. Based on the findings a mechanism for pH response was suggested. The AuNPs were characterised *in-vitro* via cellular uptake, localisation and toxicity studies.

4.2 Results and Discussion

4.2.1 Physico-chemical characterisation of AuNPs@PP75

PP75 polymer has been successfully prepared and characterised as previously published[175] (Appendix B Figure B-1). The actual degree of grafting of phenylalanine to PLP was calculated to be 62.5% via NMR. To introduce a thiol group for the loading of AuNPs, PP75 was then conjugated with cysteamine at 5 mol% (SH-PP75) using a DCC/DMAP coupling as presented in Chapter 2 Materials and Methods section 2.2.4.1. Scheme 4-1 presents the reaction synthesis of SH-PP75 and the functionalisation of AuNPs.



Scheme 4-1 Schematic of (A) the coupling reaction between PP75 and cysteamine and (B) the functionalisation of the gold nanoparticles with SH-PP75.

The NMR results and FTIR spectra for PP75 and SH-PP75 are presented in Appendix B (Figure B-1, Figure B-2 and Figure B-3). The determination of the degree of grafting of cysteamine on PP75 was challenging due to the low level of conjugation and the differences in molecular weight of the two species. The NMR spectrum of PP75 and SH-PP75 were similar and both had peaks close to 2.75 ppm characteristic for the thiol group

The thiol group usually shows a weak peak between 2550-2600 cm^{-1} on the FTIR due to S-H stretch however no peak was clearly noticeable at these wavelengths on SH-PP75. Furthermore, the FTIR spectra of SH-PP75 with 50% grafting did not show either a distinguishable peak at these wavelengths (data not shown) likely because the characteristic peaks of cysteamine overlapped with the polymer peaks. The determination of the grafting degree was thus not possible.

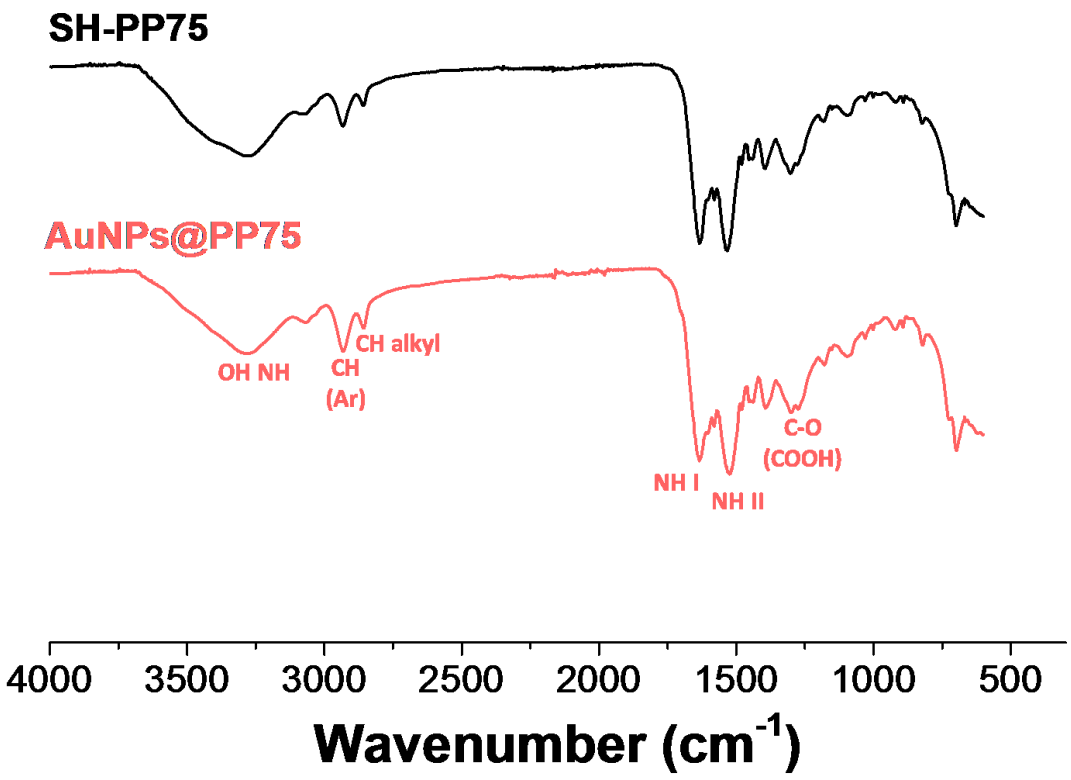


Figure 4-1 FTIR spectra of PP75 conjugated with 5 mol% cysteamine: SH-PP75 (5%) and SH-PP75 conjugated with AuNPs: AuNPs@PP75.

The FTIR spectra of SH-PP75 (5% grafting) and AuNPs@PP75 were similar (Figure 4-1) which indicates the presence of PP75 polymer in the AuNPs sample after purification via centrifugation. Unfortunately the Au-S bond is only visible in the far infrared so was not visible in the spectrum.[257]

The absorption peaks characteristic of PP75 can be found: N-H and O-H stretch (3276 cm^{-1}); aromatic C-H stretch (3061 cm^{-1}); alkyl C-H stretches (2933 cm^{-1} and 2857 cm^{-1}); amid band I and II (1635 cm^{-1} and 1525 cm^{-1}); C-O bond peak at 1299 cm^{-1} indicates the presence of the carboxylic acid.

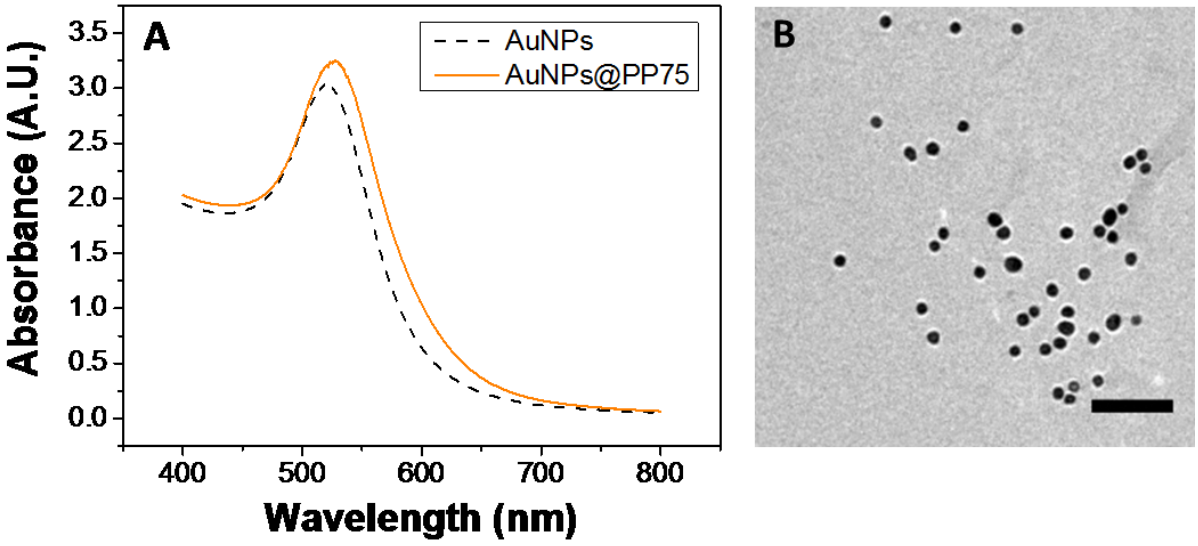


Figure 4-2 Physico chemical characterisation of AuNPs@PP75. (A) UV scans of AuNPs and AuNPs@PP75. (B) TEM image of AuNPs@PP75 (scale bar 100 nm).

The red-shift of the absorbance spectrum of AuNPs@PP75 compared to AuNPs (528 nm vs. 521 nm) (Figure 4-2(A)) and the size increase in DLS (from 23.8 ± 0.9 nm to 25.9 ± 0.4 nm for AuNPs@PP75) confirmed the successful functionalisation.[258] Furthermore, the TEM image showed a nice dispersion of the AuNPs demonstrating their stability (Figure 4-2B). The zeta potential values also showed an increase from -41.7±1.1 to -37.8±2.0 mV, indicative of the negatively charged citrate being replaced by less-negatively charged polymer chains. The successful redispersion in H_2O after centrifugation confirms the

functionalisation brought stability to the system since citrate-coated AuNPs severely agglomerated after centrifugation and redispersion.

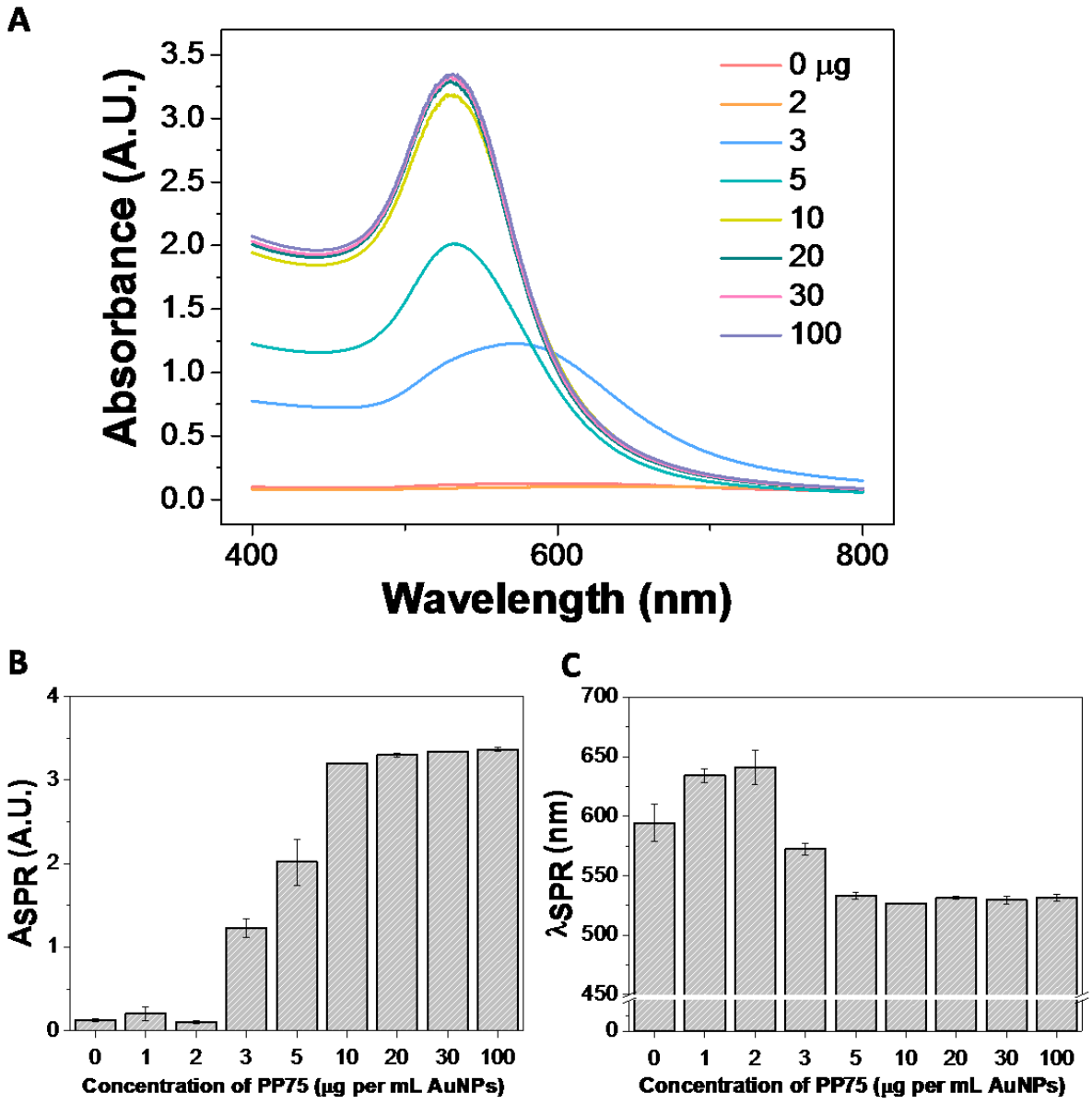


Figure 4-3 Influence of the polymer concentration on the colloidal stability in 100 mM PBS (0.15 M NaCl) pH7.4 measured via UV-vis spectrophotometry one day after redispersion. (A) UV scan of AuNPs@PP75 between 0 and 100 ug PP75 per mL AuNPs, (B) Absorbance at the SPR and (C) wavelength at the SPR with increasing PP75 concentration. Error bars represent standard deviations of triplicate measurements.

In order to optimise the colloidal stability of the nanohybrids in buffers at physiological pH, solutions with increasing amounts of grafted PP75 were redispersed in 100 mM PBS buffer (0.15 M NaCl) at pH 7.4 (Figure 4-3) and the absorbance profile was recorded after

one day. With increasing grafted degree of polymer, the peak of absorbance became narrower with a higher maximum absorbance value. The decrease of the bandwidth is explained by the influence of the AuNP size on the extinction cross section. A lower oscillation mode is obtained when the AuNPs size is decreased as a result of stabilisation.[46]

PP75 polymer was able to provide colloidal stability by grafting to the AuNPs surface and, as observed for PEG in Chapter 3 section 3.2.2 and 3.2.3, a minimum amount was required to provide stability. The minimum amount required was determined to be ~10 µg PP75 per mL AuNPs in 100 mM PBS pH 7.4.

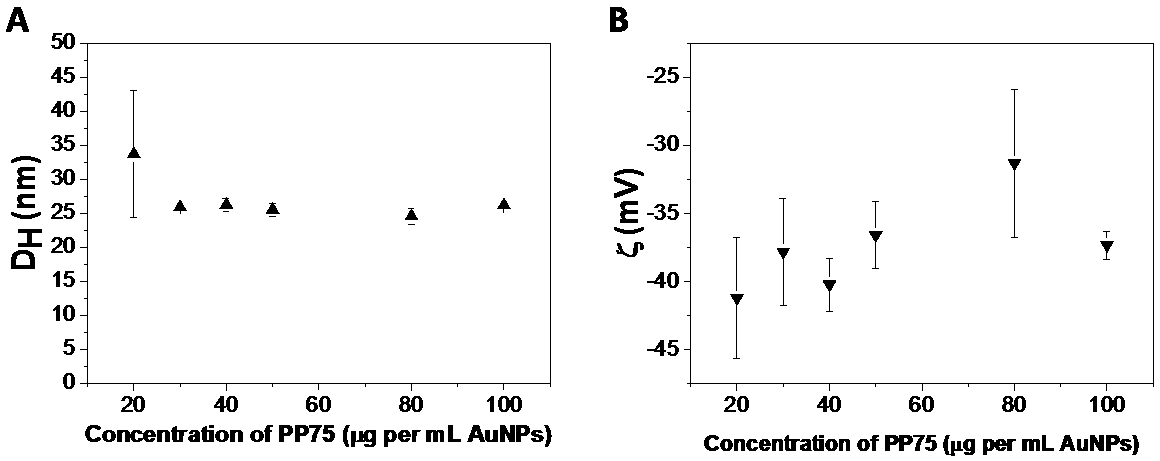


Figure 4-4 Influence of the polymer concentration on the hydrodynamic size (A) and the zeta potential (B) in 100mM PB pH7.4 measured via DLS. Error bars represent standard deviations of triplicate measurements of 6 runs each.

The ability of PP75 to bring colloidal stability was further confirmed via DLS measurements. Figure 4-4 shows stabilisation of the D_H at a value approximately ≤ 25 nm for 30 µg PP75 per mL AuNPs in 100 mM PB pH 7.4. The zeta potential profile was more fluctuating, there was no clear stabilisation plateau and high standard deviations were obtained. The general trend seemed in agreement with what could be expected since the replacement of the citrates molecules leads to the increase of the zeta potential. Nevertheless, the zeta potential measurements could be altered by the grafting density of the polymer and the presence of ions since the position of the slipping plane could be shifted with changes of the grafting density and salt concentration, thus influencing the

zeta potential measurement and making the comparison between different grafting densities delicate.[195] The media also affected the value of the hydrodynamic diameter since the DLS results in H_2O showed a plateau from 50 µg per mL AuNPs at ~30 nm (Appendix B Figure B-4) likely due to the variation of the polymer conformation.

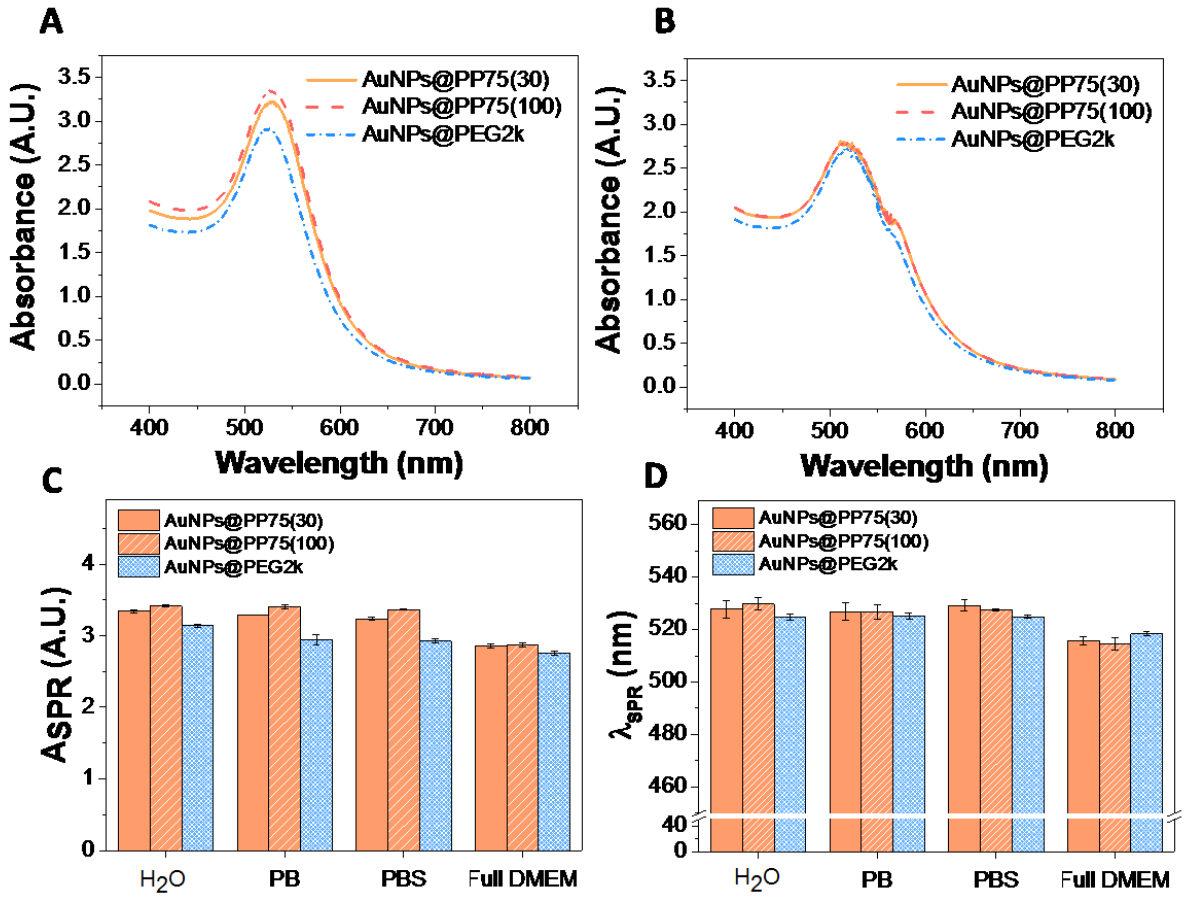


Figure 4-5 Influence of the media on the colloidal stability measured via UV spectrophotometry. UV-scans of AuNPs@PP75(30), AuNPs@PP75(100) and AuNPs@PEG2k redispersed (A) in 100mM PBS pH7.4 (0.15M NaCl) buffer and (B) in DMEM media containing 10% w/w FBS. (C) Absorbance and (D) wavelength values at the SPR for in H_2O, 100mM PB buffer pH7.4, 100mM PBS pH7.4 (0.15M NaCl) buffer and DMEM media containing 10% w/w FBS for AuNPs@PP75(30); AuNPs@PP75(100); AuNPs@PEG2k. Error bars represent standard deviations of triplicate measurements.

AuNPs@PP75(30), AuNPs prepared with 30 µg per mL AuNPs, were chosen as a suitable system for further studies based on its colloidal stability in buffers as explained above. To demonstrate further this choice, the optical properties (Figure 4-5) and the hydrodynamic diameters (Figure 4-6) of AuNPs@PP75(30) and AuNPs@PP75(100)

were compared to AuNPs@PEG2k in 4 different buffers: H_2O, PB, PBS and full DMEM, biological medium containing 10 vol% FBS.

The difference between AuNPs@PP75(30) and AuNPs@PP75(100) was neglectable in all buffers and thus it was concluded that 30 μg per mL AuNPs was sufficient to bring stability to the system, whilst more than three times higher levels of polymer did not further enhance the colloidal stability in any of the buffers of interest.

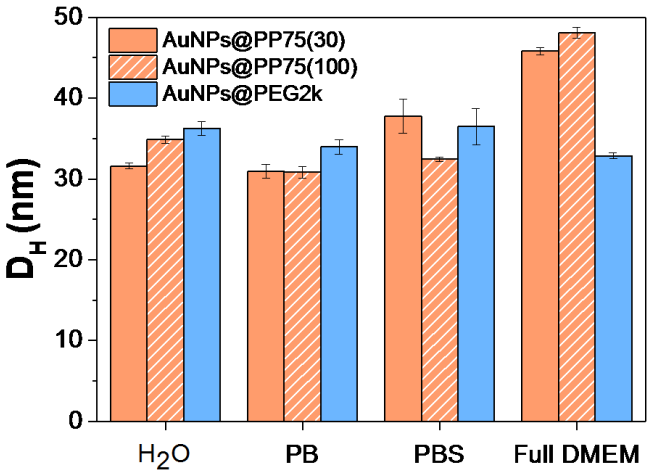


Figure 4-6 Influence of the media on the hydrodynamic diameter. D_H in H_2O, 100mM PB buffer pH7.4, 100mM PBS pH7.4 (0.15M NaCl) buffer and DMEM media containing 10% w/w FBS for AuNPs@PP75(30); AuNPs@PP75(100) and AuNPs@PEG2k. Error bars represent standard deviations of triplicate measurements.

Besides, the hybrid nanoparticles exhibited plasmonic properties and size shifts comparable to the PEGylated system in all buffers except in full DMEM. The D_H was found to increase by ~13-14 nm for the PP75 functionalised nanoparticles but remained stable for the PEGylated AuNPs (Figure 4-6). This is likely because of serum absorption. However, as reported in Chapter 3 section 3.2.6, the serum absorption favoured the stability of the AuNPs@PEG2k and the AuNPs@PP75 since a slight blue shift in the SPR peak was observed even though a red-shift would generally be expected with an increase in AuNP size. The difference of hydrodynamic size observed was a result of the use of volume distribution since large particles would shift the D_H to a higher value but this did not reflect that the whole population had an increasing size. This might explain why the SPR did not shift to higher values. However, an increase in the D_H would be expected if

adsorption of serum proteins occurred. Siriwardana *et al.*[47] reported an increase from 12 to 25 nm for citrate coated AuNPs in the presence of BSA, which was the equivalent of grafting with PEG5k. Sabuncu *et al.*[242] observed a size increase from 18 to 190 nm in DMEM containing fetal calf serum (FCS) for AuNPs capped with a carboxylic acid functionalised hydrocarbon agent (500 Da). It was suggested that the limited number of citrate molecules available for binding due to the PP75 grafting and the steric hindrance of the PP75 chains explained the low serum protein adsorption.

As a summary, AuNPs@PP75(30) exhibited a good colloidal stability in various buffers close to or at physiological pH, in the presence of salts and serum proteins. The next section will investigate the change in behaviour of the NPs in different pHs. From this point AuNPs@PP75 refers to AuNPs@PP75(30) unless stated otherwise.

4.2.2 pH-response

The pH response of the AuNPs@PP75 was easily visible to the naked eye via the colour change of the colloidal solution from red at high pH to blue at low pH. Colloidal solutions of ~10 nM AuNPs@PP75 were redispersed at pH 7.4 and then titrated with 0.1 M HCl. The optical properties were monitored after each addition via absorbance measurements.

As shown in Figure 4-7, the absorbance of a solution of AuNPs@PP75 gradually decreased when pH was reduced from 7.4 until pH 3 and then suddenly dropped at pH below 3 due to the agglomeration and sedimentation of the AuNPs@PP75. A red shift of the SPR peak is also observed at the same pH value, indicative of the size increase. The experiment was repeated in PB buffer (Figure 4-8). The same phenomenon was observed however the pH of transition appeared to be much higher (pH 6).

Both buffers had the same concentrations of H^+ protons initially, however Na^+ cations were also present in PB buffer and might reduce the interaction between COO^- charged groups thus reducing the electrostatic repulsion and leading to the quicker destabilisation of the PP75 chains into a globular shape after addition of HCl and to the agglomeration of the AuNPs.

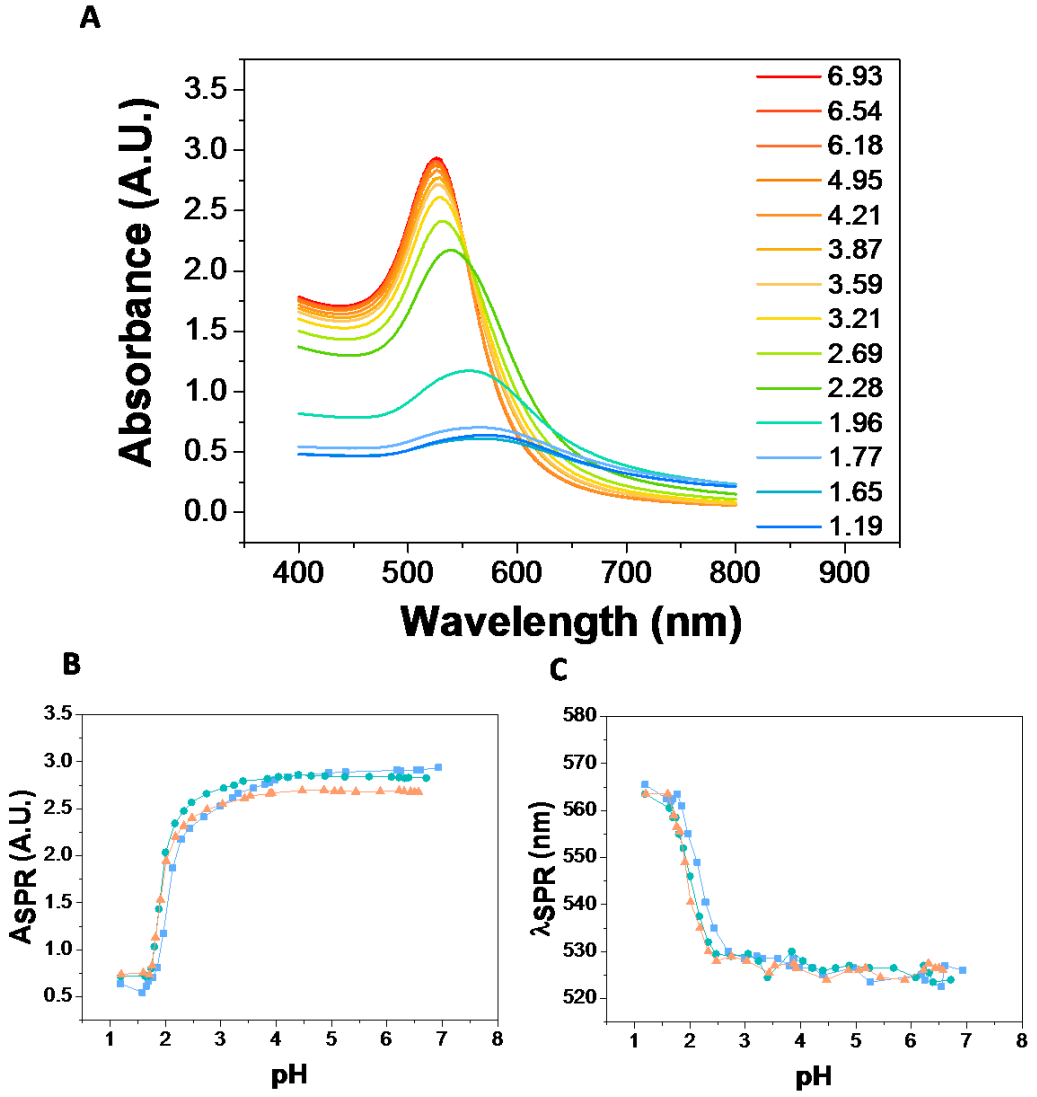


Figure 4-7 pH-response of ~10 nM AuNPs@PP75 redispersed in ultra-pure water adjusted at pH7.4 with 0.1 M NaOH and titrated with µL of 0.1 M HCl: (A) UV-vis spectra, (B) absorbance at the SPR and (C) SPR wavelengths with pH.

Since the present AuNPs are designed for therapeutic purposes it is important to know the effect of pH in the presence of electrolytes naturally present in the blood. Another factor to take into account is that the absorbance measurements were recorded shortly after the addition of HCl and did not reflect the stability of the AuNPs at equilibrium.

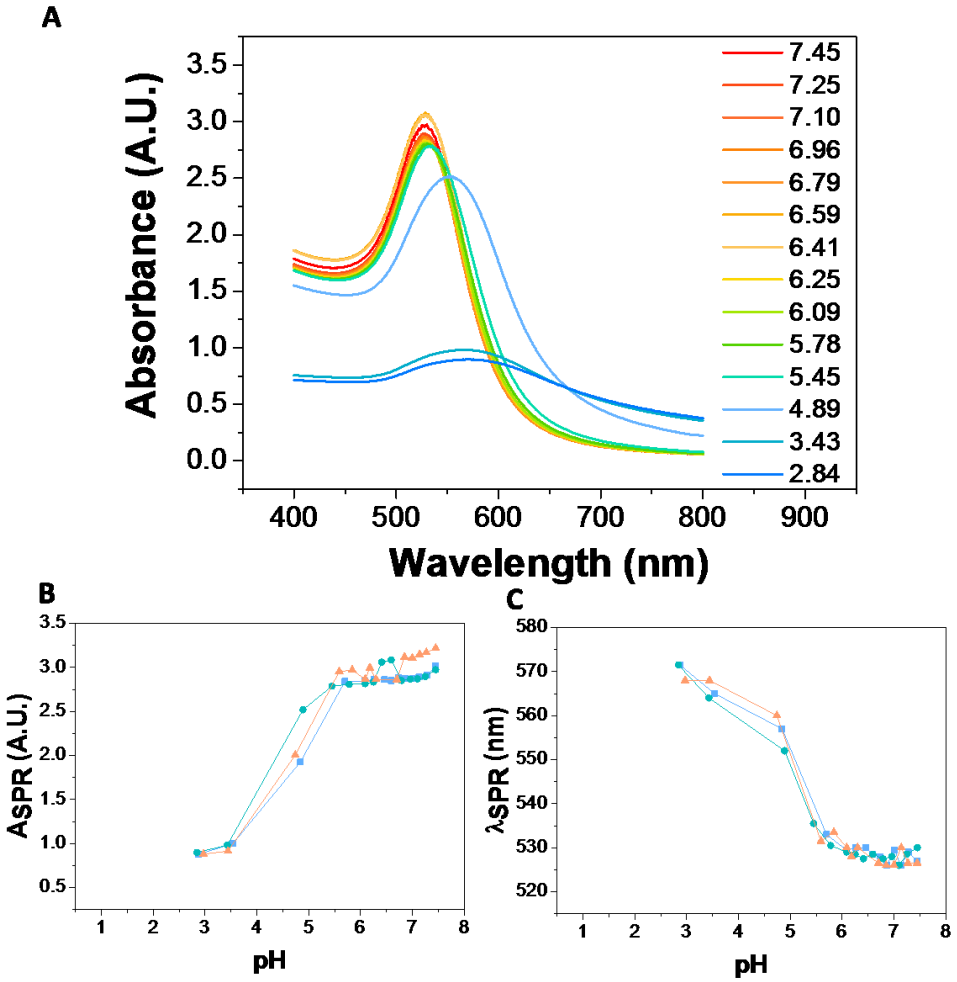


Figure 4-8 pH-response via titration of AuNPs@PP75(30) redispersed in 100 mM PB buffer pH 7.4 and titrated with µL of 0.1 M HCl: (A) UV-vis spectra, (B) absorbance at the SPR and (C) SPR wavelengths with pH.

In order to minimise the time-dependent effect, a third experiment was designed where multiple colloidal solutions were prepared and redispersed in buffers at a specific pH and the absorbance was recorded after 24 h. The results are presented in Figure 4-9.

The absorbance and wavelength at the SPR values showed a clear transition between pH 5 and 6. This well corresponds to the pH at which the polymer starts to precipitate out of the solution as measured via transmittance (Figure 4-10). 1 mg mL^{-1} PP75 solution displayed a transmittance close to ~90% from pH 7.4 to pH 5.5 and then the value dropped to ~30%, sign of the precipitation.

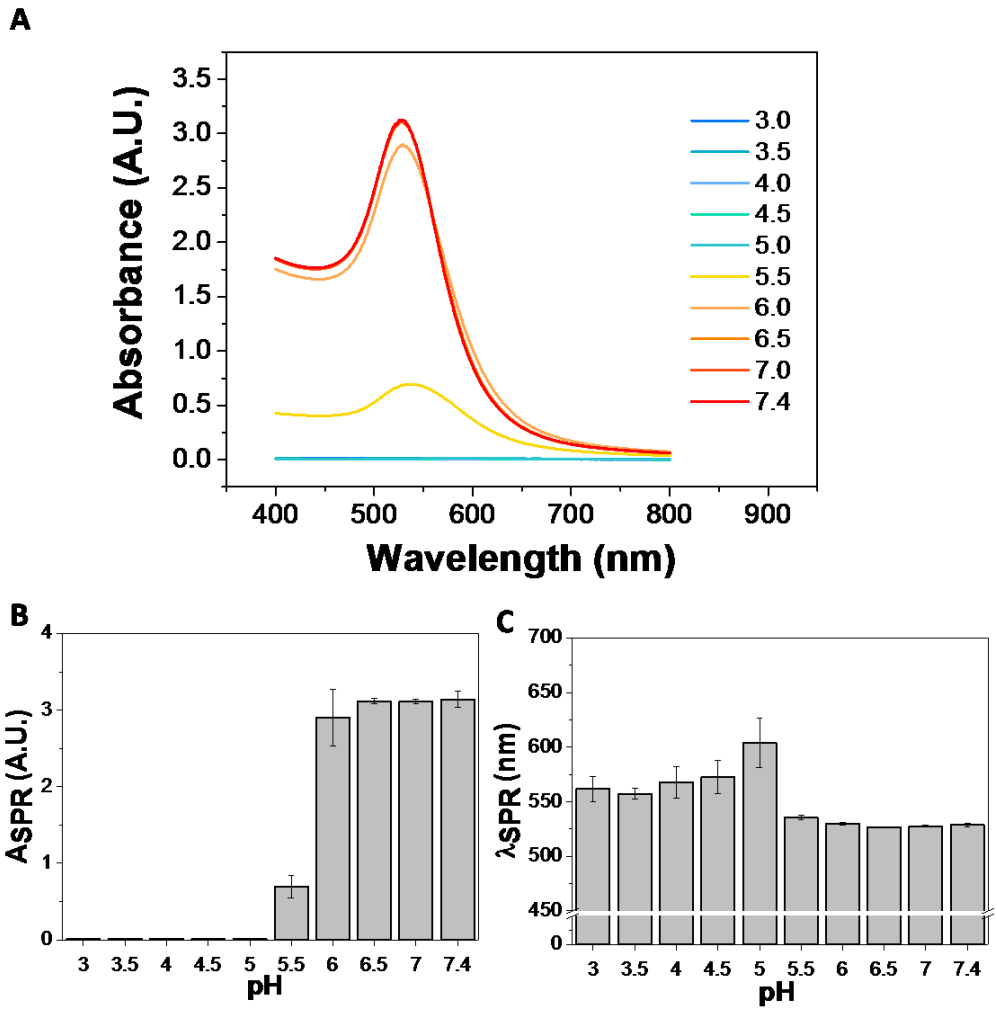


Figure 4-9 pH for transition determined via absorbance measurements. AuNPs@PP75(30) are redispersed in buffers: 100 mM PB buffers from pH 7.4 to 6 and 100 mM citrate buffers from pH 5.5 to 3. (A) UV spectra, (B) absorbance at the SPR and (C) Wavelength at the SPR measured 24 h after redispersion. Error bars represent standard deviations of triplicate measurements.

Figure 4-10(A) shows that the titration method led to a different profile displaying a continuous decrease of the transmittance, rather than a sudden drop as observed with AuNPs@PP75. One possible interpretation would be that the grafting of the polymer chains on the AuNPs surface inhibited the conformational change due to additional interchain steric interactions that did not exist (or were much weaker) for free chains in solution. Therefore, the equilibrium was more rapidly attained for free chains than for their grafted counterparts leading to a slow and continuous evolution whereas the AuNPs@PP75 suddenly agglomerated once the surface charge was completely neutralised.

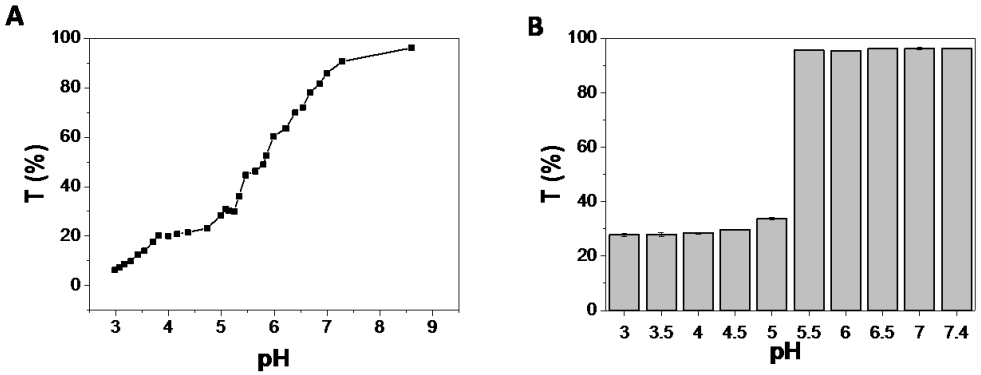


Figure 4-10 Transmittance of PP75 solution at 1 mg mL^{-1} at λ=480 nm measured via (A) titration after redispersion in ultra-pure water using 0.1 M HCl, (B) redispersion in buffers for 3 h: 100 mM PB buffers from pH 7.4 to 6 and 100 mM citrate buffers from pH 5.5 to 3. Error bars represent standard deviations of triplicate measurements.

Another factor to be taken into consideration for the interpretation of the pH for transition experiment is the influence of the electrolyte type and concentration. 100 mM PB buffers were used from pH 7.4 to 6 and 100 mM citrate buffers from pH 5.5 to 3.

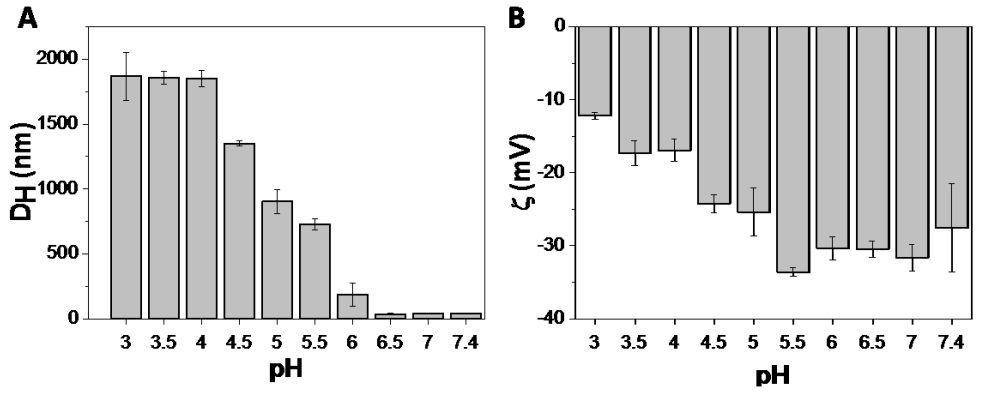


Figure 4-11 pH-dependent change of (A) the mean hydrodynamic diameter and (B) the zeta potential of the AuNPs@PP75 measured one day after redispersion in buffers: 100 mM PB buffers from pH 7.4 to 6 and 100 mM citrate buffers from pH 5.5 to 3. Error bars represent standard deviations of triplicate measurements. 10 runs per sample for D_H and 6 runs of 20 cycles each for ξ measurements were performed.

Additional studies, not shown in this thesis, further confirmed that both the salt type and the ionic strengths were crucial factors controlling the stability of the AuNPs. In particular, the stability was equivalent in 100 mM PB and 100 mM citrate buffers at pH 5.5, however it was higher in 50 mM PB pH 5.5 than in 50 mM citrate pH 5.5. Additionally, the stability was higher at 50 mM than at 100 mM buffer. These effects have also been reported in the literature. The type of salt and in particular the type of anions has been

reported to have an effect on the stability. [259] Besides, at high electrolyte concentrations the thickness of the electrical double layer decreases thus the zeta potential and the stability of the colloidal solution are lowered. [260]

As shown in Figure 4-11, the pH response of the AuNPs@PP75 was also visible via DLS. The AuNP size increased from 41.4 ± 1.0 nm at pH7.4 to 1869.8 ± 185.3 nm at pH 3.0 due to the appearance of large-size clusters. The transition pH was found in-between pH 4 and pH 6. Increasing the proton concentration also led to the increase in the zeta potential due to the protonation of the carboxylate groups on the polymer side chains.

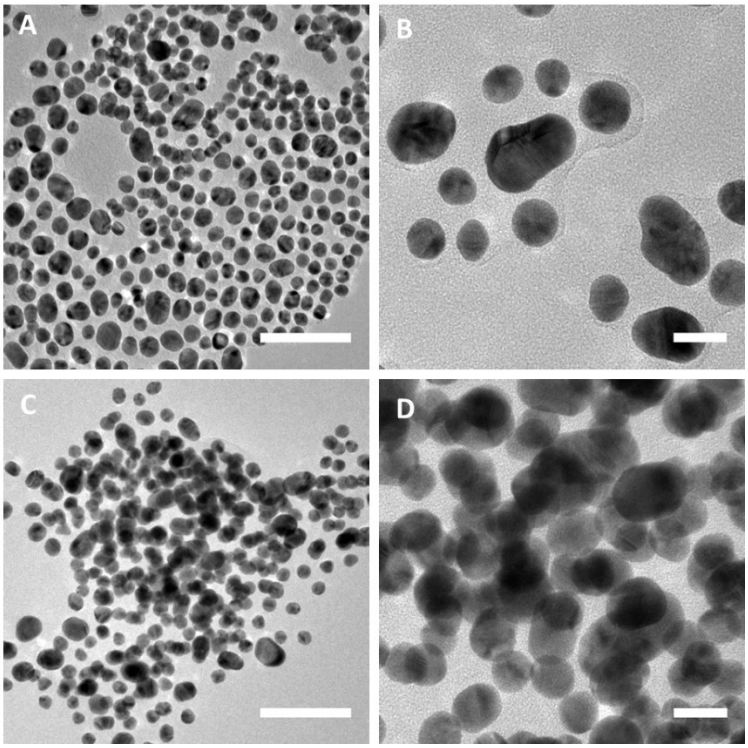


Figure 4-12 TEM images of AUNPs@PP75 redispersed in 100mM PB buffer pH 7.4 (A-B) and 100 mM citrate buffer pH 4.0 (C-D). Scale bar 100 nm (A, C) and 20 nm (B, D).

Last, the pH response was also observed under TEM (Figure 4-12). AuNPs@PP75 were well dispersed at pH 7.4, a protective layer of PP75 could also be discernible at high magnification, preventing the contact between AuNPs whereas AuNPs showed important clusters at acidic pH demonstrated by layers of AuNPs in contact with each other.

The influence of the polymer structure on the pH response has been investigated by comparing AuNPs grafted with PP75 and with its parent polymer, poly (L-lysine isophthalamide) (PLP). Figure 4-13 shows the colloidal stability over time of AuNPs, AuNPs@PLP and AuNPs@PP75 redispersed in H_2O and 50 mM MES buffer at pH 7.4, 6.5 and 5.5.

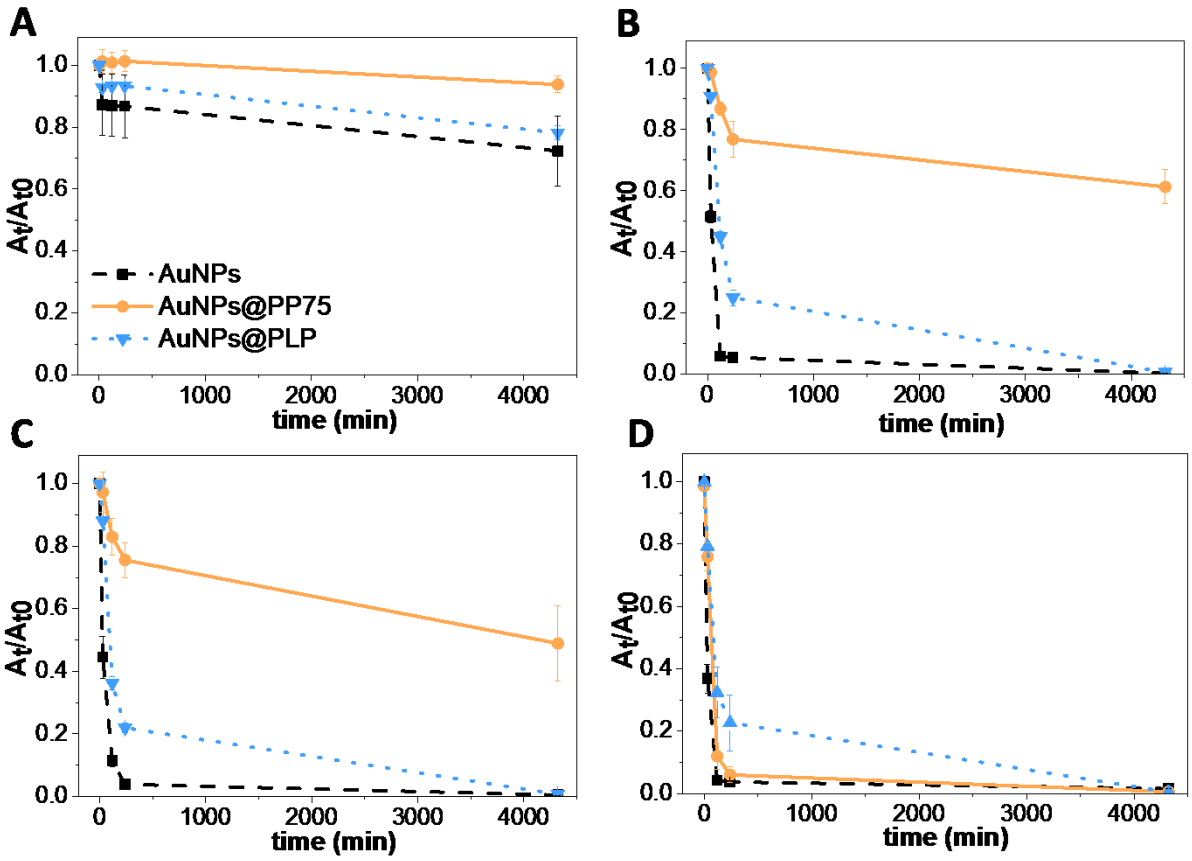


Figure 4-13 Colloidal stability over time in different media. AuNPs, AuNPs@PLP and AuNPs@PP75 redispersed (A) in H_2O, in 50 mM MES buffer (0.15 M NaCl) (B) pH 7.4, (C) pH 6.5, (D) pH 5.5. Error bars represent standard deviations of triplicate measurements.

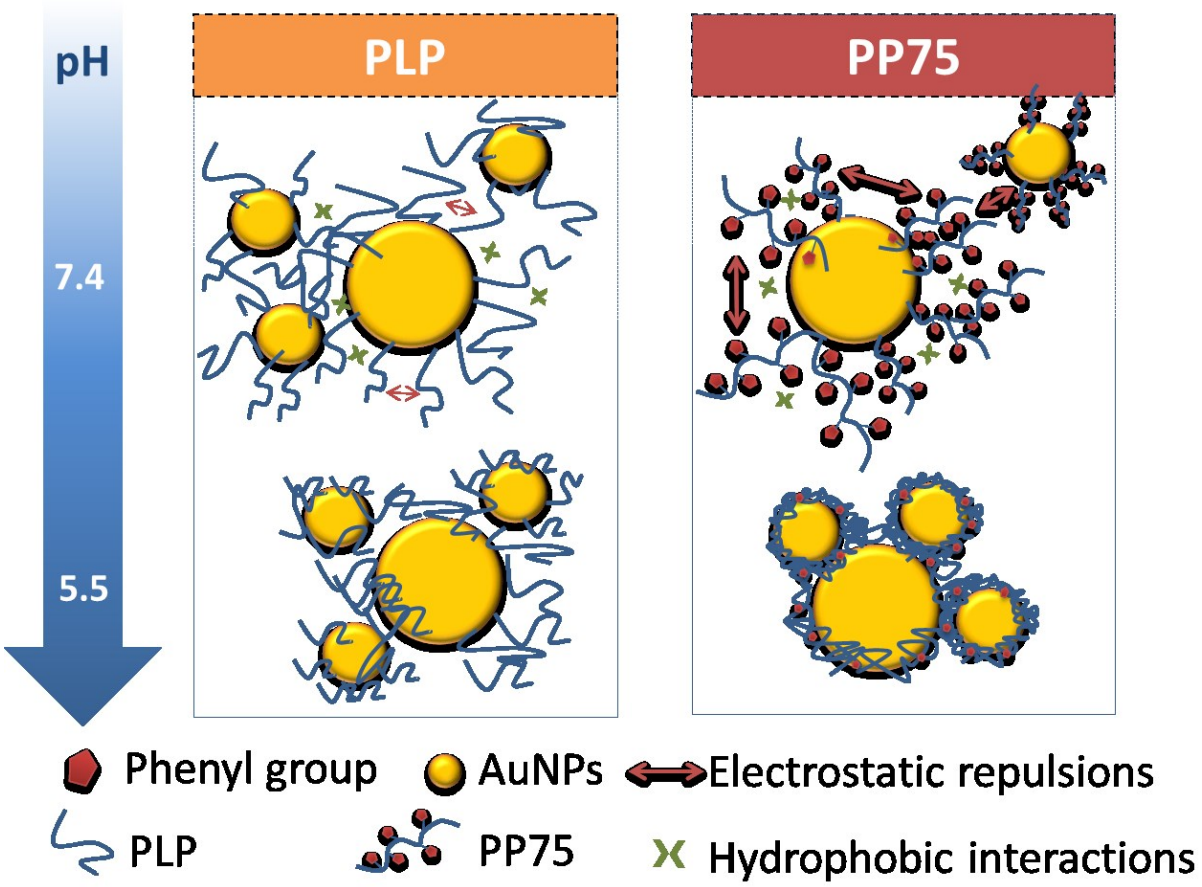
As expected, both polymers brought stability to the AuNPs over a longer period than the citrate coated AuNPs for all media. The same molar quantity of polymer has been added for the preparation of AuNPs@PLP and AuNPs@PP75, however redispersion in H_2O showed that the colloidal stability of PP75 hybrids was better. This observation could be explained by the difference in molecular weights. The molecular weight of PP75 being higher than PLP, AuNPs@PP75 would require a lower grafting density than AuNPs@PLP for stabilisation as already reported for PEGylated AuNPs in Chapter 3 section 3.2.3.

However, here, the higher molecular weight does not relate to a longer chain but a higher branching degree due to the presence of side chains which would contribute more efficiently to the steric shielding.

AuNPs@PP75 showed only 20% decrease in relative absorbance after 3 days of incubation in MES buffer at pH 7.4 whilst the PLP functionalised AuNPs showed slightly enhanced stability in the first 30 minutes but were totally agglomerated after 3 days. The PP75-functionalised AuNPs retained the significantly higher stability in MES pH 6.5, with only 20% decrease in relative absorbance in the initial 30 minutes and 40% decrease after an extended period up to 3 days. However, at pH 5.5, AuNPs@PP75 agglomerated more rapidly than AuNPs@PLP. Thus, PP75 polymer provides a higher stability than PLP to the AuNPs in MES pH 7.4 and 6.5 but not at pH 5.5.

This observation might be explained by the variations in the pH-responsive behaviour of the two hybrid NPs caused by the difference in steric hindrance but also in amphiphilic properties between the two polymers PLP and PP75.

Grafted polymers interact with each other through attractive hydrophobic interactions between hydrophobic components (polymer backbone), as well as through electrostatic repulsion between anionic groups (carboxylate) and steric interactions. As represented in Scheme 4-2, PP75 polymer, due to the phenylalanine grafted as side chains, presents additional benzyl rings. At pH7.4 and 6.5, the benzyl rings might bring rigidity to the main chain via interchain steric hindrance, as discussed by Zhou *et al.*[261], which co-exists with important electrostatic repulsions between the carboxylate on the side chains providing a higher colloidal stability to the AuNPs compared to PLP. However, at pH 5.5, the protonated PP75 displayed a change of conformation into hydrophobic globular structures[262] which enhanced the hydrophobic interparticle interactions and as a result led to the easier agglomeration of the polymer-functionalized AuNPs. On the other hand, the conformational change of PLP occurs at a lower pH around 5-4.5[170] which means that at pH 5.5 PLP chains were not totally protonated and still exhibited some electrostatic repulsion providing stability to the AuNPs. .



Scheme 4-2 Schematic representation of pH-responsive stability of the AuNPs functionalised by the anionic amphiphilic polymers PP75 and PLP

In summary, absorbance profiles, hydrodynamic sizes and EM images confirmed the agglomeration of the particles under acidic pH. The pH for transition was evaluated at pH 5-6 and well corresponded to the pH for transition of PP75. To fully confirm whether the pH response of the AuNPs@PP75 was due to the PP75 or simply the agglomeration of the AuNPs in acidic conditions by charge screening, an investigation of the reversibility of the pH response has been carried out and the results are presented below.

4.2.3 Reversibility of the pH response

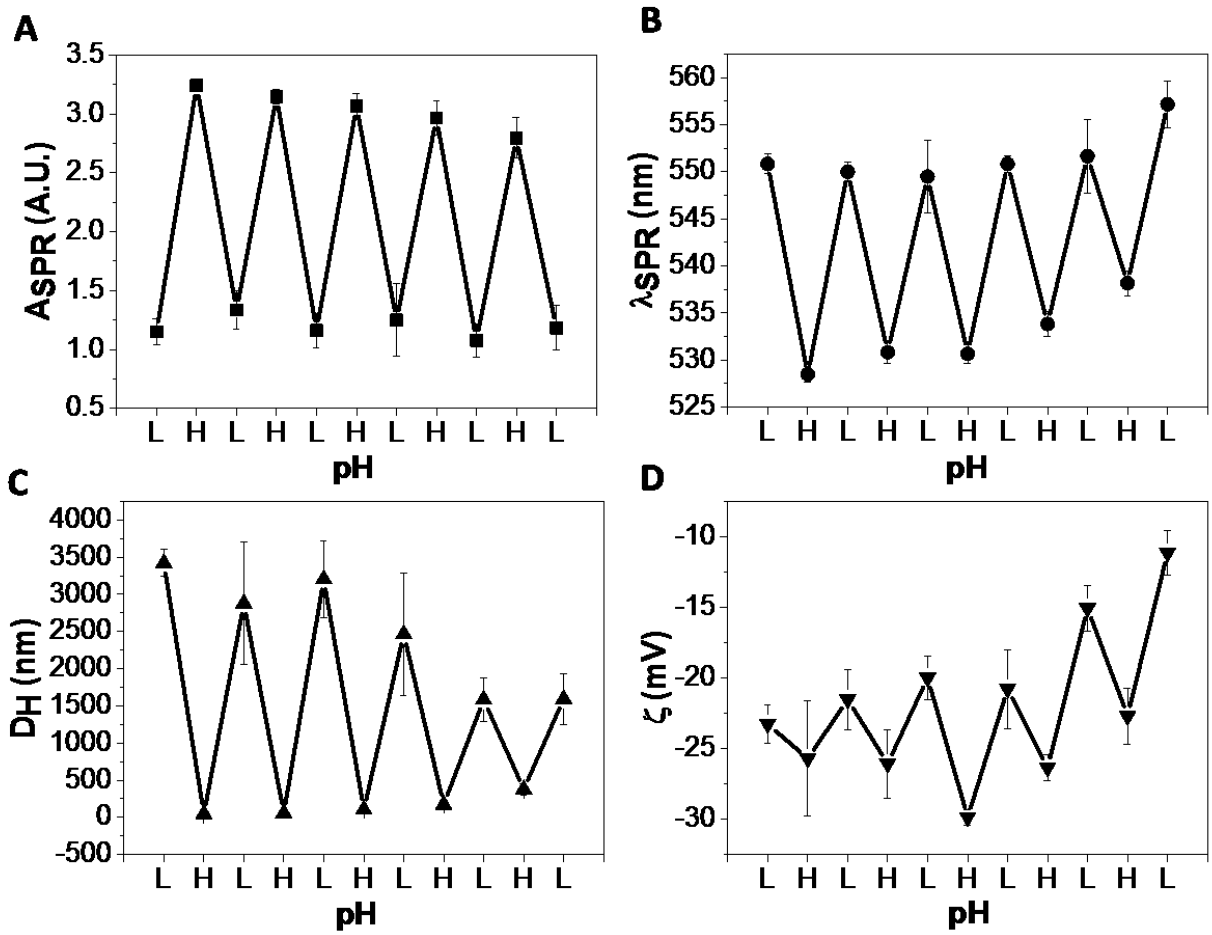
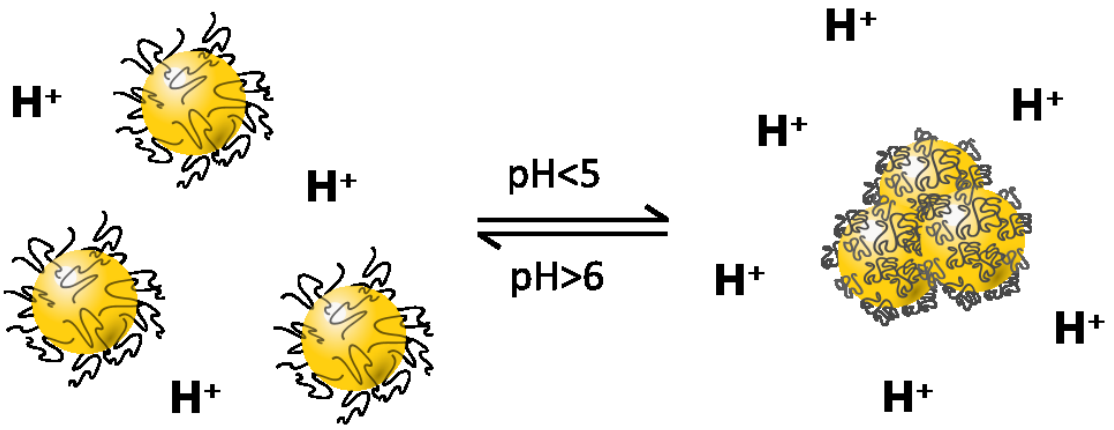


Figure 4-14 Reversible change of (A) the SPR absorbance, (B) the SPR wavelength, (C) the hydrodynamic size and (D) the zeta potential of the AuNPs@PP75(30) solution with pH cycling between low pH (pH~3.0) and high pH (H~pH7.4). Error bars represent standard deviations of triplicate measurements. 6 runs per sample for D_H and 6 runs of 20 cycles each for ξ measurements were performed.

AuNPs@PP75 were redispersed in PB buffer at pH 7.4 and after stabilisation the pH was adjusted with μL additions of 6 M HCl to pH~3 (L) and 6 M NaOH to pH~7 (H). The absorbance, hydrodynamic size and zeta potential of the solutions were recorded after each addition (Figure 4-14). Almost complete reversibility was observed for the first three cycles. AuNPs@PP75 showed strong agglomeration at pH 3 given by a peak absorbance decreased by a third compared to pH 7, a red shift to 550 nm and a hydrodynamic diameter reaching 3500 nm. When the pH increased back to pH 7, the close-to-initial values for the three parameters were found again. The zeta potential profile displayed a less convincing reversibility probably due to the higher sensibility of

the ionic strength built up after successive additions of HCl and NaOH. However, the trend observed for the zeta potential was expected since the values were closer to 0 at lower pH showing the decrease of electrostatic interactions leading to the agglomeration. A slight hysteresis starts appearing after three cycles possibly due to irreversible aggregation and the ionic strength increase.

The mechanism for the reversibility is presented in Scheme 4-3. PP75 presents amphiphilicity properties thanks to the balance between the electrostatic and hydrophobic interactions provided by the weakly ionisable carboxyl groups and the hydrophobic moieties respectively. At high pH, PP75 chains are extended due to the intra- and inter-chain electrostatic and steric interactions providing stabilisation to the colloidal solution. When the pH decreases, the PP75 chains collapse on the AuNP surface due to the change of conformation from coil to globule upon protonation of carboxyl groups. As a result, the PP75 functionalised AuNPs start to agglomerate via hydrophobic association. When the pH increases back to higher levels the PP75 chains change back to an extended conformation based on neutralisation of the protons with the OH^-.



Scheme 4-3 Schematic representation of the mechanism of the pH-triggered reversible agglomeration-deagglomeration process.

Reverse behaviour with polycationic polymer functionalised AuNPs has been reported in the literature. D'Souza-Mathew *et al.*[263] observed the reversibility of the pH responsiveness of poly(dimethylaminoethyl methacrylate) (pDMAEMA) functionalised AuNPs. Below the transition pH, between pH 6 and 8, the polymer was positively charged

due to protonated tertiary amines and the chains were extended via electrostatic repulsions providing stability to the colloidal system. When the pH increased, the agglomeration was triggered via the collapse of the chains on the AuNPs surface weakening the steric stabilisation and leading to agglomeration via hydrophobic association and possible Van der Waals forces.

The pH responsive behaviour of the hybrid nanosystems is desirable for biological applications for several reasons. First, following intravenous injection the AuNPs circulate in the blood stream, where the pH is regulated at values close to 7.4, before reaching the tumour. It is then important to provide a higher degree of dispersion at high pH values to avoid the formation of clusters that could build up in the veins. Second, the tumour extracellular environment generally exhibit a slightly lower pH due to the Warburg effect[264] and the internal cellular compartments demonstrate an acidification after internalisation[125] as previously mentioned in Chapter 1 introduction sections 1.4.1 and 1.4.2.

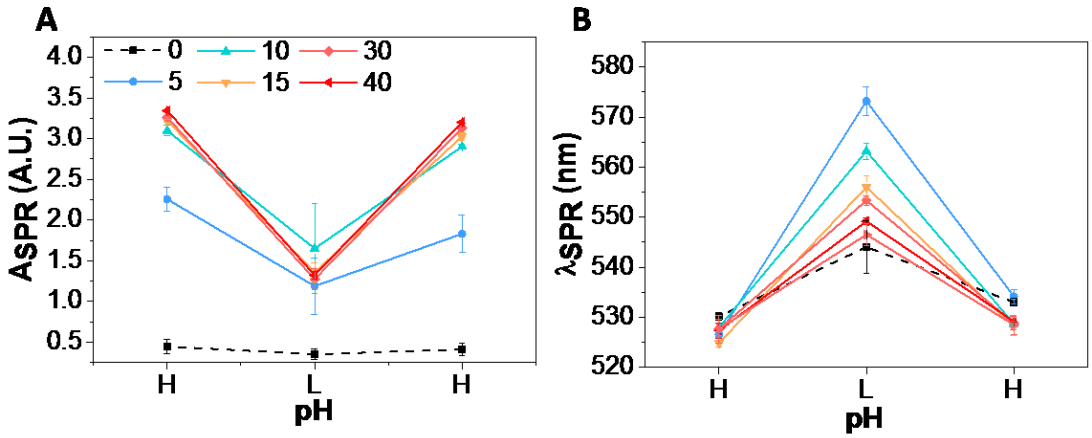


Figure 4-15 Influence of the polymer concentration (expressed as µg PP75 added per mL of ~10 nM AuNPs) on the reversibility of the pH response. (A) Absorbance values at the SPR and (B) wavelength values at the SPR for AuNPs@PP75 with the PP75 concentration ranging from 0 to 40 µg per mL AuNPs redispersed in 100 mM PB pH 7.4 (H); then the pH was adjusted to pH~3-4 with 0.1 M HCl (L); and adjusted to pH~7 with 0.1 M NaOH (H). pH (H~pH7.4). Error bars represent standard deviations of triplicate measurements.

The pH dependent agglomeration at acidic pH could be exploited in order to increase the concentration of NPs for enhanced drug release, enhanced optical absorption for phototherapeutic[265] and imaging purposes.[266] It is also easy to understand that the

reversibility of the pH response is crucial for therapeutic applications in order to avoid the presence of long term aggregates in the tissues.

The influence of the polymer concentration on the pH response was evaluated by redispersion of AuNPs@PP75 solutions prepared with an increasing amount of polymer in PB pH 7.4 and pH cycling between pH~3 and pH~7.4 with µL addition of 6 M HCl and 6 M NaOH. As seen in Figure 4-15, the pH response was strongly dependent on the initial polymer concentration during grafting.

Considering the change of SPR absorbance first, as expected the quality of the redispersion in buffer was enhanced with increasing the PP75 concentration. The citrate-coated AuNPs presented a very low absorbance indicative of a quasi-complete agglomeration. The absorbance increased with the presence of PP75 demonstrating a higher concentration of stable NPs. However, the extent of the differences between the SPR absorbance at high and low pH, $\Delta A = A_H - A_L$, differed. AuNPs@PP75 functionalised with polymer concentrations lower than 30 µg mL^{-1} showed a lower ΔA. This demonstrates a possible higher and/or quicker change in the AuNPs colloidal concentration with pH variation for the highly grafted AuNPs.

Considering the changes in SPR wavelengths, relative to the size of the NPs or clusters, it seems that the $\Delta\lambda = \lambda_H - \lambda_L$ increased with decreasing grafting densities. Considering the influence of the grafting density on ΔA and Δλ simultaneously it was concluded that the AuNPs functionalised with a lower grafting density led to the formation of larger sized clusters, as suggested from the lower A_{SPR} and higher λ_{SPR} at acidic pH, due to decreased steric hindrance between AuNPs.

AuNPs@PP75(30) presented an efficient reversibility since the colloidal stability returned to its original level after the pH was increased back to higher values. On the other hand, in the case of a high grafting density, the chains are strongly maintained in a brush conformation thus limiting their pH-dependant agglomeration. As a conclusion, the pH responsive behaviour can be tuned at different grafting densities depending on the desired properties. AuNPs@PP75(30) was chosen to avoid the formation of clusters and

obtain the highest stability at physiological pH while maintaining a noticeable pH response.

4.2.4 Membrane interaction

The haemolysis assay was used in order to investigate the membrane lytic activity of the AuNPs@PP75. Free PP75 and AuNPs@PP75 were incubated with sheep red blood cells (RBCs) and the membrane lytic activity was deduced from the extent of the haemoglobin release.

After incubation for one hour at 37°C in different pH buffers, the samples were centrifuged and the absorbance of the supernatants were measured at 541 nm where the haemoglobin strongly absorbs. The relative haemolysis was calculated (see Chapter 2 Materials and Methods section 2.3.1.13). The PP75 polymer (Figure 4-16) showed a pH-responsive haemolytic activity similar to what have been previously reported,[262] reaching a maximum haemolysis of 80% at pH 6.5. The relative haemolysis of AuNPs@PP75(30) slowly increased with pH and reached the value of 140% at pH 7.4.

These results are explained by the very high absorbance obtained for the supernatants of the AuNPs@PP75 solutions from pH 6.0 and higher. At these pHs the AuNPs@PP75 were well dispersed in buffers, as previously demonstrated, and after centrifugation small AuNPs@PP75 might be still present in the supernatant with an absorbance (Figure 4-2) overlapping the absorbance spectrum of the haemoglobin

The protocol for haemolysis was then modified by using other centrifugation parameters, such as 12,000 rpm for 12 min instead of 4,000 rpm for 4 min and AuNPs were added to the positive and negative controls.

However these changes could not overcome the following limitations: (i) the higher centrifugation time and speed and a second centrifugation step may be required to separate the smaller size AuNPs however this could damage the RBCs membrane and lead to overestimated results; (ii) the centrifugation with the AuNPs may lead to further membrane damage due to the high density of the gold; (iii) at acidic pH the agglomerated

AuNPs@PP75 can settle down and lead to the loss of interaction with RBCs during incubation; (iv) the coagulation of blood around the AuNPs can prevent their interaction with RBCs;[267] (v) AuNPs can adsorb haemoglobin leading to an underestimation of the haemolysis.[267]

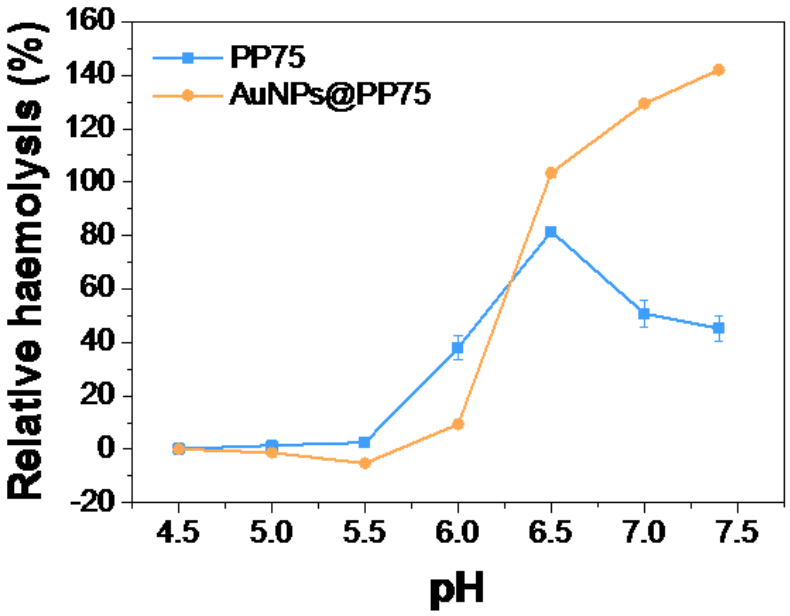


Figure 4-16 Relative haemolysis of sheep RBCs by 30ug mL^{-1} PP75 and AuNPs@PP75 at pH 6.5 incubated at 37°C for 1h. Error bars represent standard deviations of triplicate measurements. pH (H~pH7.4). Error bars represent standard deviations of triplicate measurements.

As a conclusion, even though the literature reported the use of the haemolysis assay to investigate the membrane activity of functionalised AuNPs, the reproducibility and accuracy of the results were judged to be insufficient all the more so as this assay might not be suitable with AuNPs for the reasons explained above.

Another assay was developed using liposomes as a cellular model in order to evaluate the ability of AuNPs@PP75 to interact with the cellular membrane. The release of calcein, loaded in the liposome, was monitored via fluorescence in PB pH 7.4 (Exc 490 nm, Em 510-570 nm). The results are presented in Figure 4-17.

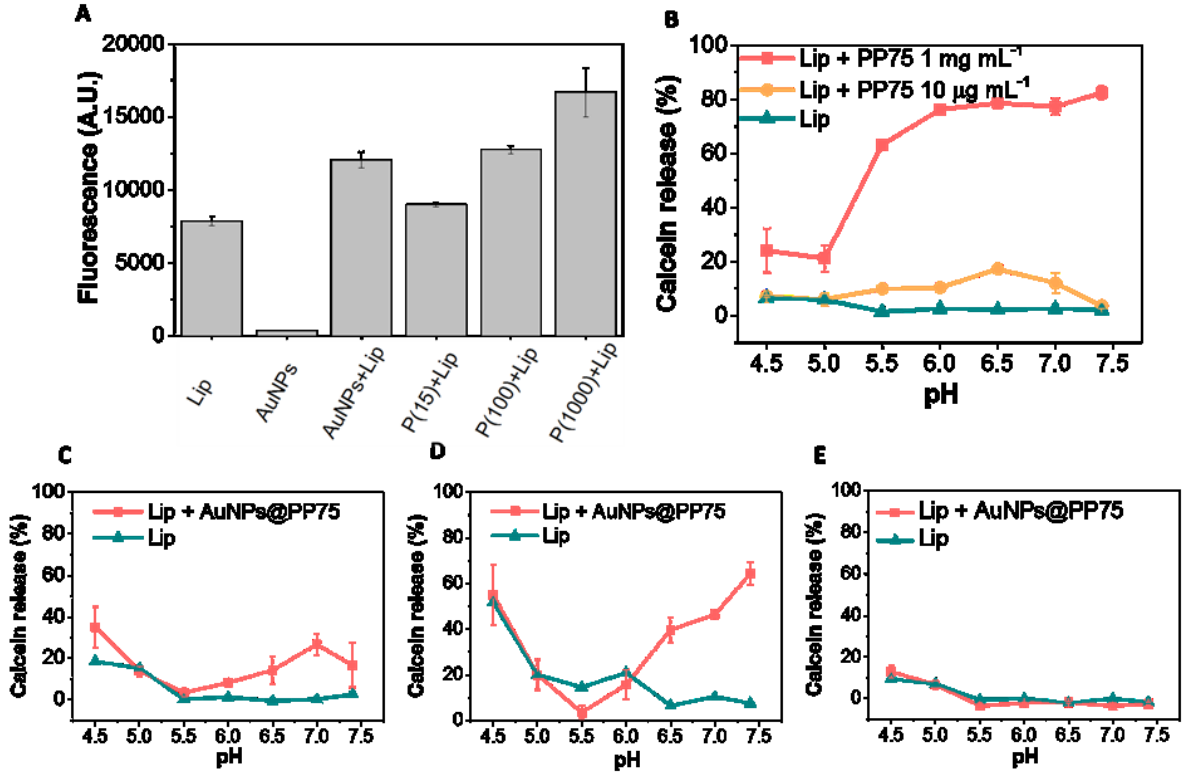


Figure 4-17 Evaluation of the pH-dependent membrane activity with calcein loaded liposomes as a model. (A) Fluorescence levels obtained after incubation for 90 min at 37°C of liposomes (Lip), AuNPs; AuNPs and liposomes (AuNPs+Lip), liposomes with PP75 at 15 µg mL^{-1}(P(15)+Lip), with PP75 at 100 µg mL^{-1} (P(100)+Lip) and with PP75 at 1000 µg mL^{-1} (P(1000)+Lip) at pH 7.4. (B) Calcein release profiles of liposomes only and liposomes incubated with PP75 in buffers from pH 4.5 to 7.4. (C-E) Calcein release profiles of liposomes only and liposomes incubated with AuNPs@PP75 obtained on different days. pH7.4). Error bars represent standard deviations of triplicate measurements. *The calcein-loaded liposomes were provided by Dr. Siyuan Chen.*

As shown in Figure 4-17(A), AuNPs alone exhibited very low fluorescence and had an impact on the calcein release since the fluorescence increased from 8,000 to 12,000 A.U, similar to the effect of 100 µg mL^{-1} of PP75 polymer which is non-negligible. This leakage occurred probably due to the collision between the AuNPs and the liposomes during the incubation under shaking. Unfortunately, the stirring of the samples was necessary to favour the contact between the liposomes and the AuNPs and was especially important at low pH where the AuNPs tend to sediment following clusters formation. As would be expected, the increase of the polymer concentration led to an increase in the calcein release.

The concentration- and pH-dependent membrane activity profiles in the presence of PP75 (Figure 4-17(A-B)) were consistent with the results reported in the literature.[262]

Unfortunately, a very high discrepancy was observed for AuNPs@PP75 with assays performed on different days (Figure 4-17(C-E)) since the calcein release at pH 7.0 was found to vary between 0% to 40% which might be due to the aging of the calcein-loaded liposomes solution or differences of calcein loading between different batches of the liposomal solution. Further studies would be required to investigate the lack of repeatability of the calcein release experiment.

It was also noted that higher calcein release was obtained at acidic pH for all the samples that could not be attributed to the AuNPs@PP75 since the phenomenon was also observed for liposomes alone. It was suggested that the liposomal membrane might be affected at pH ≤ 5. However, Chen and Chen[268] did not report any calcein leakage at acidic pH with liposomes of same composition. The storage time of the liposomal solution might be a possible explanation for the liposomes fragility.

In summary, the evaluation of the membrane activity of the polymer functionalised nanohybrids using RBCs or liposomes as cellular model revealed to be extremely challenging due to the agglomeration behaviour of the NPs but also the impact of the AuNPs themselves on the membrane disruption. The assays presented did not enable the evaluation of the membrane-lytic activity of AuNPs@PP75 furthermore these assays are far from representing the real geometry of the polymer-membrane interaction and does not take into account the complexity of the lipid layer composition. In the next section, the nanohybrids were incubated with cancer cells in order to evaluate their *in-vitro* biocompatibility, internalisation, cellular localisation and membrane activity.

4.2.5 *In-vitro* biological evaluation

HeLa cells were incubated with citrate-coated AuNPs and AuNPs@PP75 at different concentrations for 2 h, 24 h and 48 h and the cell viability was evaluated by the alamarBlue assay.

As seen in Figure 4-18(A), AuNPs@PP75 were well tolerated up to 10 nM after 2 days of treatment and up to 30 nM after 2 h of treatment with a cell viability close to 100%. The cell viability then slowly decreased until 38% at 100 nM after 48 h of incubation. The IC_{50},

defined as the concentration at which 50% of the cell growth is inhibited relative to the control (non-treated cells), was found to be 53.5 ± 7.2 nM at 48 h.

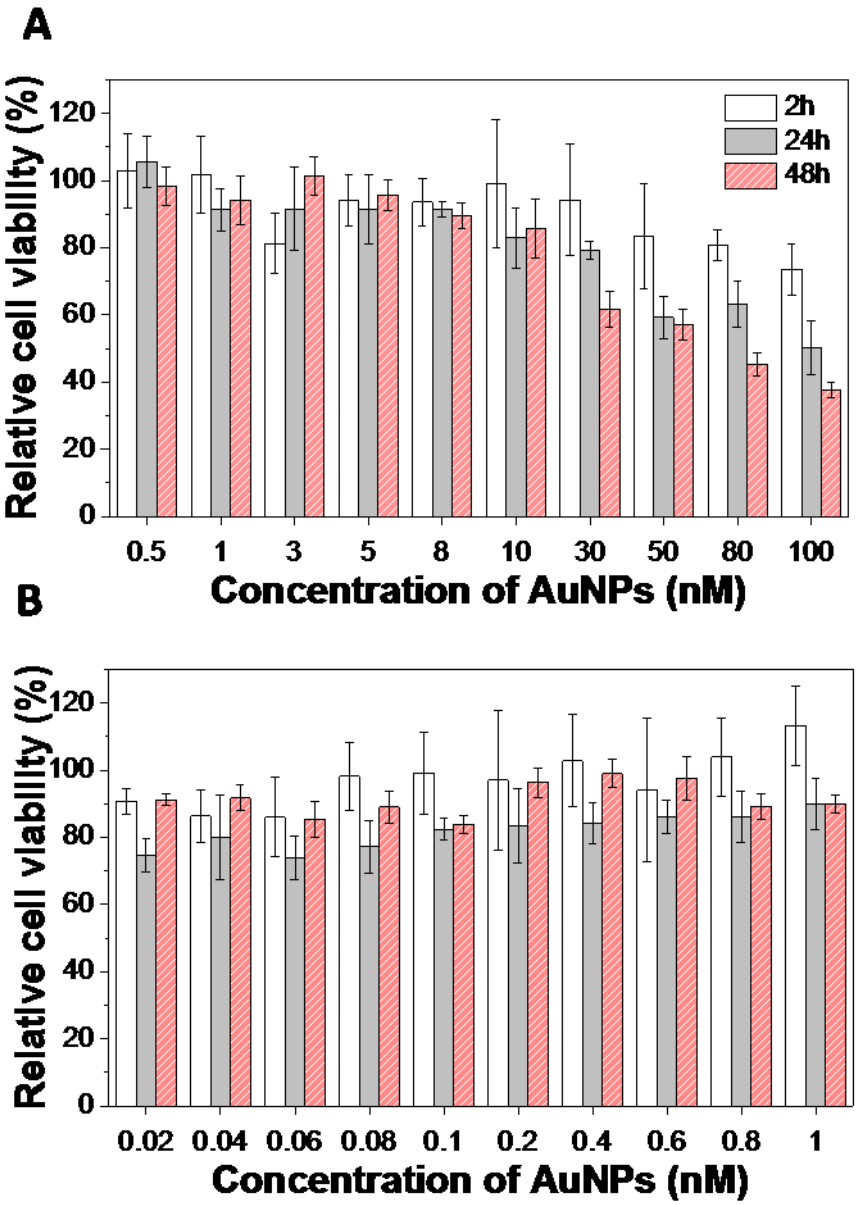


Figure 4-18 Concentration-dependent relative viabilities of HeLa cells treated with (A) AuNPs@PP75(30) and (B) citrate-coated AuNPs for 2 h, 24h and 48h as determined by alamarBlue assay. Error bars represent standard deviations of five replicates

Additionally, the relative cell viability of the citrate coated AuNPs was between 80% and 100% as shown in Figure 4-18(B) up to 1 nM.

Since the stability of the citrate coated AuNPs was very fragile, samples could not be prepared via centrifugation and redispersion in DMEM in order to avoid agglomeration but were prepared via successive dilutions which explains why the maximum tested concentration is below the as-synthesised concentration. Above 1 nM citrate-coated AuNPs would strongly agglomerate in DMEM thus the biocompatibility test was not performed.

Overall, these results suggested a very good biocompatibility of AuNPs@PP75 towards HeLa cells and this could be expected for three main reasons. First, AuNPs coated with a wide range of ligands (e.g. PEG, PAMAM, PEI)[88,90,99,269] have demonstrated high cell viabilities *in-vitro.* The present thesis also reported high level of viabilities for AuNPs@PEG incubated with Hela cells (Chapter 3 section 3.2.7). Second, as recently reported by Naha *et al.*[90] the coating material of the AuNPs was likely to affect more greatly the cell viability than the AuNP size and concentration and PP75 polymer[262] demonstrated very good biocompatibilities in the literature under these experimental conditions but also with other cell lines and *in-vivo*.[18,19,22] Third, anionic hybrid nanoparticles have proven to be less toxic than their cationic counterparts thanks to the lack of electrostatic attractions between the polymer and the negatively-charged cell membrane.[94]

Then the internalisation of the AuNPs@PP75 has been quantified after 24 h of incubation with HeLa cells using flow cytometry to calculate the number of cells in each sample and using ICP-OES to measure the concentration of gold ions internalised after digestion of the cells and the AuNPs with HNO_3. The calculation of the number of AuNPs per cells is detailed in Chapter 2 Materials and Methods section 2.4.3.

As reported in the literature, the internalisation is size, time and concentration dependent[97,270] until 24 h treatment, time after which the number of nanoparticles per cell does not increase longer.[270,271] As seen in Figure 4-19(A), the number of gold nanoparticles per cell increased with the AuNP concentration and reached 0.8×10^6 AuNPs per cell for an initial AuNP concentration of 8.8 nM which was almost three orders

of magnitude higher than 14 nm citrate-coated AuNPs per HeLa cell reported in the literature by Warren C. W. Chan and co-workers.[270]

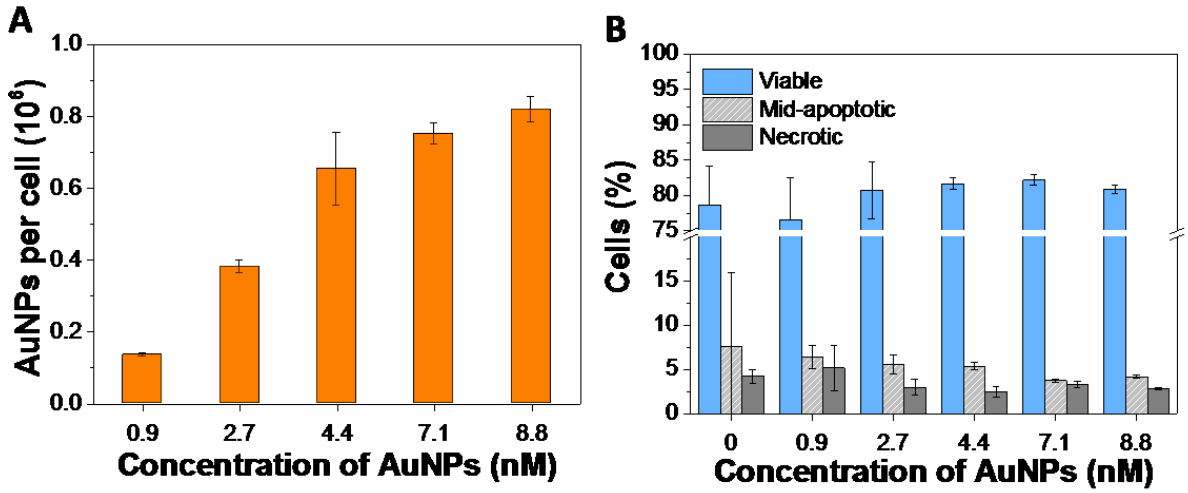


Figure 4-19 (A) Concentration dependant uptake of AuNPs@PP75 with HeLa cells after 24 h of treatment measured via ICP-OES and FACS. (B) Percentage of viable, mid-apoptotic and necrotic cells after 24 h of treatment with AuNPs@PP75 measured via flow cytometry. Error bars represent standard deviations of triplicate measurements.

In the literature, higher internalisation was obtained with smaller size AuNPs by Coulter *et al.*[97] who reported 1.3-1.6 x 10^8 1.9-nm AuNPs per cell for the human prostate cancer cell line Du145 and human breast cancer cell line MDA-MB-231. The results obtained were also compared to the AuNPs designed for enhanced internalisation, in particular those conjugated with the widely-used membrane-disruptive PEI polymer. Joydeep *et al.*[187] designed the PEI entrapped AuNPs and the PEI conjugated AuNPs for DNA delivery and reported an uptake of 2 x 10^4 and 4 x 10^3 AuNPs per cell respectively after 6 h of incubation. The large difference compared to the uptake obtained in the present thesis may also be attributed to the different cell type used since human stem cells are usually difficult to transfect. They obtained 4-7% uptake efficiency defined as the ratio of the number of AuNPs taken up by cells to the overall number incubated with cells, which is very similar to the efficiency obtained in the present thesis (3-6%, data not shown). Wang *et al.*[182] also prepared a PEI-AuNPs complex and further conjugated it with a peptide for targeting purpose and PEG chains for colloidal stabilisation. They reported an internalisation of 1.8 x 10^5 AuNPs per U-87 MG cell after 2 h of treatment, four times lower than the maximum cellular uptake reported herein after 24 h. The comparison after 2 h

treatment would be worth investigating. The experiment was also performed with AuNPs@PEG2k for comparison and no Au ion could be measured via ICP-OES confirming the very low uptake of PEGylated AuNPs as reported in the literature.[272]

The comparison with literature has to take into account the variability in AuNP size,[270] shape,[110,270] concentration,[110] capping-ligand,[205] but also in the incubation time[270] and cell lines[97] since all these parameters could have a dramatic influence on the internalisation. Overall, the results obtained in this study were higher than the internalisation obtained for similar systems but also for systems based on endosomal escape reported in the literature which confirmed the potential of AuNPs@PP75 as intracellular delivery enhancer.

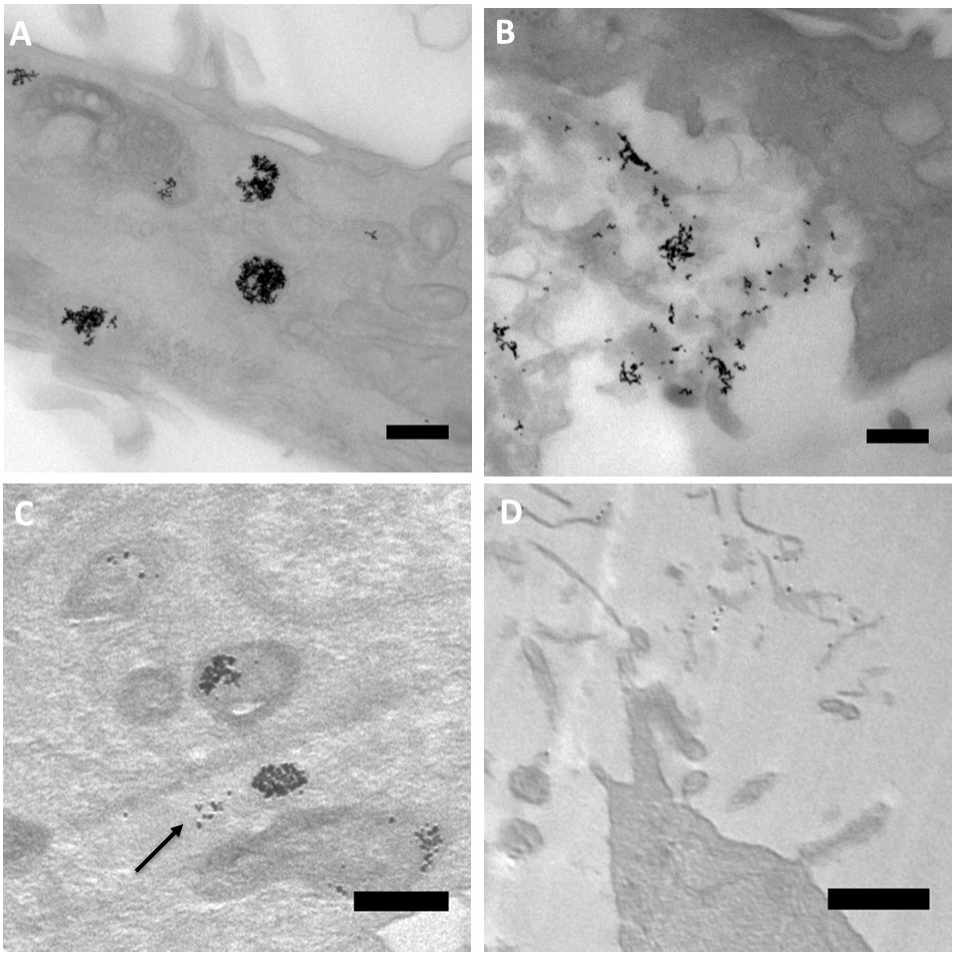


Figure 4-20 TEM images of HeLa cells treated with 3 nM AuNPs (A-B) and 10 nM AuNPs@PP75(30) (C-D) for 24 h (scale bar 200 nm, acceleration voltage 120 kV). *Tom Ellis (PhD student) provided some help for the cell fixing and staining protocol and Dr. Basmah Othman helped me with the ultramicrotomy and the visualisation of the fixed cells sections under TEM.*

Figure 4-19(B) confirmed the high biocompatibility of the nanohybrids with 80% of viable cells in the range of AuNP concentrations studied (up to 8.8 nM) against 15% necrotic and 5% apoptotic cells as average. These viability results were similar than that results obtained via alamarBlue assay even though they appeared lower at low AuNPs@PP75 concentrations. It should be noted that alamarBlue assay cannot distinguish between actively dividing cells and quiescent cells which may lead to an overestimation of the number of viable cells.[273] Besides, due to the prior trypsinisation of the cells for flow cytometry measurements, higher cell damage might be expected.

The intracellular localisation of hybrid AuNPs was observed under TEM and confocal microscopy. For TEM, HeLa cells incubated for 24 h with AuNPs and AuNPs@PP75 separately and after fixing, staining and embedding in resin, thin sections were cut with a microtome and imaged (Figure 4-20). In both cases the entrapment of the AuNPs in intracellular vesicles was observed (Figure 4-20(A, C)), supporting the endocytic uptake hypothesis. As reported by several groups, the entrapped AuNPs, in particular citrate coated AuNPs, exhibited a high level of agglomeration .[97,121,147,271] AuNPs@PP75 seemed to be less agglomerated. Cells debris with AuNPs are shown in Figure 4-20(B, D), thesNPs were either entrapped in the cells before their disruption or have been released by exocytosis[274] and once again the citrate coated AuNPs are more agglomerated than the AuNPs@PP75. Some AuNPs@PP75, indicated by an arrow, were observed in the cytoplasm (Figure 4-20(C)) and may have successfully escaped from the endosomes. They presented a higher level of dispersion likely due to (i) the "dilution" effect occurring after endosomal escape to the cytoplasm that decreased their local concentration and (ii) their reversible pH responsive behaviour, since the cytoplasm presents higher pH (~ 7.2) than the endosomes (~ 5),[158] a change from agglomerated to dispersed state is expected when the AuNPs are released to the cytoplasm.

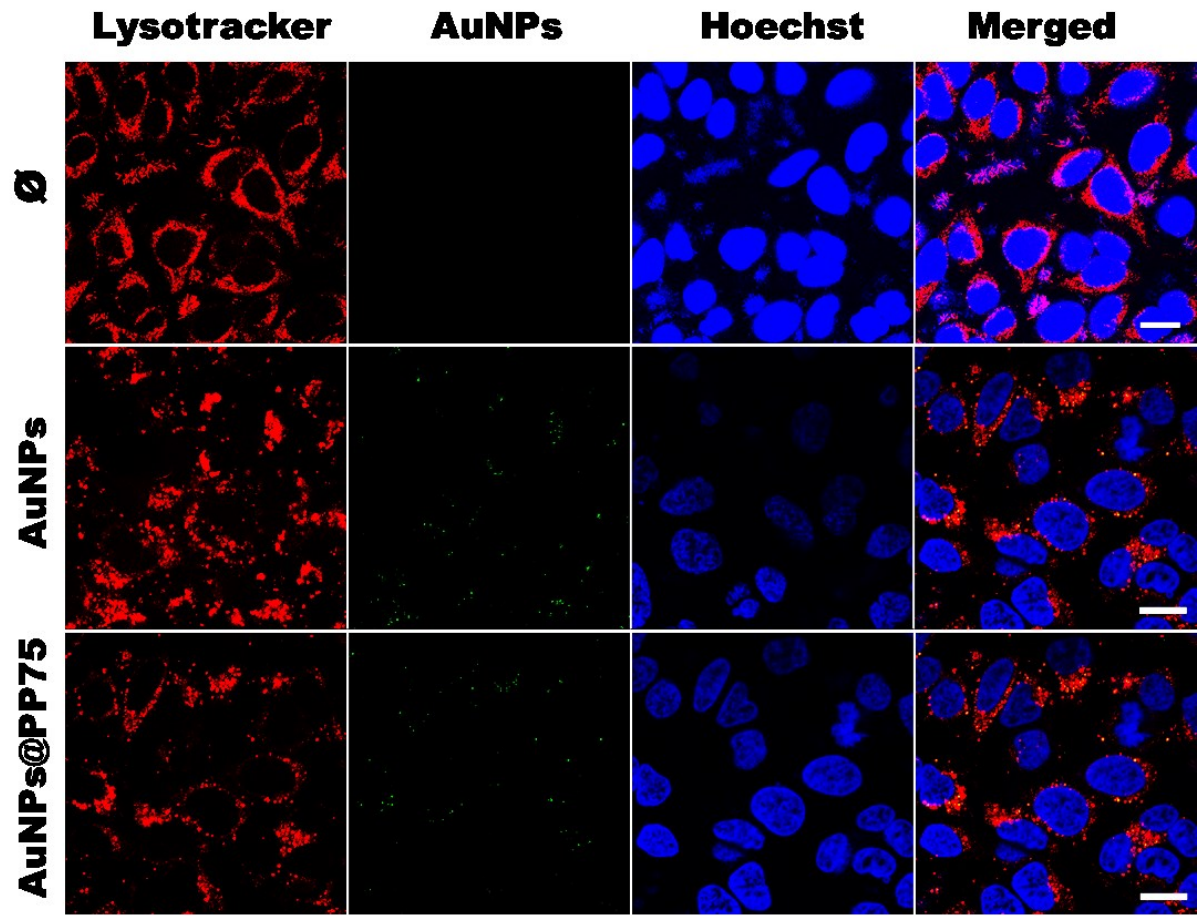


Figure 4-21 Confocal microscopy images of HeLa cells untreated, treated with 3 nM AuNPs and 10 nM AuNPs@PP75. Nuclei and lysosomes were stained with Hoechst and LysoTracker Red respectively. Images were acquired with a Zeiss LSM-510 inverted confocal unit (x63 magnification) after 24 h of uptake and fixing (scale bar: 20 µm).

For the intracellular localisation via confocal microscopy the SPR-enhanced light scattering[275] properties of the AuNPs were exploited. They were excited with a laser beam at 514 nm and the scattered light was detected. In Figure 4-21, the nucleus and intracellular compartments were stained with Hoechst (blue fluorescence) and Lysotracker (red fluorescence) respectively. No scattered light could be detected for the cells only (data not shown), demonstrating that the observed green dots was attributed to the citrate coated and PP75 functionalised AuNPs. The yellow dots in the merged images came from the overlap between the AuNPs and the endosomes/lysosomes.

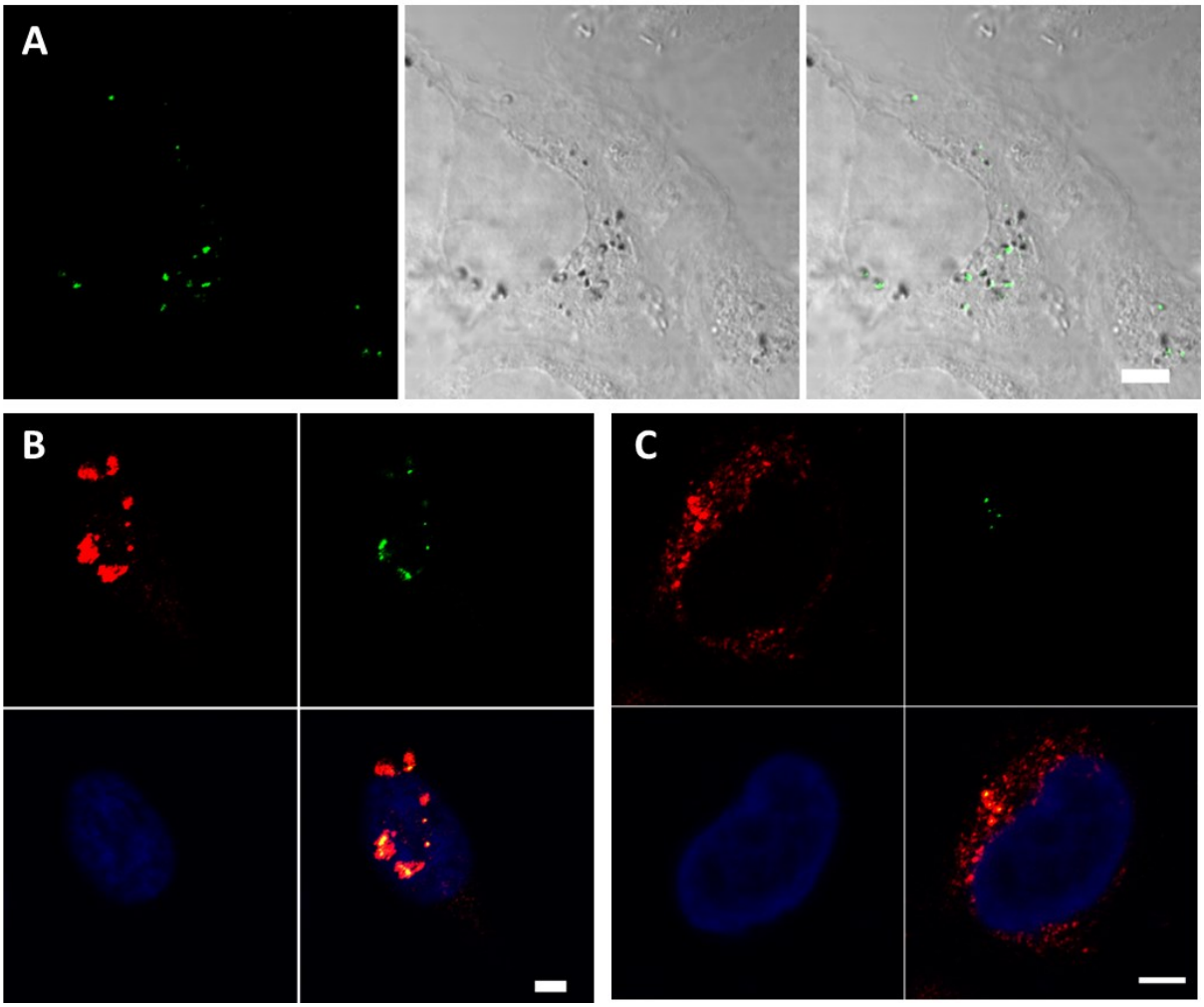


Figure 4-22 Confocal microscopy images of HeLa cells treated with 10 nM AuNPs@PP75. (A) Colocalisation of AuNPs fluorescence and bright field for Hela cells after 24h uptake. Colocalisation of AuNPs@PP75 with lysotracker at (B) 2h and (C) 24h. Nuclei and lysosomes were stained with Hoechst and LysoTracker Red respectively. Images were acquired with a Zeiss LSM-510 inverted confocal unit (x63 magnification) after 2 h (B) and 24 h (A, C) of uptake and fixing (scale bar: 5 µm).

They were more easily visible on the high magnification images in Figure 4-22. They were reproducibly observed, which confirmed the presence of small aggregates of NPs in the cellular compartments. As reported in the literature, AuNPs smaller than 50 nm would not be visible in the experimental conditions used[275] and the green dots most probably suggest the presence of clusters of few NPs that might originate from the agglomerate at endosomal pH of the nanohybrids as observed in the TEM image (Figure 4-20). Thus, the stabilised AuNPs, presented in the early endosomes or in the cytoplasm would not be visible with this method. Figure 4-22(A) show the overlap between the green and black

dots in the cells visualised under bright field. These black dots were not observed for cells without AuNPs so they likely correspond to aggregates of AuNPs.

Some brigher and large spots of lysotraker appear in Figure 4-22(B-C) and frequently show colocalisation with AuNPs@PP75. They could be explained by regions of higher lysosomal activity[276] or the leakage of the stain in the cytoplasm via rupture of the endosomal/lysosomal membrane in the presence of AuNPs@PP75.[277] It should be noted that the lysotracker stain is fluorescent at low pH only[278] which means that in case of a "leakage" the effect would only be visible shortly after the membrane rupture before the pH is adjusted to the cytoplasmic pH. This effect was visible for treatment of 2 h and 24 h demonstrating the possible efficient endosomal escape below 2 h. This is in agreement with the literature which has reported endosomal escape with membrane active AuNPs after 2 h incubation.[272]

To investigate further the endosomal escape ability of the nanohybrids, citrate-coated AuNPs, AuNPs@PEG and AuNPs@PP75 were incubated with calcein, a membrane impermeable model drug which can be visualised via fluorescence. Calcein uptake is via endocytosis, and alone it cannot escape from the endosomes. As a consequence, numerous bright spots could be observed under confocal microscopy corresponding to the entrapped calcein (Figure 4-23). The same phenomenon was observed with the control, citrate and PEG coated AuNPs. Expectedly, severe agglomeration was obtained with citrate coated AuNPs in DMEM. Punctuated spots were replaced by diffuse staining after treatment with AuNPs@PP75 as reported in the literature for PP75.[262]

As a conclusion PP75 polymer is able to retain its endosomolytic property after grafting and is able to deliver small molecules to the cytoplasm of cancer cells in the presence of serum. Since the membrane activity properties have been demonstrated to be well correlated with the pH responsive conformational change[18,22], it was concluded that the polymer still exhibits the coil-to-globule transition after grafting on the AuNPs surface which was already suggested based on the results of pH responsiveness studies.

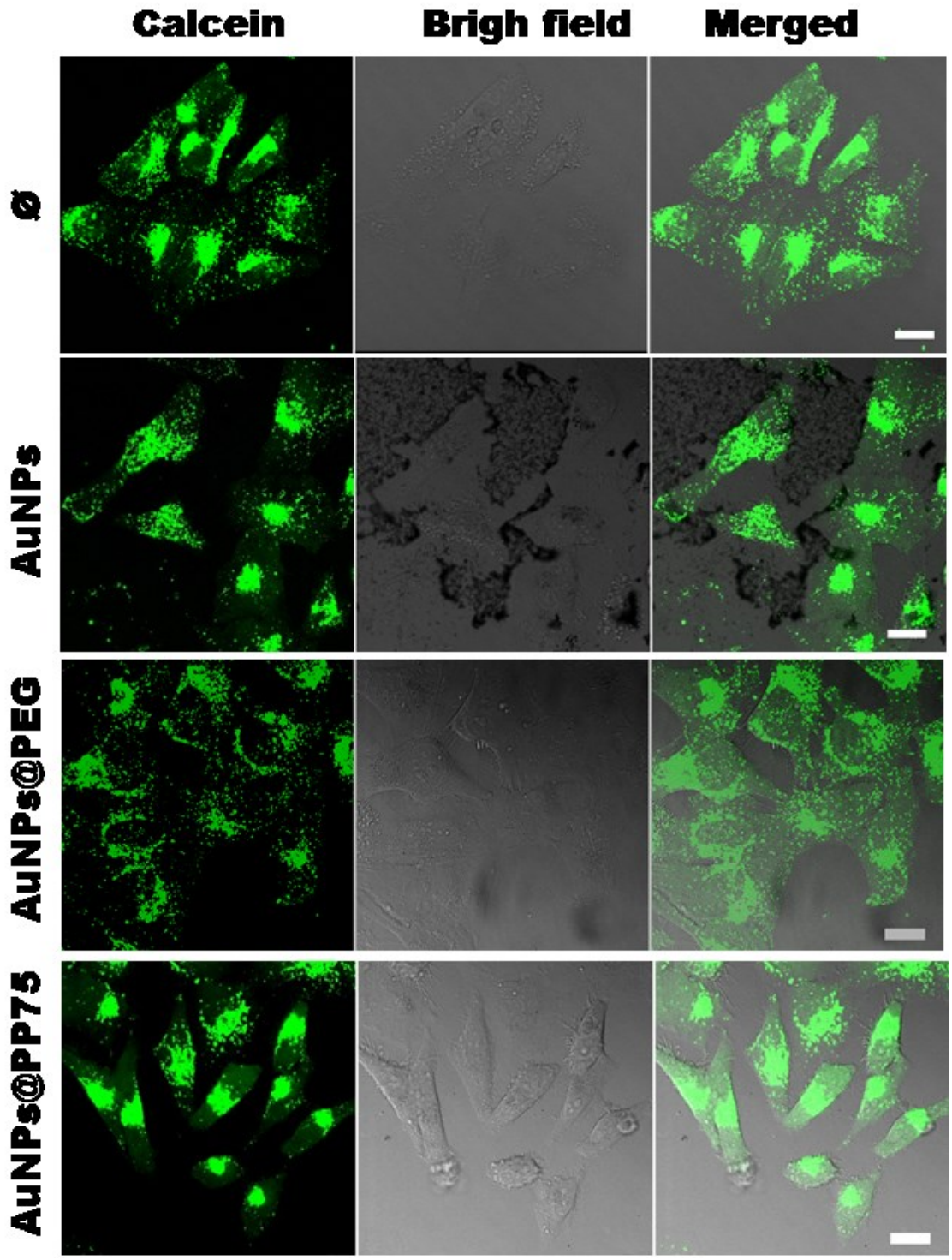


Figure 4-23 Confocal microscopy images of HeLa cells treated with 2.0 mg mL^{-1} calcein only, both 2.0 mg mL^{-1} calcein and 10 nM AuNPs, both 2.0 mg mL^{-1} calcein and 10 nM AuNPs@PEG2k and both 2.0 mg mL^{-1} calcein and 10 nM AuNPs@PP75. Images were acquired with a Zeiss LSM-510 inverted confocal unit (x40 magnification) after 24 h of uptake and 6h of further incubation. Scale bar: 20 µm.

4.3 Chapter summary

In this chapter, highly stable pH responsive endosomolytic AuNPs have been prepared via simple grafting of PP75 polymer to the surface of the AuNPs. The nanohybrids could be easily redispersed in a wide range of conditions and in the presence of salts with long term colloidal stability. The pH responsiveness of the system has also been observed below pH 6.0 where the conformation change of the polymer, from coil-to-globule, and the decrease of the steric stabilisation lead to the collapse of the chains on the AuNPs surface and the AuNPs agglomeration respectively. As for PP75, the pH responsive behaviour of the hybrid AuNPs is quick and highly reversible. *In-vitro* evaluation demonstrated a low cytotoxicity towards HeLa cells up to 10 nM after 48 h treatment with an internalisation rate estimated at 0.8 x 10^6 AuNPs per cell. Besides the conformational change, PP75 also demonstrated to retain its endosomolytic properties as demonstrated under confocal microscopy. To my knowledge this is the first time that anionic membrane active AuNPs are reported. The above properties give the nanohybrid the potential to be used as a smart platform for intracellular delivery.

Chapter 5 Chemo- and phototherapy

Chapter 5 describes the synthesis of doxorubicin (DOX) loaded AuNPs for chemo-photothermal therapy, in particular the optimisation and characterisation of the synthesis, the quantification of the loading efficiency, the optimisation of the laser settings and the *in-vitro* biological evaluation of the intracellular delivery and cytotoxicity in human uterine sarcoma cells, MES-SA and their DOX resistant analogue MESSA-Dx5.

5.1 Introduction

This chapter investigated the potential use of the AuNPs@PP75 as a drug delivery vector. Amongst the chemotherapeutics, doxorubicin, DOX, was chosen as a model drug since it is one of the most studied therapeutics.[279,280] DOX belongs to the anthracycline family of antibiotics and acts by intercalating DNA and hindering the DNA repair and generation of free radicals leading to cellular membrane damages.[236] It is commonly used as injectable formulation to treat leukaemia, ovarian and breast cancer amongst others.[281]

However, serious side effects such as heart damage and the development of MDR have reduced its clinical use.[280] Furthermore, like many other chemotherapeutic drugs, the targeting efficiency is very low leading to a large biodistribution in tumorous but also in healthy organs. AuNPs may provide a suitable platform for the successful delivery to the target cells thus improving the drug efficacy and reducing the side effects especially since NPs have demonstrated to be able to by-pass the MDR drug efflux.[124,281]

The first doxorubicin loaded nanoparticulate system approved by FDA was Doxil, the PEGylated liposome containing doxorubicin, in 1995. The liposomal system demonstrated the longer circulation time and improved pharmacokinetic profile. Several other doxorubicin-loaded liposomal systems have since then been approved.[280]

As mentioned in Chapter 1 Introduction section 1.2.3, AuNPs are a good candidate for phototherapy thanks to their photothermal properties and have gained a strong interest in research over the last decades.[55,62,282] The laser irradiation has been exploited for imaging[73,283,284], especially interesting for diagnostics purposes, temperature-triggered drug release[285] and photothermal therapy via hyperthermia.[60,142,282,286] Photothermal therapy (PTT) is a targeted therapy based on hyperthermia of the cancer cells with limited damage to the healthy cells. Used alone, PTT may not lead to the complete tumour destruction especially if zones of high vascularisation are concerned leading to the quick heat dissipation.[287]

Combining the PTT with the chemotherapy has appeared as a smart strategy and has rapidly gained in popularity.[59,61,115] The multimodal therapy has proven enhanced

toxicities via synergistic effects compared to each single treatment but also to their additive action[58]. Additionally, the light irradiation can also be used for light-triggered bond cleavage for drug release [135,136] for the design of multifunctional platforms.

The most common AuNPs used for PTT are nanoshells,[6 17] nanorods,[17] hollow gold nanospheres[287] and nanocages[61,282,288] since the localised surface plasmon resonance (LSPR) can be tuned in the NIR region where the absorption by the tissue is minimal. Thus the laser therapy can reach deeper tumours even though the distance is still limited at 10 cm below the skin, observed for breast tissues,[289] whilst fibre optics are necessary for deeper sites.[60] Gold nanospheres have also been reported with good results *in-vitro* for proof-of-concept purposes since their absorption can easily be tuned via surface or shape modification to correspond to the biological window.[142] Nevertheless, further progresses still need to be made since no AuNP-based photothermal treatment is currently available on the market and only one system (AuroLase, Nanospectra) is in clinical trial.[60]

The aim of this chapter is to explore the drug loading and release capabilities of the novel anionic membrane active hybrid AuNPs developed in Chapter 4 pH-responsive nanohybrids. The first part of this chapter details the optimisation of drug loading and stabilisation of the DOX loaded AuNP@PP75. In the second part, the simultaneous use of PTT via laser irradiation with chemotherapy was investigated and the synergistic effect on the cell growth inhibition was analysed. Two cell lines, MES-SA and MES-SA/Dx5 (the latter sensitive and resistant to DOX), were used to test the effectiveness of the nanoplatform on multi-drug resistance.

5.2 Results and discussion

5.2.1 Synthesis strategies

Several strategies can be employed for the loading of drugs on AuNP carriers. They all present their advantages and drawbacks. Furthermore, those different strategies usually determine different drug release mechanisms. That is why it is important to carefully consider the overall strategy of loading in the light of the actual purpose of the therapy.

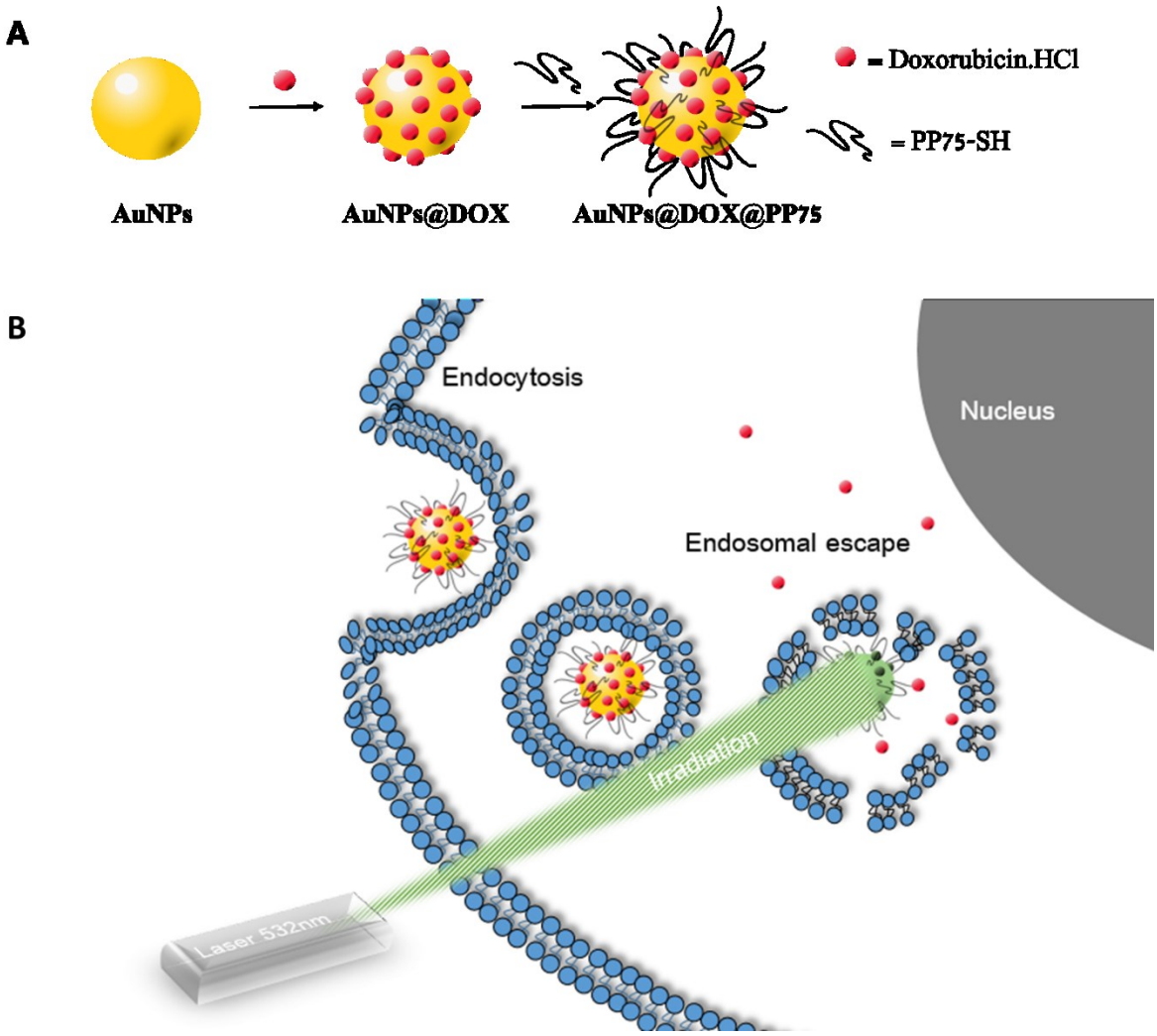
The aim of this study was to employ AuNPs functionalised with an anionic amphiphilic polymer as DOX carrier.

The most common strategies for DOX loading involve the direct adsorption of the drug molecules or the grafting requiring a pre-modification step. DOX has a ketone and an amine group suitable for pre-modification with hydrazone and amide bonding for instance. The bonding between the DOX molecules and the AuNPs or any grafted specie on the AuNP surface ideally needs to fulfil two requirements that are often contradictory: (i) a strong bond to avoid the release of free drug responsible for systemic toxicity and (ii) a loose bond for effective release to the cytoplasm and entry to the nucleus where DOX plays its anticancer action. DOX has been modified with thiol groups for direct attachment on the AuNP surface via Au-S bonds or via disulfide bonds with a sulfur containing specie. The release of payloads in that case is achieved via reduction with intracellularly abundant thiol molecules. The use of acid cleavage linkage for pH-triggered drug release is also a popular approach.

The adsorption method was chosen for four main reasons: (i) it is the easiest method since it does not require any chemical modification of DOX, hence it is perfectly adapted for a proof-of-concept study; (ii) some previous work has reported the alteration of the pH-dependant response and thus the endosomolytic properties of the polymer following modification with PEG molecules[172,173] so modification of the polymer via grafting should be avoided before investigating the real impact of the grafting ; (iii) some previous work has also shown that the endosomal escape occurred before the hydrazone bond between DOX and PLP could be cleaved leading to the unsuccessful nucleus entry;[290] (iv) the grafting of DOX via the thiol group may compete with the grafting of the polymer on the AuNPs surface since ligand-exchange can take place. Additional advantages of the loading by complexation include: easy scale-up, low cost and predictable release kinetics.[115]

Several options were then considered for the loading of both DOX and PP75: DOX first, PP75 first or simultaneous loading. The last option was rejected to gain more control on the loading. DOX was then selected as the first molecule to be added to maximise the drug loading and also to limit the interaction between positively charged DOX with COO^-

groups of PP75 that could occur in the case PP75 would be loaded first or for simultaneous loading. In AuNPs@DOX@PP75, PP75 chains play three distinct roles: pH-responsive membrane activity, stabilisation and DOX protection. The scheme of the selected synthesis process for the DOX-loaded nanohybrid is presented in Scheme 5-1.



Scheme 5-1 (A) Preparation of AuNPs@DOX@PP75. (B) Principle of the dual therapy.

5.2.2 Drug loading optimisation

The first step of the therapeutic platform optimisation was to determine the amount of drug that could be loaded without impairing the AuNPs stability. Curry *et al.*[116] reported a maximum of 550 drug molecules per 13-nm citrate-capped AuNP by fluorescence measurement. Assuming a similar footprint could be achieved, this would represent 865 DOX molecules per AuNP for a maximum coverage which is equivalent to 3.22 μg for 1 mL AuNPs. The details of the calculations are present in Appendix C (equations C-1 to C-4). It should be noted that this coverage does not correspond to the saturation of the AuNPs. Lee *et al.*[129] calculated the maximal coverage density based on the theoretical footprint of DOX molecules (Mw =543.52) conjugated with 3-[2-pyridyldithio] propionyl hydrazide (PDPH) (Mw = 229.32) and observed the aggregation of the AuNPs for coverage higher than 20% of the theoretical maximal coverage density due to the destabilisation of the electrostatic repulsion.

Table 5-1 Initial loading concentrations of DOX.

Coverage [%]	DOX [μg mL^{-1} AuNPs]	DOX/AuNPs ratio [wt%]
0	0	0.0
10	0.3	0.2
30	0.9	0.5
50	1.5	0.9
75	2.25	1.3
100	3	1.8
200	6	3.6
300	9	5.4
500	15	8.9

Solutions with DOX concentrations corresponding to 10-500% of the theoretical maximum coverage were prepared and added to the AuNPs. The DOX loading was

expressed as DOX/AuNPs wt% (Table 5-1). The details of the calculations are reported in Appendix C (equations C-5 to C-10).

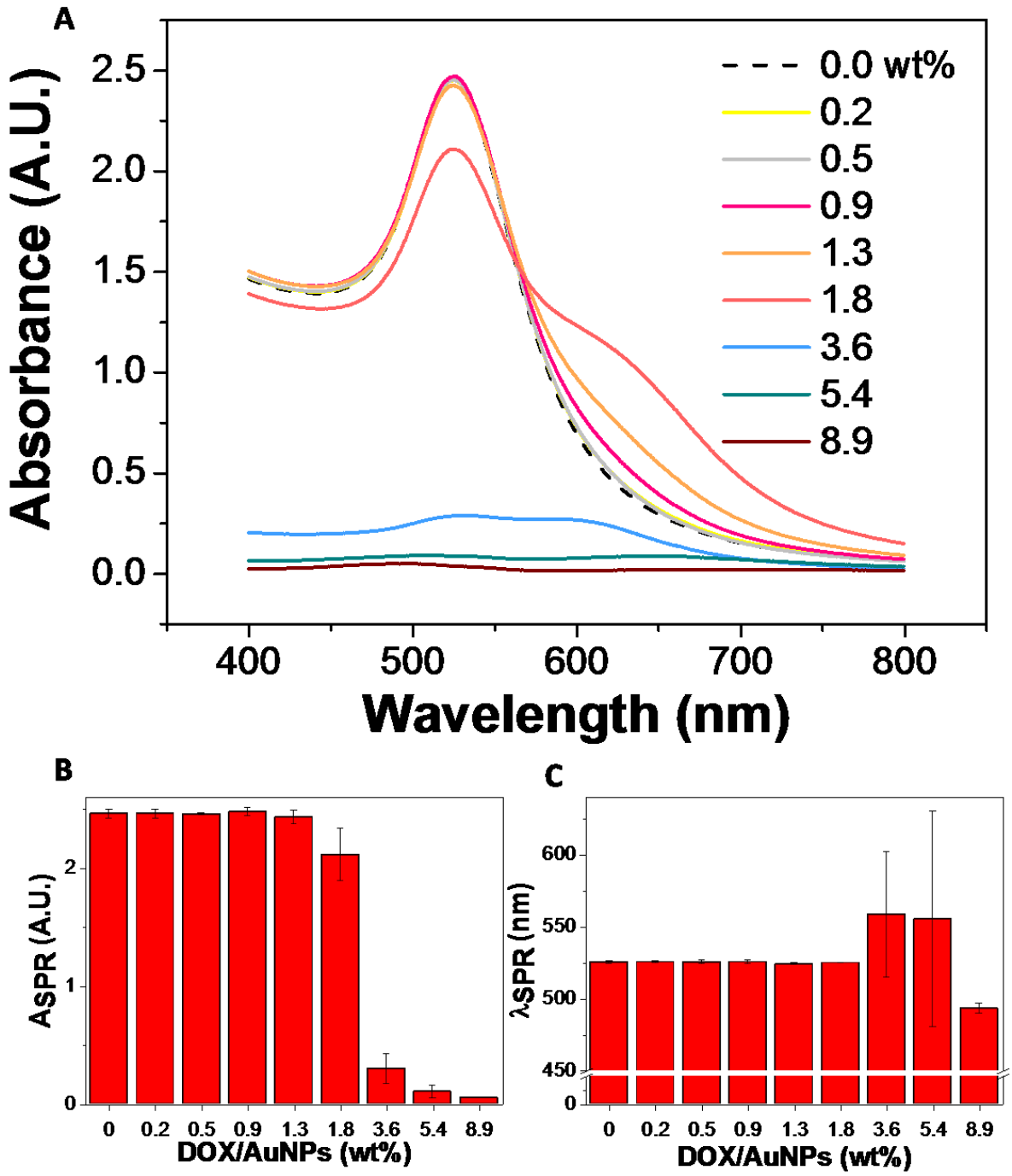


Figure 5-1 Optimisation of DOX loading. (A) UV-vis scans of AuNPs@DOX at increasing DOX/AuNP loading ratios (expressed in wt%). (B) SPR absorbance and (C) SPR wavelength at increasing DOX/AuNP ratios. Error bars represent standard deviations of triplicate measurements.

The UV spectra and fluorescence of the supernatants and the colloidal solutions after redispersion in H_2O were recorded. The results are presented Figure 5-1and Figure 5-2.

As reported in the literature[129] the adsorption of DOX above a certain amount could lead to the agglomeration of AuNPs, as evidenced by the appearance of a bump from 570 nm on the UV spectrum. The displacement of citrate molecules by DOX molecules led to destabilisation of the AuNPs due to the interparticle Van der Waals forces.[116] Based on the analysis of the UV spectra and the values of absorbance and wavelengths at the SPR, a maximum permissible loading concentration of 1.3 wt% was decreed since above this value aggregation started to appear. These results confirmed the successful adsorption of DOX on the AuNP surface. Curry *et al.*[116] reported a diffusion-limited kinetic mechanism for the adsorption of DOX on the citrate-coated AuNPs with most of the citrate molecules replaced by the DOX molecules in less than 30 seconds. The authors stated that the adsorption process was not based on electrostatic interactions but on hydrophobic associations followed by cation Au^{+}-π interactions and gold carbonyl coordination.

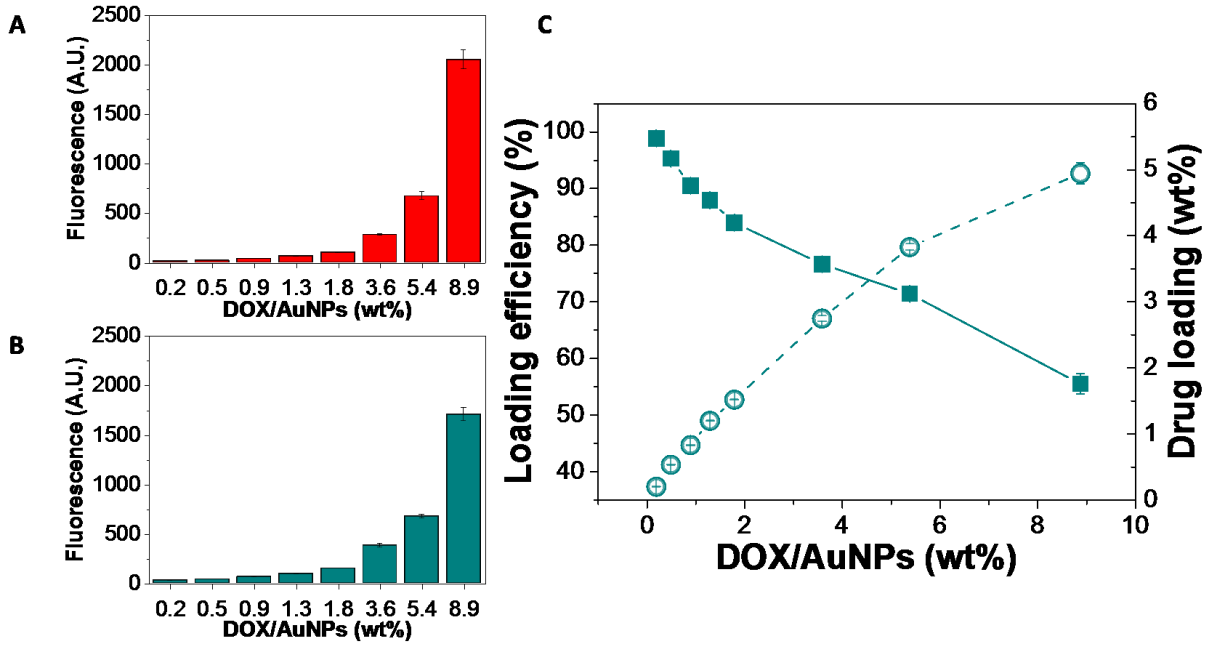


Figure 5-2 Characterisation of the loading efficiency of AuNPs@DOX at increasing DOX/AuNP loading ratios. (A) Fluorescence measurement (475nm/580-640 Exc/Em) of as synthesised AuNPs@DOX. (B) Fluorescence of the supernatants after centrifugation. (C) Drug loading (circles) and loading efficiency (squares) with the DOX/AuNPs loading ratio. Error bars represent standard deviations of triplicate measurements.

Figure 5-2(A) shows the fluorescence of the as-synthesised AuNPs@DOX samples. It is clear that the fluorescence level increased with the initial DOX loading concentration. High fluorescence values were observed when the DOX/AuNP ratio was above 3.6 wt%. The fluorescence of the AuNPs@DOX solution at 8.9 wt% of DOX/AuNPs reached 2050 A.U., which was lower than that of free DOX at the same DOX concentration (~5000 A.U. at 15 μg mL^{-1} DOX) as seen in the calibration curve in Appendix C (Figure C-1). This suggests that DOX molecules were successfully adsorbed on the AuNP surface because AuNPs are known to quench DOX fluorescence.[129]

The unadsorbed drug molecules were then effectively separated by centrifugation and the fluorescence of the supernatants was measured to evaluate the concentration of unbound drug molecules and deduce the drug loading (wt%) and the loading efficiency (%). The supernatants showed similar fluorescence levels than the as-synthesised samples proving that the centrifugation did not remove the adsorbed DOX and appears to be a suitable purification method. As shown in Figure 5-2(C), the drug loading increased with the DOX/AuNP ratio whilst the loading efficiency decreased. At 1.3 wt% AuNPs@PLP loading ratio, the drug loading and the loading efficiency were 1.2 ± 0.0 wt% and 87.8 ± 0.4% respectively.

Depending on the application one or both parameters may be considered as a factor of choice for optimisation of the platform design. Herein, a single centrifuge step was preferred to limit risk for AuNPs agglomeration. In order to maximise the loading efficiency, a low loading ratio (DOX/AuNPs = 1.3 wt%) was chosen to limit the amount of unbound DOX and to reduce the potential interactions between DOX and the COO^- groups of PP75

5.2.3 Grafting with PP75

To evaluate the impact of the successive functionalisation of PP75, AuNPs@DOX were prepared with the initial drug loading of 1.3 wt% and after purification various concentrations of thiolated PP75 were added. The initial amount of PP75 added was expressed in PP75/AuNPs weight ratios (wt%) (Table 5-2). The calculation is detailed in Appendix C (equation C-11).

Table 5-2 Initial loading concentrations of PP75.

PP75 [µg mL^{-1} AuNPs]	PP75/AuNPs [wt%]
0	0.0
10	6.0
20	11.9
30	17.9
50	29.8
100	59.5

Figure 5-3 shows the absorbance spectra of AuNPs@DOX@PP75 after redispersion in H_2O. To investigate the impact of the PP75 grafting on the drug loading, the AuNPs@DOX were purified by centrifugation before the addition of PP75. AuNPs@DOX without PP75 polymer presented agglomeration after two centrifugation steps that was not observed for AuNPs@DOX@PP75. Furthermore, the stability of the colloidal solution increased with the PP75 concentration. This suggests that PP75 was able to protect the AuNPs@DOX from agglomeration during centrifugation and enabled the stabilisation after redispersion.

To evaluate the quantity of DOX detached from the AuNP surface due to the centrifugation and/or the grafting of PP75 chains, the fluorescence of the solutions before centrifugation (Figure 5-4(A)) and their supernatants after centrifugation (Figure 5-4(B)) were measured. Before centrifugation, the fluorescence of the AuNPs@DOX@PP75 was slightly higher than that of the AuNPs@DOX (50-70 A.U. vs. 30 A.U.) which can be explained by the very limited detachment of DOX from the AuNP surface during the PP75 grafting. However, the fluorescence decreased from ~60 A.U. to ~40 A.U., indicative of less free DOX present in the solution, with further increasing the polymer concentration. The polymer might help stabilise the colloids and thus the stabilisation of the DOX loading so less detachment is observed. The trend observed is similar for the fluorescence of the supernatants, although slightly higher, which might be a sign of detachment of DOX under

centrifugation. The fluorescence values of the supernatants were used to calculate the loading efficiency and the drug loading as previously explained in section 5.2.2. (Figure 5-4(C)).

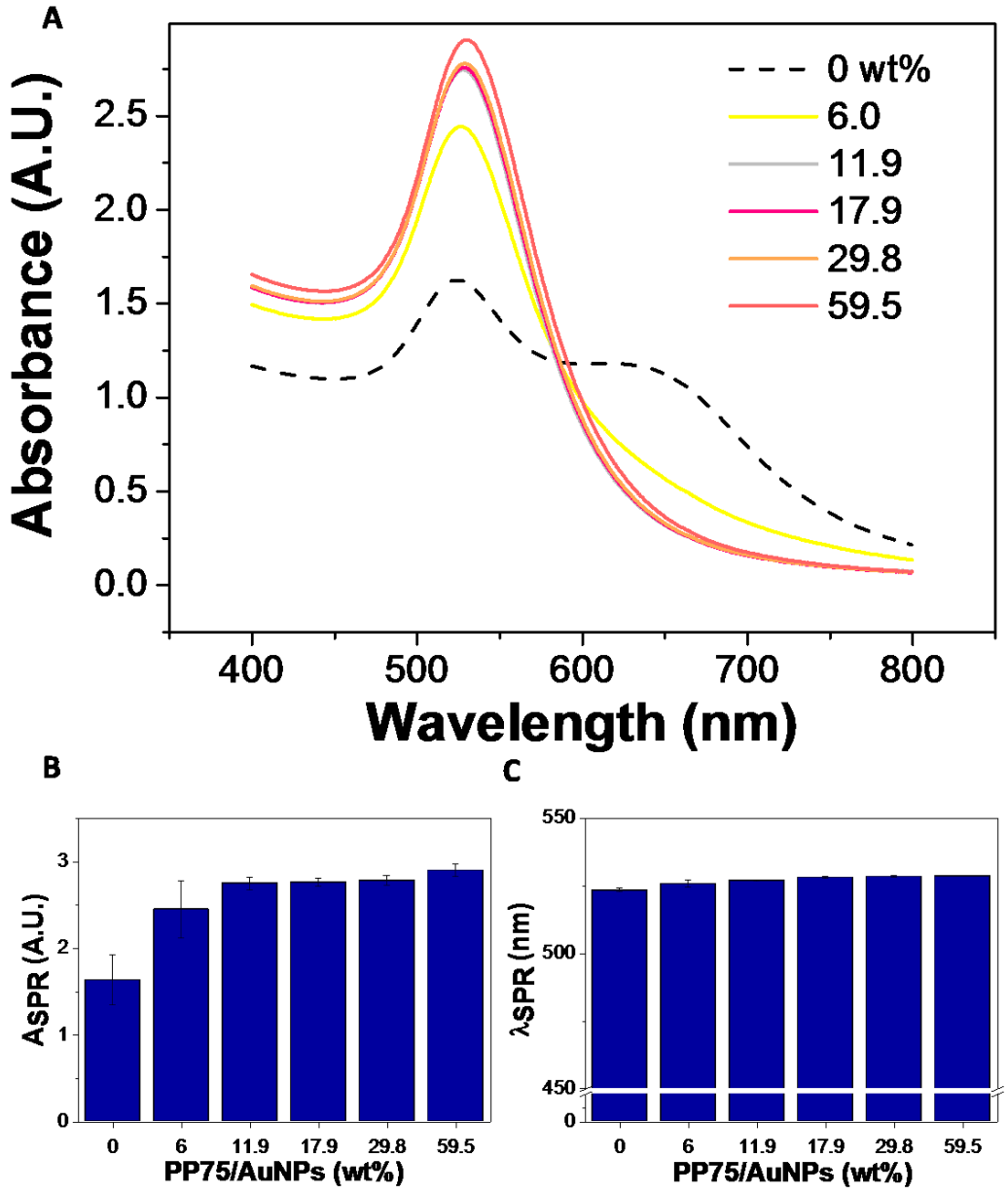


Figure 5-3 Optimisation of AuNPs@DOX@PP75 prepared with initial drug loading of 1.3 wt%. (A) UV-vis scans of AuNPs@DOX at increasing PP75/AuNP ratios. (B) SPR absorbance and (C) SPR wavelengths at increasing PP75/AuNP ratios. Error bars represent standard deviations of triplicate measurements.

After functionalisation with DOX at the initial loading of 1.3 wt%, the AuNPs@DOX showed a loading efficiency of 87.8 ± 0.4% and a drug loading of 1.2 ± 0.0 wt%. After functionalisation with PP75 the loading efficiency did not decrease significantly and varied between 89% and 93%. This result demonstrates the limited detachment of DOX molecules upon PP75 grafting as confirmed by the stable drug loading at 1.2 wt% and the fluorescent results.

Overall, PP75 stabilised the AuNPs@DOX with a very limited influence on the drug loading. Based on the optimisation results 0.9 wt% and 17.9 wt% as initial loading of DOX and PP75 respectively were chosen for the following motivations: (i) high drug loading efficiency and low concentration of unbound DOX; (ii) good stabilisation of the system and (iii) low concentration of ungrafted PP75.

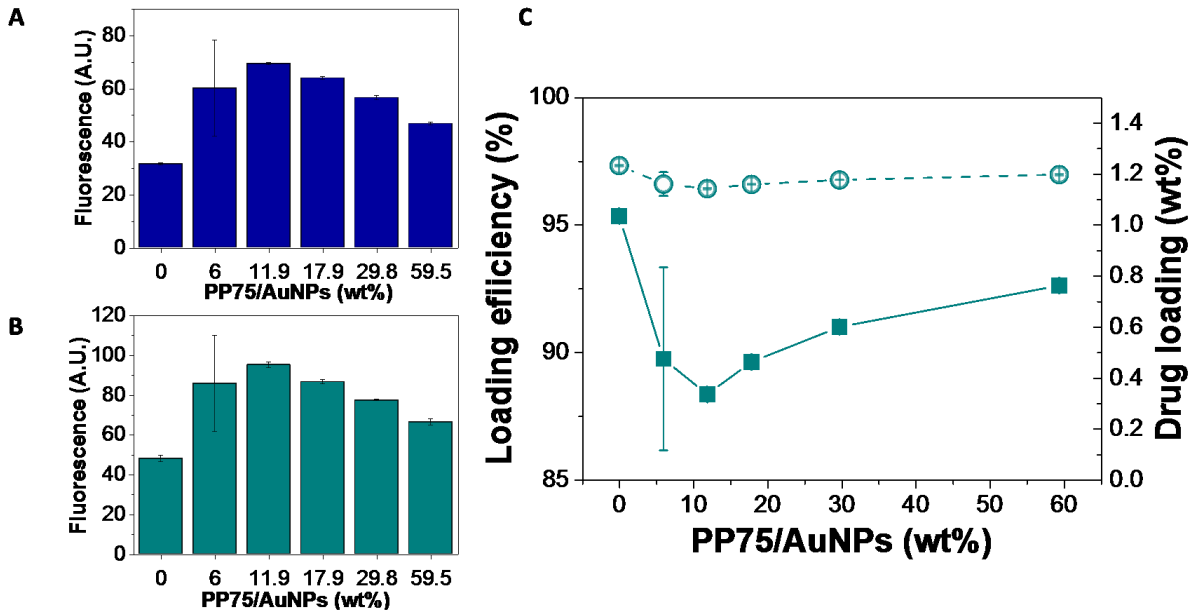


Figure 5-4 Characterisation of the loading efficiency of AuNPs@DOX@PP75 at increasing PP75@AuNP ratios with an initial DOX/AuNPs loading of 1.3 wt%. (A) Fluorescence measurement (475nm/580-640 Exc/Em) of as synthesised AuNPs@DOX@PP75. (B) Fluorescence of the supernatants after centrifugation. (C) Drug loading (circles) and loading efficiency (squares) with the PP75/AuNPs loading ratio. Error bars represent standard deviations of triplicate measurements.

To further study the impact of centrifugation on the drug loading, the levels of attached drugs have been compared between three different systems: AuNPs@DOX after one centrifugation; AuNPs@DOX@PP75 after one or two centrifugation steps (one after DOX

loading and one after PP75 loading) at an initial DOX loading of 0.9 wt% and an initial PP75 concentration of 17.9 wt%. As shown in Table 5-3, two centrifugation steps lead to the lowest levels of DOX loading. The therapeutic platform prepared with one final centrifugation step presented a DOX loading of 0.6 wt% and a loading efficiency of 70.3%. It is still unexplained why the loading efficiencies dropped from ~ 90% to ~ 70% after functionalisation with PP75 with the initial loading at 0.9 wt% compared to 1.2 wt%. Further studies might be needed on this point before drawing any conclusion. Since the loading efficiency of AuNPs@DOX@PP75 was slightly lower than for AuNPs@DOX the risk of complexation between the unbound DOX and the polymer chains was assumed to be limited.

Table 5-3 Drug loading and loading efficiencies for an initial loading ratio of DOX/AuNPs=0.9 wt%.

Samples	Number of Centrifugation steps	F_{sup} [A.U.]	DOX [µg per mL AuNPs]	DOX [wt%]	Loading [%]
AuNPs@DOX	1	123.8	1.1 ±0.0	0.7 ±	74.7 ±0.7
AuNPs@DOX@PP75	1	130.2	1.1	0.7	73.2 ±0.2
	2	80.3	0.9 ±0.0	0.5 ±0.0	59.5 ±0.6
AuNPs@DOX@PP75	1[a]	137.2	1.1 ±0.0	0.6 ±0.0	70.3 ±1.1

[a]For this sample a single centrifugation step was performed after both loadings (DOX and PP75) occurred.

Curry *et al.*[116] reported a maximum of 550 DOX molecules via adsorption per 13-nm AuNPs, equivalent to 1.14 wt%. However, Elbialy *et al.*[237] claimed a loading via adsorption of 10 wt% for the Fe_3O_4@AuNPs core shell AuNPs of ~24 nm diameter. The highest loading reported concerned covalently-conjugated doxorubicin: Aryal *et al.*[127] and F. Wang *et al.*[128] reported 23 wt% and 17 wt% DOX loading via hydrazine linker respectively. However, J. You *et al.*[115] obtained a DOX loading of 63 wt% via incubation with hollow gold nanospheres thanks to their high surface to area ratio.

AuNPs@DOX and AuNPs@DOX@PP75 after one or two centrifugation steps showed good stability after redispersion in H_2O (Figure 5-5). A slight red shift of the SPR peak can be observed for the PP75 functionalised AuNPs confirming the attachment of PP75 chains. The formulation obtained with one centrifugation step showed a slightly higher absorbance at the SPR, indicative of a better dispersion especially if compared to the formulation after two centrifugation steps.

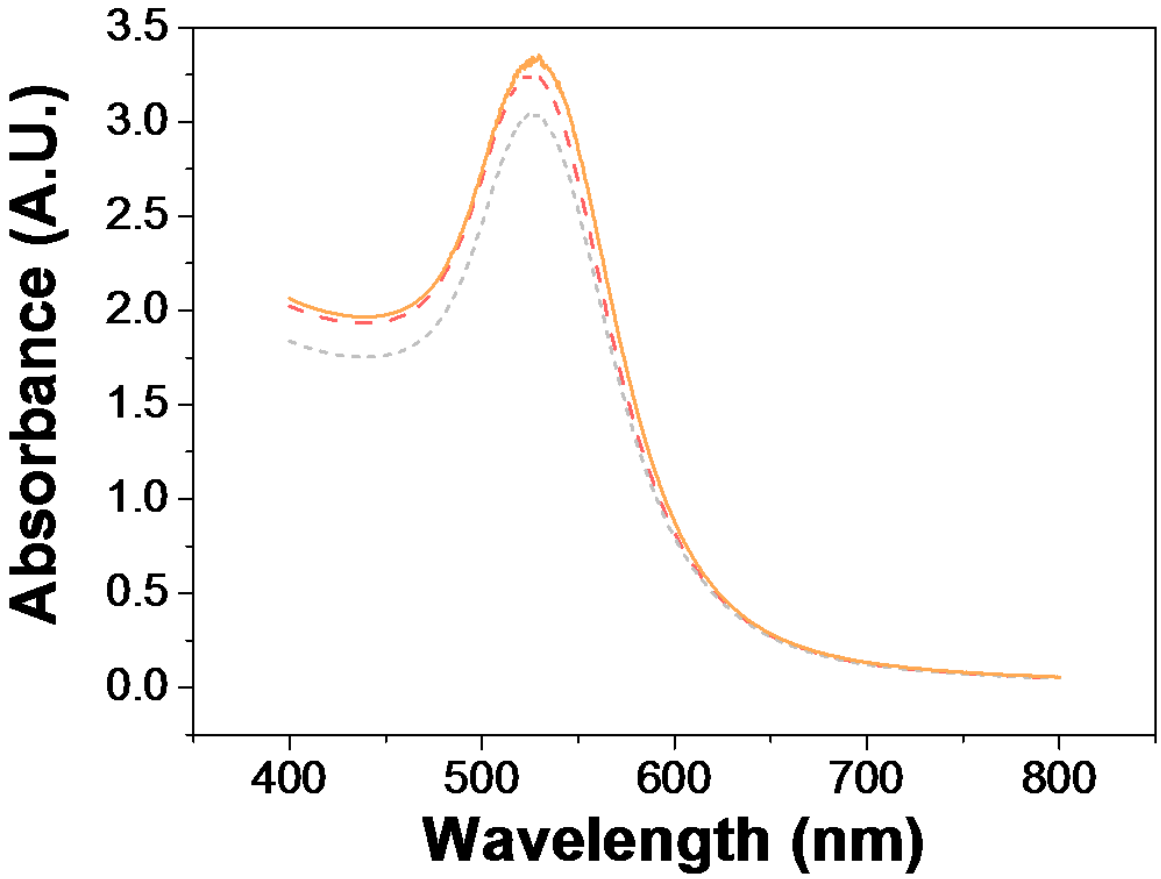


Figure 5-5 UV-vis spectra of AuNPs@DOX after one centrifugation (red long-dashed line); AuNPs@DOX@PP75 after two centrifugations (grey short-dashed line) and AuNPs@DOX@PP75 after one centrifugation (orange solid line).

5.2.4 Physico-chemical characterisation

From this point until the end of this chapter, AuNPs@DOX@PP75 refers to the formulation prepared with the initial loading ratio of 0.9 wt% and 17.9 wt% for DOX and PP75 respectively.

The FTIR spectra of AuNPs@DOX@PP75 (Appendix C Figure C-2) was very similar to AuNPs@PP75 (Chapter 4 Figure 4-1). The peak for the C=O bond at the 13-keto position (~1580 cm^{-1})[116] was not distinguishable on the FTIR spectra probably due to the overlap with the stronger neighbour bonds (amides) and the low respective quantity of DOX.

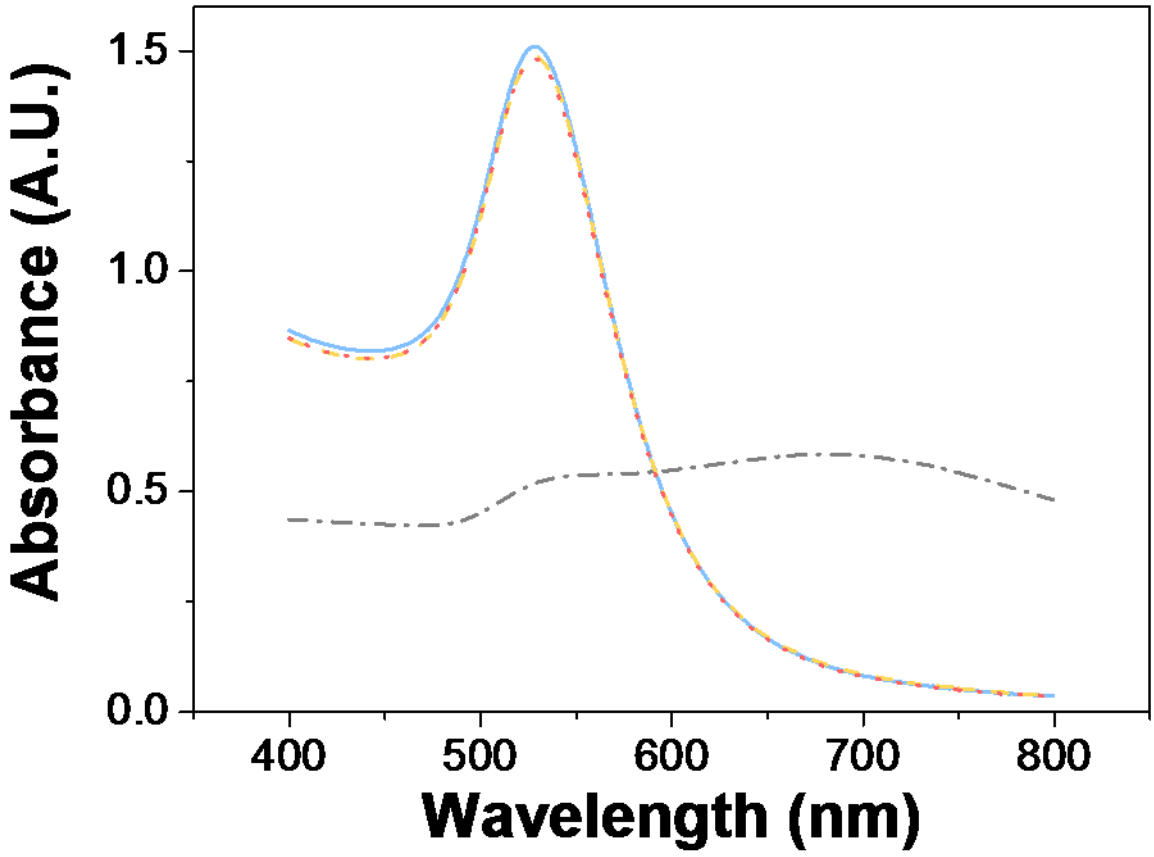


Figure 5-6 UV-vis spectra of AuNPs@DOX@PP75 solutions redispersed in H_2O (blue solid line), 100mM PB pH 7.4 (orange long-dashed line); 100mM PBS (0.15 M NaCl) at pH 7.4 (red dotted line) and 100 mM PBS (0.50 M NaCl) at pH 7.4 (grey dotted-dashed-line).

Figure 5-6 shows the absorbance spectra of the AuNPs@DOX@PP75 after one-day redispersion in different media: H_2O, PB, PBS with 0.15 M and 0.5 M NaCl at pH 7.4. The AuNPs showed a good stability upon redispersion in all the media except at 0.5 M NaCl where the maximum absorbance decreased from 1.5 to 0.5 A.U. with a flat profile characteristic of AuNPs agglomeration. As previously mentioned (section 3.2.3), ions in solution decreases the Debye length and the aggregation barrier to NPs facilitating the aggregation.[191,233] The stabilisation offered by PP75 at this grafting density was efficient until at least 0.15 M NaCl which corresponds to the physiological saline conditions.

Table 5-4 Hydrodynamic sizes and zeta potential values obtained via light scattering measurements.

Samples	AuNPs	AuNPs@DOX	AuNPs@PP75	AuNPs@DOX@PP75
D_H [nm]	23.8 ±0.9	46.4 ±2.9	30.1 ±2.1	32.1 ±0.3
PDI	0.188	0.287	0.212	0.250
ξ [mV]	-41.7 ±0.1	-32.0 ±0.0	-35.5 ±4.8	-34.9 ±2.4

Table 5-4 summarises the measurements of size and zeta potential of the four systems: citrate coated AuNPs, AuNPs@DOX, AuNPs@PP75 and AuNPs@DOX@PP75. As expected the mean diameter of AuNPs@DOX@PP75, 32 nm, was almost 10 nm bigger than the citrate coated AuNPs and slightly higher than AuNPs@PP75 which might be caused by PP75 chains in a more stretched conformation since their footprint was reduced by the presence of DOX. The mean diameter of AuNPs@DOX (46.4 nm) was far above the others, indicative of the aggregation of NPs as suggested by the higher PDI and the higher zeta potential value. This might be due to the adsorption of the positively charged DOX, which replaced or covered the negative charges of citrates on the AuNP surface. AuNPs@PP75 and AuNPs@DOX@PP75 presented similar zeta potentials demonstrating once again the successful functionalisation. AuNPs@DOX@PP75 had a lower zeta potential value than AuNPs@DOX due to the grafting of the anionic polymers bearing negative charges at this pH (~5.9).

The TEM images (Figure 5-7) also demonstrated the higher stability of the AuNPs@DOX@PP75 compared to the AuNPs@DOX. The polymer layer was unfortunately not easily visible under the TEM and could be slightly distinguished for the AuNPs close to the carbon coating boundary ((Figure 5-7(E)).

The prepared AuNPs@DOX@PP75 have been successfully prepared and characterised. The next section presents their biological evaluation in the presence of the DOX-sensitive human uterine cell line MES-SA and its drug resistant counterpart MES-SA/Dx5.

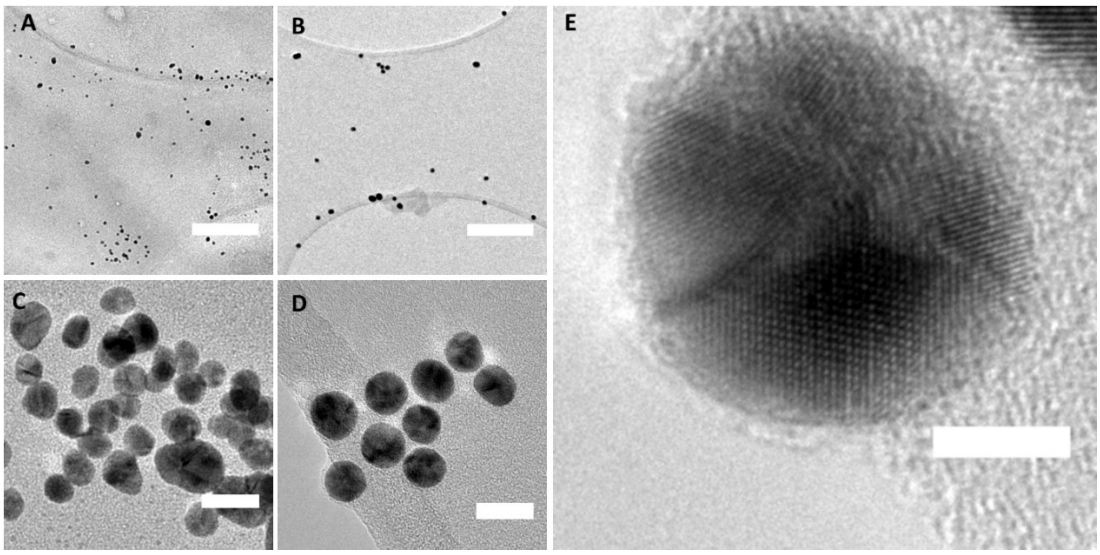


Figure 5-7 TEM images of AuNPs@DOX and AuNPs@DOX@PP75. (A) AuNPs@DOX at low magnification (scale bar 200 nm). (B) AuNPs@DOX@PP75 at low magnification (scale bar 200 nm). (C) AuNPs@DOX at high magnification (scale bar 20 nm). (D) AuNPs@DOX@PP75 at high magnification (scale bar 20 nm). (E) Zoomed in image of AuNPs@DOX@PP75 (scale bar 5 nm).

5.2.5 Biological evaluation of the multimodal therapy

The cell viability has been assessed after 2 h and 24 h of treatment of the DOX-sensitive human uterine cell line MES-SA (Figure 5-8) and its drug resistant counterpart MES-SA/Dx5 (Figure 5-9) with AuNPs@DOX@PP75 and AuNPs@PP75 respectively.

As shown in Figure 5-8, the MES-SA cells well tolerated the treatment with AuNPs@DOX@PP75 at up to ~5 nM. When the concentration of AuNPs@DOX@PP75 was further increased to 100 nM, the relative cell viability decreased to 66% after 2 h and 35% after 24 h. The IC_{50} of AuNPs@DOX@PP75 toward MES-SA was determined to be 15

nM after 24 h of treatment. The toxicity was mainly attributed to the DOX molecules since the toxicity of AuNPs@PP75 was negligible after 2 h and the relative cell viability was still 70% after 24 h at 100 nM.

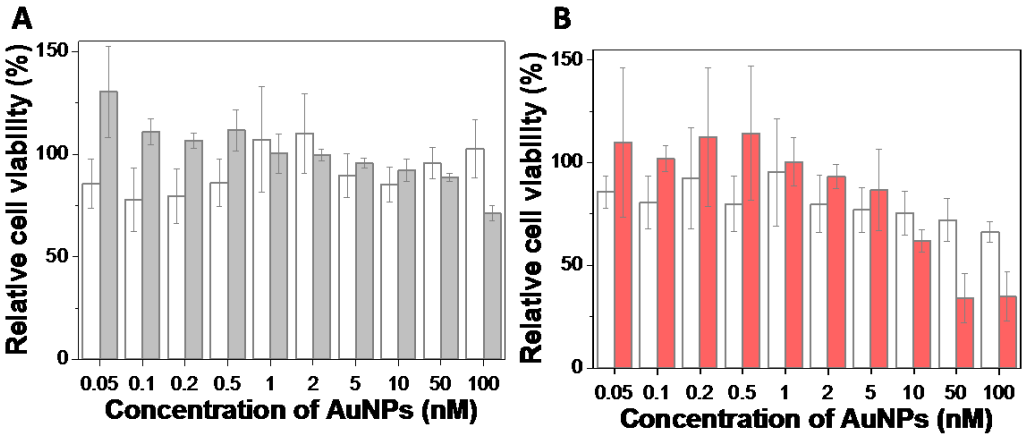


Figure 5-8 Concentration-dependent relative viabilities of MES-SA cells treated with (A) AuNPs@PP75 and (B) AuNPs@DOX@PP75 for 2 h (open bars) and 24 h (close bars) as determined by alarmarBlue assay. Error bars represent standard deviations of five replicates measurements.

The same phenomenon was observed for the DOX-resistant MES-SA/Dx5 cell line (Figure 5-9). The MES-SA/Dx5 well tolerated the AuNPs@PP75 up to 100 nM for 24 h treatment (83.4% ± 7.2 cell viability). This interesting discovery could be due to the successful by-pass of the drug efflux in the multi resistance pathway. This hypothesis will be further investigated below by comparison with free DOX.

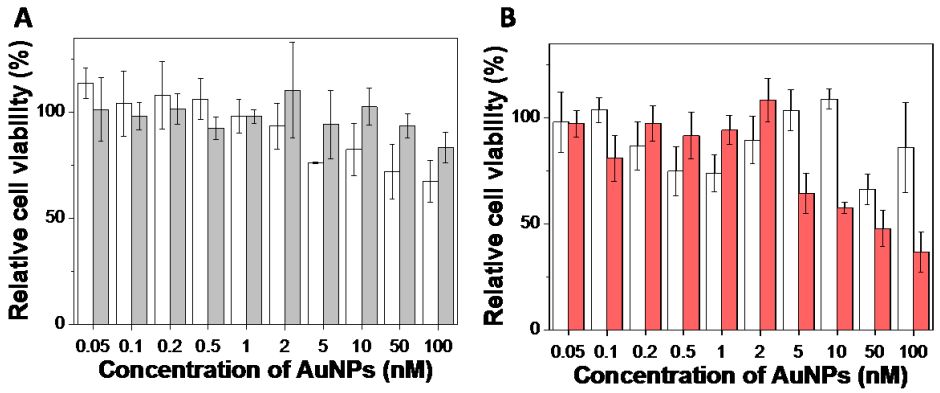


Figure 5-9 Concentration-dependent relative viabilities of MES-SA-Dx5 cells treated with (A) AuNPs@PP75 and (B) AuNPs@DOX@PP75 for 2h (open bars) and 24h (close bars) as determined by alarmarBlue assay. Error bars represent standard deviations of five replicates.

The biological response to the multimodal treatment combining chemotherapy with the action of DOX and phototherapy with the use of a laser was investigated. The 15 nm AuNPs shows a maximal absorbance at 520 nm. A green laser emitting at a wavelength of 532 nm was chosen in order to excite most efficiently the electrons on the surface of the AuNPs. The laser was placed vertically on top of the well plate during the phototherapy. The set-up is presented in Appendix C Figure C-3. The surface power density expressed as W cm^{-2} was calculated from the intensity of the laser and the laser beam diameter based on the calibration obtained with a laser power meter (Appendic C Figure C-4).

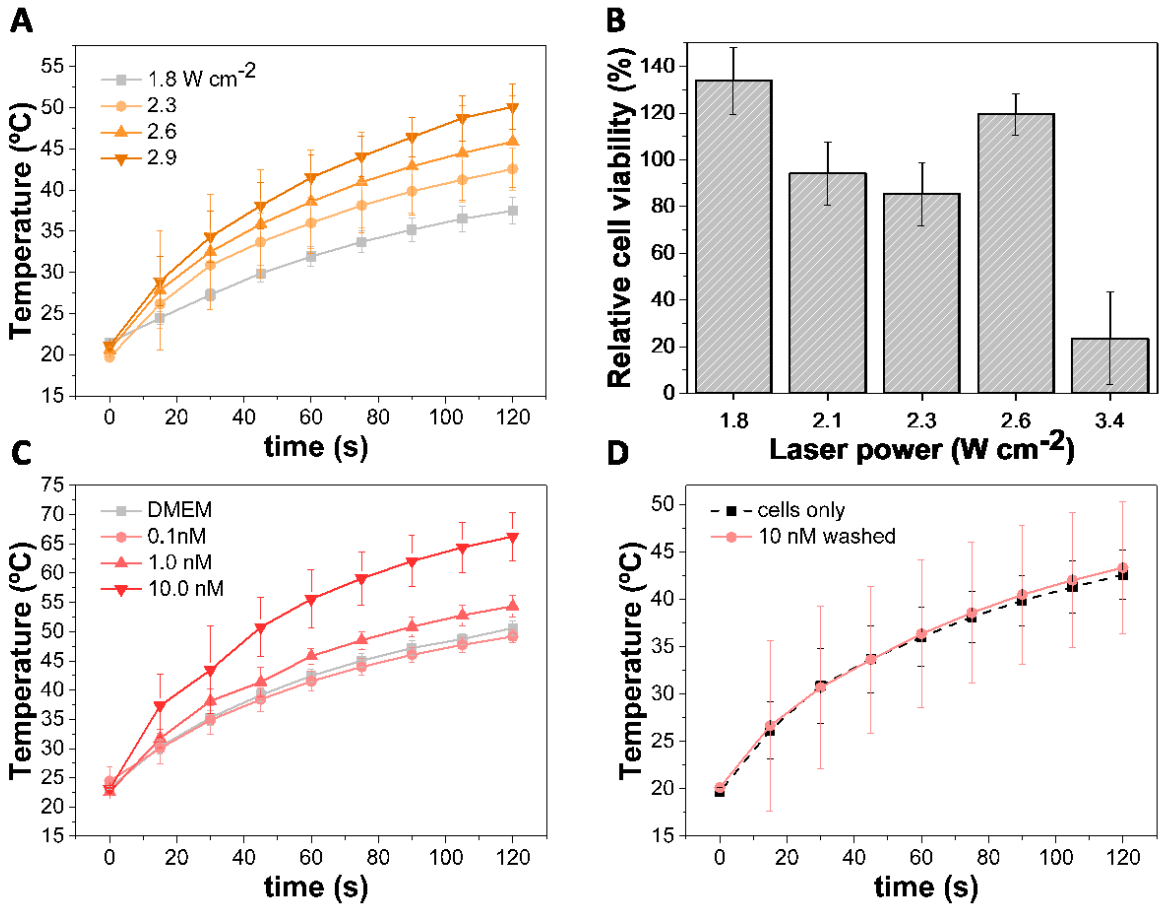


Figure 5-10 Optimisation of the laser power. (A) HeLa cell solution temperature monitoring with time. (B) Influence of the laser power on the viability of HeLa cells irradiated for 120 s as determined by alamarBlue assay. (C) Temperature monitoring of AuNPs@DOX@PP75 in DMEM medium under irradiation at 2.3 W cm^{-2}. (D) Temperature monitoring of cells only and cells incubated with AuNPs@DOX@PP75 at 10 nM for 24 h and then washed before irradiation at 2.6 W cm^{-2}. Error bars represent standard deviations of triplicate measurements.

To optimise the laser settings several experiments were performed in order to define the suitable time and laser power for: (i) noticeable effect on the temperature (usually around 42°C)[58] to obtain effective hyperthermia in the presence of AuNPs, and (ii) limited toxic effect toward the cells without AuNPs.

Figure 5-10(A) shows the increase of temperature over time of a solution in the presence of cells under irradiation at different powers. The temperature increased continuously from room temperature to 37.5°C at 1.8 W cm^{-2} and 50.1°C at 2.9 W cm^{-2} after 120 s. As seen in Figure 5-10(B) the cell viability after 120 s of irradiation was higher than 80% up to 2.6 W cm^{-2} and reached 23.5% at 3.4 W cm^{-2}. According to Figure 5-10(C), an increase of the solution temperature was observed with increasing the AuNPs concentration, demonstrating the thermal effect of AuNPs.

However, in the experimental conditions used, where the non-internalised AuNPs were washed away before irradiation of the HeLa cells, the temperature effect could not be precisely observed since both solutions, cells only and cells with the internalised AuNPs, exhibited the same temperature increase (Figure 5-10(D)). The irradiated internalised AuNPs will heat up the surrounding environment locally but the concentration of AuNPs was too low to be able to notice the effect at the scale of the solution, mainly because the thermos-couple used was detecting the bulk solution temperature. The temperature of the cell interior is expected to raise by a few degrees. Honda *et al.*[291] reported that one 40 nm AuNP irradiated at 532 nm with 1 mW increased the temperature by 10°C. Overall, 2.6 W cm^{-2} and 120 s were chosen as suitable parameters of time and laser power for the phototherapy.

The cytotoxicity of the dual therapy toward MES-SA cells was first evaluated (Figure 5-11). In this experiment, MES-SA cells were incubated with free DOX or AuNPs@DOX@PP75 for 24 h, then half of the samples were irradiated. The samples were then further incubated for 24 h before the cell viability was measured via alamarBlue assay.

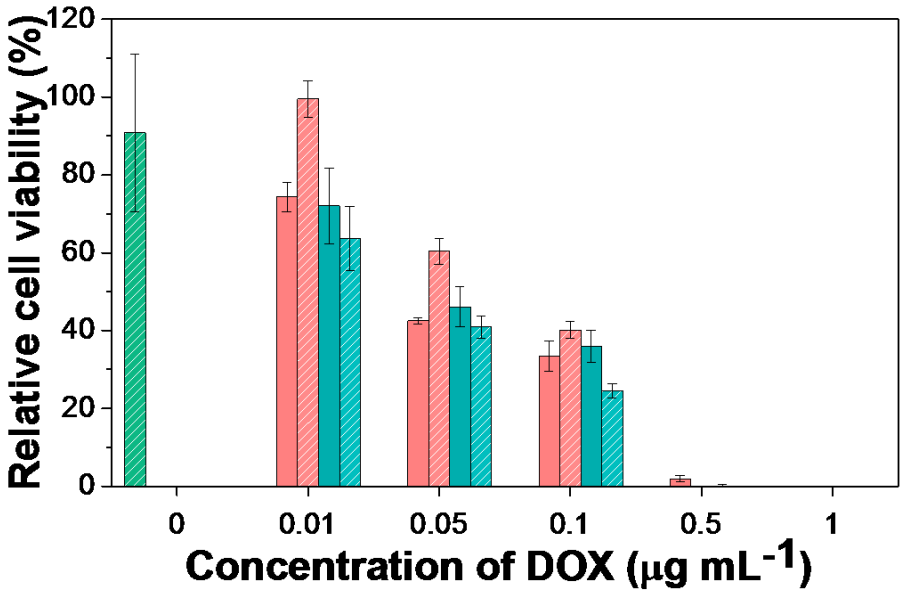


Figure 5-11 Concentration-dependent relative viabilities of MES-SA cells irradiated at 2.6W cm^{-2} for 120 s. The cells were treated with laser only (green striped bars); free DOX (red bars); free DOX and laser (red stripped bars); AuNPs@DOX@PP75 (blue bars); AuNPs@DOX@PP75 and laser (blue striped bars) as determined by alamarBlue assay. Error bars represent standard deviations of four replicates.

Three main observations could be made. First, the treatment with free DOX, with AuNPs@DOX@PP75 and with the dual therapy were significantly more toxic to the cells than the laser alone confirming the cells tolerated the laser at this laser power and the cytotoxicity was mainly caused by the effect of the drug and/or the hyperthermia in the presence of AuNPs. Second, the MES-SA cell line was extremely sensitive to the chemotherapy since the viability reached 0% at an equivalent drug concentration of 0.5 μg mL^{-1}. Third, the laser, in the presence of free DOX, seemed to lead to higher viabilities at low concentrations of DOX. It is not clear why the use of a laser had a positive influence on the cell viability in the presence of DOX and further experiments would be required to investigate this point. Overall, the nanoparticle drug delivery had a similar cell-killing activity with free drug even though free DOX entered cells by diffusion whilst nano-systems entered cells by endocytosis. This is an encouraging result considering the advantages of nanoparticles based therapy compared to free drug.

The last observation was validated by confocal microscopy (Figure 5-12). At an equivalent dose of 1 μg mL^{-1} of DOX most of the cells were dead. Nuclear localisation was

also found via the colocalisation of the blue and red fluorescence from Hoechst and DOX.[127,292]

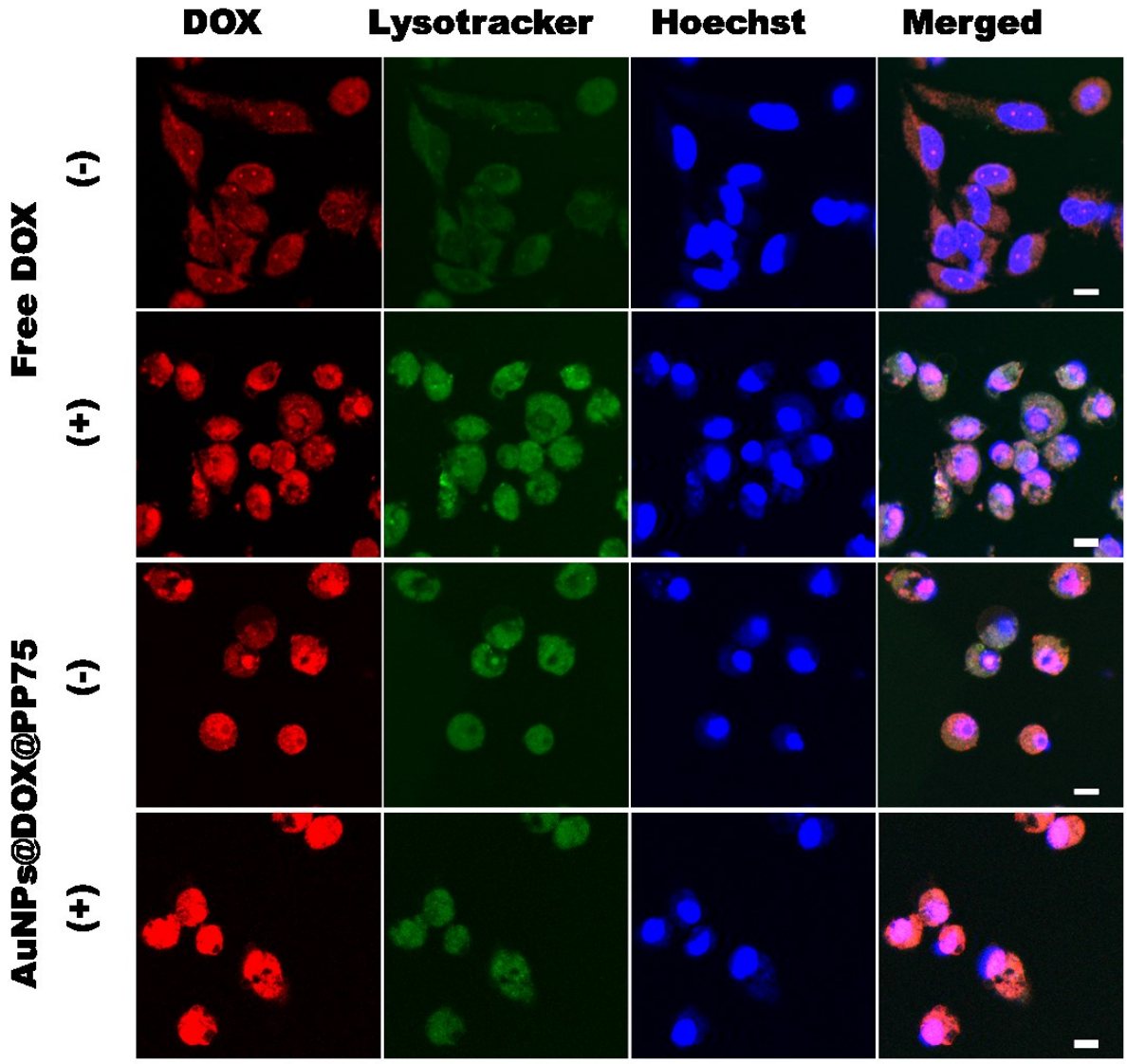


Figure 5-12 Confocal microscopy images of MES-SA cells treated with free DOX (1 μg mL^{-1}), AuNPs@DOX@PP75 (1 μg mL^{-1} DOX equivalent) for 24 h and irradiated (+) or not (-) for 120s at 2.6W cm^{-2}. Images were acquired with a Zeiss LSM-510 inverted confocal unit (x40 magnification). Scale bar: 10 μm.

The bright red fluorescence observed for the nanohybrids demonstrated the successful release of DOX molecules from the AuNPs since grafted quenched molecules would not be visible.[128] and the nuclear localisation suggests the intracellular release of DOX via thiol exchange with the intracellular thiols (e.g. GSH) has been reported many times in the literature. Curry *et al.*[116] demonstrated that 70% of DOX could be displaced by GSH in

30 min on the AuNP surface suggesting that the thiol-gold bond created by GSH was much stronger than the interactions between DOX and AuNPs. Furthermore, they observed the desorption of DOX at low pH thus it was concluded that both acidic pH in the endosomes and GSH trigger the DOX release intracellularly.

Figure 5-13 shows the relative viabilities of DOX-resistant MES-SA/Dx5 cells treated with laser only, free DOX, free DOX plus laser, AuNPs@DOX@PP75, and AuNPs@DOX@PP75 plus laser.

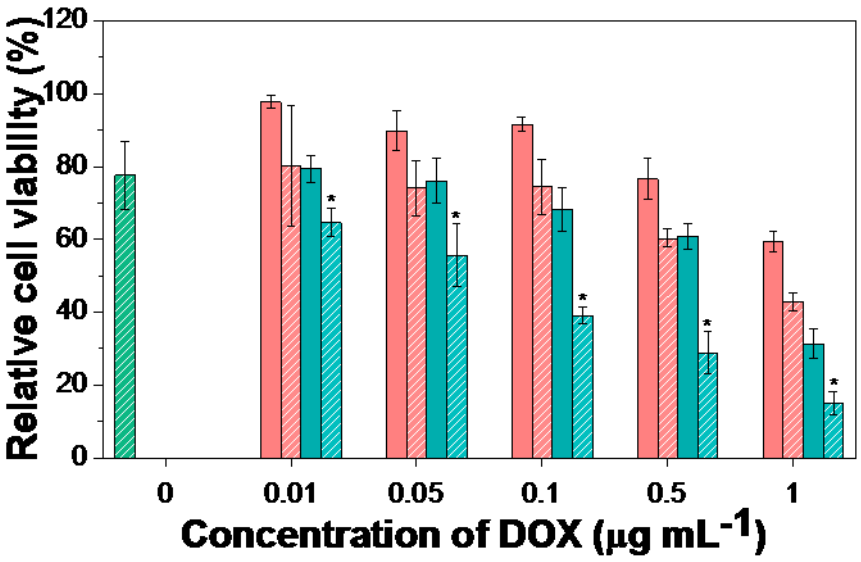


Figure 5-13 Concentration-dependent relative viabilities of MES-SA/Dx5 cells irradiated at 2.6W cm^{-2} for 120 s. The cells were treated with laser only (green striped bars); free DOX (red bars); free DOX and laser (red striped bars); AuNPs@DOX@PP75 (blue bars); AuNPs@DOX@PP75 and laser (blue striped bars) as determined by alamarBlue assay. Error bars represent standard deviations of four replicates (t-test was performed, * means $p < 0.005$).

The experimental conditions used were the same as for the treatment of DOX-sensitive MES-SA cells however diverse results were observed. Nearly all the MES-SA cells were killed when they were treated with free DOX at 0.5 μg mL^{-1} (Figure 5-11). However, as expected, the DOX-resistant MES-SA/Dx5 cells demonstrated much higher viabilities, e.g. 60% for free DOX at 1 μg mL^{-1}. Unlike the MES-SA, the MES-SA/Dx5 showed lower cell viabilities when the laser was used with free DOX. It is still unclear what could be the impact of the laser on the free drug or on the cellular activity and further experiments would be required to draw a hypothesis. It is interesting to note that the cell killing

activity of AuNPs@DOX@PP75 was similar to that of free DOX combined with laser therapy, Besides, when the DOX-resistant MES-SA/Dx5 cells were co-treated with AuNPs@DOX@PP75 (at the equivalent DOX concentration of 1 μg mL^{-1}) and laser, the relative cell viability was decreased to as low as 10%. This was attributed to the change of the mode of cell internalisation from diffusion for free DOX to endocytic pathway for the nano-system, which led to the successful by-pass of efflux drug resistance mechanism.[128]

Table 5-5 Evaluation of the synergistic effect of the dual therapy for MES-SA/DX5 cells.

[DOX] [μg mL^{-1}]	[AuNPs] [nm]	V_{Photo} [%]	V_{Chemo} [%]	$V_{Additive}$ [%]	V_{Dual} [%]
0.01	0.1	109.6 ±12.8	79.4 ±3.8	87.0 ±0.5	64.6 ±3.8
0.05	0.5	102.7 ±12.1	76.1 ±6.2	78.1 ±0.8	55.6 ±8.6
0.1	1	105.1 ±11.7	68.2±6.1	71.6 ±0.7	39.0 ±2.3
0.5	5	75.5 ±11.7	60.8 ±3.4	45.9 ±0.4	28.8 ±5.8
1	10	77.8 ±6.7	31.4 ±3.9	24.4 ±0.3	14.9 ±3.2

The synergistic effect was estimated by comparing the additive effect of laser alone and AuNPs@DOX@PP75 alone with the effect of the dual therapy. [58,61]

$$V_{Additive}(\%) = V_{Photo}.V_{Chemo}.100 \quad (5\text{-}1)$$

Where $V_{Additive}$ is the cell viability obtained by the additive effect of both phototherapy and chemotherapy, V_{Photo} is the relative cell viability after laser treatment alone, V_{Chemo} is the relative cell viability after treatment with AuNPs@DOX@PP75.

$V_{Additive}$ was compared with V_{Dual}, the measured relative cell viability after treatment with AuNPs@DOX@PP75 and irradiation (Table 5-5). For all the concentrations, the synergistic effect was enhanced compared to the additive effect of both therapies except for the lowest concentration which showed very similar cell viabilities.

At 1 μg mL^{-1} equivalent DOX concentration the dual therapy exhibited a 40% lower cell viability than the expected additive therapy (24.4% vs. 14.9%). This result demonstrated the exceptional enhancement via synergistic effect of nanoparticle based chemotherapy and laser based thermal therapy.

The cytotoxic effects toward the drug-resistant MES-SA/Dx5 cells were further confirmed by confocal microscopy (Figure 5-14). The fluorescence of the red channel was stronger for the nanohybrids than for the free drug demonstrating a more efficient cellular delivery of DOX.

Overall these results suggest that: (i) the nanohybrids were more efficient against MES-SA/Dx5 cells than the free drug since the AuNPs can bypass the MDR pathway (as reported by F. Wang *et al.*[128] with a breast cancer cell line resistant to DOX (MCF-7/ADR) treated with DOX functionalised AuNPs via hydrazone bond) and (ii) the dual therapy was more efficient than each of the monotherapy against drug resistant cell lines.

The enhancement of the cytotoxicity via synergistic effect of the chemo-photothermal therapy have been reported for various systems. Wang *et al.*[61] observed 20% cell viability for breast cancer cells (MDA-MB-23) for the synergistic effect, whilst 40% were expect by additive effects, after 24 h treatment with DOX gold nanocages and 10 min laser irradiation at 1 W cm^{-2}. Likewise, Hauck *et al.*[58] estimated it was possible to decrease by 33% the drug dosage with dual therapy on human myeloid leukemia (OCI AML3 cell line). The treatment consisted of three phases: (i) GNRs incubation for 12 h, (ii) treatment with the chemotherapeutic drug cisplatin and (iii) 30 min laser irradiation at 1 W cm^{-2}. Combining the laser therapy with the use of AuNPs as nanocarriers enabled the significant reduction of drug dosage required to obtain the same effect. As seen in Figure 5-13, the dual therapy using an equivalent loading of 0.01 μg mL^{-1} achieved similar killing efficiency that the free drug at 1 μg mL^{-1}. The synergistic effect process is not well understood and various explanations have been suggested in the literature.

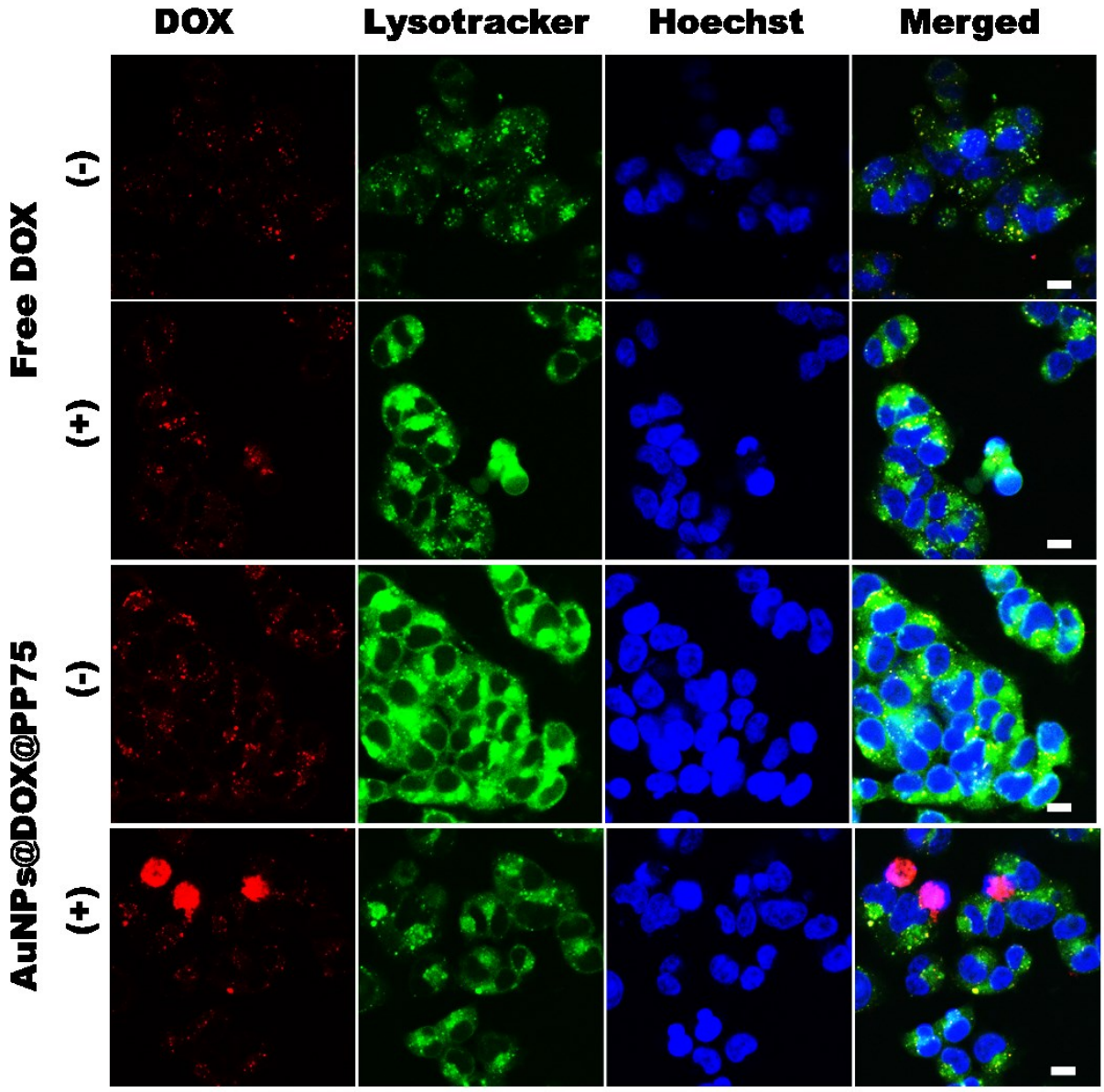


Figure 5-14 Confocal microscopy images of MES-SA/Dx5 cells treated with free DOX (10 µg mL^{-1}), AuNPs@DOX@PP75 (10 µg mL^{-1} DOX equivalent) for 24 h and irradiated (+) or not (-) for 120s at 2.6W cm^{-2}. Images were acquired with a Zeiss LSM-510 inverted confocal unit (x40 magnification). Scale bar: 10 µm.

Hauck *et al.*[58] presented several mechanisms explaining the "thermal chemopotentiation": increased membrane permeability; alteration of the DNA and its repair mechanism and membrane breakdown. Krpetic *et al.*[293] observed non-thermal local damage of the endosomal membrane upon laser exposure at low power and in the presence of AuNPs. The emission of electrons under laser irradiation would cause the production of free radicals known to damage subcellular structures. It was also hypothesised that the formation of small-size clusters in the endosomes, reported in

Chapter 4 (Figure 4-20), might increase the local temperature under laser irradiation and enhance the hyperthermia effect. Last, J. You *et al.*[115] claimed that the increase of temperature due to laser irradiation might be responsible for the release of adsorbed DOX from the surface of hollow gold nanospheres. These results hold promises in the development of more efficient and safer cancer therapies.

5.3 Chapter summary

In summary, nanohybrids were successfully prepared, optimised and characterised based on the chemotherapeutic drug doxorubicin and the PP75 polymer. The PP75 polymer contributed to the long-term stabilisation of the colloidal system. The optimised system showed a drug loading of 0.6 wt% and was resistant to centrifugation and redispersion in various media without agglomeration. The biological evaluation demonstrated the nanohybrids could transport the doxorubicin to the intracellular medium and that the drug was released at its site of action. The nanohybrids had a similar toxicity than free drug on MES-SA cells but showed higher toxicity on drug resistant cell lines. It was also demonstrated that the toxicity was mainly attributed to the chemotherapy but not the nanocarrier itself. Furthermore, the efficiency of the treatment was increased further with the laser therapy. The results of this study further confirmed the potential of the AuNPs@PP75 nanohybrid system as a future clinical tool, able to safely transport and deliver the drug to the intracellular level with the ability to be combined with phototherapy for multimodal therapy for increased efficiency towards multi-drug resistance behaviours. Future work could consider the development of additional imaging capabilities.

Chapter 6 AuNPs loaded hydrogels

Chapter 6 describes a preliminary work on the design and characterisation of AuNP based hybrid hydrogels for therapeutic applications. The optimisation of the hybrid hydrogel synthesis, their physico-chemical and mechanical characterisation, pH-responsive behaviour and *in-vitro* cytotoxicity are reported.

Note: MSc student Yubai Zhang in Dr Chen's group provided the hydrogel samples for Figure 6-3 to Figure 6-12. The XPS spectra were collected by Dr. Ignacio J. Villar-Garcia (former High-Pressure Photoelectron Spectroscopy, HiPPES, Research Officer, Department of Materials, Imperial College London, UK). The contribution of collaborators is appropriately acknowledged in the captions of the relevant figures.

6.1 Introduction

Besides their use as contact lenses or wound dressings,[150] hydrogels are considered as ideal controlled drug delivery platforms and tissue engineering scaffolds for several reasons. Their high-water content combined with their softness, crosslinked structure and their biocompatibility make them very similar to the extracellular matrix.[294] Furthermore, the tunability in their structure, by the control of the crosslinker amount for instance, but also in their properties, with the use of stimuli-responsive components make them greatly suitable to biomedical applications.[295]

Stimuli-responsive hydrogels responding to temperature,[137,296] irradiation[297] have been reported for applications in drug delivery. Oral administration is usually preferred for its ease, low cost and patient comfort however, it is limited by the enzymatic degradation and the low permeability of the intestinal membrane.[295] Chemically stimuli-responsive hydrogels responding to pH and enzymatic changes have been designed to overcome these limitations. The pH-triggered behaviour of these hydrogels allows them to protect their cargo from the degradation at acidic pH in the stomach (pH 1-3.5). Anionic pH responsive hydrogels are particularly suitable since at pH below their pKa the hydrophobic forces will lead to the structure collapse and the drug will be protected from the acidic environment.[295] Acrylic-based hydrogels are the most common for pH responsive hydrogels for oral delivery applications.[298,299]

The reduction of the hydrogel via enzymes has also been exploited for controlled drug delivery (e.g. polysaccharides[300]) via the cleavage of its crosslinker for instance[301]. The small intestine and the colon are the first targets of these kinds of hydrogels.

However, despite the numerous advantages of the hydrogels, some unfavourable characteristics have been limiting their clinical translation: premature drug release causing systemic toxicity, quick dissolution, low drug loading capacity, poor mechanical properties. The combination with inorganic nanoparticles can overcome these limitations and bring them interesting features.[302] For instance, magnetic, photoluminescence and antibacterial properties can be obtained with the incorporation of iron oxide nanoparticles (IONPs),[303] quantum dots (QDs)[303] and silver nanoparticles

(AgNPs)[304] respectively. Numerous nanoparticles have been loaded within hydrogels (e.g. carbon nanotubes, liposomes, silicon-based nanoparticles).[302]

Knowing the numerous advantages of AuNPs as drug delivery carriers, photothermal platforms, sensors and imaging agents it is easy to understand the range of functionalities these nanoparticles could bring to hydrogels aimed at biomedical applications. For example, it has been reported that AuNPs were able to increase the mechanical strength of the hydrogels[305] and alter the porosity.[306]

Composites include bulk nanocomposites[137,153], particles nanocomposites[139] and core-shell nanocomposites[154,155]. While the last two are usually applied to intravenous administration the present study will focus in bulk nanocomposites for oral drug delivery. Bulk nanocomposites can be obtained via: in-situ polymerisation in the presence of AuNPs[137,307] or via one-pot synthesis;[156] loading of the AuNPs in the preformed hydrogel[308] or reduction of gold salts into a hydrogel matrix.[153]

In the present study, the synthesis of the hydrogel is based on previous investigations reported by Chen's group.[309,310] Watkins and Chen[309] successfully prepared PLP-based hydrogels and demonstrated the pH-dependant and reversible swelling behaviour and Wang *et al.*[310] introduced dual responsiveness using disulfide based crosslinkers. AuNP-loaded hydrogels were successfully prepared via gelation in the presence of polymer functionalised AuNPs. The crosslinking occurred between free and functionalised chains simultaneously and the AuNPs were covalently functionalised within the hydrogel network.

Thermo-responsive AuNP-loaded bulk hydrogels [137,138] and injectable nanocomposites[139] have been reported. To my knowledge, this is the first report of pH responsive AuNP-loaded hydrogels for oral drug delivery. The influence of the AuNP loading on the microstructure and the mechanical properties of the hydrogels was investigated. The biocompatibility of the hydrogel composites has also been studied in order to evaluate the potential application of this system in therapy.

6.2 Results and discussion

6.2.1 Optimisation of the synthesis of hybrid hydrogels

Dr Chen's group previously reported dual-responsive hydrogels through crosslinking the pH-responsive anionic polymer PLP and a disulfide-containing crosslinker via EDC/NHS coupling.[310] Herein, hybrid hydrogels were prepared by incorporating AuNPs@PLP, AuNPs@PP75 and AuNPs@PEG2k into the PLP hydrogel structure respectively.

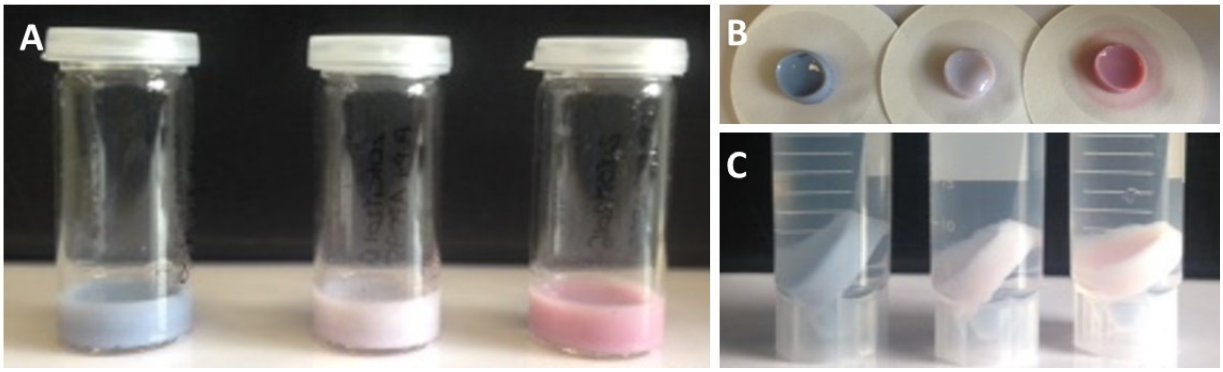


Figure 6-1 PLP hydrogels loaded with AuNPs@PLP, AuNPs@PP75 and AuNPs@PEG2k at 0.24 wt% respectively (from left to right). Hybrid hydrogel samples (A) after overnight synthesis, (B) drying on filter paper, and (C) after purification in H_2O after 5 days.

As shown in Figure 6-1, the three loading materials, AuNPs@PLP, AuNPs@PP75 and AuNPs@PEG2k, were successfully entrapped in the hydrogels and a clear difference in colour was observed between the three samples. The AuNPs@PLP/hydrogel was blue, likely caused by agglomeration of the AuNPs@PLP in the mixture before gelation. As comparison, the AuNPs@PP75/hydrogel and the AuNPs@PEG2k/hydrogel exhibited the light red and pink colours respectively, suggesting the improved colloidal stability of the AuNPs@PP75 and AuNPs@PEG2k before gelation. The initial mixture pH, around 5-6, due to the dissociation of CDE•HCl and EDC•HCl in H_2O, caused the agglomeration of AuNPs@PLP but not AuNPs@PP75 or AuNPs@PEG2k. It was consistent with the results shown in Chapter 4 section 4.2.2 that the stability of AuNPs@PLP was lower than AuNPs@PP75 at pH greater than pH 5.0. Furthermore, loading of the AuNPs with PEG coating was more efficient as evidenced by the intense pink colour, which was probably a sign of a higher concentration of well dispersed AuNPs in the gel network. Indeed, some

light agglomeration was noticed for AuNPs@PP75. However, Figure 6-1(B) shows that the AuNPs@PEG2k were rapidly released (~5 minutes) from the hydrogel network when the hybrid hydrogel was placed on a filter paper. This was consolidated by the observation shown in Figure 6-1(C) that after being placed in water for 5 days the colour of the hydrogel rapidly changed from pink to white. The crosslinking of the hydrogel was based on amide bond formation between the carboxyl groups of the polymer and the amine group of the crosslinker. It is not surprising that AuNPs@PEG2k more easily diffused out of the hydrogel since the PEG chains were not chemically conjugated into the gel network. Since almost all of the AuNPs@PEG2k were lost during the purification process, PEGylated AuNPs were not further used in hydrogel synthesis in this chapter. As comparison, the AuNPs@PLP/hydrogel and AuNPs@PP75/hydrogel well kept their original colour, indicating that majority of the AuNPs@PLP or AuNPs@PP75 remained to be encapsulated in the gel network, by covalent bonding or simple entrapment.

Table 6-1 Calculated densities and porosities of the hydrogel via the Archimede's method. *The hydrogel samples were provided by Yubai Zhang in Dr Chen's group*.

Gel	Density [w/w]	Relative density	Open porosity [%]	Total porosity [%]	Close porosity** [%]
PLP Hyd	0.06	0.05	96.74	95.09	-1.65
AuNPs@PP75/Hyd	0.08	0.06	93.63	93.54	-0.09
AuNPs@PLP/ Hyd	0.16	0.13	85.18	87.13	1.95
AuNPs@PEG2k/Hyd	0.06	0.05	96.56	95.50	-1.06

** The negative closed porosity values obtained can be explained by the approximation used for the total porosity calculations, using the density of PLGA polymer (1.25) as density of reference.

The densities and porosities of the formed hydrogels were characterised via the Archimede's method (Chapter 2 section 2.3.6 for details). As summarised in Table 6-1, the AuNPs@PLP/Hydrogel exhibited a density at least twice of the other hydrogels tested and the lowest porosity. The increased density could not be attributed to the weight of the AuNPs only (accounting for a maximum of 0.24 wt% of the hydrogel), thus it was suggested that a higher degree of crosslinking was obtained between clustered AuNPs@PLP and the PLP polymer, explaining the low porosity. The PLP hydrogel, AuNPs@PP75/hydrogel and AuNPs@PEG2k/hydrogel did not show significant differences in density. AuNPs@PP75/Hydrogel displayed a slightly higher density and lower porosity that could demonstrate the successful crosslinking.

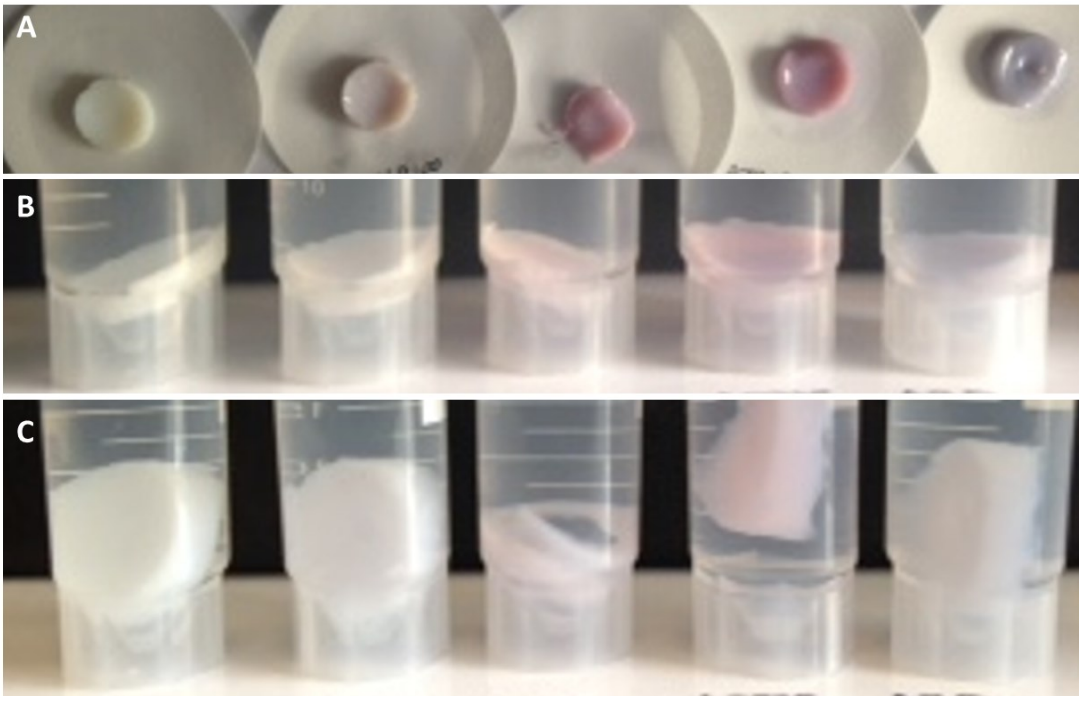
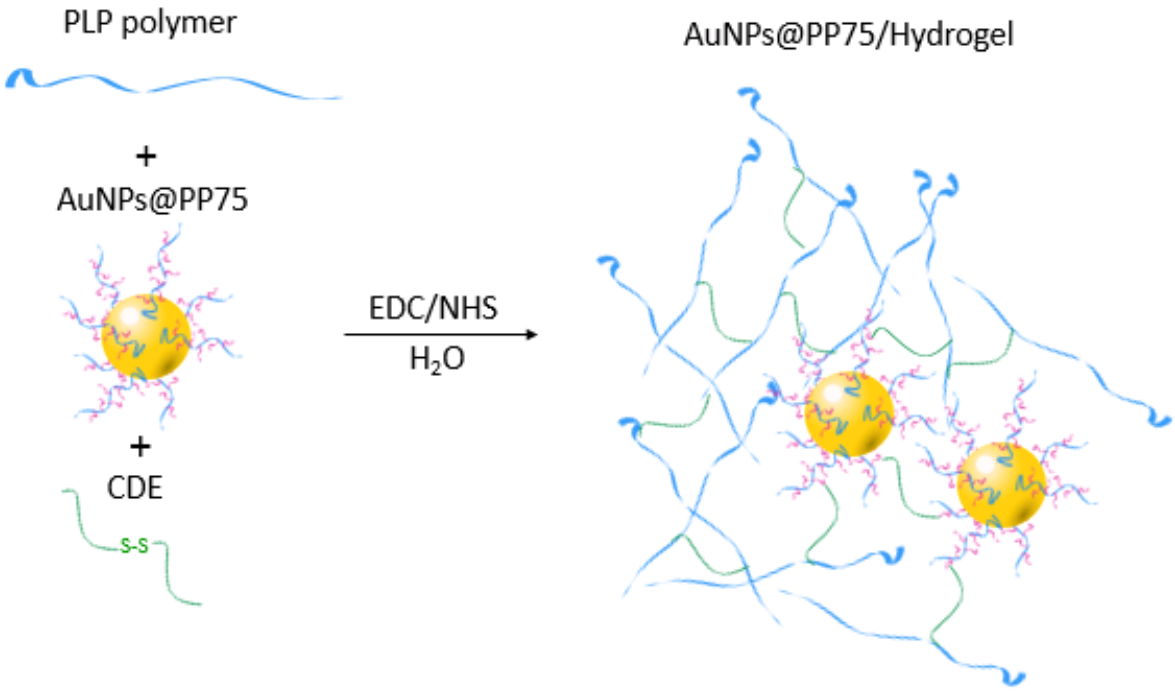


Figure 6-2 Choice of the loading ratio AuNPs/PLP. (A) Samples drying on the filter paper. (B) Purification process in H_2O after 1 day and (C) after 5 days. From left to right on all pictures: PLP hydrogels unloaded; loaded with AuNPs@PLP at 0.03 wt%, AuNPs@PP75 at 0.03 wt% and 0.08 wt%; AuNPs@PLP at 0.08 wt%.

In a second experiment, lower initial loadings AuNPs/PLP were tested, 0.03 wt% and 0.08 wt%, in order to understand whether the stability of the AuNPs in the initial reaction mixture could be improved at a lower AuNPs concentration. The synthesised hydrogels are shown in Figure 6-2. As expected lower initial loadings resulted in less intense colours for the hydrogels. The AuNPs@PP75/hydrogels exhibited a pink colour at both loading

ratios. However, the AuNPs@PLP/hydrogel was blue at the higher loading ratio and pale red at the lower loading ratio. During purification, all the hydrogel colours lost in intensity, however the AuNPs@PP75/hydrogels remained slightly red. It was concluded that the AuNP-loaded hydrogels could be obtained with both types of AuNPs, however AuNPs@PP75 could be loaded at higher ratios. It is interesting to note that in this experiment the AuNPs@PLP/hydrogel at the loading ratio of 0.08 wt% quickly lost its colour during purification whereas a stable blue colour at 0.24 wt% was observed. It is likely that the size of the clusters was much smaller at lower loading ratios thus they could escape from the network more easily.

AuNPs@PP75 were chosen as the most suitable loading material for further studies. The optimised synthesis method is presented in Scheme 6-1.



Scheme 6-1 Optimised synthesis process of the AuNPs loaded hydrogel.

6.2.2 Characterisation of the hybrid hydrogels

This section describes the characterisation of the AuNPs@PP75/hydrogels. The SEM images (Figure 6-3) of the hydrogels, which were incubated in PB buffer at pH 7.4 and then freeze dried, confirmed the successful synthesis of highly porous hydrogels with aligned pores since ordered channels can be observed.

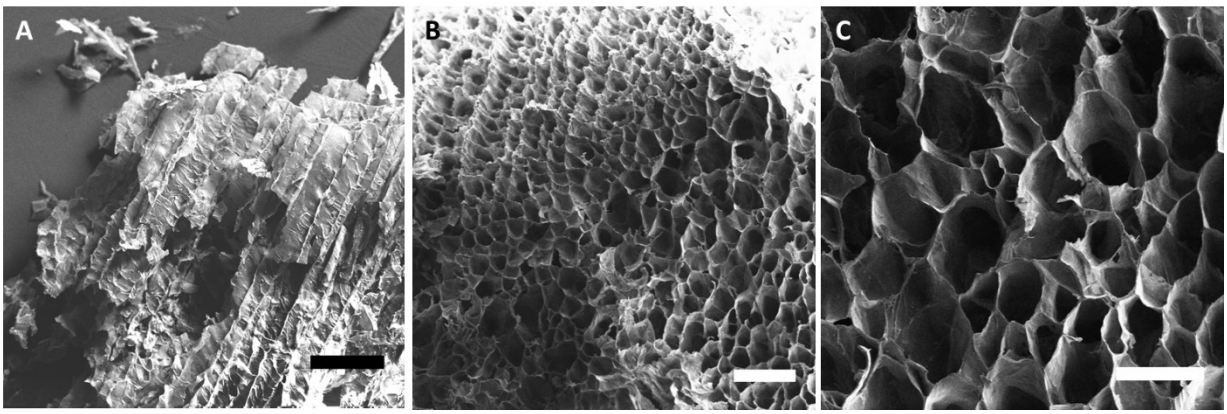


Figure 6-3 SEM images of the hybrid hydrogels. (A) Side view of pore channels (scale bar 200 µm). (B) Front view of pores channels (scale bar 100 µm) and (C) zoom image of the pores (scale bar 20 µm). *The hydrogel samples were provided by Yubai Zhang in Dr Chen's group*.

A XPS analysis (Figure 6-4) of the hydrogels confirmed the presence of carbon (C1s, 285.47 eV), nitrogen (N1s, 399.92 eV) and oxygen (O1s, 541.48 eV) but also sulfur (S2p, 171.48 eV). The spectrum of AuNPs@PP75/hydrogel was very close to the spectrum obtained for the unloaded hydrogel, confirming the successful crosslinking via disulfide bond. The crosslinking ratio was calculated from the atomic concentrations of nitrogen and sulfur (Chapter 2 Materials and Methods section 2.3.10) and ~ 17% was obtained, similar to the unloaded hydrogel. This result was expected since the same polymer/CDE ratio was used considering that the quantity of PP75 was negligible compared to PLP.

However, no contribution from the Au atoms was observed since no peak could be detected at 84 eV (Au4f). It is likely that the polymer coating on the AuNPs surface explains the lack of signal in the region characteristic for gold.

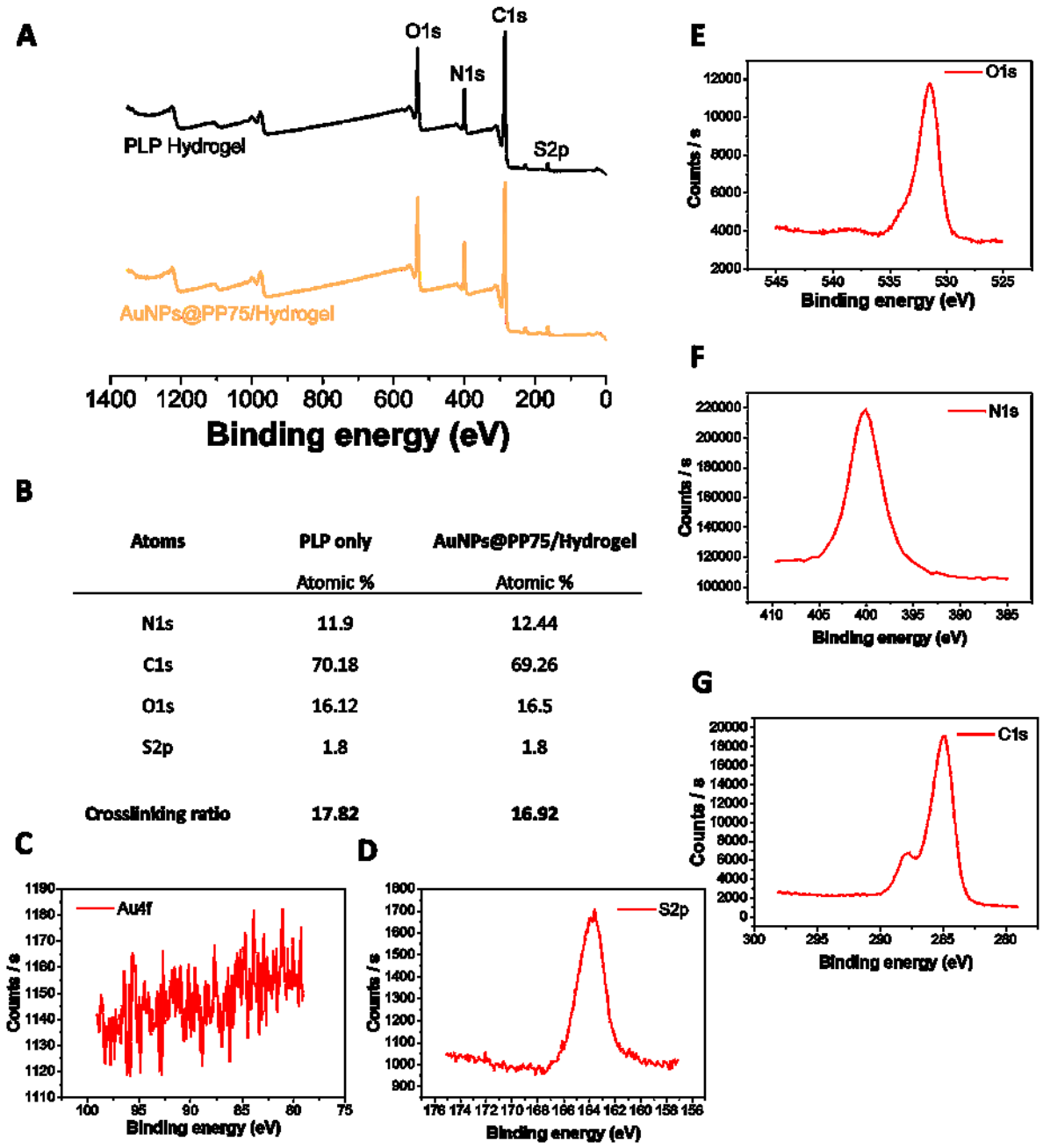


Figure 6-4 (A) XPS spectra of the PLP hydrogel and the AuNPs@PP75/hydrogel. (B) Determination of the crosslinking ratio via XPS data. (C) Au4f, (D) S2p, (E) O1s, (F) N1s and (G) C1s spectra of the AuNPs@PP75/hydrogel. *Hydrogel samples were provided by Yubai Zhang in Dr Chen's group and the XPS spectra were collected by Dr. Ignacio J. Villar-Garcia*.

A 10 μL droplet of the AuNPs@PP75/PLP mixture at the beginning of the gelation process was deposited on a copper grid and air-dried for TEM imaging (Figure 6-5). The TEM image was very blurred due to the high polymer concentration which dramatically reduced the contrast of the image but some dark spots could be distinguished. The

related EDX spectra revealed the presence of Au, suggesting that the dark spots were clusters of AuNPs with a size around 100 nm. It is difficult to confirm whether these agglomerates were formed via pH response or via gelation. It is also likely that the presence of smaller sized clusters or individual particles might not be visible on the TEM image due to the polymer presence. The strong peak for carbon on the EDX spectra was attributed to the carbon grid but also to the PLP since only a weak peak was observed for AuNPs and AuNPs@PP75 (Appendix D Figure D-1 and Figure D-2).

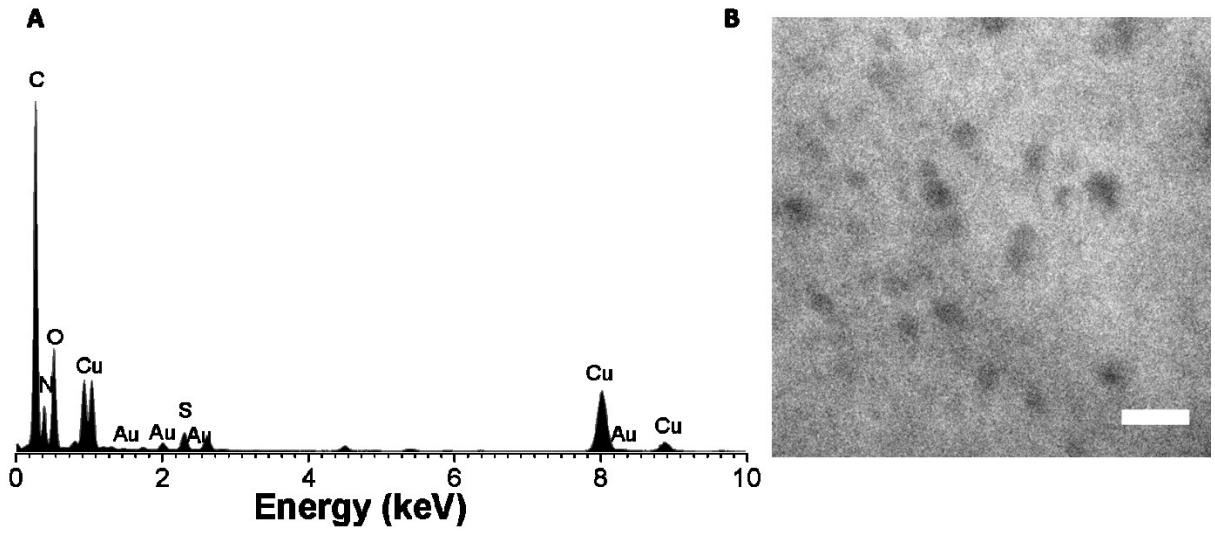


Figure 6-5 (A) EDX spectrum and (B) related TEM image of AuNPs@PP75/hydrogel (scale bar 200 nm). *The hydrogel samples were provided by Yubai Zhang in Dr Chen's group*.

A series of hybrid hydrogels were prepared with different AuNPs/PLP loading ratios and solid contents. The description of the hydrogels (Gel 1 to Gel 11) is given in Appendix D Table D-1. Gel 1 (0.16 wt% - 5.9 wt%) refers to a hydrogel prepared with 0.16 wt% AuNPs/PLP ratio and 5.9 wt% solid content. In order to determine the actual gold content after purification, the hydrogels were digested in HNO_3 and the concentration of gold was measured via ICP-OES. Table 6-2 presents the results for three of the hybrid hydrogel samples.

Table 6-2 Description of the hydrogels in solid content and AuNPs/PLP ratio. *The hydrogel samples were provided by Yubai Zhang in Dr Chen's group*.

Gel number	Initial solid content[a] [wt%]	Initial AuNPs/PLP [b] [wt%]	AuNPs/PLP exp[c] 10^{-2}[wt%]
1	5.9	0.16	1.7 ±0.4
2	5.9	0.12	2.0 ±0.9
3	7.7	0.12	2.2 ±0.2

[a] refers to the solid content calculated with the weight of chemicals added at the start of the synthesis (refer to Chapter 2 section 2.2.8 for calculations details)

[b] refers to the AuNPs/PLP calculated with the weight of AuNPs and PLP added to the synthesis (refer to Chapter 2 section 2.2.8 for calculations details).

[c] determined via ICP measurements (Chapter 2 section 2.2.8 and 2.3.9)

The first important observation was that the overall Au concentration (Figure 6-6) and the experimental AuNP/PLP ratio calculated were much lower than the initial stoichiometric AuNP/PLP ratio. As average, the actual AuNP/PLP ratio was found to be ~0.02 wt% for all the hydrogels whereas the initial stoichiometric AuNPs/PLP loading was between 0.12 wt% and 0.16 wt%.

Figure 6-6 presents the concentration of gold ions (μg mL^{-1}) per 20 mg lyophilised sample. For most of the samples the Au concentration obtained was similar over the range of parameters studied (i.e. AuNPs/PLP ratio and solid content) but varied between samples incubated in H_2O, PBS buffer at pH 7.4 and citrate buffer at pH 3.0. Ideally, if all the AuNPs@PP75 were crosslinked to the hydrogel network no difference between the three media would be expected. However, if some AuNPs@PP75 were not immobilised within the network the following trend would be expected (from higher to lower concentration): pH 3.0>H_2O>pH 7.4. As already reported[309,310] and further developed later in this chapter, the PLP hydrogel can form a highly compact structure with small pores at acidic pH whilst present a more open structure at high pH. Nevertheless, for most of the samples, the hydrogels incubated in H_2O after purification displayed a reduced Au concentration which was unexpected since all the hydrogels were first immersed in H_2O during purification and then redispersed in media. The differences between hydrogels

redispersed in the three different media could be explained by the inhomogeneous dispersion of the AuNPs in the hydrogel network as reported in the literature.[305] The low initial stoichiometric AuNPs/PLP loading ratio and the low level of crosslinking between the AuNPs@PP75 and the PLP hydrogel network might explain the lack of variation of gold content in-between samples.

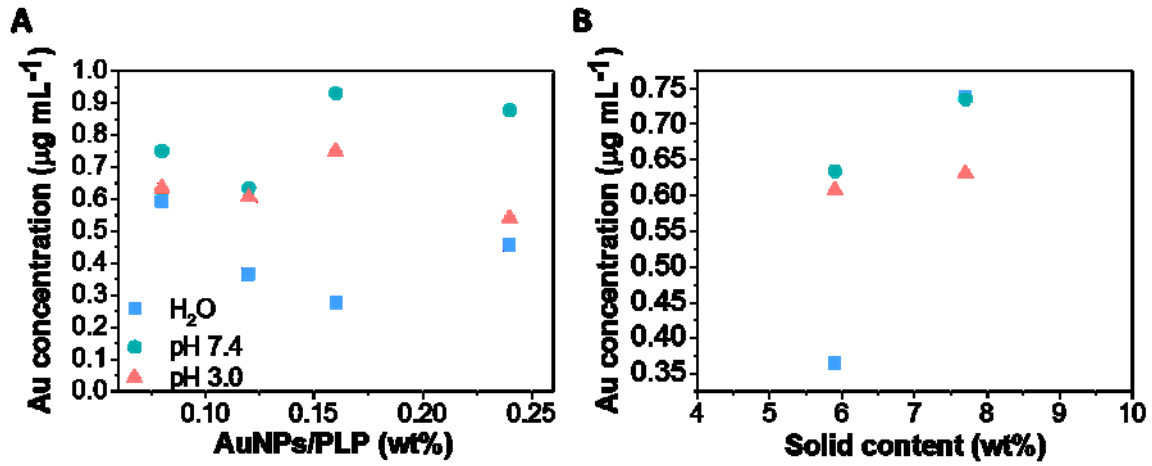


Figure 6-6 Concentrations of Au in AuNPs@PP75/hydrogels obtained via ICP (A) for different AuNPs/PLP ratios (solid content fixed at 5.9 wt%) and (B) for different solid contents (AuNPs/PLP ratio fixed at 0.12 wt%). Before ICP measurements hydrogels have been immersed in H_2O, PB buffer at pH 7.4 and citrate buffer at pH 3.0. *The hydrogel samples were provided by Yubai Zhang in Dr Chen's group*.

From this point, the initial stoichiometric AuNPs/PLP ratio and solid contents will be used to refer to the hydrogel samples bearing in mind that further studies would need to be performed to accurately determine these two values.

6.2.3 pH-responsiveness

In this section, the pH response of the AuNP-loaded hydrogels and in particular the influence of the AuNP loading on the pH response was investigated.

A compression test was performed using a Dynamic Mechanical Analysis (DMA) apparatus to evaluate the mechanical properties of the hybrid hydrogels at different pHs. The hydrogels were incubated in buffer at either pH 7.4 or 3.0 and left to equilibrate for 48 h. The measurements were performed on 8 mm x 5 mm disks of wet hydrogels clamped between parallel plates in the controlled force mode. A force ramp was applied on the upper plate from 0.02 to 1 N at a constant rate of 0.02 N s^{-1}. The force applied (load)

and the displacement of the plates were monitored. The load was converted into stress (Pa) and the displacement of the plate into deformation factor (mm/mm) (Chapter 2 Materials and Methods section 2.3.11 for details). The stress vs. deformation factor curves of the PLP hydrogel and AuNPs@PP75/hydrogel are presented in Figure 6-7.

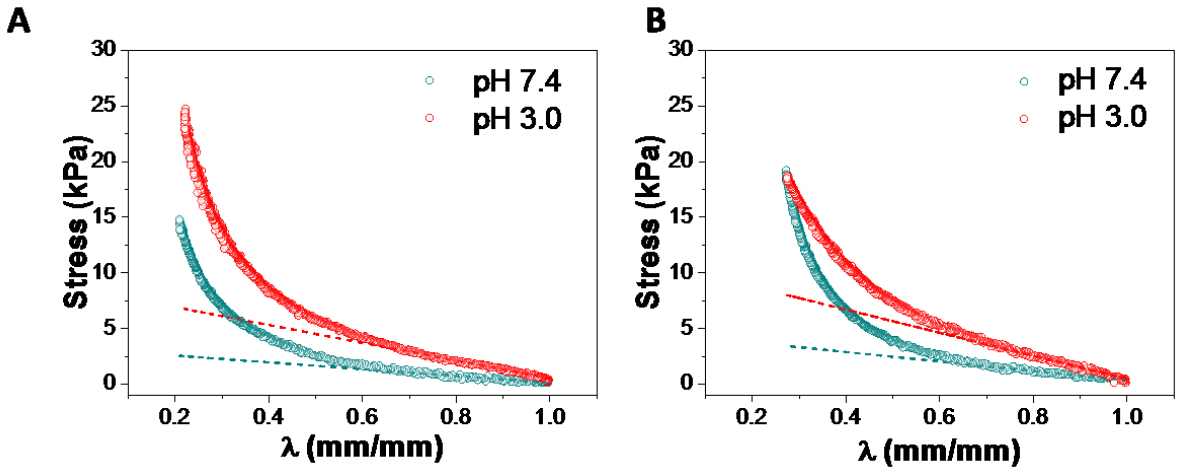


Figure 6-7 Compression profiles (stress vs. deformation factor) for hydrogels previously immersed in 0.1M PB buffer at pH 7.4 and citrate buffer at pH 3.0 of (A) PLP hydrogel and (B) AuNPs@PP75/hydrogel Gel 1 (0.16 wt% - 5.9 wt%) obtained via DMA. *The hydrogel samples were provided by Yubai Zhang in Dr Chen's group*.

Both hydrogels displayed similar compression profiles with two different regimes. In the first regime, the stress increased linearly with the deformation, related to the strain. It was then followed by a second regime where the stress increased exponentially. The exponential growth corresponded to the broadening of the diameter in the middle height of the hydrogel, or the "barrelling" effect until the final break of the hydrogel network. The barrelling induced an additional shear force which translated into a deviation from the linear range.[192] The hydrogels at low pH exhibited higher stresses than at high pH (~2.3 kPa vs. 0.9 kPa for the AuNPs@PP75/hydrogel for λ=0.8) and the deviation to linearity occurred at lower deformation factor (λ~0.6 at low pH and λ~0.5 at high pH), indicative of a quicker rupture due to limited deformation capabilities.[192] The AuNPs@PP75/hydrogel showed slightly higher stress values than the PLP hydrogel (0.9 kPa vs. 0.4 kPa at pH 7.4 and 2.3 kPa vs. 2.0 kPa at pH 3.0 for λ=0.8).

The tensile storage modulus (E') was extracted from the slope of the linear region (λ~ 0.95-0.75) and the results are presented in Figure 6-8. The values of stress at the start of the compression test were omitted to limit the artefact from the non-perfect initial contact between the plate and the hydrogel.

For both hydrogels, higher moduli were obtained for the hydrogels swollen in pH 3.0, indicative of a higher resistance to the compression force at lower pH as observed in the stress vs. λ profiles. This result was expected considering the pH-dependent properties of the polymers, PLP and PP75, and the PLP-based hydrogels.[309,310]. Specifically, at high pH, the electrostatic repulsion between the charged carboxylic acid groups were responsible for a swollen network with a high-water content, whereas at low pH the protonation of the carboxylic acid groups led to the attraction between the hydrophobic domains, stronger than the electrostatic repulsion, and the hydrogel shrank releasing its water content. The hydrogel in pH 3.0 buffer was denser and stronger thus exhibited a higher modulus. This difference in the mechanical behaviour was also observed by Wang *et al.*[310] with the PLP hydrogel subject to an oscillatory shear rheology test.

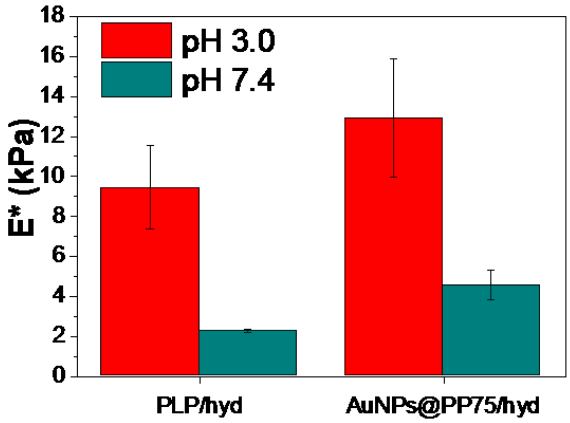


Figure 6-8 Comparison of the tensile storage modulus E' obtained via DMA at pH 7.4 and pH 3.0 for the PLP hydrogel and AuNPs@PP75/hydrogel Gel 1 (0.16 wt% - 5.9 wt%). Error bars represent the standard deviations between triplicate samples. *The hydrogel samples were provided by Yubai Zhang in Dr Chen's group*.

The difference of moduli $\Delta E' = E'_{pH3.0} - E'_{pH7.4}$ was slightly larger for the hybrid hydrogel (8 kPa) than the PLP hydrogel (~7 kPa). It was hypothesised that the presence of AuNPs@PP75 within the hydrogel could loosen the network as represented on Scheme

6-1 thus increasing the swelling capabilities.[310] However, this observation was not confirmed by XPS data which did not show significant differences in crosslinking ratios (Figure 6-4) and further DMA experiments with various AuNPs loadings would be needed before drawing any conclusions.

The tensile moduli were converted in shear moduli (Chapter 2 Materials and Methods section 2.3.11) to compare with the oscillatory shear rheology results obtained by Wang *et al.*[310]. Both results were unexpectedly found very different (data not shown) with the shear moduli values almost 10-fold higher than the converted tensile moduli. This difference could be explained by several factors: (i) the difference in the type of forces involved: shear vs. compression; it is possible that, due to the synthesis conditions, the hydrogel presents well-defined pore structures orientated in a specific direction and thus exhibits different resistance depending on the direction of the force applied; (ii) the errors due to the measurements and to the approximation made with the conversion from E' to G' and (iii) the limited reproducibility between hydrogels already observed for the shear test (data not shown) due possibly to the strong effect of the environmental conditions (temperature, stirring rate) during the synthesis process.

In order to evaluate the mechanical properties of the hydrogels, the order of magnitude of the tensile moduli obtained in the present investigation (2-14 kPa) were compared to the data found in the literature.

Tiwari and Badiger[304] performed a compressive test on the polyacrylic acid-based hydrogels prepared via the EDC coupling with the disulfide crosslinker and obtained the modulus ranging from 0.5 to 4 kPa. Several groups reported the increase of moduli following nanoparticle loading within hydrogels. Li *et al.*[311] reported a change of behaviour from liquid to viscoelastic with the increase of Fe_3O_4 NP loading within a PEG based hydrogel. Marcelo *et al.*[305] increased by 1.3 to 16-fold the shear moduli of PNIPAM hydrogel following AuNPs incorporation.

Very few papers have reported the mechanical characterisation of hybrid hydrogels designed for biomedical applications. Jaiswal *et al.*[312] improved the mechanical stiffness

of collagen based hydrogels through the incorporation of Fe_3O_4 NPs as crosslink epicentre at a very low concentration (10 000-fold lower than the concentration of the polymer). The moduli values could be tuned between 0.2 and 200 kPa depending on the size and concentration of the NPs. These hybrid hydrogels may be employed as scaffolds for tissue engineering. The increase of the mechanical strength of the hydrogel might be helpful to design carriers able to resist the mechanical stress during their transport in the GI tract. Low mechanical strength can lead to dose dumping and burst release and are usually not preferred.[313]

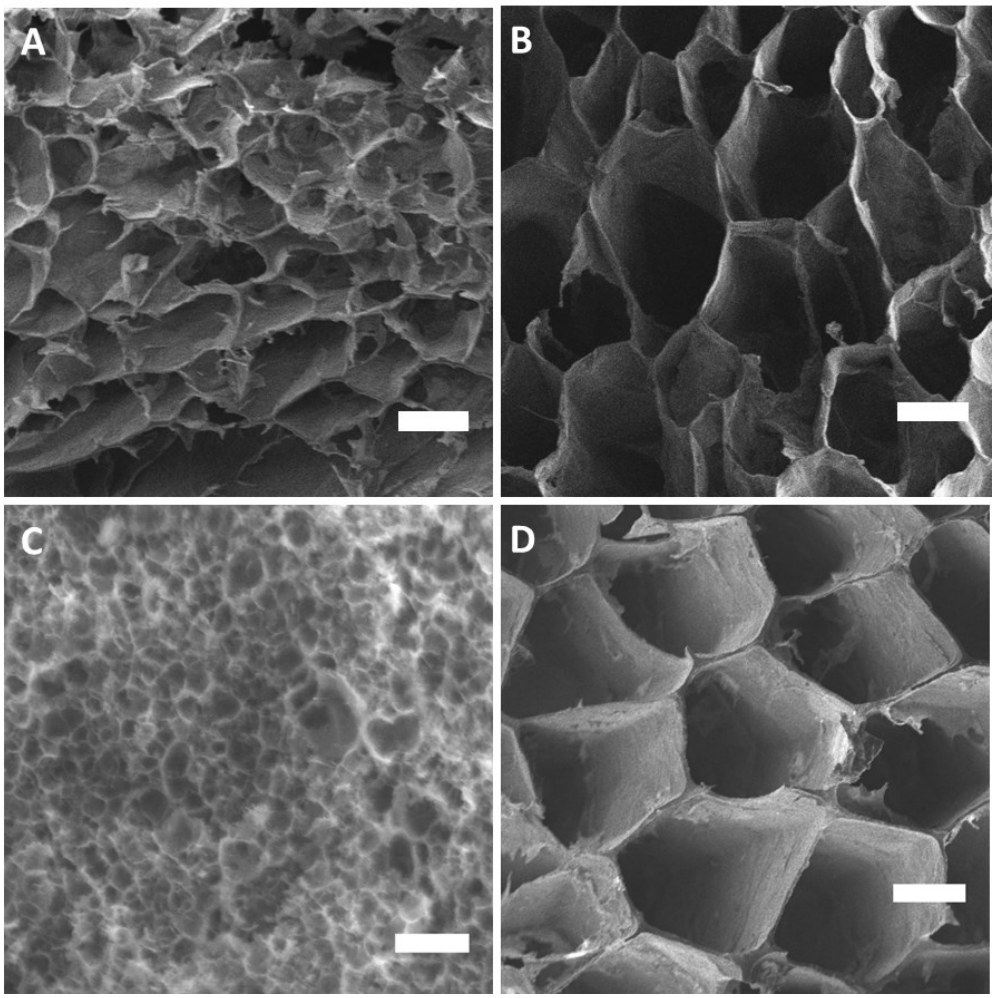


Figure 6-9 SEM images of Gel 6 (A, B) and Gel 3 (C, D) at pH 3.0 (A, C) and pH 7.4 (B, D) (scale bar 20 um). *The hydrogel samples were provided by Yubai Zhang in Dr Chen's group*.

The hydrogels at pH 7.4 and pH 3.0 were freeze dried and imaged under SEM to investigate the changes of aspect and porosity with pH. The SEM images (Figure 6-9) for acidic pHs showed narrower pores (few μm to 20 μm at pH 3.0 vs. 20-60 μm at pH 7.4) giving the overall hydrogel a more compact structure. SEM images of PLP hydrogel showed similar pore size change with pH (Appendix Figure D-3) as already reported.[310]

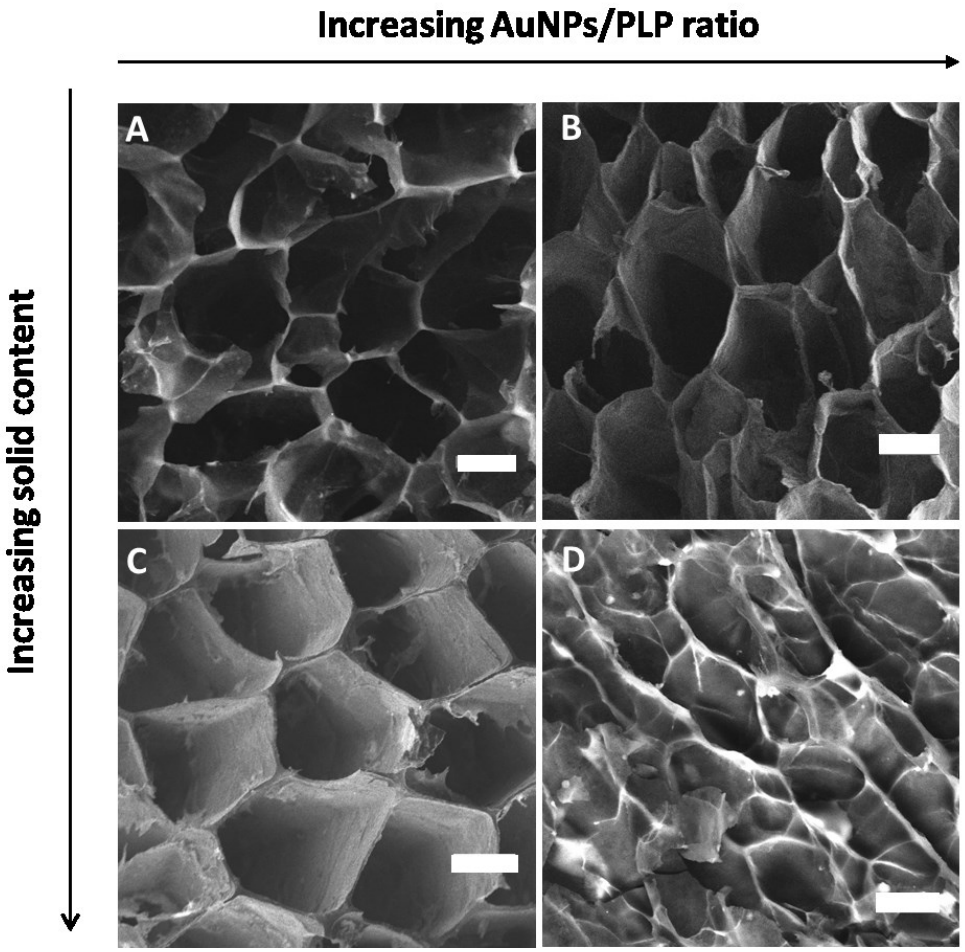


Figure 6-10 TEM images of hydrogels at different AuNPs/PLP ratios and solid contents after stabilisation in buffer at pH 7.4. (A) PLP hydrogel, (B) Gel 6 (0.24 wt% - 5.9 wt%), (C) Gel 3 (0.12 wt% - 7.7 wt%) and (D) Gel 11 (0.24 wt% - 7.7 wt%). Scale bar 20 μm. *The hydrogel samples were provided by Yubai Zhang in Dr Chen's group*.

The pore sizes and aspects of the hydrogels at different AuNPs/PLP ratios and solid contents were compared between different hydrogels but no reproducible trend was extrapolated from the images especially since the pore size was highly inhomogeneous (Appendix D Figure D-4). Few examples of SEM images of swollen hydrogels (pH 7.4) are

given in Figure 6-10. Please refer to Appendix D Table D-1 for the description of the hydrogels.

Figure 6-10(A-B) had very similar pore sizes and aspects, suggesting that the presence of AuNPs did not significantly affect the structure. However, Figure 6-10(C-D) showed extremely different hydrogel structures, the former presenting very well-defined pores with regular sizes and wide walls whereas the latter showing a weaker structure, more disorganised. As suggested in some rheological measurements at high AuNP loading (data not shown), the similarity between PLP and high AuNPs/PLP ratio might come from the destabilisation of the colloids in the initial mixture leading to the very low actual AuNP content in the resulting hydrogel. Further studies are required to confirm the influence of the AuNP loading on the overall hydrogel structure.

6.2.4 Cell viability

The biocompatibility of the hybrid hydrogels was evaluated via the alamarBlue assay (Figure 6-11) according to a method previously reported by Wang *et al.*[310]

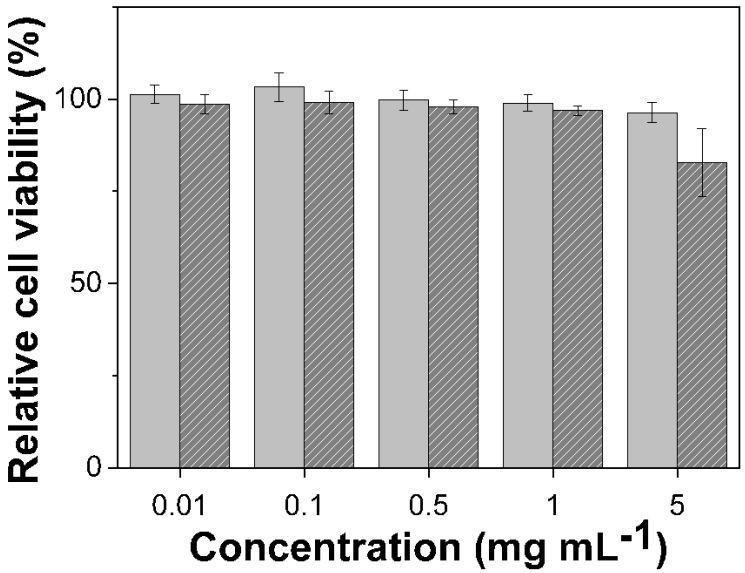


Figure 6-11 Concentration dependant cytotoxicity of Gel 1 (0.16 wt% - 5.9 wt%) evaluated via alamarBlue assay after 24 h (grey bars) and 72 h of treatment (striped bars) of HeLa cells. Error bars represent the standard deviations between 10 replicates. *The hydrogel samples were provided by Yubai Zhang in Dr Chen's group*.

Samples of hybrid hydrogels were lyophilised, broken into a fine powder and dispersed into DMEM medium. Hela cells were treated with the hydrogel-based solutions at concentrations from 0.01 to 5 mg mL^{-1} for 24 h and 72 h. The cell viability was close to 100% in the range of concentrations studied for all the hydrogels (Appendix D Figure D-5 and Figure D-6). This result is not surprising since both the PLP hydrogel[310] and the AuNPs@PP75 (Chapter 4 Figure 4-18(A)) have previously been reported to be well tolerated by HeLa cells.

6.2.5 Potential of hybrid hydrogels in therapy

Preliminary experiments of drug loading and release and swelling studies have been performed to evaluate the suitability of the hybrid hydrogels for therapeutic applications via oral delivery. This section reports the data obtained by Yubai Zhang in Dr Chen's group and have been included in the thesis to enrich the discussion on the applicability of the hybrid hydrogels.

Table 6-3 Weight incorporations and loading efficiencies. *The hydrogels and the raw data were provided by Yubai Zhang in Dr Chen's group.*

Gels	AuNPs/PLP [wt%]	Solid content [wt%]	Weight incorporation [wt%]	Loading efficiency [%]
1	0.16	5.9	17.7 ±2.1	58.8 ±7.6
2	0.12	5.9	18.4 ±1.7	58.4 ±4.2
3	0.12	7.7	14.4 ±1.4	58.4 ±6.6

Three hydrogels were chosen for drug loading and release studies. Fluorescein, a fluorescent molecule, was used as a model drug and was loaded in the hydrogel via immersion of the hydrogel in a solution of concentrated fluorescein at pH 7.4 after being equilibrated at pH 3.0. After 24 h of loading the hydrogels were immersed in pH 3.0 buffer to lock the drug within the porous structure. The weight incorporation and the loading

efficiencies were calculated (Chapter 2 Materials and Methods 2.3.1.14 for details and Appendix D Figure D-7) and are presented in Table 6-3.

No significant difference was observed in the loading efficiencies for the three hydrogels. ~ 58% of the initial amount of drug was loaded, slighlty higher that the literature (~50%)[310]. However, the weight incorporation increased as follows: Gel 3 < Gel 1<Gel 2.

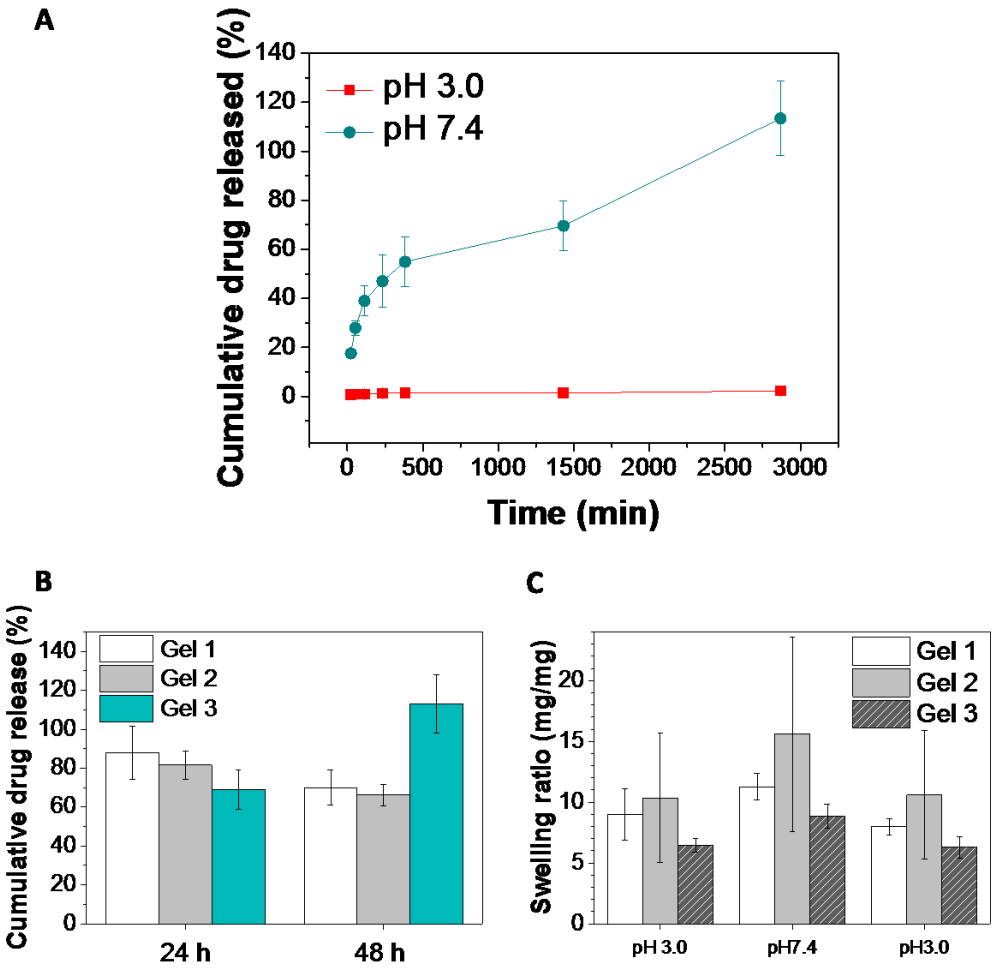


Figure 6-12 (A) Drug release profiles at pH 7.4 and pH 3.0 obtained for Gel 3 (0.12 wt%-7.7 wt%). (B) Drug released after 24 h and 48 h of Gel 1 (0.16 wt% - 5.9 wt%), Gel 2 (0.12 wt% - 5.9 wt%) and Gel 3 (0.12 wt% - 7.7 wt%). (C) pH dependence and reversibility of the swelling ratios. Error bars represent the standard deviations of triplicates. *The hydrogels and the raw data were provided by Yubai Zhang in Dr Chen's group.*

The release of the drug was monitored in a shaking thermostated bath at 37°C in buffers at pH 7.4 and pH 3.0 respectively (Figure 6-12(A-B)). A significant difference was observed in the release profiles at pH 7.4 and pH 3.0 for the three hybrid hydrogels

studied. At pH 3.0 less than 2% of the drug content was released into the medium after 48 h of incubation. However, the hybrid hydrogels immersed in buffers at pH 7.4 released ~ 60-80% of the encapsulated drug after 24 h. This observation was expected since at high pH the hydrogel networks expanded from a compact structure to a swollen state via the change of the conformation of the polymer as observed via SEM (Figure 6-9). Water can then enter in the pores of the hydrogel and the drug can diffuse freely and be released.

Gel 3 exhibited the slowliest release rate at pH 7.4 with 60% release after 24 h whereas Gel 1 and Gel 2 demonstrated ~ 80% release in less than 7 h (Appendix D Figure D-8). Gel 3 was prepared with the higher solid content (Table 6-3) which led to a higher stiffness as observed via oscillatory shear rheology (data not shown) and a slowlier swelling rate after immersion in pH 7.4, since the water penetration is hindered as confirmed by swelling studies (Figure 6-12(C)). Gel 1 and Gel 2 displayed a lower drug release at 48 h than at 24 h which cannot occur for the cumulative drug release but might be explained by the inhomogeneity of the drug concentration in the release media and the drug release variation between repeats.

Swelling study results demonstrated a good reversibility with pH-cycling for the three types of hydrogels studied. Gel 1 displayed lower swelling ratios than Gel 2 for a similar solid content but a higher AuNPs/PLP ratio. Besides, it should be noted that the hydrogels presented lower swelling ratios than the reported PLP hydrogel for similar synthesis parameters.[310] This could indicate an influence of the AuNPs that bring stiffness to the hydrogel network and would be in agreement with the DMA results. Gel 3 presented the lowest swelling ratio, the more robust porous structure (Figure 6-9(D)) and the highest storage modulus (data not shown). The higher stiffness of the hydrogel could explain the slowlier release rate.

These results suggest that the hybrid hydrogel is adapted for oral delivery of therapeutics targeted at colon. Indeed, the hydrogel would be able to retain a drug in the acidic environment of the stomach, protect it from degradation during its transit in the intestine (transit time ~3 h)[314] where the pH varies from ~6.1 to ~7.9 and slowly release the drug in the colon where the transit time, even though it greatly varies amongst individuals,

last ~ 40 h.[315] The pH-dependent release rate should be carefully considered when designing a therapeutic for oral delivery since the pH profile in the GI tract sets up important requirements. Slow and controlled release might be an asset to avoid uncontrolled release in the oesophagus (~ pH 7.0[316]) or in the small intestine (~ pH 6.15-7.88)[316] in case the target is the colon for instance. Nevertheless, the release has to be quick enough to deliver the majority of the active ingredient in the colon.

6.3 Chapter summary

This chapter reports the development of AuNP-loaded hydrogels through crosslinking the PLP polymer with the PP75 functionalised gold nanoparticles using the disulphide-containing crosslinker. The hybrid hydrogels with various AuNPs/PLP ratios and solid contents were prepared. The AuNP loading was confirmed and quantified via ICP-OES (~0.02 wt%). The influence of the pH, AuNP loading and solid contents on the porosity and the structure were evaluated. The pH responsiveness of the hybrid hydrogels was observed via SEM. The AuNP-loaded hydrogels maintained the pH-dependent structural change from a swollen network with large pores at physiological pH (~20-60 μm) to a highly compact structure with small pores at acidic pH (~5-20 μm).

Mechanical test results showed that the hybrid hydrogel had a higher resistance to compression but further experiments are required to fully confirm this argument. The improvement of the mechanical properties could be an asset of the hybrid hydrogels able to resist the degradation during its transport through the GI tract. The AuNP loaded hydrogels proved to be able to encapsulate the model drug fluorescein and to release it in a controlled way at physiological pH whereas almost no release was observed at acidic pH 3.0. The hydrogels also demonstrated a high biocompatibility towards HeLa cells. Further investigations need to be carried out to understand the role of the AuNP incorporation, to test the influence of the crosslinking ratio on the hydrogel behaviour and to evaluate the release of AuNPs via redox trigger. The present study demonstrates the suitability of these pH-responsive hydrogels as potential tool for therapy via oral administration.

Chapter 7

Chapter 7 highlights the key points of the research work presented in Chapters 3 to 6 and outlines the implications of the findings in the context of the state-of-the-art in the field of nanomaterials for drug delivery. The second part of the chapter introduces recommendations for future work on the basis of the achieved results but also additional investigations carried out within the PhD project but not reported in the thesis.

7.1 Conclusions

The development of multifunctional AuNP nanocarriers has been reported in the present thesis following a step-by-step approach. First, the colloidal stability in media mimicking the physiological environment has been achieved through the functionalisation of the AuNPs with two types of polymers, the hydrophilic PEG and the anionic amphiphilic PP75. Second, reversible pH-dependent agglomeration has been obtained via the optimisation of the grafting with the amphiphilic polymer. Third, a chemotherapeutic drug has been successfully loaded on the AuNPs and delivered at the intracellular level. Fourth, the hybrid chemo-nanoplatform exhibited potential for photothermal therapy and, in particular, for the treatment of drug resistant cells. Finally, the nanoplatform was successfully translated into a hydrogel system designed for oral drug delivery.

The main findings of the investigation are summarised below and their impacts on the field of nanomaterials for drug delivery in oncology are discussed.

7.1.1 PEGylated AuNPs

PEGylation remains today the most common route employed to provide long-term stability to nanocarriers designed for drug delivery. However, the impact of the PEGylation on the properties of the nanocarrier and its *in-vivo* fate are still poorly understood. Researchers usually choose to use a PEG that is most accessible to them without considering the influence on their intended applications. In chapter 3, the influence of the chain length on the physico chemical properties of the AuNPs has been reported. This is the first known systematic study on the influence of the molecular weight on a large set of parameters including colloidal stability, grafting density, polymer conformation, serum adsorption and interchain interactions. Longer polymeric chains were found to provide higher stability to the colloidal solution but lower grafting densities could be achieved since the chains tended to adopt a mushroom-like conformation rather than a stretched configuration. The flexibility provided by the longer chains also enabled more homogeneous interchain interactions controlling the organisation of assemblies. The specific role of the PEG, in particular the hydrogen bonding and its hydrophilicity, in the formation of assemblies under water evaporation

was elucidated. The findings of this research could help researchers interested in the use of PEG in the development of nanocarriers for drug delivery to choose the most suitable option for their system no matter if they would like to use PEG as a single or covalently bound chain. The thesis work concerned the simplest system that all researchers could refer to: ~14 nm citrate-coated AuNPs prepared via the Turkevich method and functionalised via the "grafting-to" method with PEGs having commonly used chain lengths. Some key recommendations may be deduced from the research. For instance, short chains may be preferred for higher grafting densities and thus higher payload via covalent bindings may be obtained whereas longer chains would be more suitable for core-shell architectures.

7.1.2 Properties and therapeutic potential of AuNPs@PP75

Entry to the cytoplasm usually constitutes the last step of the journey of nanocarriers before the therapy takes place. However, nanocarriers often remain entrapped in the endosomes and are susceptible to enzymatic degradation in the lysosomes. Several strategies have been employed to counteract the lysosomal degradation with various degrees of success. One of the most popular approaches involves the use of cationic polymers. These polymers have demonstrated high levels of internalisation and enhanced cytoplasmic delivery, however, immune system recognition and systemic toxicities have greatly limited their clinical translation. Even though the loading on AuNPs have demonstrated to considerably reduce these side effects, anionic systems provide a safer option avoiding the presence of free cationic polymers after thiol exchange that could cause systemic toxicity. To my knowledge, the study reported in chapter 4 is the first one concerning the design of anionic membrane active AuNPs. The amphiphilic polymer has retained its pH-dependant coil-to-globule conformational change and endosomolytic properties after grafting onto the AuNP surface. The agglomeration-deagglomeration process was found to be highly responsive to pH and the process fully reversible. This study provides an insight into the development of pH responsive hybrid systems aimed at intracellular delivery via a simple "grafting-to" method that could be extended to other amphiphilic polymers with membrane activity properties but also to other types of nanocarriers. Besides, chapter 5 reported the successful application of the

nanohybrids for combined chemotherapy and phototherapy. The optimised system demonstrated 6 times higher toxicity towards drug resistant cells than the free drug. The dual therapy represents a safer opportunity for the future of drug delivery since an enhanced efficiency is obtained with lower drug doses and a targeted therapy.

7.1.3 Hybrid hydrogels

Finally, the last study reported in this thesis concerned the development of AuNP loaded hydrogels. Combining the advantages of both systems for drug delivery can aid to overcome their respective limitations. The covalent loading of AuNPs has been achieved and the resulting hydrogels maintained their impressive pH-dependant swelling behaviour. The higher mechanical strength obtained via AuNP loading could contribute to an enhanced stability *in-vivo*. The *in-vitro* evaluation demonstrated the suitability of this system for applications in oral drug delivery. Further investigations on the control of the crosslinking ratio and the release of AuNPs via redox reduction would be interesting for intracellular delivery, photothermal therapy and imaging purposes. This study paves the way for the formulation of AuNPs loaded hydrogels for cancer therapy and intracellular delivery where very few reports have been published.

In summary, the design of a multifunctional platform aimed at the intracellular delivery of payloads is reported herein. The detailed step-by-step approach combined with the use of the most common synthesis methods and the most available materials provide other researchers with an adaptable template.

7.2 Future work

In this section are presented some insights on follow-up projects to explore further the potential application of the PP75 functionalised AuNPs as a novel multifunctional theranostic platform in oncology. Based on the previous findings, three main areas worth of investigation are introduced below.

7.2.1 Dual functionalisation with PP75 and PEG

Some work has been done on the simultaneous use of PP75 and PEG based on the respective findings reported in Chapter 3 and Chapter 4. The aim was to design a multifunctional platform where PP75 provides the pH responsiveness and membrane activity and PEG the stealth character. Three methods have been investigated: (i) the simultaneous grafting of both polymers; (ii) using PEG as a spacer and (iii) using PEG as a terminal end. The second method demonstrated the best results since a significant increase of calcein release from liposomes used as a membrane model has been observed.

Two hypothesis that could explain the phenomenon were drawn: the PEGylation of the PP75 enhanced the endosomolytic properties as previously reported[172,173] and the use of PEG as a spacer leads to the increase of the chain length with two major consequences: the first one is the higher flexibility of the chain enabling an easier coil-to-globule conformational change and the second one is the enhanced interaction of the PP75 with the cellular membrane.

It would be interesting to investigate further the impact of the use of PEG as a spacer, since this is a common strategy reported in the literature for the loading of drugs or other molecules of interests,[124,126,128,144,148,201,271,317]. The impact of the dual grafting on the pH-responsive behaviour using the methods developed in the present thesis and on the endosomal escape mechanism via CLSM imaging would be especially interesting. If the enhancement of the interaction with the membrane is confirmed, it would be worth adding the chemotherapeutic ability via drug loading and see whether higher drug loading efficiencies could be achieved since, based on chapter 3 results, longer chains would lead to more space available for loading, furthermore, the stabilisation of the

system could also contribute to higher loading levels. The quantification of the cytoplasmic release via flow cytometry is another important area of further development for the investigation. Doxorubicin, being a fluorescent molecule, enables such quantification in a direct manner without the need for conjugation of the polymer with fluorescent labels that could potentially modify its endosomolytic properties.

7.2.2 Multivalent theranostic platform

The present thesis aimed at the preparation of a multifunctional platform combining endosomolytic properties, chemotherapy and photothermal therapy. Promising results have been achieved using doxorubicin, one of the most commonly used chemotherapeutics today, and multi-drug resistant cells, MES-SA/Dx5.

To further complete the study of this system an evaluation of the drug release kinetics and in particular the influence of the endosomal pH, the serum binding and the GSH intracellular concentrations would need to be performed. This study could be carried out by quantifying the drug release over time in acidic media and media containing BSA and thiols.

Another loading strategy could be investigated in order to enhance the loading levels and obtained a more controlled release. Some work has been done on the loading of doxorubicin via disulfide bonds to design dual responsive multifunctional AuNPs. The high intracellular GSH levels could then be exploited to trigger the drug release. The PP75 was modified with a disulfide-bearing molecule (AuNPs@PP75-SS-R) and a thiol end was added to doxorubicin (DOX-SH). The doxorubicin could then be loaded onto the AuNPs@PP75-SSR via thiol exchange (AuNPs@PP75-S-S-DOX). This method has previously been reported in the literature. [128] Preliminary studies demonstrated the successful preparation of AuNPs@PP75-S-S-R however thiolated doxorubicin could not be obtained via the synthesis method selected. DOX loading via disulfide bond is of great interest and some further investigations on the correct preparation method are required.

MES-SA/Dx5 cell line exhibits a marked resistance to other chemotherapeutic agents such as paclitaxel that has been investigated in combination with doxorubicin for the

treatment of advanced breast cancer. A possible area of research would be the development of combined chemotherapeutic agent via simultaneous loading of both drugs and *in-vitro* testing with MES-SA/Dx5 cells to test whether higher toxicities could be achieved via synergistic effect.

Also, other cells types could be tested in order to further confirm the efficiency of the intracellular delivery and the robustness of the treatment compared to free drug. Other cells types may include the mouse fibroblast (NIH/3T3)[127] and human breast cells (MDA-MB-231)[318] and the breast cancer cells MCF-7 with their resistant counterparts MCF-7/ADR[128]. Cytotoxicity assays and CLSM imaging would need to be repeated with the same experimental methods as the one reported in the present study.

Furthermore, the targeting ability of the nanohybrids could be tested via functionalisation of a targeting ligand and evaluation of the targeting efficiency. To this end, folate molecules could be conjugated to PEG via DCC/DMAP coupling[130] and the uptake levels could be compared via CLSM combined with flow cytometry between a cell line expressing a high levels of folate receptors (e.g. MDA-MB-231) and a cell line expressing a low level of folate receptors (MCF-7). [201]

7.2.3 AuNPs loaded hydrogels for intracellular delivery

Chapter 6 highlighted the impact of the AuNPs presence on the mechanical properties of the hydrogel. However, a relatively low loading of AuNPs was quantified as pointed out by the ICP-OES and XPS analyses. To explore further the impact of the AuNPs on the hydrogel properties it is recommended to enhance the loading so that a more reliable quantification can be achieved. The comparison of the hydrogels properties based on their AuNPs content would then be more accurate. It has been reported that AuNPs/PLP loadings higher than 0.12 wt% led to the destabilisation of the colloidal solution and precipitation of the AuNPs. Changes to the synthesis method could be considered such as: (i) increase the concentration of the crosslinker to increase the likeliness of the AuNPs to be entrapped or conjugated; (ii) activate separately the PLP and PP75 via DCC/DMAP coupling and add PLP and the crosslinker simultaneously to ensure AuNPs@PP75 get higher chance to be crosslinked and (iii) obtain higher grafting densities for PP75 on

AuNPs, via grafting at high pH when the chain are in extended conformation for instance, in order to reduce the pH responsiveness of the functionalised nanohybrids and increase their dispersion in the acidic reaction mixture.

The second important area of research in the hydrogel project to be developed is the evaluation of the degradation of the hydrogel and the release of the AuNPs via disulfide bond reduction. Some preliminary works have demonstrated the lower release of entrapped drug with the presence of AuNPs, however it has not been fully understood yet whether the AuNPs were responsible and replication to confirm the reproducibility of the results are required.

Chapter 6 demonstrated the successful loading and release of fluorescein (Mw= 332 Da). The delivery of larger payloads could be investigated. Indeed, Watkins and Chen[309] reported the successful loading and release of molecules up to 2000 kDa with PLP-based hydrogel, which corresponds to the size of plasmids and viruses.

Finally, attempts have been carried out to prepare AuNPs loaded nanogels via the reverse emulsion method however the stability of the AuNPs@PP75 was critical. The synthesis of core-shell nanocomposites via interchain crosslinking seems to be the most innovative and promising approach for the design of novel intracellular carriers. The use of laser irradiation could further highlight the advantages of such systems in phototherapy.

Bibliography

(1) D. Bhattacharyya; S. Singh; N. Satnalika; A. Khandelwal; S.-H. Jeon. Nanotechnology big things from a tiny world a review. *International Journal of u- and e-Service, Science and Technology* **2009**, *2*, 29-38.

(2) G. Kaur; T. Singh; A. Kumar. Nanotechnology: A Review. *International Journal of Education and Applied Research* **2012**, *2*, 50-53.

(3) M.-C. Daniel; D. Astruc. Gold nanoparticles: assembly, supramolecular chemistry, quantum-sized related properties and applications towards biology catalysis and nanotechnology. *Chemical Reviews* **2004**, *104*, 296-346.

(4) M. Haruta; T. Kobayashi; H. Sano; N. Yamada. Novel gold catalysts for the oxidation of carbon monoxide at a temperature far below 0° C. *Chemistry Letters* **1987**, 405-408.

(5) B. Hvolbæk; T. V. W. Janssens; B. S. Clausen; H. Falsig; C. H. Christensen; J. K. Nørskov. Catalytic activity of Au nanoparticles. *Nano Today* **2007**, *2*, 14-18.

(6) B. Perks. Gold fever. *Chemistry world* **2010**, 48-50.

(7) T. G. Smijs; S. Pavel. Titanium dioxide and zinc oxide nanoparticles in sunscreens: focus on their safety and effectiveness. *Nanotechnology, science and applications* **2011**, *4*, 95-112.

(8) B. Le Ouay; F. Stellacci. Antibacterial activity of silver nanoparticles: A surface science insight. *Nano Today* **2015**, *10*, 339-354.

(9) K. M. M. Abou El-Nour; A. A. Eftaiha; A. Al-Warthan; R. a. A. Ammar. Synthesis and applications of silver nanoparticles. *Arabian Journal of Chemistry* **2010**, *3*, 135-140.

(10) M. Mirjalili; N. Yaghmaei; M. Mirjalili. Antibacterial properties of nano silver finish cellulose fabric *Journal of Nanostructure in Chemistry* **2013**, *3*.

(11) W. Cui; W. Lu; Y. Zhang; G. Lin; T. Wei; L. Jiang. Gold nanoparticle ink suitable for electric-conductive pattern fabrication using in ink-jet printing technology. *Colloids and Surfaces A: Physicochemical and Engineering Aspects* **2010**, *358*, 35-41.

(12) M. F. Beaux; D. N. Mcilroy; K. E. Gus. Utilization of solid nanomaterials for drug delivery. *Expert Opinion Drug Delivery* **2008**, *5*, 725-735.

(13) J. A. Barreto; W. O'malley; M. Kubeil; B. Graham; H. Stephan; L. Spiccia. Nanomaterials: applications in cancer imaging and therapy. *Advanced Materials* **2011**, *23*, H18-40.

(14) N. Trivedi; N. Patel; U. M. Upadhyay; V. Shah. Gold nanoparticulate drug delivery system: a review. *Pharmacie Globale (IJCP)* **2012**, *6*.

(15) M. S. Khan; G. D. Vishakante; H. Siddaramaiah. Gold nanoparticles: A paradigm shift in biomedical applications. *Advances in colloid and interface science* **2013**, *199*, 44-58.

(16) S. Madsen; P. Kempen; R. Sinclair. Characterization of E-beam fabricated gold nanoparticles. *Microscopy and Microanalysis* **2013**, *19*, 1554-1555.

(17) Alam Abedini; Abdul Razak Daud; M. A. A. Hamid; Norinsan Kamil Othman; A. E. Saion. A review on radiation-induced nucleation and growth of colloidal metallic nanoparticles. *Nanoscale Research Letters* **2013**, *8*, 474-483.

(18) N. S. Yusof; M. Ashokkumar. Sonochemical synthesis of gold nanoparticles by using high intensity focused ultrasound. *Chemphyschem* **2015**, *16*, 775-781.

(19) Y. Shang; C. Min; J. Hu; T. Wang; H. Liu; Y. Hu. Synthesis of gold nanoparticles by reduction of HAuCl4 under UV irradiation. *Solid State Sciences* **2013**, *15*, 17-23.

(20) G. Herrera; A. Padilla; S. Hernandez-Rivera. Surface enhanced Raman scattering (SERS) studies of gold and silver nanoparticles prepared by laser ablation. *Nanomaterials* **2013**, *3*, 158-172.

(21) R. Herizchi; E. Abbasi; M. Milani; A. Akbarzadeh. Current methods for synthesis of gold nanoparticles. *Artificial cells, nanomedicine, and biotechnology* **2016**, *44*, 596-602.

(22) J. Turkevich; P. C. Stevenson; J. Hillie. A study of the nucleation and growth processes in the synthesis of colloidal gold. *Discussions of the Faraday Society* **1951**, *11*, 55-75.

(23) J. Polte; T. Torsten Ahner; F. Delissen; S. Sokolov; F. Emmerling; A. F. Thunemann; A. R. Kraehnert. Mechanism of gold nanoparticle formation in the classical citrate synthesis method derived from coupled in situ xANES and sAXS evaluation. *Journal of American Chemical Society* **2010**, *132*, 1296-1301.

(24) J.-Y. Kim; C. S. Ah; D.-J. Jang. Controlled aspect ratios of gold nanorods in reduction-limited conditions. *Journal of Nanomaterials* **2011**, *2011*, 1-7.

(25) G. Mountrichas; S. Pispas; E. I. Kamitsos. Effect of temperature on the direct synthesis of gold nanoparticles mediated by poly(dimethylaminoethyl methacrylate) homopolymer. *The Journal of Physical Chemistry C* **2014**, *118*, 22754-22759.

(26) D. V. Goia; E. Matijevic. Tailoring the particle size of monodispersed colloidal gold nanoparticles. *Colloids and Surfaces A: Physicochemical and Engineering Aspects* **1999**, *146*, 139-152.

(27) X. Ji; X. Song; J. Li; Y. Bai; W. Yang; A. X. Peng. Size control of gold nanocrystals in citrate reduction the third role of citrate. *Journal of American Chemical Society* **2007**, *129*, 13939-13948.

(28) G. Frens. Controlled nucleation for the regulation of the particle size in monodisperse gold suspensions. *Nature Physical Science* **1972**, *241*, 1973-.

(29) P. Zhao; N. Li; D. And Astruc. State of the art in gold nanoparticle synthesis. *Coordination Chemistry Reviews* **2013**, *257*, 638-665.

(30) S. K. Sivaraman; S. Kumar; V. Santhanam. Monodisperse sub-10 nm gold nanoparticles by reversing the order of addition in Turkevich method - the role of chloroauric acid. *Journal of Colloid and Interface Science* **2011**, *361*, 543-547.

(31) Y. C. Yeh; B. Creran; V. M. Rotello. Gold nanoparticles: preparation, properties, and applications in bionanotechnology. *Nanoscale* **2012**, *4*, 1871-1880.

(32) M. Brust; M. Walker; D. Bethell; D. J. Schiffrin; A. R. Whyman. Synthesis of thiol-derivatised gold nanoparticles in a two-phase liquid-liquid system. *Journal of the Chemical Society, Chemical Communications* **1994**, 801-802.

(33) M.J. Hostetler; A.C. Templeton; A. R. W. Murray. Dynamics of place-exchange reactions on monolayer-protected gold cluster molecules. *Langmuir* **1999**, *15*, 3782-3789.

(34) A. C. Templeton; W. P. Wuelfing; R. W. Murray. Monolayer-Protected Cluster Molecules. *Accounts of Chemical Research* **2000**, *33*, 27-36.

(35) M. Brust; J. Fink; D. Bethella; D. J. Schiffrina; C. Kielyb. Synthesis and reactions of functionalised gold nanoparticles. *Journal of the Chemical Society, Chemical Communications* **1995**, 1655-1656.

(36) W. Li; X. Chen. Gold nanoparticles for photoacoustic imaging. *Nanomedicine (Lond.)* **2015**, *10*, 299-320.

(37) Y-Y. Yu; S-S. Chang; C-L. Lee; A. C. R. C. Wang. Gold nanorods: electrochemical synthesis and optical properties. *The Journal of Physical Chemistry B* **1997**, *101*, 6661-6664.

(38) Y. Gao; J. Gu; L. Li; W. Zhao; Y. Li. Synthesis of gold nanoshells through improved seed-mediated growth approach: brust-like, in situ seed formation. *Langmuir* **2016**, *32*, 2251-2258.

(39) M.-C. Daniel; D. Astruc. Gold nanoparticles assembly, supramolecular chemistry, quantum-sized related properties and applications towards biology catalysis and nanotechnology. *Chemical Reviews* **2004**, *104*, 296-346.

(40) G. Mie. Beiträge zur Optik trüber Medien, speziell kolloidaler Metallösungen (Contributions to the optics of diffuse media, especially colloid metal solutions). *Annalen der Physik* **1908**, 377-445.

(41) S. Link; M. El-Sayed. Shape and size dependence of radiative, non-radiative and photothermal properties of gold nanocrystals. *International Reviews in Physical Chemistry* **2000**, *19*, 409-453.

(42) W. Haiss; N. T. K. Thanh; J. Aveyard; D. G. Fernig. Determination of size and concentration of gold nanoparticles from UV−Vis spectra. *Analytical Chemistry* **2007**, *79*, 4215-4221.

(43) H.-B. Xing; Y.-G. Wu; S.-S. Zhan; P. Zhou. A rapid colorimetric detection of melamine in raw milk by unmodified gold nanoparticles. *Food Analytical Methods* **2013**, *6*, 1441-1447.

(44) K. Ai; Y. Liu; A. L. Lu. Hydrogen-bonding recognition-induced color change of gold nanoparticles for visual detection of melamine in raw milk and infant formula. *Journal of the Americal Chemical Society* **2009**, *131*, 9496-9497.

(45) Y. R. Kim; R. K. Mahajan; J. S. Kim; H. Kim. Highly sensitive gold nanoparticle-based colorimetric sensing of mercury(II) through simple ligand exchange reaction in aqueous media. *ACS applied materials & interfaces* **2010**, *2*, 292-295.

(46) K. Rahme; L. Chen; R. G. Hobbs; M. A. Morris; C. O'driscoll; J. D. Holmes. PEGylated gold nanoparticles: polymer quantification as a function of PEG lengths and nanoparticle dimensions. *RSC Advances* **2013**, *3*, 6085.

(47) K. Siriwardana; M. Gadogbe; S. M. Ansar; E. S. Vasquez; W. E. Collier; S. Zou; K. B. Walters; D. Zhang. Ligand adsorption and exchange on pegylated gold nanoparticles. *The Journal of Physical Chemistry C* **2014**, *118*, 11111-11119.

(48) S. Hong; X. Li. Optimal Size of Gold Nanoparticles for Surface-Enhanced Raman Spectroscopy under Different Conditions. *Journal of Nanomaterials* **2013**, *2013*, 1-9.

(49) L. Polavarapu; Q.-H. Xu. Water-soluble conjugated polymer-induced self-assembly of gold nanoparticles and its application to SERS. *Langmuir* **2008**, *24*, 10608-10611.

(50) Y. Liu; L. Qiao; L. Liu; R. Guo. pH controlled assembly of gold nanoparticles coated with glutamic acid: assembly mechanism, the effect of NaBr, and SERS performance. *Colloids and Surfaces A: Physicochemical and Engineering Aspects* **2015**, *474*, 92-100.

(51) M. Roy Chowdhury; C. Schumann; D. Bhakta-Guha; G. Guha. Cancer nanotheranostics: strategies, promises and impediments. *Biomedicine & pharmacotherapy* **2016**, *84*, 291-304.

(52) M. Z. Ahmad. Metallic nanoparticles technology overview & drug delivery applications in oncology. *Expert Opinion on Drug Delivery* **2010**, *7*, 927-942.

(53) D. F. Baban; L. W. Seymour. Control of tumour vascular permeability. *Advanced Drug Delivery Reviews* **1998**, *34*, 109-119.

(54) R. A. Petros; J. M. Desimone. Strategies in the design of nanoparticles for therapeutic applications. *Nature Reviews Drug Discovery* **2010**, *9*, 615-627.

(55) X. Huang; P. K. Jain; I. H. El-Sayed; M. A. El-Sayed. Plasmonic photothermal therapy (PPTT) using gold nanoparticles. *Lasers in Medical Science* **2008**, *23*, 217-228.

(56) S. C. Nguyen; Q. Zhang; K. Manthiram; X. Ye; J. P. Lomont; C. B. Harris; H. Weller; A. P. Alivisatos. Study of heat transfer dynamics from gold nanorods to the environment via time-resolved infrared spectroscopy. *ACS Nano* **2016**, *10*, 2144-2151.

(57) F. Jabeen; M. Najam-Ul-Haq; R. Javeed; C. W. Huck; G. K. Bonn. Au-nanomaterials as a superior choice for near-infrared photothermal therapy. *Molecules* **2014**, *19*, 20580-20593.

(58) T. S. Hauck; T. L. Jennings; T. Yatsenko; J. C. Kumaradas; W. C. W. Chan. Enhancing the toxicity of cancer chemotherapeutics with gold nanorod hyperthermia. *Advanced Materials* **2008**, *20*, 3832-3838.

(59) X. Li; M. Takashima; E. Yuba; A. Harada; K. Kono. PEGylated PAMAM dendrimer-doxorubicin conjugate-hybridized gold nanorod for combined photothermal-chemotherapy. *Biomaterials* **2014**, *35*, 6576-6584.

(60) N. S. Abadeer; C. J. Murphy. Recent progress in cancer thermal therapy using gold nanoparticles. *The Journal of Physical Chemistry C* **2016**, *120*, 4691-4716.

(61) Z. Wang; Z. Chen; Z. Liu; P. Shi; K. Dong; E. Ju; J. Ren; X. Qu. A multi-stimuli responsive gold nanocage-hyaluronic platform for targeted photothermal and chemotherapy. *Biomaterials* **2014**, *35*, 9678-9688.

(62) J. A. Webb; R. Bardhan. Emerging advances in nanomedicine with engineered gold nanostructures. *Nanoscale* **2014**, *6*, 2502-2530.

(63) Y. Cheng; A. C. Samia; J. D. Meyers; I. Panagopoulos; B. Fei; C. Burda. Highly efficient drug delivery with gold nanoparticle vectors for in vivo photodynamic therapy of cancer. *Journal of American Chemical Society* **2008**, *130*, 10643-10647.

(64) Y. S. Chen; W. Frey; S. Kim; P. Kruizinga; K. Homan; S. Emelianov. Silica-coated gold nanorods as photoacoustic signal nanoamplifiers. *Nano Letters* **2011**, *11*, 348-354.

(65) N. Manohar; F. J. Reynoso; P. Diagaradjane; S. Krishnan; S. H. Cho. Quantitative imaging of gold nanoparticle distribution in a tumor-bearing mouse using benchtop x-ray fluorescence computed tomography. *Scientific Reports* **2016**, *6*, 22079.

(66) C. C. Chien; H. H. Chen; S. F. Lai; K. C. Wu; X. Cai; Y. Hwu; C. Petibois; Y. Chu; G. Margaritondo. Gold nanoparticles as high-resolution X-ray imaging contrast agents for the analysis of tumor-related micro-vasculature. *Journal of nanobiotechnology* **2012**, *10*, 10.

(67) M. Zhang; L. Lin. Enhancement of coherent optical signal from tissue phantom by gold nanorods in near-infrared range. *Optik - International Journal for Light and Electron Optics* **2016**, *127*, 8983-8987.

(68) O. Liba; E. D. Sorelle; D. Sen; A. De La Zerda. Contrast-enhanced optical coherence tomography with picomolar sensitivity for functional in vivo imaging. *Scientific Reports* **2016**, *6*, 23337.

(69) X. Y. Wan; L. L. Zheng; P. F. Gao; X. X. Yang; C. M. Li; Y. F. Li; C. Z. Huang. Real-time light scattering tracking of gold nanoparticles- bioconjugated respiratory syncytial virus infecting HEp-2 cells. *Scientific Reports* **2014**, *4*, 4529.

(70) P. J. Debouttière; S. Roux; F. Vocanson; C. Billotey; O. Beuf; A. Favre-Réguillon; Y. Lin; S. Pellet-Rostaing; R. Lamartine; P. Perriat; O. Tillement. Design of gold nanoparticles for magnetic resonance imaging. *Advanced Functional Materials* **2006**, *16*, 2330-2339.

(71) S. Jung; J. Nam; S. Hwang; J. Park; J. Hur; K. Im; N. Park; S. Kim. Theragnostic pH-sensitive gold nanoparticles for the selective surface enhanced Raman scattering and photothermal cancer therapy. *Analytical Chemistry* **2013**, *85*, 7674-7681.

(72) Z. Wang. Plasmon-resonant gold nanoparticles for cancer optical imaging. *Science China Physics, Mechanics & Astronomy* **2013**, *56*, 506 – 513.

(73) S. Kim; Y.-S. Chen; G. P. Luke; S. Y. Emelianov. In-vivo ultrasound and photoacoustic image- guided photothermal cancer therapy using silica-coated gold nanorods. *IEEE Transactions on Ultrasonics, Ferroelectrics, and Frequency Control* **2014**, *61*, 891-897.

(74) S. Lee; H. Chon; J. Lee; J. Ko; B. H. Chung; D. W. Lim; J. Choo. Rapid and sensitive phenotypic marker detection on breast cancer cells using surface-enhanced Raman scattering (SERS) imaging. *Biosensors & Bioelectronics* **2014**, *51*, 238-243.

(75) C. L. Zavaleta; B. R. Smith; I. Walton; W. Doering; G. Davis; B. Shojaei; M. J. Natan; S. S. Gambhir. Multiplexed imaging of surface enhanced Raman scattering nanotags in living mice using noninvasive Raman spectroscopy. *Proceedings of the National Academy of Sciences* **2009**, *106*, 13511-13516.

(76) C. H. Li; T. R. Kuo; H. J. Su; W. Y. Lai; P. C. Yang; J. S. Chen; D. Y. Wang; Y. C. Wu; C. C. Chen. Fluorescence-Guided Probes of Aptamer-Targeted Gold Nanoparticles with Computed Tomography Imaging Accesses for in Vivo Tumor Resection. *Scientific Reports* **2015**, *5*, 15675.

(77) A. Kumar; B. Mazinder Boruah; X.-J. Liang. Gold nanoparticles: promising nanomaterials for the diagnosis of cancer and HIV/AIDS. *Journal of Nanomaterials* **2011**, *2011*, 1-17.

(78) E. Boisselier; D. Astruc. Gold nanoparticles in nanomedicine: preparations, imaging, diagnostics, therapies and toxicity. *Chemical Society Reviews* **2009**, *38*, 1759-1782.

(79) Colin D. Medley; Joshua E. Smith; Zhiwen Tang; Yanrong Wu; Suwussa Bamrungsap; A. W. Tan. Gold nanoparticle-based colorimetric assay for the direct detection of cancerous cells. *Analytical Chemistry* **2008**, *80*, 1067-1072.

(80) Z. Li; X. Miao; Z. Cheng; P. Wang. Hybridization chain reaction coupled with the fluorescence quenching of gold nanoparticles for sensitive cancer protein detection. *Sensors and Actuators B: Chemical* **2017**, *243*, 731-737.

(81) A. B. Chinen; C. M. Guan; J. R. Ferrer; S. N. Barnaby; T. J. Merkel; C. A. Mirkin. Nanoparticle probes for the detection of cancer biomarkers, cells, and tissues by fluorescence. *Chemical Reviews* **2015**, *115*, 10530-10574.

(82) Y. Li; Z. Zhong; Y. Chai; Z. Song; Y. Zhuo; H. Su; S. Liu; D. Wang; R. Yuan. Simultaneous electrochemical immunoassay of three liver cancer biomarkers using distinguishable redox probes as signal tags and gold nanoparticles coated carbon nanotubes as signal enhancers. *Chemical communications* **2012**, *48*, 537-539.

(83) D. Kim; S. Jon. Gold nanoparticles in image-guided cancer therapy. *Inorganica Chimica Acta* **2012**, *393*, 154-164.

(84) N. Zhao; Y. Pan; Z. Cheng; H. Liu. Gold nanoparticles for cancer theranostics - a brief update. *Journal of Innovative Optical Health Sciences* **2016**, *09*, 1630004.

(85) L. A. Dykman; N. G. Khlebtsov. Multifunctional gold-based nanocomposites for theranostics. *Biomaterials* **2016**, *108*, 13-34.

(86) H. Deng; F. Dai; G. Ma; X. Zhang. Theranostic gold nanomicelles made from biocompatible comb-like polymers for thermochemotherapy and multifunctional imaging with rapid clearance. *Advanced Materials* **2015**, *27*, 3645-3653.

(87) A. M. Alkilany; E. C. Goldsmith; S. C. Baxter; C. J. Murphy; A. M. Gole; J. W. Stone; P. N. Sisco. Gold nanoparticles in biology beyond toxicity to cellular imaging. *Accounts of chemical research* **2008**, *41*.

(88) E. E. Connor; J. Mwamuka; A. Gole; C. J. Murphy; M. D. Wyatt. Gold nanoparticles are taken up by human cells but do not cause acute cytotoxicity. *Small* **2005**, *1*, 325-327.

(89) S. W. Tsai; J. W. Liaw; Y. C. Kao; M. Y. Huang; C. Y. Lee; L. R. Rau; C. Y. Huang; K. C. Wei; T. C. Ye. Internalized gold nanoparticles do not affect the osteogenesis and apoptosis of MG63 osteoblast-like cells: a quantitative, in vitro study. *PLoS One* **2013**, *8*, e76545.

(90) P. C. Naha; P. Chhour; D. P. Cormode. Systematic in vitro toxicological screening of gold nanoparticles designed for nanomedicine applications. *Toxicology in vitro* **2015**, *29*, 1445-1453.

(91) N. Pernodet; X. Fang; Y. Sun; A. Bakhtina; A. Ramakrishnan; J. Sokolov; A. Ulman; M. Rafailovich. Adverse effects of citrate/gold nanoparticles on human dermal fibroblasts. *Small* **2006**, *2*, 766-773.

(92) Y. S. Chen; Y. C. Hung; I. Liau; G. S. Huang. Assessment of the in vivo toxicity of gold nanoparticles. *Nanoscale research letters* **2009**, *4*, 858-864.

(93) W. Jiang; B. Y. Kim; J. T. Rutka; W. C. Chan. Nanoparticle-mediated cellular response is size-dependent. *Nature nanotechnology* **2008**, *3*, 145-150.

(94) C. M. Goodman; C. D. Mccusker; T. Yilmaz; V. M. Rotello. Toxicity of gold nanoparticles functionalized with cationic and anionic side chains. *Bioconjugate Chemistry* **2004**, *15*, 897-900.

(95) A. M. Alkilany; P. K. Nagaria; C. R. Hexel; T. J. Shaw; C. J. Murphy; M. D. Wyatt. Cellular uptake and cytotoxicity of gold nanorods: molecular origin of cytotoxicity and surface effects. *Small* **2009**, *5*, 701-708.

(96) M. Tarantola; A. Pietuch; D. Schneider; J. Rother; E. Sunnick; C. Rosman; S. Pierrat; C. Sonnichsen; J. Wegener; A. Janshoff. Toxicity of gold-nanoparticles: synergistic effects of shape and surface functionalization on micromotility of epithelial cells. *Nanotoxicology* **2011**, *5*, 254-268.

(97) J. A. Coulter; S. Jain; K. T. Butterworth; L. E. Taggart; G. R. Dickson; S. J. Mcmahon; W. B. Hyland; M. F. Muir; C. Trainor; A. R. Hounsell; J. M. O'sullivan; G. Schettino; F. J. Currell; D. G. Hirst; K. M. Prise. Cell type-dependent uptake, localization, and cytotoxicity of 1.9 nm gold nanoparticles. *International Journal of Nanomedicine* **2012**, *7*, 2673-2685.

(98) B. D. Chithrani; A. A. Ghazani; W. C. W. Chan. Determining the size and shape dependance of gold nanoparticle uptake into mammalian cells. *Nano Letters* **2006**, *6*, 662-668.

(99) S. Wang; W. Lu; O. Tovmachenko; U. S. Rai; H. Yu; P. C. Ray. Challenge in understanding size and shape dependent toxicity of gold nanomaterials in human skin keratinocytes. *Chemical Physics Letters* **2008**, *463*, 145-149.

(100) I. Fratoddi; I. Venditti; C. Cametti; M. V. Russo. How toxic are gold nanoparticles? The state-of-the-art. *Nano Research* **2015**, *8*, 1771-1799.

(101) N. Lewinski; V. Colvin; R. Drezek. Cytotoxicity of nanoparticles. *Small* **2008**, *4*, 26-49.

(102) E. Blanco; H. Shen; M. Ferrari. Principles of nanoparticle design for overcoming biological barriers to drug delivery. *Nature Biotechnology* **2015**, *33*, 941-951.

(103) R. Ramachandran; C. Krishnaraj; A. S. Sivakumar; P. Prasannakumar; V. K. Abhay Kumar; K. S. Shim; C.-G. Song; S.-I. Yun. Anticancer activity of biologically synthesized silver and gold nanoparticles on mouse myoblast cancer cells and their toxicity against embryonic zebrafish. *Materials Science and Engineering: C* **2017**, *73*, 674-683.

(104) A. Wicki; D. Witzigmann; V. Balasubramanian; J. Huwyler. Nanomedicine in cancer therapy: challenges, opportunities, and clinical applications. *Journal of Controlled Release* **2015**, *200*, 138-157.

(105) V. Weissig; T. K. Pettinger; N. Murdock. Nanopharmaceuticals (part 1): products on the market. *International Journal of Nanomedicine* **2014**, *9*, 4357-4373.

(106) A. C. Anselmo; S. Mitragotri. Nanoparticles in the clinic. *Bioengineering & Translational Medicine* **2016**, *1*, 10-29.

(107) P. Pedrosa; R. Vinhas; A. Fernandes; P. Baptista. Gold Nanotheranostics: Proof-of-Concept or Clinical Tool? *Nanomaterials* **2015**, *5*, 1853-1879.

(108) S. Guo; L. Huang. Nanoparticles escaping RES and endosome: challenges for siRNA delivery for cancer therapy. *Journal of Nanomaterials* **2011**, *2011*, 1-12.

(109) W. Shao; P. Arghya; M. Yiyong; L. Rodes; S. Prakash: Carbon nanotubes for use in medicine: potentials and limitations. In *Carbon Nanotubes for Use in Medicine: Potentials and Limitations*; Suzuki, S., Ed., 2013.

(110) Arnida; A. Malugin; H. Ghandehari. Cellular uptake and toxicity of gold nanoparticles in prostate cancer cells: a comparative study of rods and spheres. *Journal of Applied Toxicology* **2010**, *30*, 212-217.

(111) R. Cheheltani; R. M. Ezzibdeh; P. Chhour; K. Pulaparthi; J. Kim; M. Jurcova; J. C. Hsu; C. Blundell; H. I. Litt; V. A. Ferrari; H. R. Allcock; C. M. Sehgal; D. P. Cormode. Tunable, biodegradable gold nanoparticles as contrast agents for computed tomography and photoacoustic imaging. *Biomaterials* **2016**, *102*, 87-97.

(112) M. Bachelet. Design of pH-responsive gold nanoparticles in oncology. *Materials Science and Technology* **2016**, *32*, 794-804.

(113) A. O. Elzoghby; A. L. Hemasa; M. S. Freag. Hybrid protein-inorganic nanoparticles: From tumor-targeted drug delivery to cancer imaging. *Journal of Controlled Release* **2016**, *243*, 303-322.

(114) P. Zhao; N. Li; D. Astruc. State of the art in gold nanoparticle synthesis. *Coordination Chemistry Reviews* **2013**, *257*, 638-665.

(115) J. You; G. Zhang; A. C. Li. Exceptionally high payload of doxorubicin in hollow gold nanospheres for near-infrared light-triggered drug release. *ACS Nano* **2010**, *4*, 1033-1041.

(116) D. Curry; A. Cameron; B. Macdonald; C. Nganou; H. Scheller; J. Marsh; S. Beale; M. Lu; Z. Shan; R. Kaliaperumal; H. Xu; M. Servos; C. Bennett; S. Macquarrie; K. D. Oakes; M. Mkandawire; X. Zhang. Adsorption of doxorubicin on citrate-capped gold nanoparticles: insights into engineering potent chemotherapeutic delivery systems. *Nanoscale* **2015**, *7*, 19611-19619.

(117) C.K. Kim; P. Ghosh; C. Pagliuca; Z-J. Zhu; S. Menichetti; A. V. M. Rotello. Entrapment of hydrophobic drugs in nanoparticle monolayers with efficient release into cancer cells. *Journal of American Chemical Society* **2009**, *131*, 1360-1361.

(118) A. Madhusudhan; G. B. Reddy; M. Venkatesham; G. Veerabhadram; D. A. Kumar; S. Natarajan; M. Y. Yang; A. Hu; S. S. Singh. Efficient pH dependent drug delivery to target cancer cells by gold nanoparticles capped with carboxymethyl chitosan. *International Journal of Molecular Sciences* **2014**, *15*, 8216-8234.

(119) G. H. Rui Hong, Joseph M. Fernandez, Byoung-Jin Kim, Neil S. Forbes, and Vincent M. Rotello. Glutathione-mediated delivery and release using monolayer protected nanoparticle carriers. *Journal of American Chemical Society* **2006**, *128*, 1078-1079.

(120) D. Kumar; B. J. Meenan; D. Dixon. Glutathione-mediated release of Bodipy(R) from PEG cofunctionalized gold nanoparticles. *International Journal of Nanomedicine* **2012**, *7*, 4007-4022.

(121) K. Ock; W. I. Jeon; E. O. Ganbold; M. Kim; J. Park; J. H. Seo; K. Cho; S. W. Joo; S. Y. Lee. Real-time monitoring of glutathione-triggered thiopurine anticancer drug release in live cells investigated by surface-enhanced Raman scattering. *Analytical Chemistry* **2012**, *84*, 2172-2178.

(122) C. Park; H. Youn; H. Kim; T. Noh; Y. H. Kook; E. T. Oh; H. J. Park; C. Kim. Cyclodextrin-covered gold nanoparticles for targeted delivery of an anti-cancer drug. *Journal of Materials Chemistry* **2009**, *19*, 2310-2315.

(123) Y.-H. Chen; C.-Y. Tsai; P.-Y. Huang; M.-Y. Chang; P.-C. Cheng; C.-H. Chou; D.-H. Chen; C.-R. Wang; A.-L. Shiau; C.-L. Wu. Methotrexate conjugated to gold nanoparticles inhibits tumor growth. *Molecular Pharmaceutics* **2007**, *4*, 713-722.

(124) Y. J. Gu; J. Cheng; C. W. Man; W. T. Wong; S. H. Cheng. Gold-doxorubicin nanoconjugates for overcoming multidrug resistance. *Nanomedicine* **2012**, *8*, 204-211.

(125) S. Mukherjee; R. N. Gosh; A. F. R. Maxfield. Endocytosis. *Physiological Reviews* **1997**, *77*, 759-803.

(126) Y. Xiao; H. Hong; V. Z. Matson; A. Javadi; W. Xu; Y. Yang; Y. Zhang; J. W. Engle; R. J. Nickles; W. Cai; D. A. Steeber; S. Gong. Gold nanorods conjugated with doxorubicin and cRGD for combined anticancer drug delivery and PET imaging. *Theranostics* **2012**, *2*, 757-768.

(127) S. Aryal; J. J. Grailer; S. Pilla; D. A. Steeber; S. Gong. Doxorubicin conjugated gold nanoparticles as water-soluble and pH-responsive anticancer drug nanocarriers. *Journal of Materials Chemistry* **2009**, *19*, 7879.

(128) F. Wang; Y-C. Wang; S. Dou; M-H. Xiong; T-M. Sun; A. J. Wang. Doxorubicin-tethered responsive gold nanoparticles facilitate intracellular drug delivery for overcoming multidrug resistance in cancer cells. *ACS Nano* **2011**, *5*, 3679-3692.

(129) K. Y. J. Lee; Y. Wang; S. Nie. In vitro study of a pH-sensitive multifunctional doxorubicin – gold nanoparticle system: therapeutic effect and surface enhanced Raman scattering. *RSC Advances* **2015**, *5*, 65651-65659.

(130) M. Prabaharan; J. J. Grailer; S. Pilla; D. A. Steeber; S. Gong. Gold nanoparticles with a monolayer of doxorubicin-conjugated amphiphilic block copolymer for tumor-targeted drug delivery. *Biomaterials* **2009**, *30*, 6065-6075.

(131) S. Ruan; M. Yuan; L. Zhang; G. Hu; J. Chen; X. Cun; Q. Zhang; Y. Yang; Q. He; H. Gao. Tumor microenvironment sensitive doxorubicin delivery and release to glioma using angiopep-2 decorated gold nanoparticles. *Biomaterials* **2015**, *37*, 425-435.

(132) E.-J. Cha; I.-C. Sun; S. C. Lee; K. Kim; I. C. Kwon; C.-H. Ahn. Development of a pH sensitive nanocarrier using calcium phosphate coated gold nanoparticles as a platform for a potential theranostic material. *Macromolecular Research* **2012**, *20*, 319-326.

(133) L. Song; V. H. Ho; C. Chen; Z. Yang; D. Liu; R. Chen; D. Zhou. Efficient, pH-triggered drug delivery using a pH-responsive DNA-conjugated gold nanoparticle. *Advanced Healthcare Materials* **2013**, *2*, 275-280.

(134) J. Nakanishi; H. Nakayama; T. Shimizu; H. Ishida; Yukiko Kikuchi; K. Yamaguchi; A. Y. Horiike. Light-regulated activation of cellular signaling by gold nanoparticles that captures and releases amines. *Journal of the American Chemical Society* **2008**, *131*, 3822-3823.

(135) A. C. Sarit S. Agasti, Chang-Cheng You, Partha Ghosh, Chae Kyu Kim, And; V. M. Rotello. Photoregulated release of caged anticancer drugs from gold nanoparticles. *Journal of American Chemical Society* **2009**, *131*, 5728-5729.

(136) G. Bisker; D. Yeheskely-Hayon; L. Minai; D. Yelin. Controlled release of Rituximab from gold nanoparticles for phototherapy of malignant cells. *Journal of Controlled Release* **2012**, *162*, 303-309.

(137) Y. Qu; B. Y. Chu; J. R. Peng; J. F. Liao; T. T. Qi; K. Shi; X. N. Zhang; Y. Q. Wei; Z. Y. Qian. A biodegradable thermo-responsive hybrid hydrogel: therapeutic applications in preventing the post-operative recurrence of breast cancer. *NPG Asia Materials* **2015**, *7*, e207.

(138) C. R. Souza; H. R. Oliveira; W. M. Pinheiro; L. S. Biswaro; R. B. Azevedo; A. J. Gomes; C. N. Lunardi. Gold Nanoparticle and berberine entrapped into hydrogel matrix as drug delivery system. *Journal of Biomaterials and Nanobiotechnology* **2015**, *06*, 53-63.

(139) N. Zhang; X. Xu; X. Zhang; D. Qu; L. Xue; R. Mo; C. Zhang. Nanocomposite hydrogel incorporating gold nanorods and paclitaxel-loaded chitosan micelles for

combination photothermal-chemotherapy. *International Journal of Pharmaceutics* **2016**, *497*, 210-221.

(140) T. Niidome; M. Yamagata; Y. Okamoto; Y. Akiyama; H. Takahashi; T. Kawano; Y. Katayama; Y. Niidome. PEG-modified gold nanorods with a stealth character for in vivo applications. *Journal of Controlled Release* **2006**, *114*, 343-347.

(141) F. Geng; K. Song; J. Z. Xing; C. Yuan; S. Yan; Q. Yang; J. Chen; B. Kong. Thio-glucose bound gold nanoparticles enhance radio-cytotoxic targeting of ovarian cancer. *Nanotechnology* **2011**, *22*, 285101.

(142) I. H. El-Sayed; X. Huang; M. A. El-Sayed. Selective laser photo-thermal therapy of epithelial carcinoma using anti-EGFR antibody conjugated gold nanoparticles. *Cancer Letters* **2006**, *239*, 129-135.

(143) V. Cebrian; F. Martin-Saavedra; L. Gomez; M. Arruebo; J. Santamaria; N. Vilaboa. Enhancing of plasmonic photothermal therapy through heat-inducible transgene activity. *Nanomedicine* **2013**, *9*, 646-656.

(144) C. H. Choi; C. A. Alabi; P. Webster; M. E. Davis. Mechanism of active targeting in solid tumors with transferrin-containing gold nanoparticles. *Proceedings of the National Academy of Sciences of the United States of America* **2010**, *107*, 1235-1240.

(145) P. Ghosh; G. Han; M. De; C. K. Kim; V. M. Rotello. Gold nanoparticles in delivery applications. *Advanced Drug Delivery Reviews* **2008**, *60*, 1307-1315.

(146) M. V. a. I. A. Bahareh Asadishad. Folate-Receptor-Targeted Delivery of Doxorubicin Using Polyethylene Glycol Functionalized Gold Nanoparticles. *Industrial and Engineering Chemistry Research* **2010**, *49*, 1958-1963.

(147) V. Dixit. Synthesis and grafting of thioctic acid-PEG-folate conjugates onto Au nanoparticles for selective targeting of folate receptor-positive tumour cells. *Bioconjugate Chemistry* **2006**, *17*, 603-609.

(148) E. C. Dreaden; S. C. Mwakwari; Q. H. Sodji; A. K. Oyelere; M. A. El-Sayed. Tamoxifen-poly(ethylene glycol)-thiol gold nanoparticle conjugates: enhanced potency and selective delivery for breast cancer treatment. *Bioconjugate Chemistry* **2009**, *20*, 2247-2253.

(149) M. Das. Ligand-based targeted therapy for cancer tissue. *Expert opinion drug delivery* **2009**, *6*, 285-304.

(150) E. Caló; V. V. Khutoryanskiy. Biomedical applications of hydrogels: A review of patents and commercial products. *European Polymer Journal* **2015**, *65*, 252-267.

(151) P. Thoniyot; M. J. Tan; A. A. Karim; D. J. Young; X. J. Loh. Nanoparticle-hydrogel composites: concept, design, and applications of these promising, multi-functional materials. *Advanced science* **2015**, *2*, 1400010.

(152) N. S. Satarkar; D. Biswal; J. Z. Hilt. Hydrogel nanocomposites: a review of applications as remote controlled biomaterials. *Soft Matter* **2010**, *6*, 2364.

(153) C. Wang; N.T. Flynn; A. R. Langer. Controlled structure and properties of thermoresponsive nanoparticle hydrogel composites. *Advanced Materials* **2004**, *16*, 1074-1079.

(154) T. Kawano; Y. Niidome; T. Mori; Y. Katayama; A. T. Niidome. PNIPAM gel-coated gold nanorods for targeted delivery responding to a NIR laser. *Bioconjugate Chemistry* **2009**, *20*, 209-212.

(155) H. H. Park; T. R. Lee. Thermo- and pH-responsive hydrogel-coated gold nanoparticles prepared from rationally designed surface-confined initiators. *Journal of Nanoparticle Research* **2010**, *13*, 2909-2918.

(156) N. Dolya; O. Rojas; S. Kosmella; B. Tiersch; J. Koetz; S. Kudaibergenov. "One-Pot" in situ formation of gold nanoparticles within poly(acrylamide) hydrogels. *Macromolecular Chemistry and Physics* **2013**, *214*, 1114-1121.

(157) N. Oh; J. H. Park. Endocytosis and exocytosis of nanoparticles in mammalian cells. *International Journal of Nanomedicine* **2014**, *9 Suppl 1*, 51-63.

(158) H. Schulze; T. Kolter; K. Sandhoff. Principles of lysosomal membrane degradation: Cellular topology and biochemistry of lysosomal lipid degradation. *Biochimica et Biophysica Acta* **2009**, *1793*, 674-683.

(159) Z. Shen; M.-P. Nieh; Y. Li. Decorating nanoparticle surface for targeted drug delivery: opportunities and challenges. *Polymers* **2016**, *8*, 83.

(160) S. Chai; K.K.W. To; A. G. Lin. Circumvention of multi-drug resistance of cancer cells by Chinese herbal medicines. *Chinese Medicine* **2010**, *5*.

(161) X. Dong; A. R. J. Mumper. Nanomedicinal strategies to treat multidrug-resistant tumors: current progress. *Nanomedicine* **2010**, *5*, 597-615.

(162) A. K. Varkouhi; M. Scholte; G. Storm; H. J. Haisma. Endosomal escape pathways for delivery of biologicals. *Journal of Controlled Release* **2011**, *151*, 220-228.

(163) V. Mundra; R. I. Mahato. Design of nanocarriers for efficient cellular uptake and endosomal release of small molecule and nucleic acid drugs: learning from virus. *Frontiers of Chemical Science and Engineering* **2014**, *8*, 387-404.

(164) C. Plank; W. Zauner; E. Wagner. Application of membrane-active peptides for drug and gene delivery across cellular membranes. *Advanced Drug Delivery Reviews* **1998**, *34*, 21-35.

(165) O. Warburg; F. Wind; E. Negelein. The metabolism of tumors in the body. *The journal of General Physiology* **1926**, 519-530.

(166) M. Bahram; N. Mohseni; M. Moghtader: *Chapter 2: An Introduction to Hydrogels and Some Recent Applications, Emerging Concepts in Analysis and Applications of Hydrogels*, 2016.

(167) M. A. Yessine; J. C. Leroux. Membrane-destabilizing polyanions: interaction with lipid bilayers and endosomal escape of biomacromolecules. *Advanced drug delivery reviews* **2004**, *56*, 999-1021.

(168) D. Fischera; Y. Lib; B. Ahlemeyerc; J. Krieglsteinc; A. T. Kissela. In vitro cytotoxicity testing of polycations influence of polymer structure on cell viability and hemolysis. *Biomaterials* **2003**, *24*, 1121-1131.

(169) N. Murthy; J. Campbell; N. Fausto; A. S. Hoffman; P. S. Stayton. Design and synthesis of pH-responsive polymeric carriers that target uptake and enhance the intracellular delivery of oligonucleotides. *Journal of Controlled Release* **2003**, *89*, 365-374.

(170) M.E. Eccleston; M. Kuiper; F.M. Gilchrist; A. N. K. H. Slater. pH-responsive pseudo-peptides for cell membrane disruption. *Journal of Controlled Release* **2000**, *69*, 297-307.

(171) G. Lin; P. Mi; C. Chu; J. Zhang; G. Liu. Inorganic nanocarriers overcoming multidrug resistance for cancer theranostics. *Advanced science* **2016**, *3*, 1600134.

(172) R. Chen; Z. Yue; M. E. Eccleston; S. Williams; N. K. And Slater. Modulation of cell membrane disruption by pH-responsive pseudo-peptides through grafting with hydrophilic side chains. *Journal of Controlled Release* **2005**, *108*, 63-72.

(173) R. Chen; Z. Yue; M. E. Eccleston; N. K. And Slater. Aqueous solution behaviour and membrane disruptive activity of pH-responsive PEGylated pseudo-peptides and their intracellular distribution. *Biomaterials* **2008**, *29*, 4333-4340.

(174) S. Zhang; A. Nelson; Z. Coldrick; R. Chen. The effects of substituent grafting on the interaction of pH-responsive polymers with phospholipid monolayers. *Langmuir* **2011**, *27*, 8530-8539.

(175) R. Chen; M. E. Eccleston; Z. Yue; N. K. H. Slater. Synthesis and pH-responsive properties of pseudo-peptide containing hydrophobic aminoacids grafts. *Journal of Materials Chemistry* **2009**, *19*, 4217-4224.

(176) R. Chen; S. Khormaee; M. E. Eccleston; N. K. And Slater. The role of hydrophobic amino acid grafts in the enhancement of membrane-disruptive activity of pH-responsive pseudo-peptides. *Biomaterials* **2009**, *30*, 1954-1961.

(177) S. Khormaee; R. Chen; J. K. Park; N. K. Slater. The influence of aromatic side-chains on the aqueous properties of pH-sensitive poly(L-lysine iso-phthalamide) derivatives. *Journal of Biomaterials Science Polymer Edition* **2010**, *21*, 1573-1588.

(178) A. L. Lynch; R. Chen; N. K. Slater. pH-responsive polymers for trehalose loading and desiccation protection of human red blood cells. *Biomaterials* **2011**, *32*, 4443-4449.

(179) S. Khormaee; Y. Choi; M. J. Shen; B. Xu; H. Wu; G. L. Griffiths; R. Chen; N. K. Slater; J. K. Park. Endosomolytic anionic polymer for the cytoplasmic delivery of siRNAs in localized applications. *Advanced Functional Materials* **2013**, *23*.

(180) V. H. Ho; N. K. Slater; R. Chen. pH-responsive endosomolytic pseudo-peptides for drug delivery to multicellular spheroids tumour models. *Biomaterials* **2011**, *32*, 2953-2958.

(181) W. B. Liechty; R. Chen; F. Farzaneh; M. Tavassoli; N. K. Slater. Synthetic pH-responsive polymers for protein transduction. *Advanced Materials* **2009**, *21*, 3910-3914.

(182) F. Wang; Y. Shen; W. Zhang; M. Li; Y. Wang; D. Zhou; S. Guo. Efficient, dual-stimuli responsive cytosolic gene delivery using a RGD modified disulfide-linked polyethylenimine functionalized gold nanorod. *Journal of Controlled Release* **2014**, *196*, 37-51.

(183) V. Cebrian; F. Martin-Saavedra; C. Yague; M. Arruebo; J. Santamaria; N. Vilaboa. Size-dependent transfection efficiency of PEI-coated gold nanoparticles. *Acta Biomaterialia* **2011**, *7*, 3645-3655.

(184) P.S. Ghosh; C-K. Kim; G. Han; N.S. Forbes; A. V. M. Rotello. Efficient gene delivery vectors by tuning the surface charge density of amino acid-functionalized gold nanoparticles. *ACS Nano* **2008**, *2*, 2213-2218.

(185) W. H. Kong; K. H. Bae; S. D. Jo; J. S. Kim; T. G. Park. Cationic lipid-coated gold nanoparticles as efficient and non-cytotoxic intracellular siRNA delivery vehicles. *Pharmaceutical Research* **2012**, *29*, 362-374.

(186) Y. Lee; S. H. Lee; J. S. Kim; A. Maruyama; X. Chen; T. G. Park. Controlled synthesis of PEI-coated gold nanoparticles using reductive catechol chemistry for siRNA delivery. *Journal of Controlled Release* **2011**, *155*, 3-10.

(187) D. Joydeep; Y. J. Choi; H. Yasuda; J. W. Han; C. Park; H. Song; H. Bae; J. H. Kim. Efficient delivery of C/EBP beta gene into human mesenchymal stem cells via polyethylenimine-coated gold nanoparticles enhances adipogenic differentiation. *Scientific Reports* **2016**, *6*, 33784.

(188) M. Thomas; A. M. Klibanov. Conjugation to gold nanoparticles enhances polyethylenimine's transfer of plasmid DNA into mammalian cells. *Proceedings of the National Academy of Sciences of the United States of America* **2003**, *100*, 9138-9143.

(189) S. Son; J. Nam; J. Kim; S. Kim; A. W. J. Kim. i‐Motif-driven Au nanomachines in programmed siRNA delivery for gene-silencing and photothermal ablation. *ACS Nano* **2014**, *8*, 5574-5584.

(190) J. Hardie; Y. Jiang; E. R. Tetrault; P. C. Ghazi; G. Y. Tonga; M. E. Farkas; V. M. Rotello. Simultaneous cytosolic delivery of a chemotherapeutic and siRNA using nanoparticle-stabilized nanocapsules. *Nanotechnology* **2016**, *27*, 374001.

(191) E. M. Hotze; T. Phenrat; G. V. Lowry. Nanoparticle aggregation: challenges to understanding transport and reactivity in the environment. *Journal of Environment Quality* **2010**, *39*, 1909.

(192) T. K. L. Meyvis; B. G. Stubbe; M. J. V. Steenbergen; W. E. Hennink; S. C. D. Smedt; J. Demeester. A comparison between the use of dynamic mechanical analysis and oscillatory shear rheometry for the characterisation of hydrogels. *International Journal of Pharmaceutics* **2002**, *244*, 163-168.

(193) F.G. Hoogland; A. J. J. Boon. Analytical mass spectrometry of poly(ethylene glycol) additives in artists' acrylic emulsion media, artists' paints, and microsamples from acrylic paintings using MALDI-MS and nanospray-ESI-MS. *International Journal of Mass Spectrometry* **2009**, *284*, 72-80.

(194) B. Chakrabarty; A. K. Ghoshal; M. K. Purkait. Effect of molecular weight of PEG on membrane morphology and transport properties. *Journal of Membrane Science* **2008**, *309*, 209-221.

(195) J. M. Rabanel; P. Hildgen; X. Banquy. Assessment of PEG on polymeric particles surface, a key step in drug carrier translation. *Journal of Controlled Release* **2014**, *185*, 71-87.

(196) S. N. S. Alconcel; A. S. Baas; H. D. Maynard. FDA-approved poly(ethylene glycol) – protein conjugate drugs. *Polymer Chemistry* **2011**, *2*, 1442.

(197) M. Zheng; F. Davidson; X. Huang. Ethylene glycol monolayer protected nanoparticles for eliminating nonspecific binding with biological molecules. *Journal of the American Chemical Society* **2003**, *125*, 7790-7791.

(198) F. D. Ming Zheng; X. Huang. Ethylene Glycol Monolayer Protected Nanoparticles for Eliminating Nonspecific Binding with Biological Molecules. *J. Am. Chem. Soc* **2003**, *125*, 7790-7791.

(199) S. T. Camli; F. Buyukserin; C. T. Yavuz; M. S. Yavuz. One-pot facile synthesis of PEGylated Au nanoparticles in an aqueous media. *Materials Chemistry and Physics* **2012**, *134*, 1153-1159.

(200) D. Shenoy; W. Fu; J. Li; C. Crasto; G. Jones; C. Dimarzio; S. Sridhar; M. Amiji. Surface functionalization of gold nanoparticles using hetero-bifunctional poly(ethylene glycol) spacer for intracellular tracking and delivery. *International Journal of Nanomedicine* **2006**, *1*, 51-57.

(201) H. Banu; D. K. Sethi; A. Edgar; A. Sheriff; N. Rayees; N. Renuka; S. M. Faheem; K. Premkumar; G. Vasanthakumar. Doxorubicin loaded polymeric gold nanoparticles targeted to human folate receptor upon laser photothermal therapy potentiates chemotherapy in breast cancer cell lines. *Journal of Photochemistry and Photobiology B: Biology* **2015**, *149*, 116-128.

(202) X. Xia; M. Yang; Y. Wang; Y. Zheng; Q. Li; J. Chen; A. Y. Xia. Quantifying the coverage density of poly(ethylene glycol) chains on the surface of gold nanostructures. *ACS Nano* **2012**, *6*, 512-522.

(203) S. Takae; Y. Akiyama; H. Otsuka; T. Nakamura; Y. Nagasaki; A. K. Kataoka. Ligand density effect on biorecognition by PEGylated gold nanoparticles: regulated interaction of RCA120 lectin with lactose installed to the distal end of tethered PEG strands on gold surface. *Biomacromolecules* **2005**, *6*, 818-824.

(204) H. Chen; H. Paholak; M. Ito; K. Sansanaphongpricha; W. Qian; Y. Che; D. Sun. 'Living' PEGylation on gold nanoparticles to optimize cancer cell uptake by controlling targeting ligand and charge densities. *Nanotechnology* **2013**, *24*, 355101.

(205) C. D. Walkey; J. B. Olsen; H. Guo; A. Emili; W. C. Chan. Nanoparticle size and surface chemistry determine serum protein adsorption and macrophage uptake. *Journal of the American Chemical Society* **2012**, *134*, 2139-2147.

(206) Y. Liu; M. K. Shipton; J. Ryan; E. D. Kaufman; S. Franzen; D. L. Feldheim. Synthesis, stability, and cellular Internalization of gold nanoparticles containing mixed peptide–poly(ethylene glycol) monolayers. *Analytical Chemistry* **2007**, *79*, 2221-2229.

(207) J. Manson; D. Kumar; B. J. Meenan; D. Dixon. Polyethylene glycol functionalized gold nanoparticles: the influence of capping density on stability in various media. *Gold Bulletin* **2011**, *44*, 99-105.

(208) W. Wang; Q. Q. Wei; J. Wang; B. C. Wang; S. H. Zhang; Z. Yuan. Role of thiol-containing polyethylene glycol (thiol-PEG) in the modification process of gold

nanoparticles (AuNPs): stabilizer or coagulant? *Journal of Colloid and Interface Science* **2013**, *404*, 223-229.

(209) X. Liu; N. Huang; H. Wang; H. Li; Q. Jin; J. Ji. The effect of ligand composition on the in vivo fate of multidentate poly(ethylene glycol) modified gold nanoparticles. *Biomaterials* **2013**, *34*, 8370-8381.

(210) C.A. Simpson; A.C. Agrawal; A. Balinski; K.M. Harkness; D. E. Cliffel. Short-chain PEG mixed monolayer protected gold clusters increase clearance and red blood cell counts. *ACS Nano* **2011**, *5*, 3577-3584.

(211) Z. L. Wang. Structural analysis of self-assembling nanocrystal superlattice. *Advanced Materials* **1998**, *10*, 13-30.

(212) L. Xu; W. Ma; L. Wang; C. Xu; H. Kuang; N. A. Kotov. Nanoparticle assemblies: dimensional transformation of nanomaterials and scalability. *Chemical Society Reviews* **2013**, *42*, 3114-3126.

(213) B. G. Prevo; D. M. Kuncicky; O. D. Velev. Engineered deposition of coatings from nano- and micro-particles: A brief review of convective assembly at high volume fraction. *Colloids and Surfaces A: Physicochemical and Engineering Aspects* **2007**, *311*, 2-10.

(214) H. Zhang; J. Shih; J. Zhu; N. A. Kotov. Layered nanocomposites from gold nanoparticles for neural prosthetic devices. *Nano Letters* **2012**, *12*, 3391-3398.

(215) L. Wang; Y. Zhu; L. Xu; W. Chen; H. Kuang; L. Liu; A. Agarwal; C. Xu; N. A. Kotov. Side-by-side and end-to-end gold nanorod assemblies for environmental toxin sensing. *Angewandte Chemie International Edition* **2010**, *49*, 5472-5475.

(216) R. Sardar; A. J. S. Shumaker-Parry. Asymmetrically functionalized gold nanoparticles organized in one-dimensional chains. *Nano Letters* **2008**, *8*, 731-736.

(217) J. Lee; G. Bhak; J. H. Lee; W. Park; M. Lee; D. Lee; N. L. Jeon; D. H. Jeong; K. Char; S. R. Paik. Free-standing gold-nanoparticle monolayer film fabricated by protein self-assembly of alpha-synuclein. *Angewandte Chemie Internation Edition* **2015**, *54*, 4571-4576.

(218) J. Xiao; Z. Li; X. Ye; Y. Ma; L. Qi. Self-assembly of gold nanorods into vertically aligned, rectangular microplates with a supercrystalline structure. *Nanoscale* **2014**, *6*, 996-1004.

(219) E. V. Shevchenko; D. V. Talapin; N. A. Kotov; S. O'brien; C. B. Murray. Structural diversity in binary nanoparticle superlattices. *Nature* **2006**, *439*, 55-59.

(220) O. D. Velev; K. H. Bhatt. On-chip micromanipulation and assembly of colloidal particles by electric fields. *Soft Matter* **2006**, *2*, 738-750.

(221) J. Lin; W. Zhou; A. Kumbhar; J. Wiemann; J. Fang; E. E. Carpenter; C. J. O'connor. Gold-Coated Iron (Fe@Au) Nanoparticles: Synthesis, Characterization, and Magnetic Field-Induced Self-Assembly. *Journal of Solid State Chemistry* **2001**, *159*, 26-31.

(222) S. Bhattacharya; S. Narasimha; A. Roy; S. Banerjee. Does shining light on gold colloids influence aggregation? *Scientific Reports* **2014**, *4*, 5213.

(223) D. Nykypanchuk; M. M. Maye; D. Van Der Lelie; O. Gang. DNA-guided crystallization of colloidal nanoparticles. *Nature* **2008**, *451*, 549-552.

(224) R. C. Mucic; J. J. Storhoff; C. A. Mirkin; R. L. Letsinger. DNA-directed synthesis of binary nanoparticle network materials. *Journal of the American Chemical Society* **1998**, *120*, 12674-12675.

(225) K. Larson-Smith; D. C. Pozzo. Scalable synthesis of self-assembling nanoparticle clusters based on controlled steric interactions. *Soft Matter* **2011**, *7*, 5339.

(226) T. Ming; X. Kou; H. Chen; T. Wang; H. L. Tam; K. W. Cheah; J. Y. Chen; J. Wang. Ordered gold nanostructure assemblies formed by droplet evaporation. *Angewandte Chemie International Edition* **2008**, *47*, 9685-9690.

(227) Z. Nie; A. Petukhova; E. Kumacheva. Properties and emerging applications of self-assembled structures made from inorganic nanoparticles. *Nature nanotechnology* **2010**, *5*, 15-25.

(228) A. Apte; P. Bhaskar; R. Das; S. Chaturvedi; P. Poddar; S. Kulkarni. Self-assembled vertically aligned gold nanorod superlattices for ultra-high sensitive detection of molecules. *Nano Research* **2014**.

(229) B. Nikoobakht; Z. L. Wang; M. A. El-Sayed. Self-Assembly of Gold Nanorods. *The Journal of Physical Chemistry B* **2000**, *104*, 8635-8640.

(230) T. K. Sau; C. J. Murphy. Self-assembly patterns formed upon solvent evaporation of aqueous cetyltrimethylammonium bromide-coated gold nanoparticles of various shapes. *Langmuir* **2005**, *21*, 2923-2929.

(231) S. Link; M. A. El-Sayed. Size and temperature dependence of the plasmon absorption of colloidal gold nanoparticles. *The Journal of Physical Chemistry B* **1999**, *103*, 4212-4217.

(232) M. Bachelet; R. Chen. Self-assembly of PEGylated gold nanoparticles with satellite structures as seeds. *Chemical Communications* **2016**, *52*, 9542-9545.

(233) J. Polte. Fundamental growth principles of colloidal metal nanoparticles – a new perspective. *CrystEngComm* **2015**, *17*, 6809-6830.

(234) S. Bhattacharjee. DLS and zeta potential - What they are and what they are not? *Journal of Controlled Release* **2016**, *235*, 337-351.

(235) G. Zhang; Z. Yang; W. Lu; R. Zhang; Q. Huang; M. Tian; L. Li; D. Liang; C. Li. Influence of anchoring ligands and particle size on the colloidal stability and in vivo biodistribution of polyethylene glycol-coated gold nanoparticles in tumor-xenografted mice. *Biomaterials* **2009**, *30*, 1928-1936.

(236) D. Dhamecha; S. Jalalpure; K. Jadhav; S. Jagwani; R. Chavan. Doxorubicin loaded gold nanoparticles: Implication of passive targeting on anticancer efficacy. *Pharmacological Research* **2016**, *113*, 547-556.

(237) N. S. Elbialy; M. M. Fathy; W. M. Khalil. Preparation and characterization of magnetic gold nanoparticles to be used as doxorubicin nanocarriers. *Physica Medica* **2014**, *30*, 843-848.

(238) S.D. Perrault; C. Walkey; T. Jennings; H.C. Fischer; A. W. C. W. Chan. Mediating tumor targeting efficiency of nanoparticles through design. *Nano Letters* **2009**, *9*, 1909-1915.

(239) P. G. D. Gennes. Conformations of polymers attached to an interface. *Macromolecules* **1980**, *13*, 1069-1075.

(240) K. Rahme; L. Chen; R. G. Hobbs; M. A. Morris; C. O'driscoll; J. D. Holmes. PEGylated gold nanoparticles: polymer quantification as a function of PEG lengths and nanoparticle dimensions. *RSC Advances* **2013**, *3*, 6085-6094.

(241) F. Oesterhelt; M. Rief; H. E. Gaub. Single molecule force spectroscopy by AFM indicates helical structure of poly(ethylene glycol) in water. *New Journal of Physics* **1999**, *1*, 6.

(242) A. C. Sabuncu; J. Grubbs; S. Qian; T. M. Abdel-Fattah; M. W. Stacey; A. Beskok. Probing nanoparticle interactions in cell culture media. *Colloids and Surfaces B: Biointerfaces* **2012**, *95*, 96-102.

(243) S. I. Stoeva; B. L. V. Prasad; S. Uma; P. K. Stoimenov; V. Zaikovski; C. M. Sorensen; K. J. Klabunde. Face-centered cubic and hexagonal closed-packed nanocrystal superlattices of gold nanoparticles prepared by different methods. *The Journal of Physical Chemistry B* **2003**, *107*, 7441-7448.

(244) A. Anne; C. Demaille; J. Moiroux. Terminal attachment of polyethylene glycol (PEG) chains to a gold electrode surface. cyclic voltammetry applied to the quantitative characterization of the flexibility of the attached PEG Chains and of their penetration by mobile PEG chains. *Macromolecules* **2002**, *35*, 5578-5586.

(245) F. Oesterhelt; M. Rief; H. E. Gaub. Single molecule force spectroscopy by AFM indicates helical structure of poly(ethylene glycol) in water. *New Journal of Physics* **1999**, *1*, 1-11.

(246) F.-C. Wang; H.-A. Wu. Pinning and depinning mechanism of the contact line during evaporation of nano-droplets sessile on textured surfaces. *Soft Matter* **2013**, *9*, 5703.

(247) J. Wu; J. Xia; W. Lei; B.-P. Wang. Generation of the smallest coffee-ring structures by solute crystallization reaction on a hydrophobic surface. *RSC Adv.* **2013**, *3*, 5328.

(248) P. J. Yunker; T. Still; M. A. Lohr; A. G. Yodh. Suppression of the coffee-ring effect by shape-dependent capillary interactions. *Nature* **2011**, *476*, 308-311.

(249) P. C. Ohara; D. V. Leff; J. R. Heath; W. M. Gelbart. Crystallization of opals from polydisperse nanoparticles. *Physical Review Letters* **1995**, *75*, 3466-3469.

(250) B. L. V. Prasad; C. M. Sorensenb; K. J. Klabundec. Gold nanoparticle superlattices. *Chemical Society Reviews* **2008**, *37*, 1881-1883.

(251) S. Guo; Y. Huang; Q. Jiang; Y. Sun; L. Deng; Z. Liang; Q. Du; J. Xing; Y. Zhao; P. C. Wang; A. Dong; X. J. Liang. Enhanced gene delivery and siRNA silencing by gold nanoparticles coated with charge-reversal polyelectrolyte. *ACS Nano* **2010**, *4*, 5505-5511.

(252) J. M. D. L. Fuente; C. C. Berry. Tat peptide as an efficient molecule to translocate gold nanoparticles into the cell nucleus. *Bioconjugate Chemistry* **2005**, *16*, 1176-1180.

(253) H. Hatakeyama; E. Ito; H. Akita; M. Oishi; Y. Nagasaki; S. Futaki; H. Harashima. A pH-sensitive fusogenic peptide facilitates endosomal escape and greatly enhances the gene silencing of siRNA-containing nanoparticles in vitro and in vivo. *Journal of Controlled Release* **2009**, *139*, 127-132.

(254) Y. L. Lin; G. Jiang; L. K. Birrell; M. E. El-Sayed. Degradable, pH-sensitive, membrane-destabilizing, comb-like polymers for intracellular delivery of nucleic acids. *Biomaterials* **2010**, *31*, 7150-7166.

(255) A. J. Convertine; D. S. Benoit; C. L. Duvall; A. S. Hoffman; P. S. Stayton. Development of a novel endosomolytic diblock copolymer for siRNA delivery. *Journal of Controlled Release* **2009**, *133*, 221-229.

(256) B. Yang; Y. Lv; J. Y. Zhu; Y. T. Han; H. Z. Jia; W. H. Chen; J. Feng; X. Z. Zhang; R. X. Zhuo. A pH-responsive drug nanovehicle constructed by reversible attachment of cholesterol to PEGylated poly(l-lysine) via catechol-boronic acid ester formation. *Acta Biomaterialia* **2014**, *10*, 3686-3695.

(257) I. Dolamic; B. Varnholt; T. Burgi. Far-infrared spectra of well-defined thiolate-protected gold clusters. *Physical Chemistry Chemical Physics* **2013**, *15*, 19561-19565.

(258) H. Hakkinen. The gold-sulfur interface at the nanoscale. *Nature Chemistry* **2012**, *4*, 443-455.

(259) C. Pfeiffer; C. Rehbock; D. Huhn; C. Carrillo-Carrion; D. J. De Aberasturi; V. Merk; S. Barcikowski; W. J. Parak. Interaction of colloidal nanoparticles with their local environment: the (ionic) nanoenvironment around nanoparticles is different from bulk and determines the physico-chemical properties of the nanoparticles. *Journal of the Royal Society Interface* **2014**, *11*, 20130931.

(260) F. Y. Alzoubi; J. Y. Alzouby; M. K. Alqadi; H. A. Alshboul; A. K. M. Aljarrah. Synthesis and characterization of colloidal gold nanoparticles controlled by the pH and ionic strength. *Chinese Journal of Physics* **2015**, *53*.

(261) H. Zhou; L. Zheng; H. Jia. Facile control of the self-assembly of gold nanoparticles by changing the capping agent structures. *Colloids and Surfaces A: Physicochemical and Engineering Aspects* **2014**, *450*, 9-14.

(262) R. Chen; S. Khormaee; M. E. Eccleston; N. K. Slater. The role of hydrophobic amino acid grafts in the enhancement of membrane-disruptive activity of pH-responsive pseudo-peptides. *Biomaterials* **2009**, *30*, 1954-1961.

(263) M. D'souza-Mathew; O. J. Cayre; T. N. Hunter; S. R. Biggs. Facile synthesis of gold core-polymer shell responsive particles. *Journal of Colloid and Interface Science* **2013**, *407*, 187-195.

(264) R. A. Cairns; I. S. Harris; T. W. Mak. Regulation of cancer cell metabolism. *Nature Reviews Cancer* **2011**, *11*, 85-95.

(265) V. P. Zharov; E. N. Galitovskaya; C. Johnson; T. Kelly. Synergistic enhancement of selective nanophotothermolysis with gold nanoclusters: potential for cancer therapy. *Lasers in Surgery and Medicine* **2005**, *37*, 219-226.

(266) K. L. Wustholz; A.-I. Henry; J. M. Mcmahon; R. G. Freeman; N. Valley; M. E. Piotti; M. J. Natan; G. C. Schatz; R. P. Van Duyne. Structure-activity relationships in gold nanoparticle dimers and trimers for surface-enhanced raman spectroscopy. *Journal of the Americal Chemical Society* **2010**, *132*, 10903-10910.

(267) M. A. Dobrovolskaia; J. D. Clogston; B. W. Neun; J. B. Hall; A. K. Patri; S. E. Mcneil. Method for analysis of nanoparticle hemolytic properties in vitro. *Nano Letters* **2008**, *8*, 2180-2187.

(268) S. Chen; R. Chen. A virus-mimicking, endosomolytic liposomal system for efficient, pH-triggered intracellular drug delivery. *ACS Applied Materials & Interfaces* **2016**, *8*, 22457-22467.

(269) F. Perreault; S. P. Melegari; C. F. Fuzinatto; N. Bogdan; M. Morin; R. Popovic; W. G. Matias. Toxicity of pamam-coated gold nanoparticles in different unicellular models. *Environmental Toxicology* **2012**.

(270) B. D. Chithrani; A. A. Ghazani; W. C. W. Chan. Determining the size and shape dependance of gold nanoparticle uptake into mammalian cells. *Nano Letters* **2006**, *6*, 662-668.

(271) Y. J. Gu; J. Cheng; C. C. Lin; Y. W. Lam; S. H. Cheng; W. T. Wong. Nuclear penetration of surface functionalized gold nanoparticles. *Toxicology and Applied Pharmacology* **2009**, *237*, 196-204.

(272) P. Nativo; I. A. Prior; A. M. Brust. Uptake and intracellular fate of surface-modified gold nanoparticles. *ACS Nano* **2008**, *2*, 1639-1644.

(273) S. N. Rampersad. Multiple applications of Alamar Blue as an indicator of metabolic function and cellular health in cell viability bioassays. *Sensors* **2012**, *12*, 12347-12360.

(274) B. D. Chithrani; A. W. C. W. Chan. Elucidating the mechanism of cellular uptake and removal of protein-coated gold nanoparticles of different sizes and shapes. *Nano Letters* **2007**, *7*, 1542-1550.

(275) S. Klein; S. Petersen; U. Taylor; D. Rath; S. Barcikowski. Quantitative visualization of colloidal and intracellular gold nanoparticles by confocal microscopy. *Journal of Biomedical Optics* **2010**, *15*, 036015.

(276) M. B. Ganem; M. C. De Marzi; M. J. Fernandez-Lynch; C. Jancic; M. Vermeulen; J. Geffner; R. A. Mariuzza; M. M. Fernandez; E. L. Malchiodi. Uptake and intracellular trafficking of superantigens in dendritic cells. *PLoS One* **2013**, *8*, e66244.

(277) I. Maejima; A. Takahashi; H. Omori; T. Kimura; Y. Takabatake; T. Saitoh; A. Yamamoto; M. Hamasaki; T. Noda; Y. Isaka; T. Yoshimori. Autophagy sequesters damaged lysosomes to control lysosomal biogenesis and kidney injury. *The EMBO Journal* **2013**, *32*, 2336-2347.

(278) T. F. Martensa; K. Remauta; J. Demeestera; S. C. D. Smedta; K. Braeckmansa. Intracellular delivery of nanomaterials: how to catch endosomal escape in the act. *Nano Today* **2014**, *9*, 344-364.

(279) A. J. Trouiller; S. Hebie; F. El Bahhaj; T. W. Napporn; P. Bertrand. Chemistry for oncotheranostic gold nanoparticles. *European Journal of Medicinal Chemistry* **2015**, *99*, 92-112.

(280) G. Pillai. Nanomedicines for cancer therapy: an update of FDA approved and those under various stages of development. *SOJ Pharmacy & Pharmaceutical Sciences* **2014**, *1*, 13.

(281) N. S. Elbialy; M. M. Fathy; W. M. Khalil. Doxorubicin loaded magnetic gold nanoparticles for in vivo targeted drug delivery. *International Journal of Pharmaceutics* **2015**, *490*, 190-199.

(282) D. P. O'neal; L. R. Hirsch; N. J. Halas; J. D. Payne; J. L. West. Photo-thermal tumor ablation in mice using near infrared-absorbing nanoparticles. *Cancer Lett* **2004**, *209*, 171-176.

(283) L. Cheng; H. Gong; W. Zhu; J. Liu; X. Wang; G. Liu; Z. Liu. PEGylated Prussian blue nanocubes as a theranostic agent for simultaneous cancer imaging and photothermal therapy. *Biomaterials* **2014**, *35*, 9844-9852.

(284) A. J. Coughlin; J. S. Ananta; N. Deng; I. V. Larina; P. Decuzzi; J. L. West. Gadolinium-conjugated gold nanoshells for multimodal diagnostic imaging and photothermal cancer therapy. *Small* **2014**, *10*, 556-565.

(285) J. Shao; R. J. Griffin; E. I. Galanzha; J. W. Kim; N. Koonce; J. Webber; T. Mustafa; A. S. Biris; D. A. Nedosekin; V. P. Zharov. Photothermal nanodrugs: potential of TNF-gold nanospheres for cancer theranostics. *Scientific Reports* **2013**, *3*, 1293.

(286) J. A. Schwartz; A. M. Shetty; R. E. Price; R. J. Stafford; J. C. Wang; R. K. Uthamanthil; K. Pham; R. J. Mcnichols; C. L. Coleman; J. D. Payne. Feasibility study of particle-assisted laser ablation of brain tumors in orthotopic canine model. *Cancer Research* **2009**, *69*, 1659-1667.

(287) J. You; R. Zhang; C. Xiong; M. Zhong; M. Melancon; S. Gupta; A. M. Nick; A. K. Sood; C. Li. Effective photothermal chemotherapy using doxorubicin-loaded gold nanospheres that target EphB4 receptors in tumors. *Cancer Research* **2012**, *72*, 4777-4786.

(288) S. Kessentini; A. D. Barchiesi. Quantitative comparison of optimised nanorods, nanoshells and hollow nanospheres for photothermal therapy. *Biomedical Optics Express* **2012**, *3*, 590-604.

(289) R. Weissleder. A clearer vision for in vivo imaging. *Nature Biotechnology* **2001**, *19*, 316-317.

(290) M. E. Eccleston; S. L. Williams; Z. Yue; R. Chen; C. K. Lee; E. Anikina; C. Pawlyn; M. A. Barrand; A. N. K. H. Slater. Design and in vitro testing of effective poly L lysine iso phtalamide based drug targeted systems for solid tumours. *Food and Bioproducts Processing*, *83*, 141-146.

(291) M. Honda; Y. Saito; N. I. Smith; K. Fujita; A. S. Kawata. Nanoscale heating of laser irradiated single gold nanoparticles in liquid. *Optics Express* **2011**, *19*, 12375-12383.

(292) X. Wang; X. Cai; J. Hu; N. Shao; F. Wang; Q. Zhang; J. Xiao; Y. Cheng. Glutathione-triggered "off-on" release of anticancer drugs from dendrimer-encapsulated gold nanoparticles. *Journal of the American Chemical Society* **2013**, *135*, 9805-9810.

(293) Z. Krpetic; P. Nativo; V. See; I. A. Prior; M. Brust; M. Volk. Inflicting controlled nonthermal damage to subcellular structures by laser-activated gold nanoparticles. *Nano Letters* **2010**, *10*, 4549-4554.

(294) M. W. Tibbitt; K. S. Anseth. Hydrogels as extracellular matrix mimics for 3D cell culture. *Biotechnology and Bioengineering* **2009**, *103*, 655-663.

(295) L. A. Sharpe; A. M. Daily; S. D. Horava; N. A. Peppas. Therapeutic applications of hydrogels in oral drug delivery. *Expert Opinion on Drug Delivery* **2014**, *11*, 901-915.

(296) B. Jeong; S. W. Kim; Y. H. Bae. Thermosensitive sol – gel reversible hydrogels. *Advanced Drug Delivery Reviews* **2012**, *64*, 154-162.

(297) Y.-L. Zhao; J. F. Stoddart. Azobenzene-based light-responsive hydrogel system. *Langmuir* **2009**, *25*, 8442-8446.

(298) X. Gao; C. He; C. Xiao; X. Zhuang; X. Chen. Biodegradable pH-responsive polyacrylic acid derivative hydrogels with tunable swelling behavior for oral delivery of insulin. *Polymer* **2013**, *54*, 1786-1793.

(299) Cristi L. Bell; N. A. Peppas. Modulation of drug permeation through interpolymer complexed hydrogels for drug delivery applications. *journal of Controlled Release* **1996**, *39*, 201-207.

(300) H. Basan; M. Gumusderelioglu; M. Tevfik Orbey. Release characteristics of salmon calcitonin from dextran hydrogels for colon-specific delivery. *European Journal of Pharmaceutics and Biopharmaceutics* **2007**, *65*, 39-46.

(301) P.-Y. Yeh; P. Kopeckova; J. Kopecek. Degradability of hydrogels containing azoaromatic crosslinks. *Macromolecular Chemistry and Physics* **1995**, *196*, 2183-2202.

(302) F. Zhao; D. Yao; R. Guo; L. Deng; A. Dong; J. Zhang. Composites of polymer hydrogels and nanoparticulate systems for biomedical and pharmaceutical applications. *Nanomaterials* **2015**, *5*, 2054-2130.

(303) A. Riedinger; M. Pernia Leal; S. R. Deka; C. George; I. R. Franchini; A. Falqui; R. Cingolani; T. Pellegrino. "Nanohybrids" based on pH-responsive hydrogels and inorganic nanoparticles for drug delivery and sensor applications. *Nano Letters* **2011**, *11*, 3136-3141.

(304) N. Tiwari; Manohar v. Badiger. Enhanced drug release by selective cleavage of cross-links in a double-cross-linked hydrogel. *RSC Advances* **2016**, *6*, 102453-102461.

(305) G. Marcelo; M. López-González; F. Mendicuti; M. P. Tarazona; M. Valiente. Poly(N-isopropylacrylamide)/gold hybrid hydrogels prepared by catechol redox chemistry. characterization and smart tunable catalytic activity. *Macromolecules* **2014**, *47*, 6028-6036.

(306) L. Castaneda; J. Valle; N. Yang; S. Pluskat; A. K. Slowinska. Collagen cross-linking with Au nanoparticles. *Biomacromolecules* **2008**, *9*, 3383 – 3388.

(307) S. R. Sershen; S. L. Westcott; N. J. Halas; J. L. West. Independent optically addressable nanoparticle-polymer optomechanical composites. *Applied Physics Letters* **2002**, *80*, 4609-4611.

(308) V. Pardo-Yissar; R. Gabai; A. N. Shipway; T. Bourenko; I. Willner. Gold nanoparticle hydrogel composites with solvent-switchable electronic properties. *Advanced Materials* **2001**, *13*, 1320-1323.

(309) K. A. Watkins; R. Chen. pH-responsive, lysine-based hydrogels for the oral delivery of a wide size range of molecules. *International Journal of Pharmaceutics* **2015**, *478*, 496-503.

(310) S. Wang; X. Liu; I. J. Villar-Garcia; R. Chen. Amino acid based hydrogels with dual responsiveness for oral drug delivery. *Macromolecular Bioscience* **2016**, *16*, 1258-1264.

(311) Q. Li; D. G. Barrett; P. B. Messersmith; N. Holten-Andersen. Controlling hydrogel mechanics via bio-inspired polymer-nanoparticle bond dynamics. *ACS Nano* **2016**, *10*, 1317-1324.

(312) M. K. Jaiswal; J. R. Xavier; J. K. Carrow; P. Desai; D. Alge; A. K. Gaharwar. Mechanically stiff nanocomposite hydrogels at ultralow nanoparticle content. *ACS Nano* **2016**, *10*, 246-256.

(313) P.J. Honey; J. Rijo; A. Anju; K. R. Anoop. Smart polymers for the controlled delivery of drugs - a concise overview. *Acta Pharmaceutica Sinica B* **2014**, *4*, 120-127.

(314) V. V. Khutoryanskiy. Supramolecular materials: longer and safer gastric residence. *Nature Materials* **2015**, *14*, 963-964.

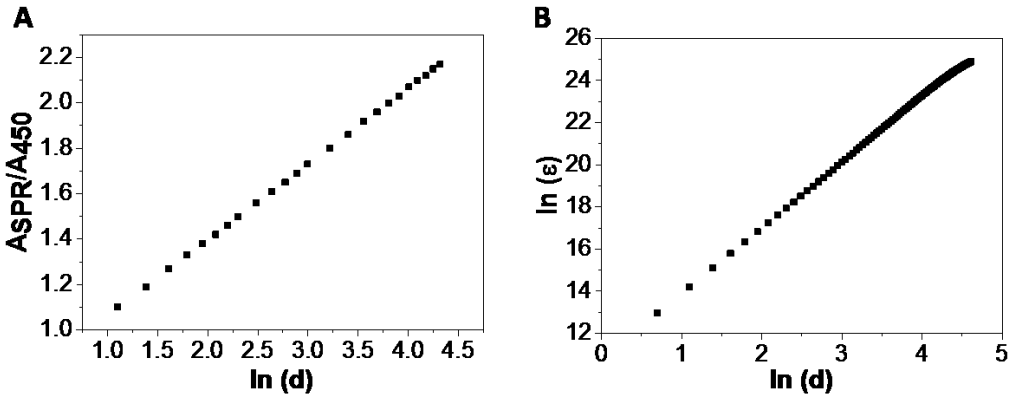
(315) S. Wagener; K. R. Shankar; R. R. Turnock; G. L. Lamont; C. T. Baillie. Colonic transit time - what is normal? *Journal of Pediatric Surgery* **2004**, *39*, 166-169.

(316) M. T. Cook; G. Tzortzis; D. Charalampopoulos; V. V. Khutoryanskiy. Microencapsulation of probiotics for gastrointestinal delivery. *Journal of Controlled Release* **2012**, *162*, 56-67.

(317) Y. Wang; Z. Zhang; S. Xu; F. Wang; Y. Shen; S. Huang; S. Guo. pH, redox and photothermal Tri-responsive DNA/polyethylenimine conjugated gold nanorod as nanocarrier for specific intracellular Co-release of doxorubicin and chemosensitizer pyronaridine to combat multidrug resistant cancer. *Nanomedicine* **2017**.

(318) D. Dhamecha; S. Jalalpure; K. Jadhav. Doxorubicin functionalized gold nanoparticles: Characterization and activity against human cancer cell lines. *Process Biochemistry* **2015**, *50*, 2298-2306.

Appendix A



C

	A_{SPR}/A_{450} vs. ln d	Ln(Ɛ) vs. ln(d)
Slope	0.33 (m)	3.09
Intercept	0.73 (B_0)	10.87
R^2	1.00	1.00

Figure A-1 (A) A_{SPR}/A_{450} vs. ln (d) using the fit parameters from the experimental results reported by Haiss *et al.*[42]. (B) ln(Ɛ) vs ln(d) obtained from the fit to the theoretical extinction efficiencies for AuNPs in the size range 2 to 100 nm reported by Haiss *et al.*[42]. (C) Table giving the fit values for the slope and intercept of Figures A and B.

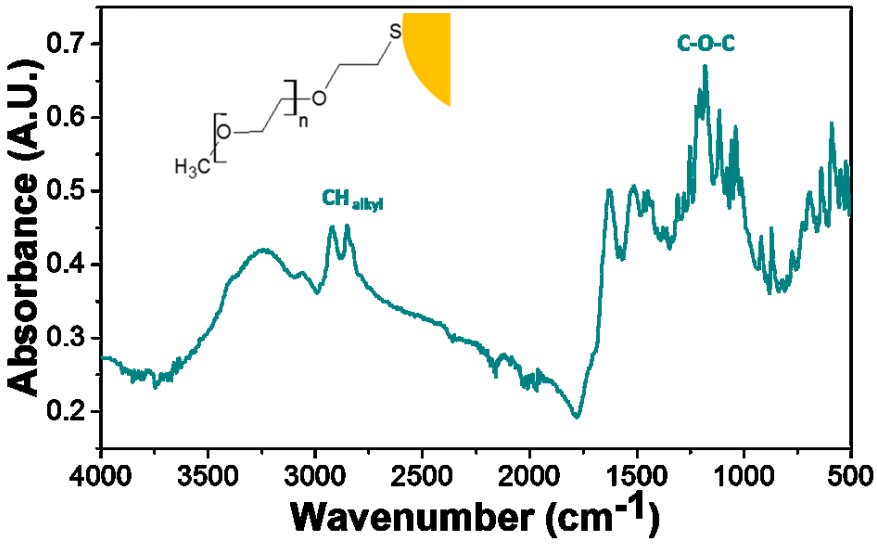


Figure A-2 FTIR spectra for AuNPs@PEG0.8k.

The FTIR peaks are assigned as follows: alkyl C-H stretches (2915 and 2848 cm^{-1}) and C-O-C ether stretch (1179 cm^{-1}) and indicate the presence of bound PEG.[207]

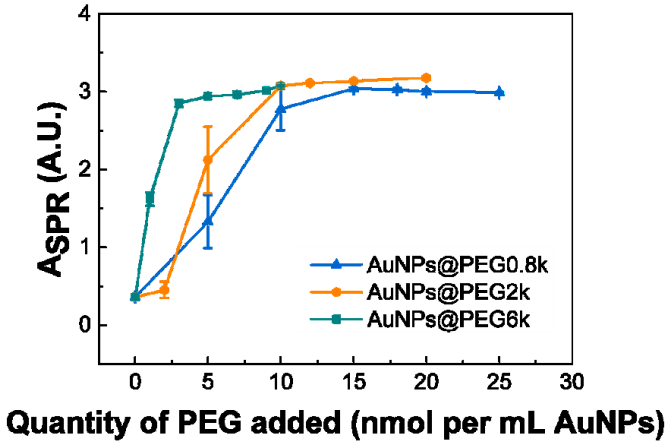
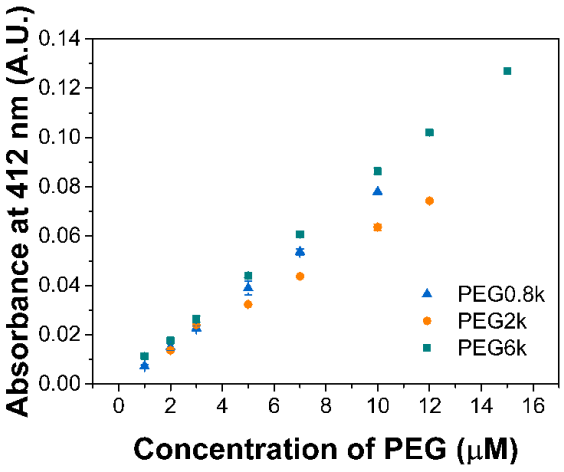


Figure A-3 A_{SPR} of PEGylated AuNPs redispersed in H_2O versus quantity of PEG added.

A



B

	PEG0.8k	PEG2k	PEG6k
Concentration range (μM)	1-10	2-12	1-15
Absorbance range (A.U.)	0.0073-0.078	0.0137-0.0743	0.0113-0.127
Slope	0.0078	0.0059	0.0083
Intercept	-0.0006	0.0034	0.0020
R^2	0.9998	0.9951	0.9998

Figure A-4 Calibration curves for the Ellman assay obtained via UV-vis. B. Calibration characteristics.

Table A-1 Results of grafting density for AuNPs@PEG0.8k obtained via the Ellman's assay.

PEG Mw	n_i[a]	n_{g2}[b] [chain/NP]	σ_{Ellman}[c]	FP[d]
0.8k	12	781.25 ±0.00	1.23±0.02	0.82 ±0.00
	15	976.56 ±0.00	1.53 ±0.02	0.65 ±0.00
	17	1106.77 ±0.00	1.74 ±0.02	0.58 ±0.00
	20	1291.80 ±13.56	2.03 ±0.02	0.49 ±0.01
	25	1369.13 ±13.22	2.15 ±0.02	0.47 ±0.00
	30	1241.26 ±11.92	1.95 ±0.02	0.51 ±0.00

[a]n_i is the initial amount of PEG chains added in the solution which is equal to the molar amount of PEG added

[b]n_{g2} is the number of chains grafted per AuNPs

[c]σ_{Ellman} is the grafting density expressed as number of chains grafted per nm^2

[d]*FP* is the footprint of the PEG chain defined as the inverse of the grafting density

Table A-2 Results of grafting density for AuNPs@PEG2k obtained via the Ellman's assay.

PEG Mw [g mol^{-1}]	n_i [nmol]	n_{g2} [chain/NP]	σ_{Ellman} [chain nm^{-2}]	FP [nm^2]
2k	8	512.80 ±4.37	0.80 ±0.01	1.24 ±0.01
	10	630.65 ±13.11	0.99 ±0.02	1.01 ±0.02
	12	780.01 ±0.87	1.22 ±0.00	0.82 0.00
	15	943.81 ±8.74	1.48 ±0.01	0.68 ±0.01
	20	1031.43 ± 52.43	1.62 ±0.08	0.62 ±0.03
	30	888.43 ±69.91	1.39 ±0.11	0.72 ±0.05

Table A-3 Results of grafting density for AuNPs@PEG6k obtained via the Ellman's assay.

PEG Mw [g mol^{-1}]	n_i [nmol]	n_{g2} [chain/NP]	σ_{Ellman} [chain nm^{-2}]	FP [nm^2]
6k	5	307.78 ±9.13	0.48 ±0.01	2.07 ±0.06
	7	386.36 ±4.56	0.61 ±0.01	1.65 ±0.02
	10	452.62 ±0.00	0.71 ±0.00	1.41 ±0.00
	15	594.24 ±20.53	0.93 ±0.04	1.07 ±0.04
	20	627.77 ±59.32	0.99 ±0.09	1.02 ±0.09
	30	704.52 ±20.53	1.11 ±0.03	0.91 ±0.03

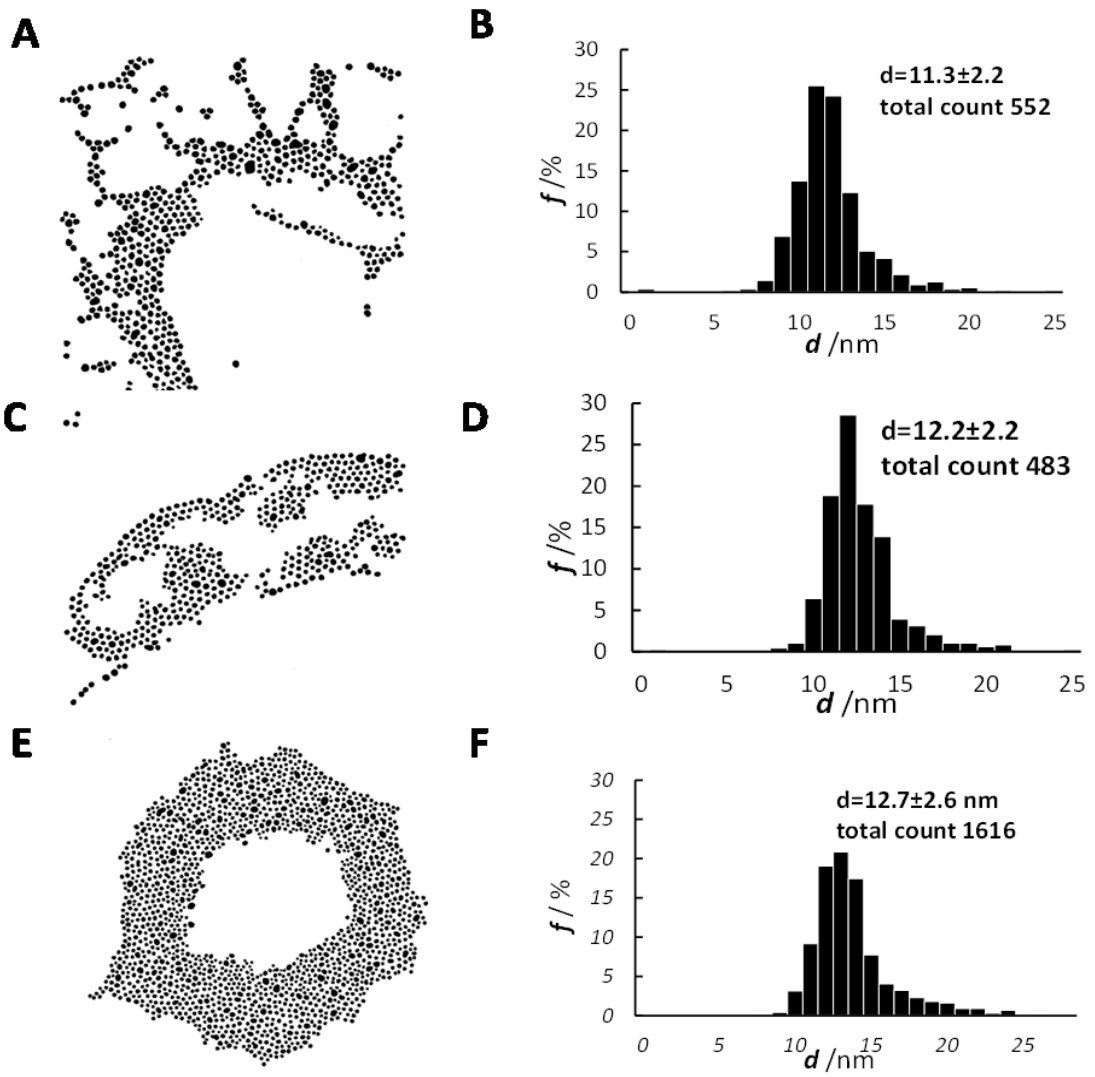


Figure A-5 ImageJ mask images (A, C, E) and related PSD (B, D, F) of the TEM images of PEGylated AuNPs. Reproduced from Bachelet and Chen[232], copyright 2016, from The Royal Society of Chemistry.

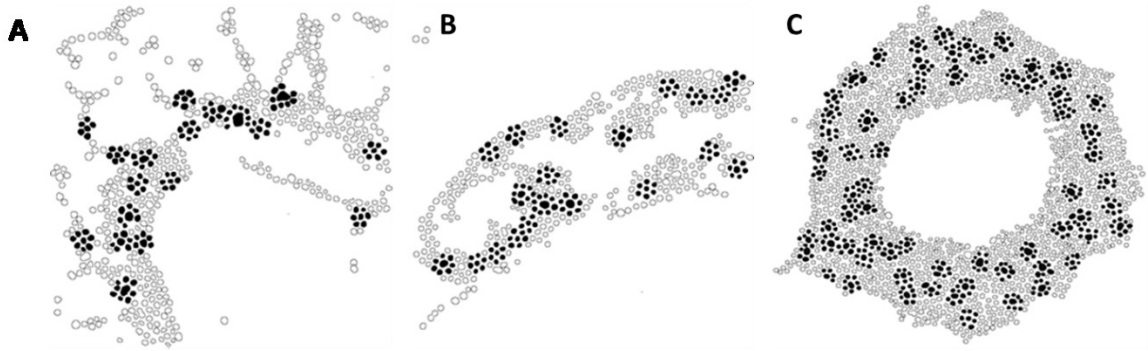


Figure A-6 Individual satellites structures for (A) AuNPs@PEG0.8k, (B) AuNPs@PEG2k and (C) AuNPs@PEG6k. Reproduced from Bachelet and Chen[232], copyright 2016, from The Royal Society of Chemistry.

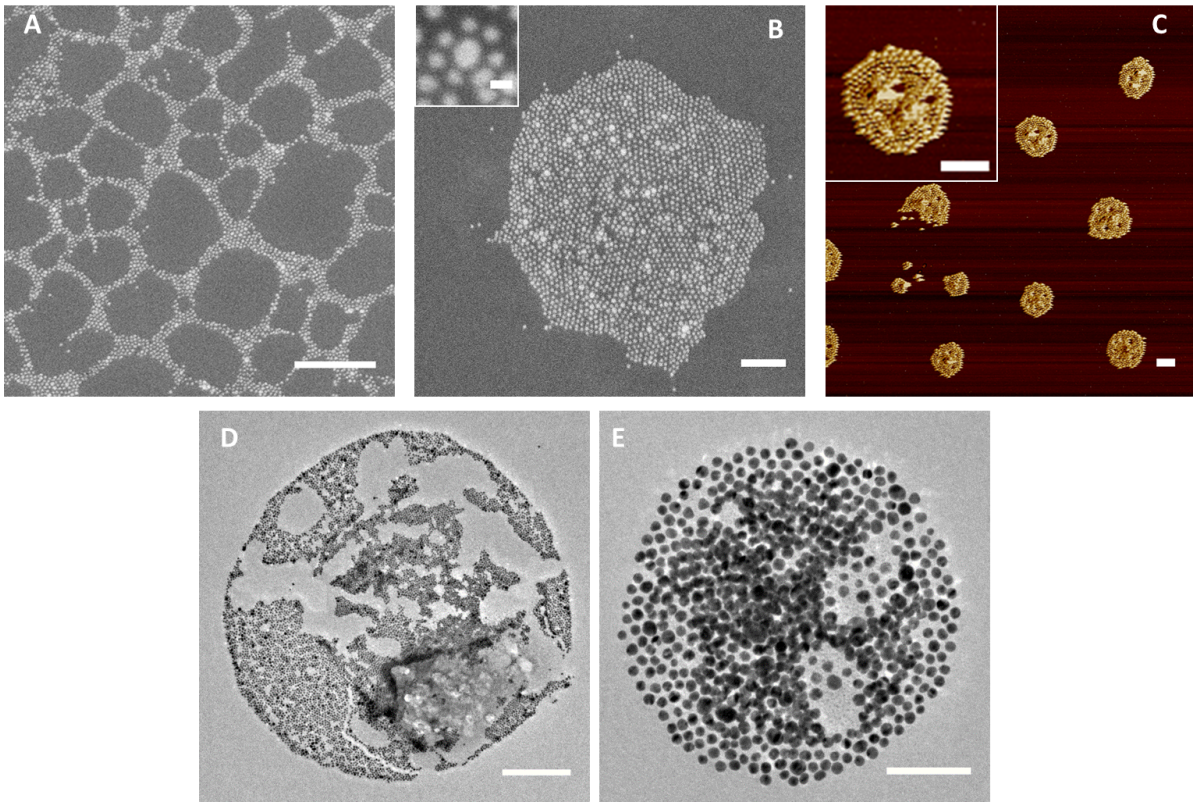


Figure A-7 Images of the self-assembled AuNPs@PEG6k. (A) SEM image on silicon wafer (scale bar 500 nm). (B) SEM image on TEM grid (scale bar 200 nm) with zoomed satellite structure as inset (scale bar 20 nm). (C) AFM image under tapping mode with zoomed assembly as inset on mica sheet (scale bar 500 nm). (D) SEM image of large scale assembly (scale bar 500 nm). (E) Short-scale assembly (scale bar 100 nm). *The AFM images were acquired by Dr. Edward Parsons.*

Appendix B

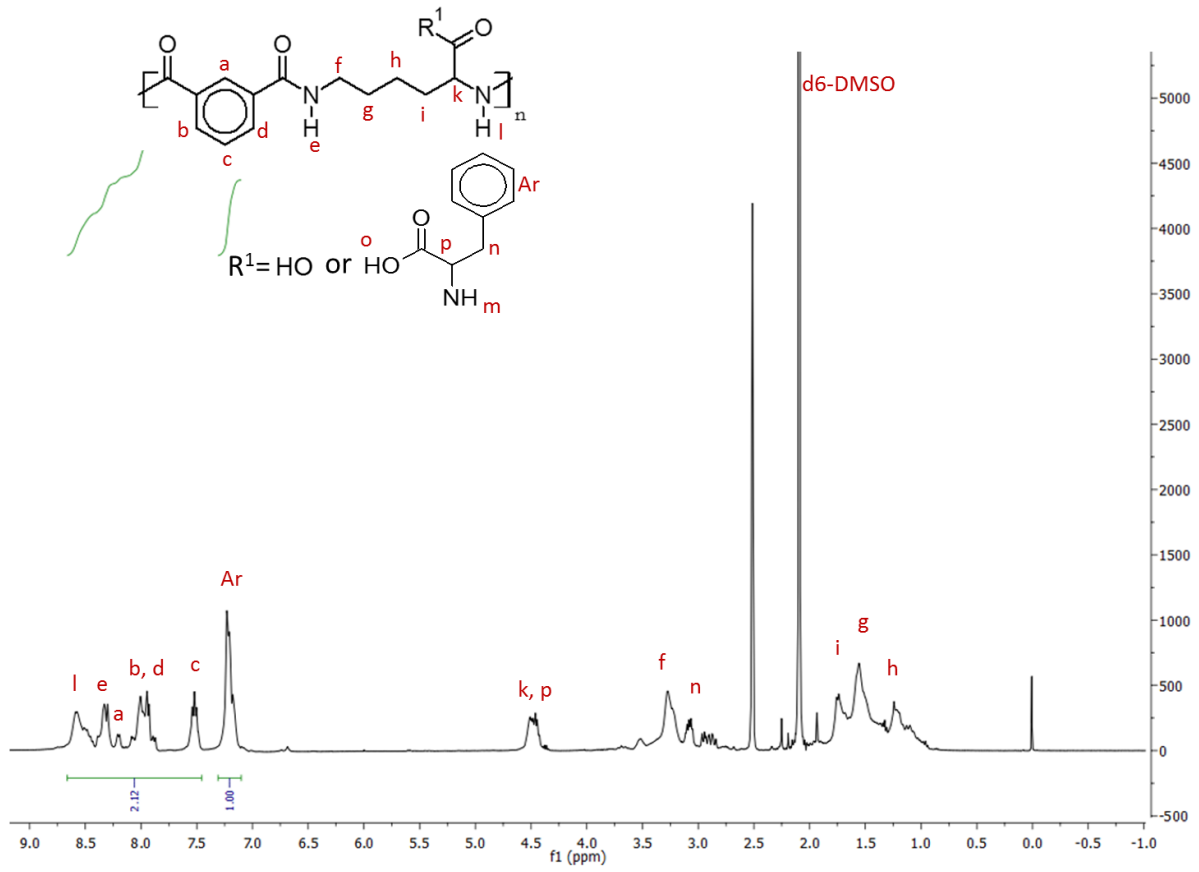


Figure B-1 ^{1}H-NMR spectra of PP75 in d^{6}-DMSO at 400 MHz.

Figure B-1 confirms the successful grafting of PLP with L-phenylalanine and the synthesis of PP75. The chemical shift of protons are as follows: δ (ppm) 8.59 (H_l-NH), 8.33 (H_e-NH), 8.21 (complex multiplet aromatic H_a-CH), 8.01-7.95 (complex multiplet aromatic H_b-CH, H_d-CH), 7.52 (complex multiplet aromatic H_c-CH), 7.10-7.31 (complex multiplet aromatic HAr-CH), 4.51-4.44 (H_k-CH, H_p-CH), 3.28 (H_f-CH_2), 3.06 (H_n-CH_2), 1.76 (H_i-CH_2), 1.55 (H_g-CH_2),1.24 (H_h-CH_2).

The degree of grafting was determined as follows:

$$A = \frac{\int 7.10 - 7.31}{\int 7.45 - 8.67} = \frac{5X}{6(100 - X) + 7X}$$

Where:

- X is the degree of grafting
- 5 is the number of protons of H_{Ar}
- 6 is the number of protons of $H_{a,b,c,d,e,l}$
- 7 is the number of protons of $H_{a,b,c,d,e,l,\ m}$

The calculations give:

$$A = \frac{1}{2.12}$$

$$X = \frac{600A}{5 - A} = 62.5\%$$

The theoretical degree of grafting is 75% but the actual degree of grafting is 62.5%, sign that the reaction is not 100% efficient.

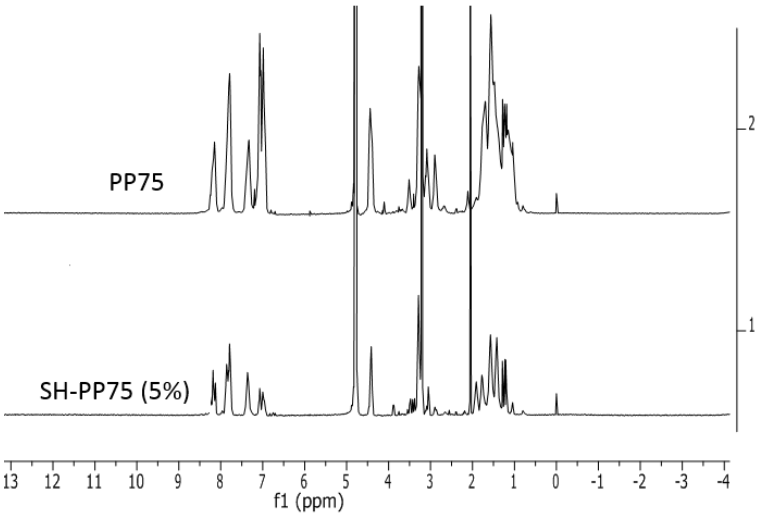


Figure B-2 ^{1}H-NMR spectra of PP75 (top) and SH-PP75(5%) (bottom) in d^{6}-DMSO at 400 MHz.

Figure B-2 shows a clear difference between the NMR spectra of PP75 and SH-PP75(5%) between δ1-2ppm which can be attributed to the additional protons from CH_2 and SH in cysteamine. The characterisation of the degree of grafting via NMR analysis is complex due to the structure of PP75 itself.

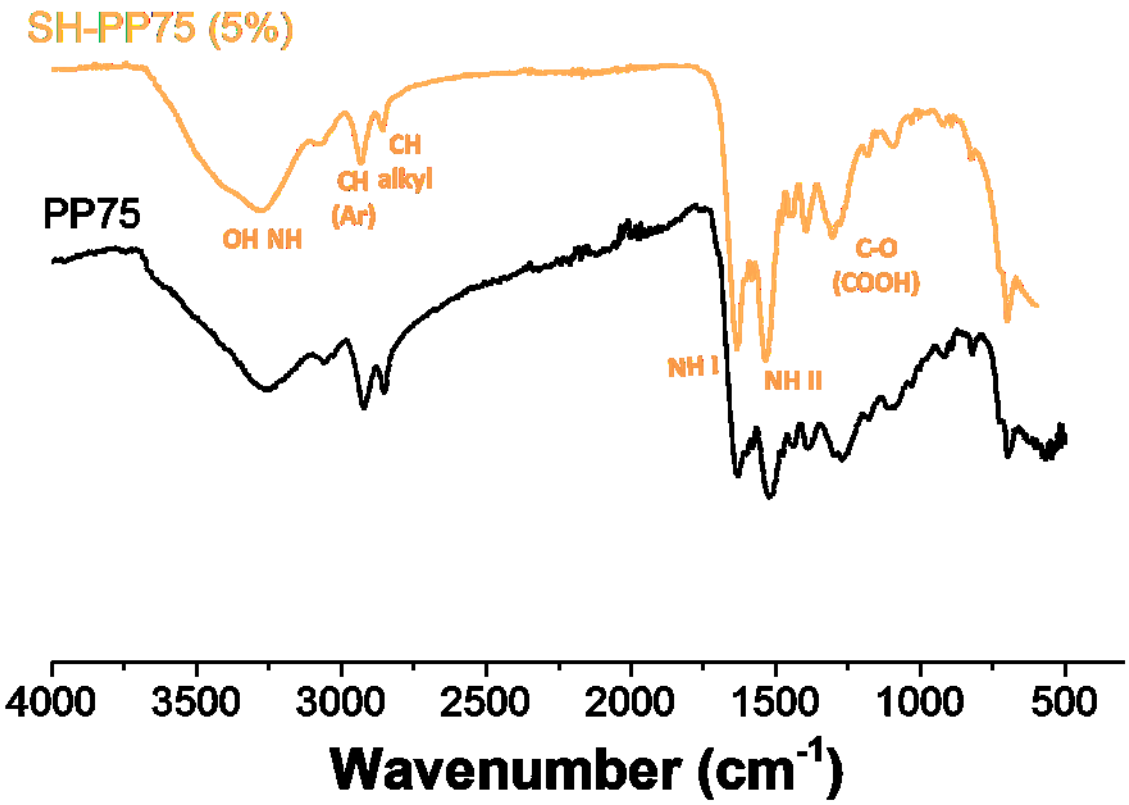


Figure B-3 FTIR spectra of PP75 polymer and PP75 conjugated with 5 mol% cysteamine: SH-PP75 (5%)

The FTIR spectra shows absorption peaks characteristic of N-H and O-H stretch (3271 cm^{-1}); aromatic C-H stretch (3069 cm^{-1}); alkyl C-H stretches (2931 cm^{-1} and 2857 cm^{-1}); amid band I and II (1634 cm^{-1} and 1532 cm^{-1}) indicating secondary amide bond formation following poly-condensation during the synthesis of PLP; C-O bond peak at 1304 cm^{-1} indicating the presence of the carboxylic acid.

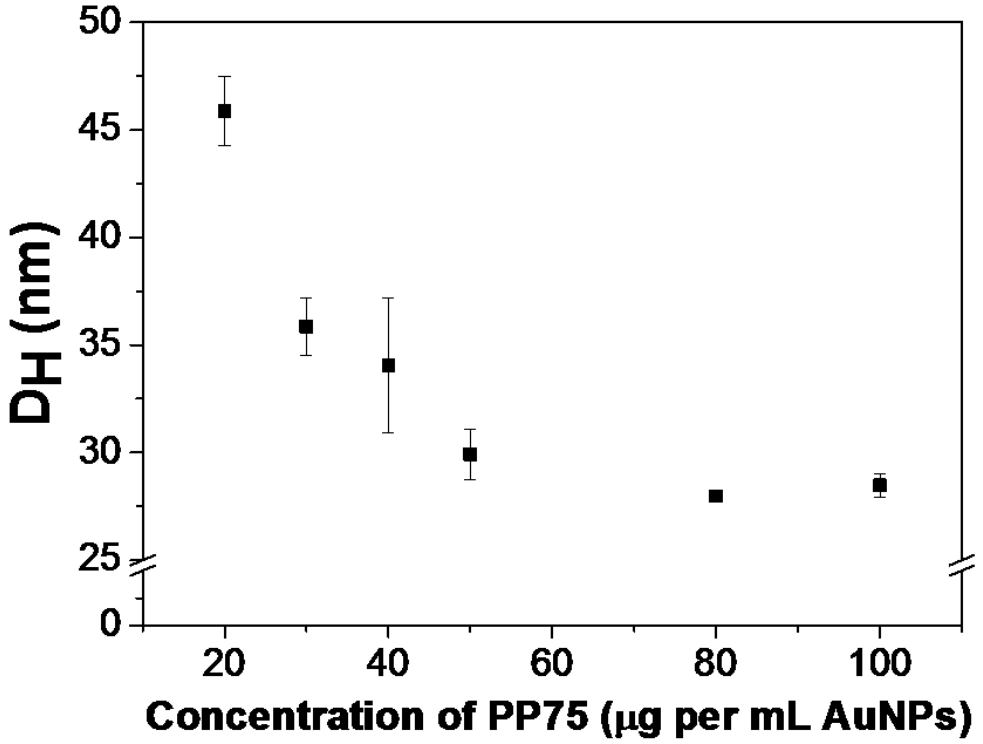
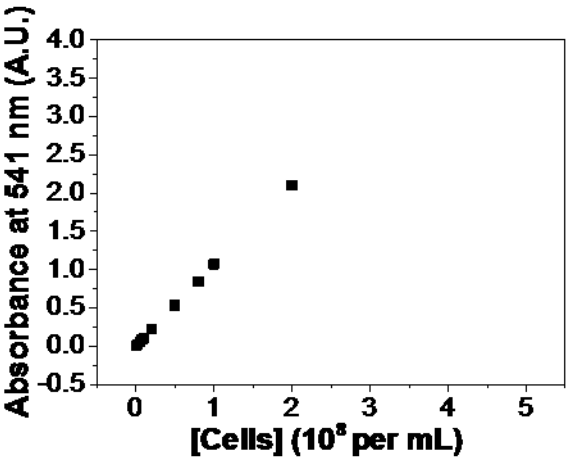


Figure B-4 Influence of the polymer concentration on the hydrodynamic size in H_2O measured via DLS. Error bars represent standard deviations of three samples with six runs each.

A



B

Linear fit $[0.01\text{-}2].10^8$	[Cells] 10^8 per mL
Slope	1.064
Intercept	-0.00
R^2	1.00

Figure B-5 (A) Calibration curve of RBCs haemoglobin. (B) Calibration linear fit parameters.

Appendix C

- Determination of the amount of DOX for maximum coverage.

$$FP_1\ (nm^2\ per\ molecule) = \frac{S_1}{N_{DOX/NP_1}} = \frac{4\pi r_1^2}{N_{DOX/NP1}} \quad \text{(C-1)}$$

$$FP_2\ (nm^2\ per\ molecule) = \frac{S_2}{N_{DOX/NP_2}} = \frac{4\pi r_2^2}{N_{DOX/NP2}} \quad \text{(C-2)}$$

Where *FP* is the foot print of the drug molecule; S the surface of one AuNPs assuming they are spherical; r the radius of AuNPs and $N_{DOX/NP}$ the number of molecules per NP. The numbers "1" and "2" refer to the literature[116] and to the system reported herein respectively.

Using (C-1) = (C-2) $N_{DOX/NP2}$ was estimated at 865 DOX molecules per NP with r_2 = 8.15nm and S_2=835nm^2.

$$\mathrm{n_{DOX}}\ (\text{mol per mL AuNPs}) = N_{DOX/NP2}.C_{AuNPs} \quad \text{(C-3)}$$

Where n_{DOX} is the maximum number of moles of DOX molecules per mL AuNPs and C_{AuNPs} is the molar concentration of AuNPs ($6.41.10^{-6}$ M). n_{DOX} was found to be equal at $5.55.10^{-9}$ moles.

$$\mathrm{m_{DOX}}\ (\text{g per mL AuNPs}) = 3.22 \quad \text{(C-4)}$$

Where m_{DOX} is the amount of DOX added per mL AuNPs solution. In order to achieve 100% maximum coverage 3.22 µg have to be added to 1 mL AuNPs.

- Determination of the initial loading DOX/AuNPs ratios

The initial concentrations of DOX in the mixture are expressed as wt% and have been calculated as follows:

$$DOX/AuNPs\ (wt\%) = \frac{m_{DOX}}{m_{AuNPs}} \quad \text{(C-5)}$$

$$m_{AuNPs}(g\ per\ mL\ AuNPs) = M_{wAuNPs}.C_{AuNPs} \quad \text{(C-6)}$$

$$M_{wAuNPs}(g/mol\ AuNPs) = m_{1part}.N_A \quad \text{(C-7)}$$

$$m_{1part}(g) = \frac{\frac{N_{Au}.M_{Au}}{NP}}{N_A} \quad \text{(C-8)}$$

$$N_{Au/NP}\ (number) = \frac{V_{AuNP}}{V_{Au}} = \frac{\frac{4}{3}\pi\left(\frac{d}{2}\right)^3}{\frac{M_{Au}}{(d_{Au}.N_A)}} \quad \text{(C-9)}$$

Where m_{AuNPs} is the mass of AuNPs in 1 mL of solution; M_{wAuNPs} is the molecular weight of the AuNPs solution; m_{1part} is the mass of one AuNP; N_A is the Avogadro constant; $N_{Au/NP}$ is the number of gold atoms per AuNP; M_{Au} is the molecular weight of gold (197g mol^{-1}); d_{Au} is the density of gold (19.3.10^{6}g m^{-3}).

Combining (C-6) to (C-9) the mass of AuNPs was obtained:

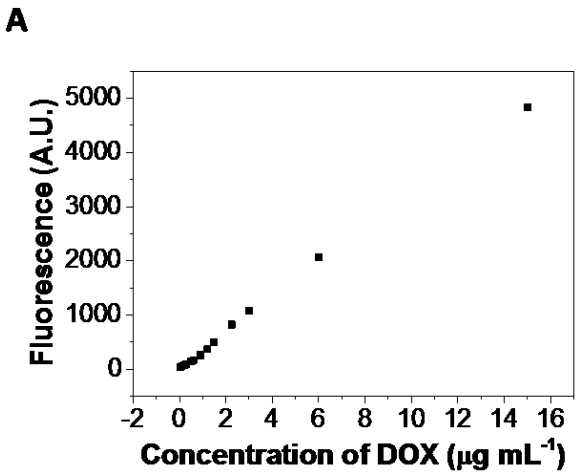
$$m_{AuNPs} = \frac{4}{3}\pi\left(\frac{d}{2}\right)^3.d_{Au}.N_A.C_{AuNPs} \quad \text{(C-10)}$$

And the mass concentration of AuNPs was found to be 168 µg mL^{-1}.

The mass ratio was then calculated according to equation (C-5) and are presented in Table 5-1.

Likewise, the initial amount of PP75 added were expressed in PP75/AuNPs weight ratios (wt%) (Table 5-2) and were calculated with the below formula:

$$PP75/AuNPs\ (wt\%) = \frac{m_{PP75}}{m_{AuNPs}} \quad \text{(C-11)}$$



B

Linear fit	
Slope	324.74179
Intercept	16.64792
R^2	0.99826

Figure C-1 (A) Calibration of DOX via fluorescence. (B) Calibration linear fit parameters.

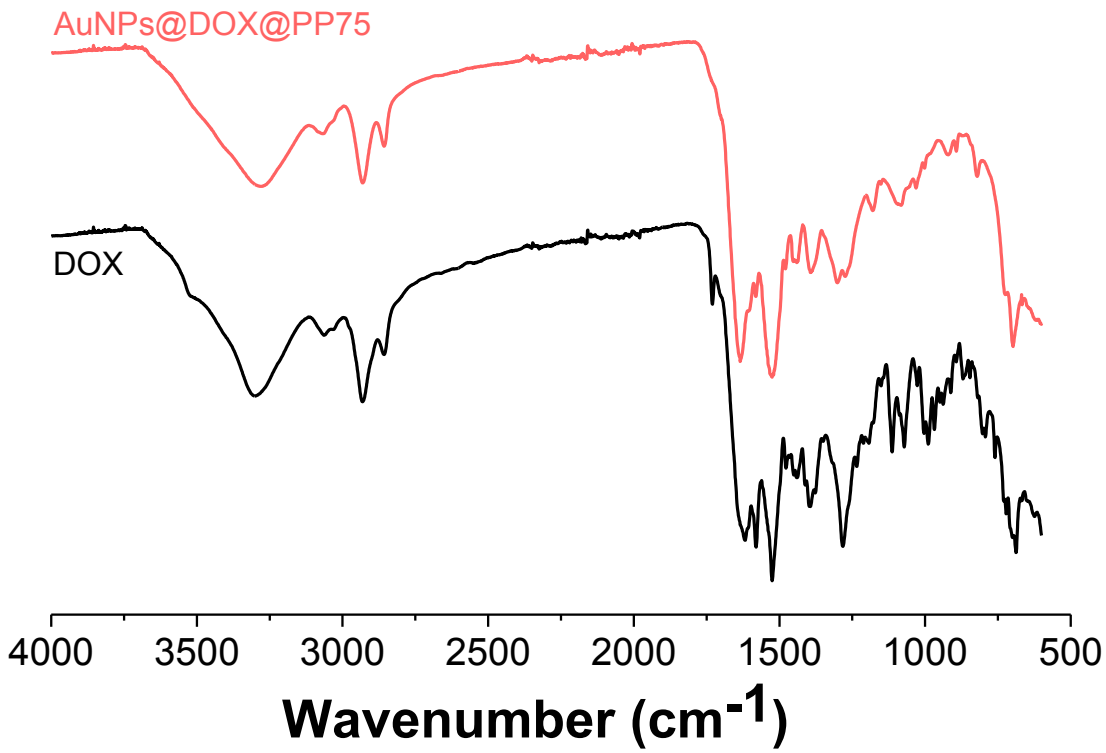


Figure C-2 FTIR spectra of DOX and AuNPs@DOX@PP75.

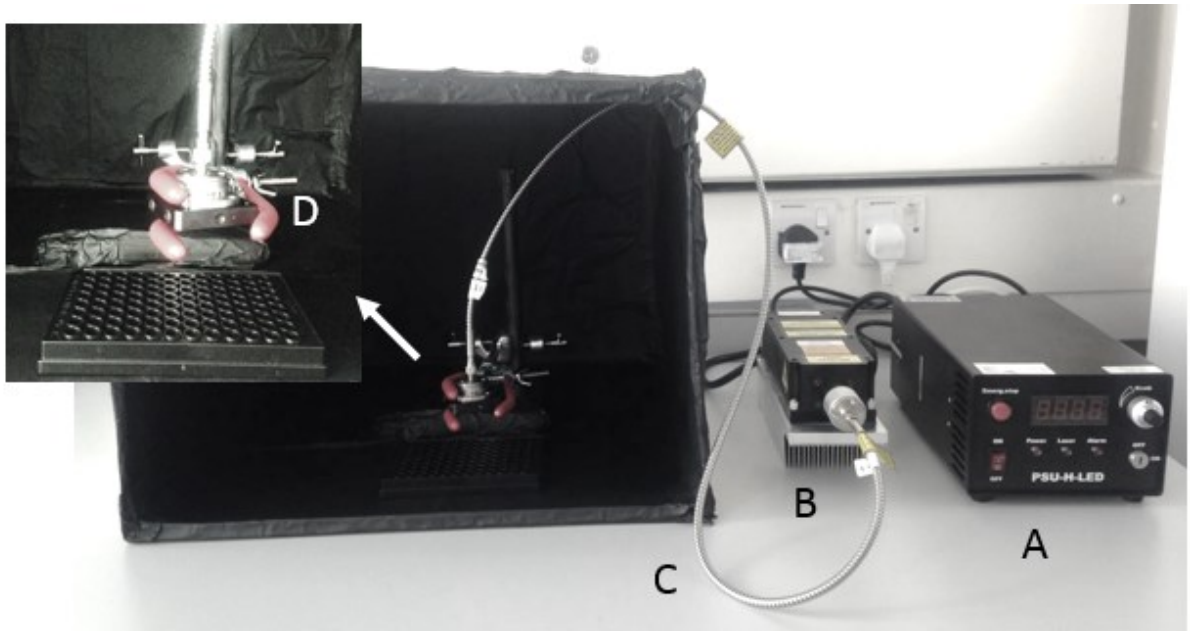
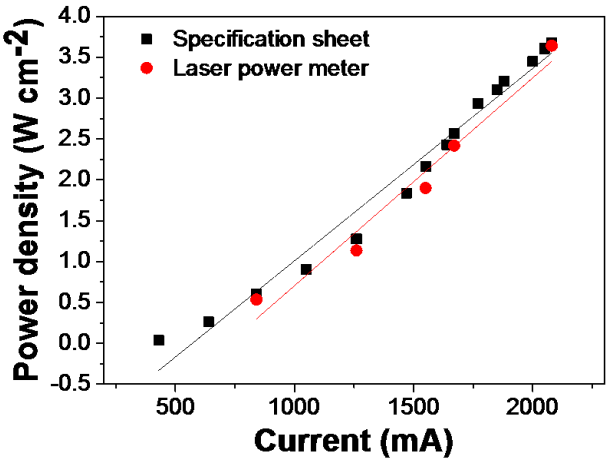


Figure C-3 Set up for laser-therapy. (A) Laser power, (B) laser head, (C) fibre, (D) collimator.

A



B

	Specification sheet	Laser power meter
Slope	0.00236	0.00254
Intercept	-1.34528	-1.8378
R^2	0.97567	0.9565

Figure C-4 (A) Calibration of the laser power density vs. current based on the specifications sheet provided and the power measured with the laser power meter. (B) Calibration linear fit parameters. *Dr. Roberto Ibarra Hernandez assisted me for the measure of the calibration of the laser.*

Appendix D

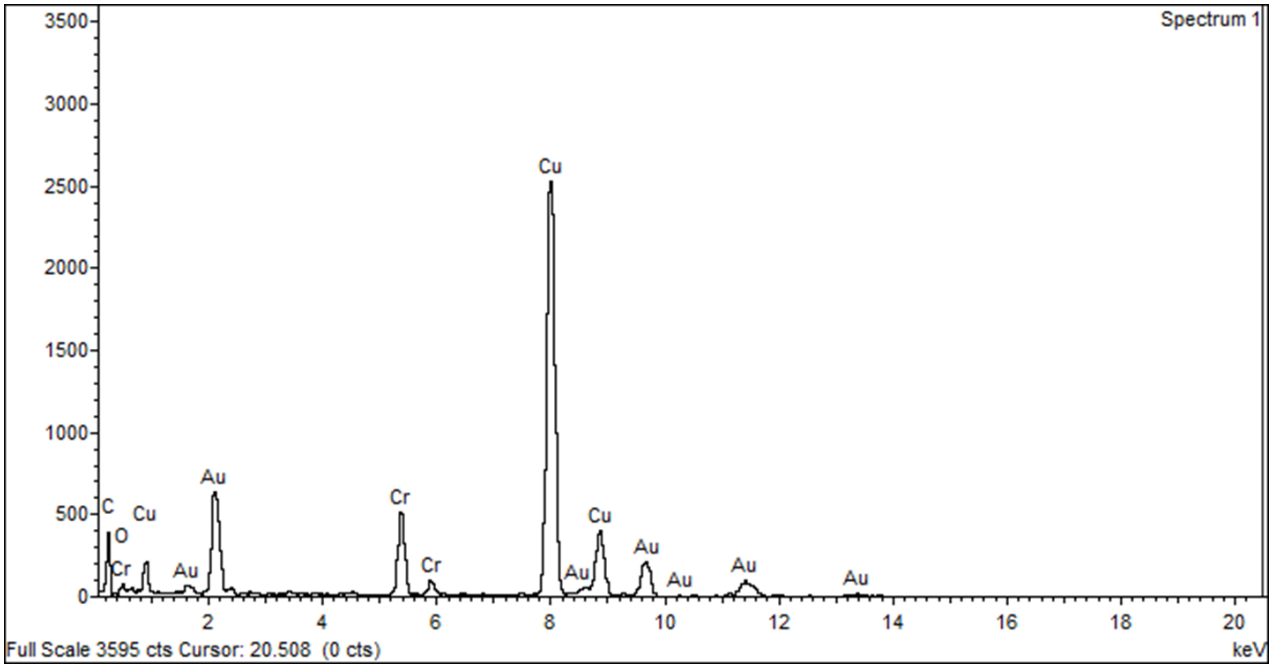


Figure D-1 EDX spectra of AuNPs. *The hydrogels samples were provided by Yubai Zhang.*

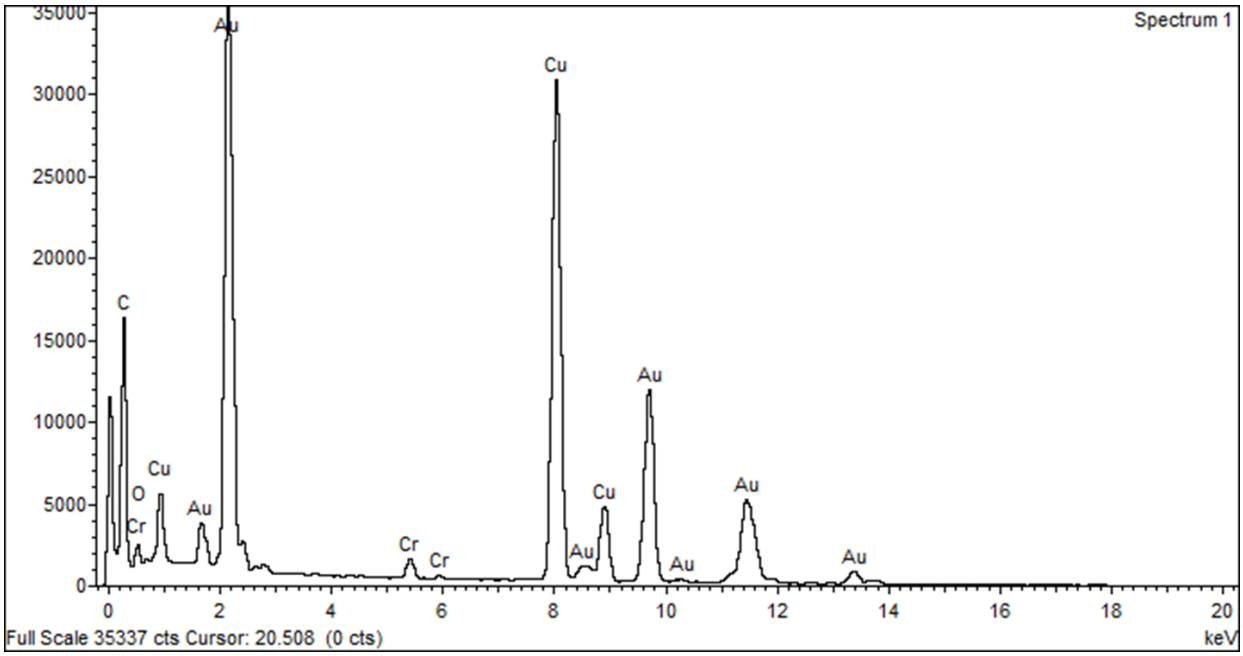


Figure D-2 EDX spectra of AuNPs@PP75. *The hydrogels samples were provided by Yubai Zhang.*

Table D-1 AuNPs loaded hydrogels formulae. *The hydrogel samples were provided by Yubai Zhang in Dr Chen's group*.

Gels number	PLP [mg]	CDE [mg]	AuNPs [µL]	AuNPs/PLP[b] [wt%]	Solid content[c] [wt%]
PLP	75	19	0	0	5.9
1	75	19	600	0.16	5.9
2	75	19	450	0.12	5.9
3	100	25	600	0.12	7.7
4	75	19	150	0.04	5.9
5	75	19	300	0.08	5.9
6	75	19	900	0.24	5.9
7	75	19	900(2x) [a]	0.48	5.9
8	100	25	360	0.09	7.7
9	25	6	150	0.12	2.0
10	50	13	300	0.12	4.0
11	100	25	600(2x) [a]	0.24	7.7

[a]corresponds to ~20 nM AuNPs

[b-c] refer to Chapter 2 Materials and Methods section 2.2.8 for calculations details.

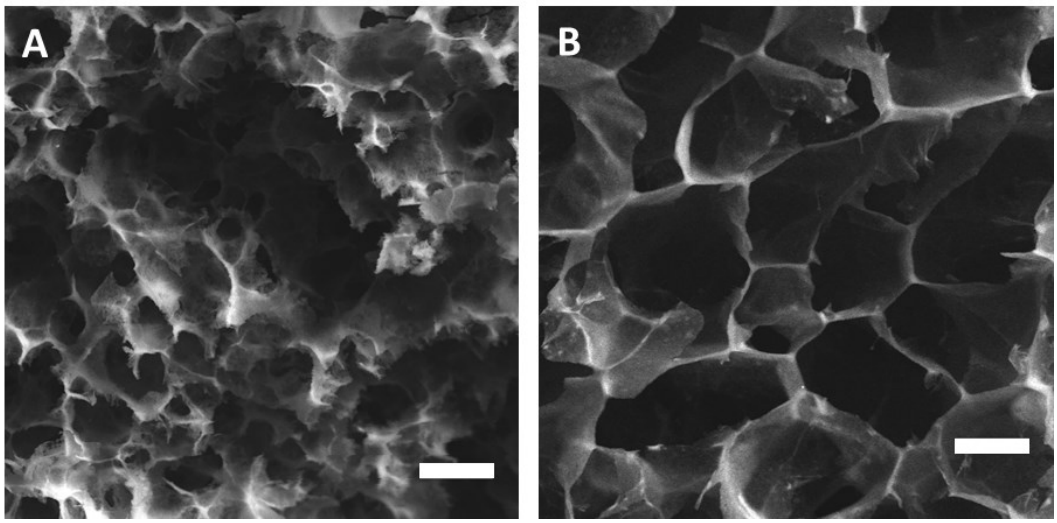


Figure D-3 TEM images of PLP hydrogel at A. pH 3.0 and B. pH 7.4. Scale bar 20 µm. *The hydrogel samples were provided by Yubai Zhang in Dr Chen's group*.

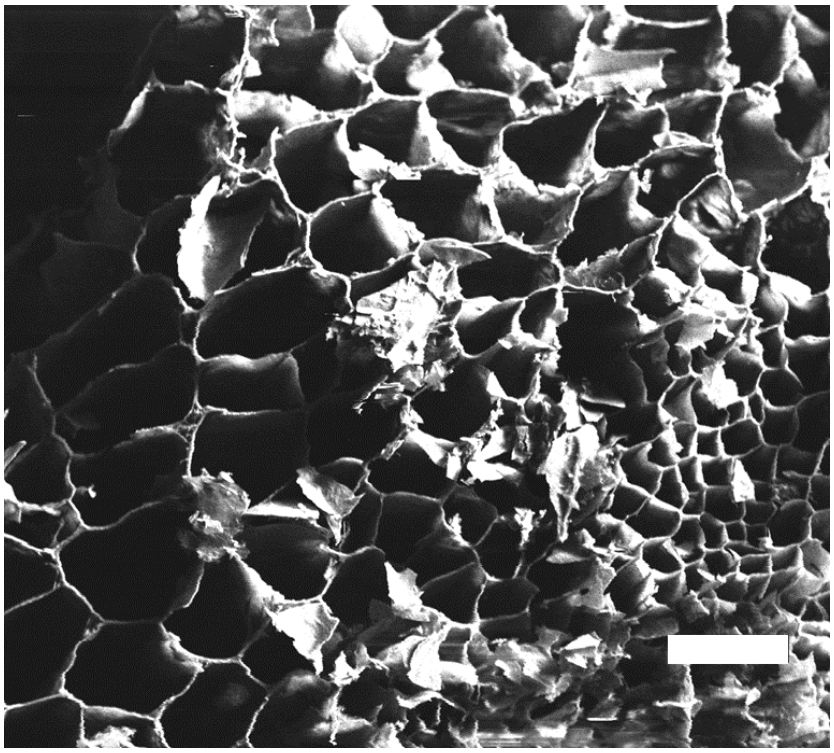


Figure D-4 TEM images of gel 5 at pH 7.4. Scale bar 100 μm. *The hydrogel samples were provided by Yubai Zhang in Dr Chen's group*.

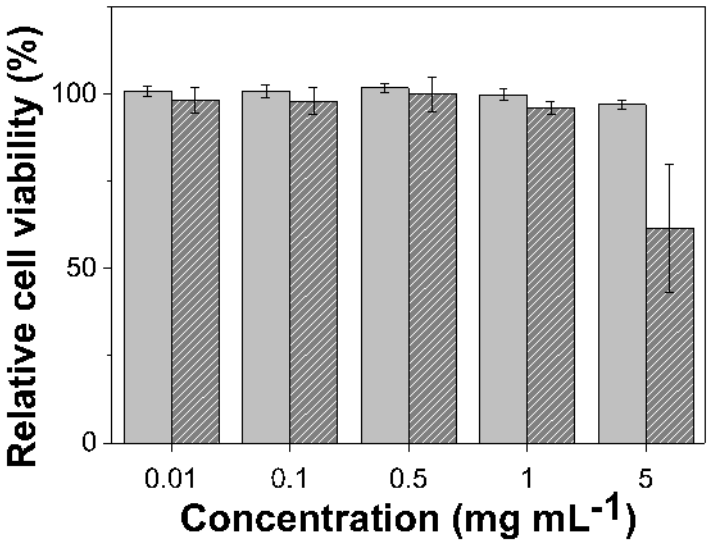


Figure D-5 Concentration dependant cytotoxicity of Gel 2 evaluated via alamarBlue assay for 24h treatment (grey bars) and 72h treatment (striped bars) of HeLa cells. Error bars represent the deviation between 10 replicates. *The hydrogel samples were provided by Yubai Zhang in Dr Chen's group*.

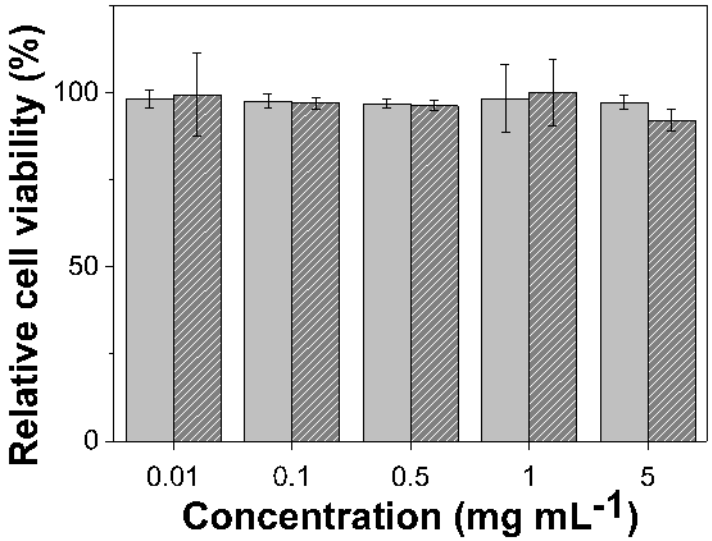
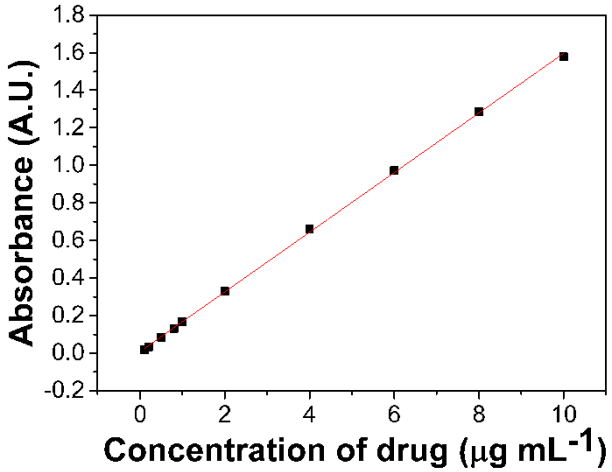


Figure D-6 Concentration dependant cytotoxicity of Gel 3 evaluated via alamarBlue assay for 24h treatment (grey bars) and 72h treatment (striped bars) of HeLa cells. Error bars represent the deviation between 10 replicates. *The hydrogel samples were provided by Yubai Zhang in Dr Chen's group*.



	Linear fit
Slope	0.15886
Intercept	0.00832
R^2	0.99965

Figure D-7 Curve of the fluorescein via absorbance and relative linear fit data. *Performed by Yubai Zhang in Dr Chen's group*.

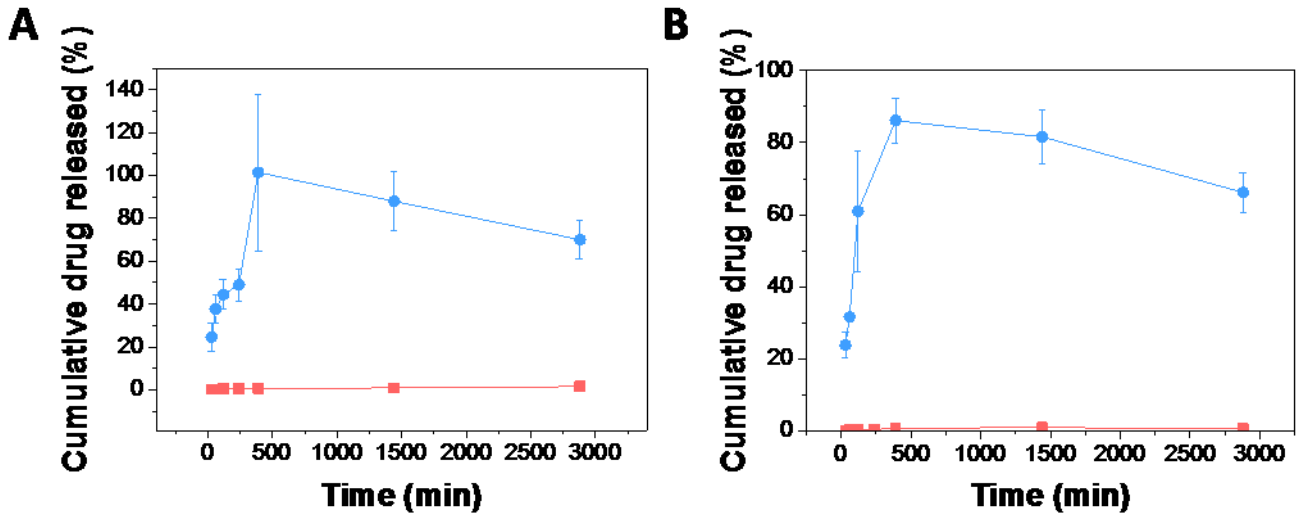


Figure D-8 Drug release profiles at pH 7.4 and pH 3.0 obtained for AuNPs@PP75/hydrogels (A) Gel 1 and (B) Gel 2. *Performed by Yubai Zhang in Dr Chen's group*.

Appendix E Copyright permissions

Page No.	Type of work	Name of work	Source of work	Copyright holder and contact	Permission requested on	Permission	Permission note
71	Figure	Figure 5. Representation of how PEGylation avoids clearance of NPs by the RES.	Barreto *et al.*[13]	2011 WILEY-VCH Verlag GmbH & Co. KGaA, Weinheim	09/02/2017	YES	Copyright permission obtained via the Copyright Clearance Center's RightsLink service (License number: 4044701334587). Type of use: Dissertation/Thesis. Format: Print and electronic.
46	Figure	Figure 7. Examples of NPs used for cancer treatment and diagnosis. a) polymeric nanoparticles, b) liposomes, c) QDs, which usually posses a CdSe core, d) gold NPs, e) zeolite L, f) magnetic NPs, traditionally iron oxide, g)	Barreto *et al.*[13]	2011 WILEY-VCH Verlag GmbH & Co. KGaA, Weinheim	09/02/2017	YES	Copyright permission obtained via the Copyright Clearance Center's RightsLink service (License number: 4044701334587). Type of use: Dissertation/Thesis. Format: Print and electronic.

		dendrimers, h) nanotubes, i) upconverting nanophosphors.					
46	Image	AN1066672001 AN1066673001 AN1066982001 AN1377384001	British museum website http://www.britishmuseum.org/research/collection_online/collection_object_details/collection_image_gallery.aspx?assetId=36154001&objectId=61219&partId=1#more-views	The Trustees of the British Museum	09/02/2017	YES	You are permitted to use images from the British Museum website subject to our terms of use. The image released to you under a Creative Commons Attribution-NonCommercial-ShareAlike 4.0 International (CC BY-NC-SA 4.0) license.
50	Figure	Figure 1. Scanning electron microscope and transmission electron microscope micrographs of gold nanostructures of various shapes and sizes. (A)	Li and Chen[36]	Future Medicine 2015	09/02/2017	YES	Mail sent (from website) on 09/02/2017 Confirmation received on 14/02/2017

		Nanospheres, (B) nanorods, (C) nanoshells, (D) nanoprismss, (E) nanocages, (F) nanostars, (G) nanovesicles, (H) rhombic dodecahedras, and (I) bipyramids.					
53	Figure	Fig. 1 (a) UV-visible spectra of Au NPs with different mean diameters synthesized in this study (absorbance adjusted to the same value). (b) Spectra of 15 nm AuNPs before and after PEGylation, the inset shows the clear red shift of about 2 nm after PEGylation. Fig. 2 TEM micrographs of Au nanoparticles with mean diameters of (a) ~15 nm, (b) ~23 nm, (c) ~30 nm, (d) ~63 nm, (e) ~93 nm and (g) ~135 nm. SEM images of Au nanoparticles with mean diameters of (f) y115 nm and (h) y170 nm. The insets show higher magnification electron	Rahme *et al.*[46]	The Royal Society of Chemistry 2013	19/02/2017	YES	Copyright permission obtained via the Copyright Clearance Center's RightsLink service (License number: 4052350392370). Type of use: Dissertation/Thesis. Format: Print and electronic.

		micrographs, and optical photographs of the corresponding colloidal solutions.					
53	Figure	Figure 3. Photograph of (AuNP/PEG-SH) overnight/adenine. The PEG-SH concentrations in vials a to k are 0, 0.0003, 0.003, 0.03, 0.17, 0.3, 0.7, 1.3, 2, 2.7, and 3.3 μM, respectively.	Siriwardana *et al.*[47]	American Chemical Society 2014	19/02/2017	YES	Copyright permission obtained via the Copyright Clearance Center's RightsLink service. Type of use: Dissertation/Thesis. Format: Print and electronic.
57	Figure	Fig. 10. A schematic illustration of drug delivery via 'active' and 'passive' targeting, solid and dotted line respectively	Ghosh *et al.*[145]	Elsevier BV 2008	18/02/2017	YES	Copyright permission obtained via the Copyright Clearance Center's RightsLink service (License number: 4051800312289). Type of use: Dissertation/Thesis. Format: Print and electronic.
76	Figure	Figure 1 Framework of sequential biological barriers to nanoparticle drug delivery.	Blanco *et al.*[102]	Nature America, Inc. 2015	19/02/2017	YES	Copyright permission obtained via the Copyright Clearance Center's RightsLink service (License number: 4052450974943). Type of use:

64		Figure 5 Nanoparticle size, shape and surface charge dictate biodistribution among the different organs including the lungs, liver, spleen and kidneys.					Dissertation/Thesis. Format: Print and electronic.
59	Figure	Fig. 4 Schematic describing the principle of photothermal light to heat conversion by plasmonic nanostructures	Webb and Bardhan[62]	Royal Society of Chemistry 2014	19/02/2017	YES	Copyright permission obtained via the Copyright Clearance Center's RightsLink service (License number: 4052520834849). Type of use: Dissertation/Thesis. Format: Print and electronic.
60	Figure	Figure 4. Contrast enhancement of OCT images of an in vivo tumor model.	Liba *et al.*[68]	Creative Commons Attribution 4.0 International License	19/02/2017	YES	Copyright permission obtained via the Copyright Clearance Center's RightsLink service "The article for which you have requested permission has been distributed under a Creative Commons CC-BY license (please see the article itself for the license version number). You may reuse this material without obtaining permission from Nature Publishing Group, providing that the author and the original source

							of publication are fully acknowledged, as per the terms of the license."
60	Figure	Fig. 1. Schematic illustration of SERS-based cell imaging for the rapid detection and quantification of growth factor receptors on breast cancer cell membranes	Lee *et al.*[74]	Elsevier B.V. 2013	19/02/2017	YES	Copyright permission obtained via the Copyright Clearance Center's RightsLink service (License number: 4052541290476). Type of use: Dissertation/Thesis. Format: Print and electronic.
60	Figure	Figure 4. (a)–(c) Combined ultrasound and photoacoustic images, and (d)–(f) photoacoustic-based thermal images. The arrow represents the direction of CW laser irradiation (808 nm, 1 W).	Kim *et al.*[73]	IEEE 2014	19/02/2017	YES	The IEEE does not require individuals working on a thesis to obtain a formal reuse license. Statement printed in pdf.
61	Figure	Fig. 1. The principle of AGR2 detection based on HCR amplification. (For interpretation of the references to colour in the text, the reader	Li *et al.*[80]	Elsevier B.V. 2016	19/02/2017	YES	Copyright permission obtained via the Copyright Clearance Center's RightsLink service (License number: 4052571217178). Type of use: Dissertation/Thesis. Format: Print and electronic.

		is referred to the web version of this article.)					
62	Figure	Figure 1. A Schematic representation of synthesis of DOX@Gold NMs and their potential theranostic application.	Deng *et al.*[86]	WILEY-VCH Verlag GmbH & Co. KGaA, Weinheim 2015	20/02/2017	YES	Copyright permission obtained via the Copyright Clearance Center's RightsLink service (License number: 4053151181466). Type of use: Dissertation/Thesis. Format: Print and electronic.
63	Figure	Figure 8 Viability data (derived from MTT assay) collected from recent literature on HeLa cells incubated with AuNPs of different sizes and at different concentrations. AuNPs are differently functionalized.	Fratoddi *et al.*[100]	Tsinghua University Press and Springer-Verlag Berlin Heidelberg 2015	20/02/2017	YES	Copyright permission obtained via the Copyright Clearance Center's RightsLink service (License number: 4053140108937). Type of use: Dissertation/Thesis. Format: Print and electronic.
66	Figure	Figure 1. Total number of publications (Web of Science®) and clinical trials (clinicaltrials.gov) during the last 10 years.	Wicki *et al.*[104]	Elsevier B.V. 2014	20/02/2017	YES	Copyright permission obtained via the Copyright Clearance Center's RightsLink service (License number: 4053170333195). Type of use:

65 67	Figure Table	Figure 3 Schematic illustration of established nanotherapeutic platforms. Table 6. Inorganic nanoparticles in clinical trials.					Dissertation/Thesis. Format: Print and electronic.
69	Figure	Figure 3 Multifunctional nature of AuNPs	Bachelet[112]	Institute of Materials, Minerals and Mining 2016	19/012/2016	YES	Copyright permission obtained via the Copyright Clearance Center's RightsLink service.
74	Figure	Figure 6, Schematic illustration for the enhanced cellular uptake of AuNPs by anti-EGFR antibody and glutathione-mediated intracellular release of AuNP-2 carriers.	Park *et al.*[122]	Royal Society of Chemistry 2009	21/02/2017	YES	Authors contributing to RSC publications (journal articles, books or book chapters) do not need to formally request permission to reproduce material contained in this article provided that the correct acknowledgement is given with the reproduced material.
75	Figure	Fig. 1 Different forms of hydrogel nanocomposites: bulk nanocomposites, particle	Satarkar *et al.*[152]	Royal Society of Chemistry 2009	21/02/2017	YES	Authors contributing to RSC publications (journal articles, books or book chapters) do not need to formally request permission to reproduce material contained in this article

		nanocomposites, and core-shell nanocomposites.					provided that the correct acknowledgement is given with the reproduced material.
77	Figure	Figure 1 Schematic of endocytosis and exocytosis patterns of nanoparticles. Nanoparticles enter the cell via four types of pathway: clathrin/caveolar-mediated endocytosis, phagocytosis, macropinocytosis, and pinocytosis. Nanoparticles exit the cell via three types of pathway: lysosome secretion, vesicle-related secretion, and non-vesicle-related secretion.	Oh and Park[157]	Oh and Park 2014	21/02/2017	YES	This work is published by Dove Medical Press Ltd, and licensed under Creative Commons Attribution – Non Commercial (unported, v3.0) License. Non-commercial uses of the work are permitted without any further permission from Dove Medical Press Ltd, provided the work is properly attributed.
78	Figure	Figure 7. Internalization process of PEGylated NPs and related free energy change. (A) Snapshots of PEGylated NPs used in the dissipative particle dynamics (DPD) simulations with two grafting densities: 0.2	Shen *et al.*[159]	NA	NA	YES	Open access

		and 1.6 chains/nm2. The diameter of the NP core is about 8 nm.					
79	Figure	Figure 1 Mechanisms of MDR towards cancer chemotherapeutic drugs. Figure 2 Proposed drug efflux mechanism for ABC transporters. Substrate and ATP bind to ATP transporters. After ATP hydrolysis, the substrate is effluxed out of the cell. Phosphate group is released and the substrate is then excreted to extracellular matrix.	S. Chai *et al.*[160]	Chai et al 2010	NA	YES	This is an Open Access article distributed under the terms of the Creative Commons Attribution License (http://creativecommons.org/licenses/by/2.0), which permits unrestricted use, distribution, and reproduction in any medium, provided the original work is properly cited.
80	Figure	Fig. 2 Mechanism of endosomal escape of nanocarrier. Uptake of nanocarriers by endocytosis leads to entrapment of drugs and nucleic acid drugs within the endosomes and is not available for pharmacological	Mundra and Mahato[163]	Higher Education Press and Springer-Verlag Berlin Heidelberg 2014	21/02/2017	YES	Copyright permission obtained via the Copyright Clearance Center's RightsLink service (License number: 4053740860043). Type of use: Dissertation/Thesis.

		action. Acidification of endosomes by V type proton pump is utilized as stimuli by nanocarriers and virus for formation of pores across the membrane, for fusion of endosomal membrane and carrier, for disruption of membrane and for osmolysis of endosomes by proton sponge effect					
81	Figure	Figure 10. pH-dependent ionization of polyelectrolytes. (a) Poly(acrylic acid) and (b) poly(N,N'-diethylaminoethyl methacrylate).	Bahram *et al.*[166]	The authors	21/02/2017	YES	This chapter is distributed under the terms of the Creative Commons Attribution License (http://creativecommons.org/licenses/by/3.0), which permits unrestricted use, distribution, and reproduction in any medium, provided the original work is properly cited

86	Figure	Abstract figure	P.S. Ghosh *et al.*[184]	American Chemical Society 2008	21/02/2017	21/02/2017	Copyright permission obtained via the Copyright Clearance Center's RightsLink service. Type of use: Dissertation/Thesis. Permission is granted for your request in both print and electronic formats, and translations.
86	Figure	Abstract figure	S. Son *et al.*[189]	American Chemical Society 2014	22/02/2017	YES	Copyright permission obtained via the Copyright Clearance Center's RightsLink service. Type of use: Dissertation/Thesis. Permission is granted for your request in both print and electronic formats, and translations.
131	Figure	Figure S1. (a) TEM image of the citrate-coated AuNPs and (b) their particle size distribution via TEM image analysis.	Bachelet and Chen[232]	Royal Society of Chemistry 2016	YES	19/12/2016	Authors contributing to RSC publications (journal articles, books or book chapters) do not need to formally request permission to reproduce material contained in this article provided that the correct acknowledgement is given with the reproduced material.

141	Figure	Figure S6. Determination of the minimum amount of PEG for stabilization of AuNPs in 50 mM MES buffer at pH 5.5 (0.15 M NaCl). Absorbance profiles of (a) AuNPs@PEG0.8k, (b) AuNPs@PEG2k and(c) AuNPs@PEG6k at 6 h after redispersion in the MES buffer with different amounts of PEG added. (d) Maximal absorbance of these samples redispersed in the MES as a function of the quantity PEG added. Errors bars represent the standard deviations of triplicates.	Bachelet and Chen[232]	Royal Society of Chemistry 2016	YES	19/12/2016	Authors contributing to RSC publications (journal articles, books or book chapters) do not need to formally request permission to reproduce material contained in this article provided that the correct acknowledgement is given with the reproduced material.
144	Scheme	Scheme 1. Model of the thiol-PEG modification process of AuNPs.	Wang *et al.*[208]	Elsevier Inc. 2013	YES	10/03/2017	Copyright permission obtained via the Copyright Clearance Center's RightsLink service (License number: 4065301372947). Type of use:

							Dissertation/Thesis. Format: Print and electronic
145	Figure	Figure S7. Grafting density of the PEGylated AuNPs determined via the Ellman's assay. Errors bars represent the standard deviation between triplicates.	Bachelet and Chen[232]	Royal Society of Chemistry 2016	YES	19/12/2016	Authors contributing to RSC publications (journal articles, books or book chapters) do not need to formally request permission to reproduce material contained in this article provided that the correct acknowledgement is given with the reproduced material.
147	Figure	Figure S8. Relative absorbance (ratio of the SPR absorbance after and before redispersion) of the AuNPs and the PEGylated AuNPs in different media: dH2O (pH~6); Buffer 1 (50 mM PBS at pH 7.4, 0.15 M NaCl) and Buffer 2 (50 mM MES at pH 5.5, 0.15 M NaCl). Errors bars represent the	Bachelet and Chen[232]	Royal Society of Chemistry 2016	YES	19/12/2016	Authors contributing to RSC publications (journal articles, books or book chapters) do not need to formally request permission to reproduce material contained in this article provided that the correct acknowledgement is given with the reproduced material.

		standard deviation between triplicates.					
149	Figure	Figure S9. TEM images of (a) the AuNPs@PEG0.8k showing the visible polymer layer, and (b) the representative single nanoparticle in the AuNPs@PEG0.8k.	Bachelet and Chen[232]	Royal Society of Chemistry 2016	YES	19/12/2016	Authors contributing to RSC publications (journal articles, books or book chapters) do not need to formally request permission to reproduce material contained in this article provided that the correct acknowledgement is given with the reproduced material.
150	Scheme	Figure S10. Schematic of the PEG conformation (a) in a mushroom regime and (b) in a brush regime. D is the distance between PEG attachments, L is the height of the brush domain, RF is the Flory radius and FP is	Bachelet and Chen[232]	Royal Society of Chemistry 2016	YES	19/12/2016	Authors contributing to RSC publications (journal articles, books or book chapters) do not need to formally request permission to reproduce material contained in this article provided that the correct acknowledgement is given with the reproduced material.

		the footprint of the polymer (nm2 per chain).					
150 152 163	Table	Table 1 Characteristics of the satellite structures and the polymer layers Table S1. Characteristics of the polymer layer	Bachelet and Chen[232]	Royal Society of Chemistry 2016	YES	19/12/2016	Authors contributing to RSC publications (journal articles, books or book chapters) do not need to formally request permission to reproduce material contained in this article provided that the correct acknowledgement is given with the reproduced material.
156	Figure	Figure 5. Schematic illustrating the influence of PEG density on serum protein adsorption to gold nanoparticles and their subsequent uptake by macrophages.	Walkey *et al.*[205]	American Chemical Society 2011	YES	11/03/2017	Copyright permission obtained via the Copyright Clearance Center's RightsLink service. PERMISSION/LICENSE IS GRANTED FOR YOUR ORDER AT NO CHARGE
157 293	Figure Figure	Fig. 1 TEM images of (a) AuNPs@PEG0.8k, (b) AuNPs@PEG2k and (c) AuNPs@ PEG6k (scale bar 100 nm) with one representative satellite structure shown in	Bachelet and Chen[232]	Royal Society of Chemistry 2016	YES	19/12/2016	Authors contributing to RSC publications (journal articles, books or book chapters) do not need to formally request permission to reproduce material contained in this article provided that the correct

		their respective insets (scale bar 20 nm). (d) Particle size distribution of the satellite structures in AuNPs@PEG6k via TEM image analysis.					acknowledgement is given with the reproduced material.
162	Figure	Fig. 2 TEM images of (a) AuNPs@PEG2k under defocused conditions (scale bar 50 nm) and (b) representative satellite structure in the AuNPs@ PEG2k assembly under defocused conditions (scale bar 20 nm).	Bachelet and Chen[232]	Royal Society of Chemistry 2016	YES	19/12/2016	Authors contributing to RSC publications (journal articles, books or book chapters) do not need to formally request permission to reproduce material contained in this article provided that the correct acknowledgement is given with the reproduced material.
164	Figure	Fig. 3 Multilayer assembly of the AuNPs@PEG showing apparent (a) chainlike structures in AuNPs@PEG6k (scale bar 50 nm) and (b) a Moire´ pattern in AuNPs@PEG2k (scale bar 20 nm).	Bachelet and Chen[232]	Royal Society of Chemistry 2016	YES	19/12/2016	Authors contributing to RSC publications (journal articles, books or book chapters) do not need to formally request permission to reproduce material contained in this article provided that the correct acknowledgement is given with the reproduced material.

165	Figure	Figure 1. a) Schematic showing a Au nanorod stabilized by a cetyltri- methylammonium bromide (CTAB) bilayer, and the droplet-evaporation-induced formation of ordered Au nanorod superstructures;	Ming *et al.*[226]	Wiley-VCH Verlag GmbH & Co. KGaA, Weinheim 208	YES	11/03/2017	Copyright permission obtained via the Copyright Clearance Center's RightsLink service (License number: 4066060723565). Type of use: Dissertation/Thesis. Format: Print and electronic
166	Figure	Fig. 4 Schematic of the suggested self-assembly mechanism during the slow evaporation process on a carbon-coated grid.	Bachelet and Chen[232]	Royal Society of Chemistry 2016	YES	19/12/2016	Authors contributing to RSC publications (journal articles, books or book chapters) do not need to formally request permission to reproduce material contained in this article provided that the correct acknowledgement is given with the reproduced material.

159	Figure	Figure S2. Particle size distributions in (a) AuNPs@PEG0.8k, (b) AuNPs@PEG2k and (c) AuNPs@PEG6k via TEM image analysis.	Bachelet and Chen[232]	Royal Society of Chemistry 2016	YES	19/12/2016	Authors contributing to RSC publications (journal articles, books or book chapters) do not need to formally request permission to reproduce material contained in this article provided that the correct acknowledgement is given with the reproduced material.
160 160	Table Figure	Figure S5. Typical independent satellite structures in (a) AuNPs@PEG0.8k, (b) AuNPs@PEG2k and (c) AuNPs@PEG6k via TEM image analysis	Bachelet and Chen[232]	Royal Society of Chemistry 2016	YES	19/12/2016	Authors contributing to RSC publications (journal articles, books or book chapters) do not need to formally request permission to reproduce material contained in this article provided that the correct acknowledgement is given with the reproduced material.